

Institute of Geography  
University of Fribourg, Switzerland

**RELATIONSHIP BETWEEN HAILFALL INTENSITY AND HAIL  
DAMAGE ON GROUND, DETERMINED BY RADAR AND LIGHTNING  
OBSERVATIONS**

THESIS

Presented to the faculty of Science of the University of Fribourg  
for obtaining the grade of  
*Doctor rerum naturalium*

presented by  
ROMAN MARCO HOHL  
born June 14, 1971  
citizen of Wolfhalden (AR), Switzerland

THESIS No. 1357

ADAG Copy AG, Zurich, Switzerland  
Zurich, November 2001

Accepted by the faculty of Science of the University of Fribourg, Switzerland on the proposition of the jury:

Prof. Dr. M. Beniston, University of Fribourg, Switzerland

Prof. Dr. H. Richner, Swiss Federal Institute of Technology (ETH), Zurich, Switzerland

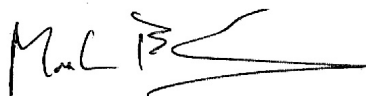
Dr. H.H. Schiesser, Swiss Federal Institute of Technology (ETH), Zurich, Switzerland

Prof. Dr. A. Weis, president of the jury, University of Fribourg, Switzerland

Fribourg, 22 November 2001

The thesis director:

Prof. Dr. M. Beniston

A handwritten signature in black ink, appearing to read 'M. Beniston', with a stylized flourish at the end.

The dean:

Prof. Dr. A. von Zelewsky

A handwritten signature in black ink, appearing to read 'A. von Zelewsky', with a long, sweeping flourish at the end.

**Cover Page:**

Thunderstorm over the Jura mountains, Switzerland, during the afternoon of 19 June 1977.

Picture taken by Dr. Willi Schmid, Atmospheric Science ETH, Zurich, Switzerland with permission

# Contents

<b>Abstract</b>	<b>v</b>
<b>Zusammenfassung</b>	<b>ix</b>
<b>Introduction</b>	<b>1</b>
1.1 Outline.....	1
1.2 Thunderstorm Theory .....	1
1.2.1 Severe Thunderstorms.....	2
1.2.2 Hail Formation .....	4
1.2.3 Hail Suppression .....	6
1.3 Remote Detection of Hail .....	7
1.3.1 Ground Measurements of Hail ( <i>in-situ</i> Detection).....	7
1.3.2 Satellite Measurements of Hail .....	8
1.3.3 Radar Measurements of Hail.....	9
1.3.4 Radar-Based Criteria for the Detection of Hail.....	11
1.3.5 Hail Kinetic Energy: Radar vs. Hailpad Data .....	13
1.3.6 Hail Kinetic Energy: Radar vs. Hail Damage Data.....	15
1.3.7 Radar Data in Switzerland .....	17
1.4 Hail Damage Assessment and Risk Response .....	18
1.4.1 Hail Damage Assessment.....	19
1.4.2 Response to Hail Risk .....	19
1.4.3 Hail Damage Data in Switzerland.....	21
1.5 Prediction of Hailfall.....	23
1.6 Lightning Activity in Severe Thunderstorms.....	24
1.6.1 Lightning Discharges .....	24
1.6.2 Thunderstorm Electrification Processes.....	26
1.6.3 Observation of CG Lightning Activity in Severe Thunderstorms .....	28
1.6.4 CG Lightning Data in Switzerland.....	32
1.7 Introducing the Three Articles .....	32

<b>2. The use of weather radars to estimate hail damage to automobiles: An exploratory study in Switzerland</b>	<b>35</b>
2.1 Abstract .....	35
2.2 Introduction .....	36
2.3 Data .....	38
2.3.1 Insurance Data.....	38
2.3.2 Radar Data.....	40
2.4 Methods.....	42
2.4.1 Attribution of Hailfall Intensity and Damage Claims .....	42
2.4.2 Cross-Correlation and Storm Shifting Method .....	42
2.5 Results .....	45
2.5.1 Storm Scale Analyzes .....	45
2.5.2 The Influence of Seasonal Hailfall Intensity on Damage Variables .....	47
2.5.3 Shifting and Correlation Analyses .....	49
2.5.4 Hailfall Intensity vs. Loss Ratios .....	50
2.5.5 Hailfall Intensity vs. Mean Damages .....	52
2.5.6 Hailfall Intensity vs. Damage Extents.....	52
2.6 Discussion .....	53
2.7 Conclusion .....	55
<b>3. Hailfall: The relationship between radar-derived hail kinetic energy and hail damage to buildings</b>	<b>57</b>
3.1 Abstract .....	57
3.2 Introduction .....	58
3.3 Data .....	61
3.3.1 Radar Data.....	61
3.3.2 Hail Damage Claim Data .....	63
3.4 Methods.....	65
3.4.1 Cross-Correlation of Storm Intensity and Hail Damage Variables.....	65
3.4.2 Damage Functions.....	68
3.5 Results .....	69
3.5.1 Storm Variables.....	70
3.5.2 Storm Shifting and Cross-Correlation Analyses .....	71
3.5.3 Radar-Derived Hail Kinetic Energy vs. Mean Damages .....	72
3.5.4 Radar-Derived Hail Kinetic Energy vs. Total Loss Ratios .....	74
3.5.5 Calibration of Damage Functions for Total Loss Ratios .....	75

3.5.6 The hailstorm of 5 July 1999 .....	77
3.6 Discussion .....	80
3.7 Conclusion .....	83
<b>4. Cloud-to-ground lightning activity in relation to the radar-derived hail kinetic energy in Switzerland</b>	<b>85</b>
4.1 Abstract .....	85
4.2 Introduction .....	86
4.3 Data .....	87
4.3.1 Radar .....	87
4.3.2 CG Lightning .....	88
4.4 Method and Data Correction .....	89
4.4.1 Radar and Lightning Data Analyzes Method .....	89
4.4.2 Data Correction Methods .....	92
4.5 Results .....	94
4.5.1 Storm Scale Analyzes .....	94
4.5.2 Hail Kinetic Energy at Upper and Lower Storm-Level .....	95
4.5.3 Total Hail Kinetic Energy vs. Total CG Stroke Rates .....	95
4.5.4 Temporal-Spatial Relation between Hail Kinetic Energy and CG Stroke Rates .....	96
4.6 Discussion .....	99
4.7 Conclusion .....	102
<b>5. The determination of hailfall areas with cloud-to-ground lightning location data</b>	<b>105</b>
5.1 Introduction .....	105
5.2 Cross-Correlation between –CG Stroke and Hailfall Patterns .....	106
5.3 Methodological Approaches .....	109
5.3.1 Relationship between Individual Surfaces .....	110
5.3.2 Relationship between Entire Surfaces .....	111
5.4 Outlook and Possible Applications .....	113
<b>References</b>	<b>117</b>
<b>Curriculum Vitae</b>	<b>135</b>
<b>Acknowledgement</b>	<b>139</b>



# Abstract

Weather radars are now available in many countries for operational observations and measurements of hailstorms and provide detailed information on the formation and structure of severe thunderstorms. Much research has been devoted to the quantitative measurement of hailfalls and the nowcasting of hail-bearing thunderstorms which is of interest for national weather services and airports (warning), the agricultural community (protection) and the insurance industry (damage estimation and mitigation). Although dual-polarization techniques have been improving in recent years, hail detection and measuring methods still have to rely on single-polarization radars. One of the most successful methods to derive hailfall intensities from single-polarization radars is hail kinetic energy that is calculated from radar reflectivity measurements and represents the total volume of hailfall per surface unit. Radar-derived hail kinetic energy ( $E_{\text{KINPIX}}$ ) showed valuable results in relation to ground-based measurements of hailfalls (hailpads) and amounts of hail damage to various crops. Based on the good agreement between radar- and ground-measured hailfall intensity,  $E_{\text{KINPIX}}$  is related in this thesis to hail damage amounts on automobiles, buildings and cloud-to-ground (CG) lightning activity in analyzing a large number of radar-measured hail cells. The thesis consists of three parts: an introduction, three articles (submitted or published in *Atmospheric Research*) that are reproduced in individual chapters and a final chapter that presents two methodological approaches of how CG lightning location data could be used in the future to directly determine hailfall areas.

**Article 1** deals with the relationship between hailfall intensities and damages to automobiles, whereas **Article 2** investigates a corresponding relationship for residential and agricultural buildings in Switzerland. Radar measurements were available from the C-band Doppler radar located at the Swiss Federal Institute of Technology (ETH) near Zurich, Switzerland. Damage claim data on automobiles were available from Winterthur Insurance (1992-1998) and several cantonal building insurance companies provided hail damage data of buildings (1992-1999). Relationships between hailfall intensity ( $E_{\text{KINPIX}}$ ) and damages to automobiles (buildings) have been analyzed for 12 (nine) hail cells with the following results:

- As the amount of hail damage depends strongly on the exposure and the physical characteristics of the units insured, some assumptions and simplifications were necessary.
- The relationship between mean damages and  $E_{\text{KINPIX}}$  depends on the hailstorm season: high season storms (15 June-15 August) produced higher damages than low season storms

(before and after). A seasonal difference in hailfall intensity between high and low season storm appears also from numbers and maximum hailstone diameters that were available from hailpad measurements conducted during Grossversuch IV in central Switzerland (1976-1983).

- The nonlinear relationships between  $E_{KINPIX}$  and the damage variables are best described by logistic damage functions that yield correlation coefficients of 0.80. After suitable verification and calibration, logistic functions for total loss ratios (ratio between damage amounts and total sums insured) of both residential and agricultural buildings, predicted damages that are in the range of occurred losses from hailfall. Relative prediction errors for the most severe hailstorms are below 30%.
- The results suggest that the established logistic damage functions between radar-derived hail kinetic energy and hail damage amounts could be used by insurance companies to determine possible maximum losses (PMLs), shifting a radar-measured hail cell over a motor and/or a building portfolio of interest (e.g., over a major city).

In **Article 3**, CG lightning measurements from Lightning Location and Tracking Systems (LPATS) of Switzerland and southern Germany are compared to determine relative detection efficiencies. CG lightning measurements of the Swiss LPATS are attributed to individual hail cells (5-min resolution), so that the entire lifecycle can be assessed and be related to radar-derived hail kinetic energy (ETH C-band Doppler radar). Analyzes of 41 hail cells that propagated over the Swiss Mittelland (1992-1995) show the following key results:

- Total hail kinetic energy ( $E_{KINTOT}$ ) shows good linear correspondence (correlation coefficient of 0.95) with totals of negative CG (–CG) stroke counts but reveals no direct relationship regarding positive CG (+CG) stroke totals, although hail cells were stratified according to the type of cell organization.
- Temporal and spatial locations of maximally expected hailfall correlate with temporal (0.88) and spatial (0.84) peaks of –CG strokes. Most hail cells (66%) show –CG stroke peaks on the average 22 min (0-65 min) and 19 km (3-58 km) prior to maximally expected hailfall.
- Locations of +CG stroke peaks reveal large variance relative to maximally expected hailfall. +CG strokes in weak cells tend to peak on the average 10 min before and 3.5 km after maxima in hail kinetic energy, whereas +CG stroke peaks in strong large isolated cells lag maximally expected hailfall up to 30 min and 45 km.
- The results of the relatively large data sample confirm the importance of the non-inductive graupel-ice charging mechanisms that explains the majority of –CG strokes at the beginning of thunderstorm development and the fact that most CG discharges are of positive polarity at mature storm phase, when an electrical charge reversal occurs in the thunderstorm with the fallout of precipitation.



- The spatial-temporal relationship between peaks in CG strokes and maximum hailfall intensity could be used to improve nowcasting systems of severe thunderstorms, particularly through an increase of the time of onset between CG lightning initiation and the fallout of hail.

In the last chapter, the spatial relationship between patterns of –CG strokes and radar-derived hail kinetic energy is analyzed for 18 selected hail cells. Cross-correlations between lightning and energy patterns produced coefficients between 0.33 and 0.66, which are the basis for a promising approach to determine hailfall surfaces directly from lightning location data. This chapter shows two methodological approaches of how hail kinetic energy could be distributed in space, whereas the full implementation of these methods is not covered in the thesis. Once accurate methods are available, it would be possible to determine entire areas of hailfall without relying on radar data.



# Zusammenfassung

Wetterradargeräte werden mittlerweile in vielen Ländern zur Beobachtung und Messung von Hagelstürmen verwendet und liefern einen detaillierten Überblick über die Entwicklung und die Struktur von starken Gewittern. Viel Aufwand wurde in die quantitative Messung von Hagelschlägen und Kurzfristprognosen (Nowcasting) von hagelträchtigen Gewittern investiert, was für nationale Wetterdienste und Flughäfen (Warnungen), die Landwirtschaft (Hagelschutz) und Versicherungen (Schadenabschätzung und Prävention) von grossem Interesse ist. Obwohl Dual-Polarisation Techniken in letzter Zeit entscheidend verbessert wurden, basieren Methoden zur Hagelerkennung und –messung immer noch auf Single-Polarisations Radargeräten. Eine der besten Methoden zur Bestimmung der Hagelintensität mit Single-Polarisation Radargeräten ist die kinetische Hagelenergie, die aus der Radarreflektivität berechnet wird und das gesamte Hagelvolumen pro Fläche repräsentiert. Es hat sich gezeigt, dass die radarvermessene kinetische Hagelenergie ( $E_{\text{KINPIX}}$ ) gut mit Bodenmessungen von Hagel (Hailpads) und Hagelschäden an landwirtschaftlichen Kulturen korreliert. Aufgrund der guten Beziehung zwischen radar- und bodenvermessener Hagelintensität, wird  $E_{\text{KINPIX}}$  in dieser Dissertation in Beziehung zu Hagelschäden an Autos, an Gebäuden und zur Häufigkeit von Wolken-Boden Blitzen (WB) gesetzt und anhand einer grossen Anzahl Hagelzellen analysiert. Die Dissertation besteht aus den folgenden drei Teilen: einer Einführung, drei wissenschaftlichen Publikationen (eingereicht oder publiziert in *Atmospheric Research*) die in einzelnen Kapiteln wiedergegeben sind, und einem abschliessenden Kapitel, in dem zwei methodische Ansätze wie aus räumlichen Verteilungen von WB Blitzen gesamte Hagelflächen abgeleitet werden könnten.

**Artikel 1** zeigt die Beziehung zwischen Hagelintensitäten und Hagelschäden an Autos, während in **Artikel 2** der Zusammenhang mit Schäden an Wohn- und Landwirtschaftsgebäuden untersucht wird. Die Radardaten stammen vom C-Band Doppler-Radar, der von der Eidgenössischen Technischen Hochschule (ETH) in der Nähe von Zürich (Schweiz) betrieben wird. Hagelschäden an Autos waren durch die Winterthur Versicherungen (1992-1998) und Hagelschäden an Gebäuden durch verschiedene Kantonale Gebäudeversicherungen (1992-1999) erhältlich. Die Beziehung zwischen Hagelintensitäten ( $E_{\text{KINPIX}}$ ) und Schäden an Autos (Gebäuden) wurden für 12 (neun) Hagelzellen analysiert, mit den folgenden Resultaten:

- Da das Ausmass eines Hagelschadens sehr stark vom *Exposure* und den physikalischen Eigenschaften der versicherten Objekte abhängt, wurden verschiedene Annahmen getroffen und Vereinfachungen eingeführt.

- Die Beziehung zwischen den mittleren Schäden und  $E_{\text{KINPIX}}$  hängt von der Hagelsaison ab: Hagelzellen der Hauptsaison (15. Juni-15. August) produzierten generell höhere Schäden als Gewitter der Nebensaison (vorher und nachher). Ein saisonaler Unterschied in der Hagelintensität zeigt sich auch aus der Anzahl und der maximalen Hagelkorngrösse von *Hailpad* Daten, die aus dem Grossversuch IV stammen, welcher in der Zentralschweiz durchgeführt wurde (1976-1983).
- Die nicht-linearen Beziehungen zwischen  $E_{\text{KINPIX}}$  und den Schadenvariablen lassen sich am besten mit logistischen Funktionen beschreiben, wobei Korrelationskoeffizienten von 0.80 resultieren. Nach entsprechender Verifikation und Kalibrierung generierten die logistischen Funktionen für die Schadenrate (Verhältnis zwischen Schäden und Gesamtversicherungssumme) Schäden an Wohn- und Landwirtschaftsgebäuden, die in der Grössenordnung der tatsächlich vorgekommenen Schäden liegen. Der relative Fehler zwischen realen und mit den Schadenfunktionen geschätzten Schäden liegt für die stärksten Stürme unter 30%.
- Die erarbeiteten logistischen Schadenfunktionen zwischen radarvermessener kinetischer Hagelenergie und Hagelschäden könnten von Versicherungen zur Bestimmung von maximal möglichen Schäden (PMLs) gebraucht werden, indem eine radarvermessene Hagelzelle über ein Auto- und/oder Gebäudeportefeuille eines bestimmten Gebietes (z.B. einer grösseren Stadt) verschoben werden kann.

In **Artikel 3** werden WB Blitze, die von den Blitzmessnetzen der Schweiz und Süddeutschland geortet wurden, miteinander verglichen, um eine Angabe über die relative Erfassungseffizienz zu erhalten. WB Blitzmessungen des Schweizer Ortungssystems werden einzelnen Hagelzellen (5 min. Auflösung) zugeordnet, so dass der gesamte Lebenszyklus einer Zelle erfasst und in Beziehung zur radarvermessenen kinetischen Hagelenergie (ETH C-Band Doppler-Radar) gesetzt werden kann. Die Auswertung von 41 Hagelzellen die über das Schweizer Mittelland gezogen sind (1992-1995), zeigt die folgenden Resultate:

- Die totale kinetische Hagelenergie steht in einer linearen Beziehung (Korrelationskoeffizient von 0.95) mit der totalen Anzahl negativer WB Blitzen (–WB). Kein direkter Zusammenhang wurde dagegen mit der Anzahl positive geladener WB Blitzen (+WB) gefunden, obwohl zwischen verschiedenen Gewittertypen unterschieden wurde.
- Positionen von maximaler Hagelintensität korrelieren mit zeitlichen (0.88) und räumlichen (0.84) Höchstwerten in der Häufigkeit von –WB Blitzen. Die meisten Hagelzellen (66%) zeigen, dass –WB Blitze im Mittel 22 min. (0-65 min.) und 19 km (3-58 km) vor der höchsten Hagelintensität vorkommen.
- Im Bezug zur maximalen Hagelenergie zeigt sich eine grosse Varianz in Positionen von Höchstwerten in der Anzahl von +WB Blitzen. In schwachen Hagelzellen befindet sich der Höchstwert von +WB Blitzen im Mittel 10 min. vor und 3.5 km nach der höchsten Hagelintensität. In grossen isolierten Zellen liegt hingegen die Position der meisten +WB Blitze 30 min. und 45 km nach der höchsten Hagelintensität.

- Die Resultate der relativ grossen Anzahl untersuchter Gewitter bestätigen den Einfluss des nicht-induktiven Graupel-Eis Ladungsmechanismus. Dieser erklärt die Tatsache, dass die Mehrheit der –WB Blitze zu Beginn der Gewitterentwicklung vorkommen, während die meisten +WB Blitze eher am Ende der Gewittertätigkeit, während einer Umkehrung der Ladungsteilung beim Ausfall des Niederschlags, auftreten.
- Die zeitliche und räumliche Beziehung zwischen Höchstwerten von WB Blitzen und maximaler Hagelintensität könnte in der Zukunft für die Verbesserung der Kurzvorhersagen (Nowcasting) von starken Gewittern verwendet werden, speziell durch eine frühere Erkennung eines Hagelschlags anhand von WB-Blitz Informationen.

Im letzten Kapitel wird die räumliche Beziehung zwischen Mustern von –WB Blitzen und radarvermessener kinetischer Hagelenergie für 18 ausgewählte Hagelzellen untersucht. Kreuzkorrelationen zwischen den Blitz- und Energiemuster ergeben Koeffizienten zwischen 0.33 und 0.66, was ein vielversprechender Ansatz für eine direkte Bestimmung von Hagelflächen mittels Blitzdaten ist. Zwei methodische Ansätze zur räumlichen Verteilung der Hagelenergie werden in diesem Kapitel diskutiert, wobei die vollständige Ausarbeitung der Methoden nicht mehr im Rahmen dieser Arbeit liegt. Falls dies jedoch gelingt, können Hagelflächen für grosse Gebiete bestimmt werden, ohne direkt auf Radardaten angewiesen zu sein.





Japanese kanji for hail



Japanese kanji for lightning

In Japanese, similar characters (kanji) are used for hail and lightning. The upper parts of both characters symbolize *precipitation*, whereas the lower part of the hail kanji means *wrapping* and *field* in the case of the lightning character.

As in the Japanese calligraphy, the close link between hailfall and lightning activity is studied in this thesis from a meteorological point of view.

I am very grateful to Hiroshi Sakai, my father-in-law, who revealed the meaning of the characters and kindly drafted the two kanji.







# Chapter 1

## Introduction

### 1.1 Outline

This thesis consists of the following three articles:

Hohl, R., Schiesser, H.H. and Knepper, I., 2001. The use of weather radars to estimate hail damage to automobiles: An exploratory study in Switzerland. *Atmospheric Research*. Accepted September 2001.

Hohl, R., Schiesser, H.H. and Aller, D., 2001. Hailfall: The relationship between radar-derived hail kinetic energy and hail damage to buildings. *Atmospheric Research*. Submitted October 2001.

Hohl, R. and Schiesser, H.H., 2001. Cloud-to-ground lightning activity in relation to the radar-derived hail kinetic energy in Switzerland. *Atmospheric Research* 56, 375-96.

that are reproduced in Chapters 2, 3 and 4. Chapter 1 puts the three articles in a broader context and introduces the basic concepts of radar-based hail detection and hail kinetic energy, hail insurance terminology as well as general characteristics of lightning activity in severe thunderstorms. The contents of the individual articles are given in abstracts at the beginning of the relevant chapters, while the articles are introduced in Section 1.7. Chapter 5 relates lightning and hailfall distributions and discusses two methodological approaches of how cloud-to-ground lightning patterns could be used to derive entire areas of hailfall, which in turn can be used to determine hail-damage prone areas without relying on radar data.

### 1.2 Thunderstorm Theory

Over the last 50 years, much research has been devoted to convective thunderstorms and their classification according to storm severity, rain or hailfall intensities, propagation modes, storm environments and other features. Most work focused on severe thunderstorms, defined as storms that produce strong wind ( $> 26 \text{ ms}^{-1}$ ), hailfall ( $> 19 \text{ mm}$ ) and/or weak to moderate

tornadoes (Johns and Doswell, 1992). Detailed descriptions of storm types and characteristic features can be found in Browning (1977), Burgess and Lemon (1990), Houze (1993) and Schiesser and Waldvogel (2000), from which a large part of this chapter is taken.

Thunderstorms are made of basic units of fundamental kinematic and thermodynamic building blocks described as *cells* (e.g., Browning, 1977) that are sometimes referred to as non-severe ordinary thunderstorms. A cell is a dynamical unity that is well characterized by a compact region of vertical air motion (updraft) that can be identified by radar measurements. The lifecycle of a cell typically lasts 30 min and shows three distinct stages: (1) a *cumulus stage* that is characterized by an updraft alone and begins on radar with the first echo generally between 3-6 km height; (2) a *mature stage* with updraft and downdraft together, tallest cloud tops and highest radar reflectivities and (3) a *dissipating stage* where downdrafts prevail and spread down to lower storm level where precipitation falls out. New cell formation frequently occurs on the flanks of the old cell as a result of low-level convergence. Ordinary thunderstorms count for a large majority of thunderstorms and are the basic unit from which severe thunderstorms develop.

### 1.2.1 Severe Thunderstorms

Severe convective storms are associated with deep convection which needs three necessary ingredients (Johns and Doswell, 1992): (1) a moist layer of sufficient depth in the low or mid-troposphere; (2) a steep enough lapse rate of the temperature profile to allow a substantial positive buoyancy or convective available potential energy (CAPE) and (3) sufficient lifting of a parcel from the moist layer to allow it to reach its level of free convection where it can move upwards just with its buoyancy. Synoptic scale disturbances (e.g., cold fronts) help to destabilize thermodynamical structures, but the lift needed to initiate deep moist convection is provided by mesoscale or storm-scale processes (e.g., convergence lines, stationary fronts, outflow boundaries or orographic lifting). The dynamical structure and severity of a storm is strongly influenced by the environment, mainly by storm-relative winds and the nature of the vertical wind shear, i.e., the change in wind direction and speed with height. Under radar-based perception, severe thunderstorms are commonly divided into the following categories:

The *single cell thunderstorm* closely resembles the ordinary thunderstorm with a few notable exceptions. The intense updrafts are relatively short lived (< 30 min) taking the form of a single pulse and the first radar echo is higher (6-9 km) than for the ordinary storm. At mature storm phase, the area of highest reflectivities (> 50dBZ) maintains continuity with descend to the ground and strong wind gusts (downbursts) and brief large hail may occur.

The *multicell thunderstorm* consists of an organized sequence of severe cells at various stages of development with new cells developing periodically, preferentially at one storm flank. Over storm propagation, new cells do not move in the storm but become the mature storm as older cells dissipate on the opposite storm flank. Associated with new cell development a

characteristic echo region occurs at mid-storm level (overhang), below which a weak echo region (WER) is visible at low-level radar measurements. Individual cells have lifetimes of 30 min, but the storm as a whole can last over several hours. Beside severe downbursts and large hail, multicells can generate weak to moderate tornadoes. Typical multicell environments show significant instability and moderate wind shears.

*Supercell thunderstorms* are rare events that often develop out of a multicell thunderstorm. Supercells are characterized through a pair of large and intense updrafts ( $25\text{--}50\text{ ms}^{-1}$ ) and downdrafts that can coexist during several hours. In plan view of a radar scan, mature supercells show a WER which persists for a long time near the updraft center. As updrafts strengthen further, the WER becomes bounded (BWER) and a characteristic hook signature appears at low-level radar scans indicating the presence of a mesocyclone (rotating updraft region) at mid-storm level. When the BWER starts to collapse and the low-level hook begins to wrap up, largest hailfall and the formation of tornadoes and very strong wind gusts (downbursts) are most likely. A cross-section through a supercell thunderstorm is shown in Fig. 1.1.

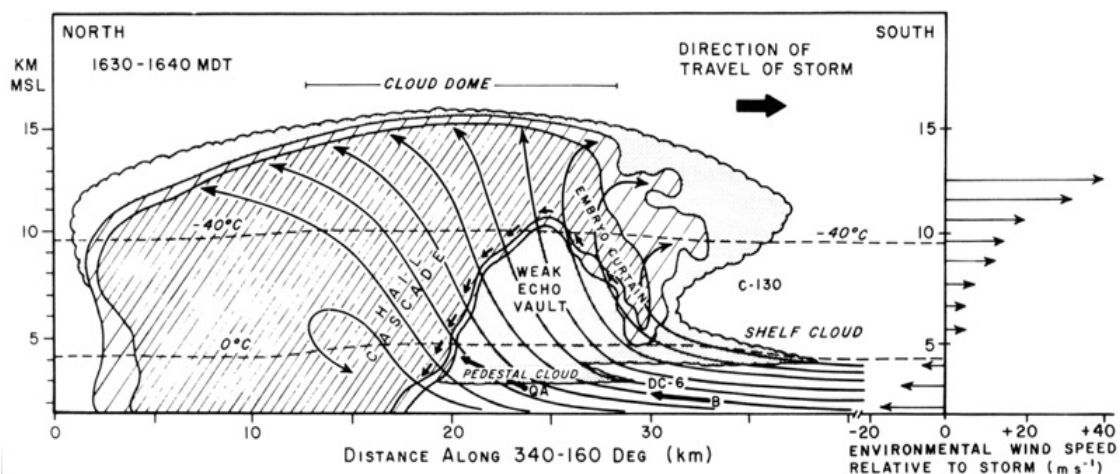


**Figure 1.1.** Vertical cross-section through a hail-bearing supercell storm in NE Colorado. The section is orientated along the direction of travel of the storm, through the center of the main updraft. Two levels of radar reflectivity are presented by different densities of hatched shading. Areas of cloud devoid of detectable echo are shown stippled. Bold arrows denote wind vectors in the plane of the diagram as measured by aircraft whereas the scale is only half of that of winds plotted on the right side of the diagram. Short thin arrows skirting the boundary of the vault represent a hailstone trajectory. The thin lines are streamlines of airflow relative to the storm drawn to be consistent with other observations. To the right of the diagram is a profile of the wind component along the storm's direction of travel, derived from a sounding 50 km south of the storm. (after Browning, 1977)

Supercells can be classified according to the motion relative to the direction of the mean vertical shear vector of the environmental wind (Klemp and Wilhelmson, 1978; Moller et al., 1994) into right-moving storms (clockwise turning of the shear vector with increased height) and left-moving storms (counter-clockwise veering). Based on the amounts and spatial distributions of precipitation relative to airflow, Doswell and Burgess (1993) classified

supercells into low-precipitation, classic and heavy-precipitation supercell storms. Generally, supercell environments are characterized by large instabilities, strong vertical wind shears and moist low levels where wind speeds exceed  $10 \text{ ms}^{-1}$ . Radar-based characteristics of supercells in Switzerland are given in Houze et al. (1993), Schmid et al. (1997) and Schiesser et al. (1997). Meteorological conditions and indices for severe thunderstorms in Switzerland have been analyzed in Huntrieser et al. (1997).

The distinction between above storm types has been presented as sharp since in reality, one storm can develop from one storm type to another as intensity increases and combinations of storm types occur both in structure and steadiness. As an active convective entity, a cell can split into two or more cells (cell splitting) or merge with one or two cells (cell merging). It has often been observed that a few isolated single cell thunderstorms become severe multicell or supercell storms and can under ideal conditions evolve into a *mesoscale convective system* (MCS). An MCS is defined as a cloud system that occurs in connection with an ensemble of non-severe and severe thunderstorms which produces a continuous precipitation area of  $> 100 \text{ km}$  in one direction (Houze et al., 1990). The damaging entity of an MCS is the cell of hail or intensive rain, defined as a region enclosed by a 47dBZ radar echo contour. The region of echoes bounded by the 40dBZ contour and containing one or more cells during mature storm phase is called a *cell complex*. According to the organizational structure of a cell complex, MCSs are classified into four categories: (1) an *isolated cell complex*; (2) a *group of cell complexes* in which multiple closed 40dBZ contours are separated from each other and arranged with no apparent organization within the area of  $\geq 25\text{dBZ}$  echo intensity; (3) a *broken line* where two or more cell complexes are arranged in a line more or less perpendicular to the apparent direction of movement of the whole line with separation of the 40dBZ contours of the individual cell complexes and (4) a *continuous line* where the area of precipitation with reflectivities  $> 40\text{dBZ}$  is elongated in one direction, usually two or more cells appear within it and the length-to-width ratio of the elongation is more than 3:1. MCSs last over several hours and produce long lasting rainfalls, severe hailfall and sometimes tornadoes. For a more exhaustive discussion of MCSs see Houze (1993) or Cotton (2000) and for characteristics of MCSs in Switzerland, Schiesser et al. (1995).

### 1.2.2 Hail Formation

The formation of hail within a thunderstorm cloud is a complex process as the dynamic and kinematics of the storm interact with cloud microphysics. A preliminary condition for the development of hail is a strong updraft that supports growing hailstones. Updraft velocities are mainly influenced by the convective available potential energy (CAPE): the greater the CAPE, the higher the potential for large hail to develop in a thunderstorm. Hailstone size can therefore be taken as a rough approximation of updraft velocity (Johns and Doswell, 1992). However, updrafts  $> 40 \text{ ms}^{-1}$  are typically too strong to allow hydrometeors to remain in the prime growth region long enough for maximum growth to occur (e.g., Miller et al., 1988).

Nelson (1987) showed that thunderstorms with broad regions of moderate updraft strengths ( $20\text{--}40\text{ ms}^{-1}$ ) are more likely to produce significant hailfall than storms having strong but compact updrafts. A close relationship exists between divergent outflows at upper storm level and maximum hailstone sizes at ground (Witt and Nelson, 1991). Beside the CAPE and pure updraft strength, Johns and Doswell (1992) suggested that interactions between updrafts and environmental winds create perturbation pressure gradients that results in vertical acceleration of the updrafts. This effect may dominate the buoyancy. Supercells and multicells that occur in similar wind environments can therefore show differences in hailstone sizes and distributions (Schiesser and Waldvogel, 2000). In supercells, storm-scale wind structures and updrafts accelerated by perturbation pressure gradients enhance the growth of large hailstones.

The growth of hailstones in thunderstorms has been described in Browning and Foote (1976) in three stages as indexed in Fig. 1.2: (1) small particles grow during a first ascent in a region of relatively weak updrafts on the right flank of the main updraft by accretion of supercooled water droplets; (2) some of these particles travel within weak updrafts around the forward edge of the main updraft (embryo curtain) before entering the core of the main updraft as embryos with a diameter of several millimeters and (3) although there might be minor oscillations owing to small fluctuations in updraft intensity, these recycled embryos gradually grow from graupel into hailstones (diameter  $> 5\text{ mm}$ ) essentially during a single up-and-down trajectory. As a result, hailstones reveal different shells (onion structure) with layers that can be either dry or wet, depending on whether or not all of the accreted supercooled droplets can be frozen by the forced ventilation process of heat conduction and evaporation from the hailstone surface. Details of growth stages of hail are given in List (1986) and characteristics of hailstones are discussed in Macklin (1977).

Once hailstones fall out of an updraft zone and start falling towards ground, melting starts below the  $0^{\circ}\text{C}$  isotherm as an influence of the fall distance between freezing level and ground, mean temperatures of downdrafts and fall velocities depending on the size and density of the hailstones. Hailstone spectra (i.e., numbers of hailstones per diameter class) can show high variability, differing with the storm type, the storm environment, the area and the season. As hail can vary from smallest to largest stones and stones fall at velocities that depend on their sizes, it is not unusual for largest hailstones to fall out first, followed by smaller stones. The gravitational sorting that produces this along with the fact that most hailstorms move at moderate speeds can combine to make one point on ground to have large hail while nearby locations will have much smaller hail. Most damaging hailstorms produce large numbers of medium-sized hailstones, whereas only a small percentage are giant hailstones. Patterns of hailfall on ground reveal a fragmented structure on both temporal and spatial scales, where the average area affected by hail is usually only a few tens of square kilometers large. The smallest area of a continuous event is called a *hailstreak* (the area affected by one cell),

several of which become *hailswaths* that are relatively concentrated areas of hailfall with some spatial breaks. Major hailswaths reach some 100 km in length and some 10 km in width.

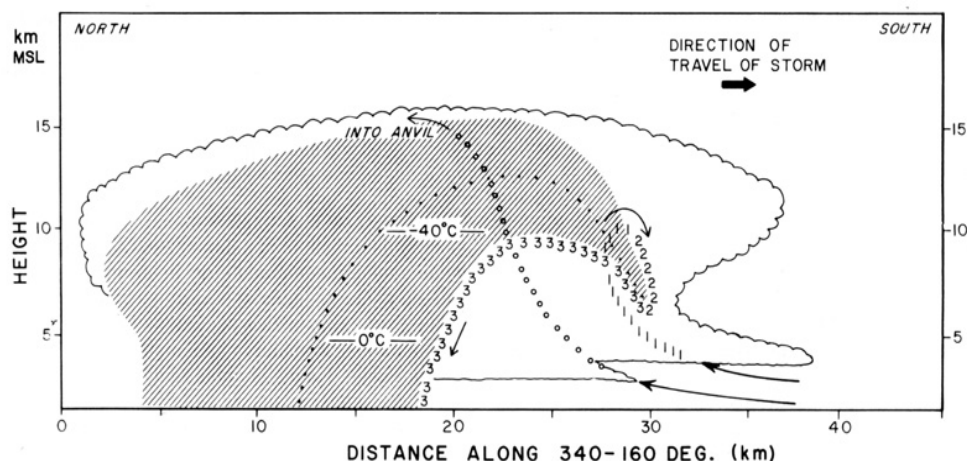


**Figure 1.2.** Vertical section through a supercell storm shown as echo distributions and cloud boundary. Trajectories 1, 2 and 3 represent three stages in the growth of large hailstones (see text). The transition from stage 2 to 3 corresponds to the re-entry of a hailstone embryo into the main updraft prior to a final up-and-down trajectory during which the hailstone may grow large, especially if it grows close to the boundary of the vault as in the case of the indicated trajectory 3. Other less favored hailstones will grow a little farther from the edge of the vault and will follow the dotted trajectory. Cloud particles growing "from scratch" within the updraft core are carried rapidly up and out into the anvil along trajectory 0 before they can attain precipitation size. (after Browning, 1977)

### 1.2.3 Hail Suppression

The location and size of the embryo curtain (indicated in Fig. 1.2) is essential for hail suppression purposes where additional condensation nuclei (e.g., silver iodides particles) are artificially introduced into the embryo formation zone to start more competition about the supercooled cloud water suppressing the growth of large hailstones (Smith, 1992). However, seeding the appropriate cloud volume with the right amount of a seeding agent to the available supercooled water in real time is very difficult if not impossible. Furthermore, the natural variability of hailfalls demand a large sample of seeded and non-seeded control cells to extract possible results of cloud seeding and resulting reductions of hailstone sizes and numbers. Several field-based hail suppression experiments such as the National Hail Research Experiment (NHRE, 1972-1974) in the US (Borland, 1977) and Grossversuch IV (1976-1983) in Switzerland (Federer et al., 1986), with confirmative tests did not prove the efficiency of hail suppression with an acceptable statistical significance. Other similar hail suppression programs came to the same results (WMO, 1995). However, some operational hail suppression projects (particularly in Russia and North Dakota) claimed success, which has however to be seen with caution since these programs are based on crop and hail data that can be difficult to interpret. The present situation of no clear evidence for the efficiency of hail

suppression has contributed to a better knowledge of the hail formation and continuing research will provide deeper understanding.

## 1.3 Remote Detection of Hail

As hailfalls typically show large spatial distributions and temporal variations far greater than that of precipitation, good ground-based measurements of hail are difficult to conduct, labor intensive and therefore rare. Routine hail observations of weather services do not satisfy the increasing demand for precise information on spatial and temporal occurrences of damaging hail. The advantage of remote sensing devices (mainly satellites and radars) is the high temporal and spatial resolution and the possibility to observe and track severe thunderstorms, to detect hail in thunderstorm clouds and to predict hailfall. Ground measurements of hailfall are essential for ground-truth verification and calibration of remotely measured hailfalls.

### 1.3.1 Ground Measurements of Hail (*in-situ* Detection)

On some occasions, large hail has been reported by trained weather observers and the public including comments on the time and location of hailfalls with occasional indication on maximum hailstone sizes. Such observations provide a crude overview of hailfall distributions, but analyzes have shown that the public commonly over-estimate maximum sizes of hailstones by 20% or more (Charlton et al., 1995). As hailstones are randomly collected, public reports provide no information on the complete hailstone spectra and mostly lack temporal and spatial consistency.

A more systematic approach to distributions of hailfalls are *hailpads* as used during special field experiments such as NHRE in the US (Foote and Knight, 1979) or Grossversuch IV (Federer et al., 1986) in Switzerland. Hailpads used in Grossversuch IV consisted of a 2-3 cm thick square piece of styrofoam of about 30 cm on each side that is covered with a sun-resistant paint. Indentations record the size distribution and concentration of hailstones during the time interval of exposure. After the passage of a hailstorm, hailpad surfaces have to be changed to expose fresh surfaces for the record of the next hailfall. For an introduction to hailpad measurements see Waldvogel et al. (1978b) or Lozowski and Strong (1978). Smith and Waldvogel (1989) compared the maximum hailstone size from hailpad measurements and from observers near the hailpad sites and suggested that the maximum observed diameter can be expected to be about 9-14 mm larger than the measured one. Dense networks of hailpads (Section 1.3.5) have been used to resolve some of the fine-structures within hailswaths. Mezeix and Admirat (1978) showed how kinetic energy can be calculated from hailstone spectra measured by hailpads. Schiesser (1988) analyzed hailstone spectra from numerous hailpad measurements in Switzerland (1976-1983) and found a relationship between average

numbers of hailstones per diameter class for several thresholds of hail kinetic energy calculated from hailpads (Fig. 1.3).

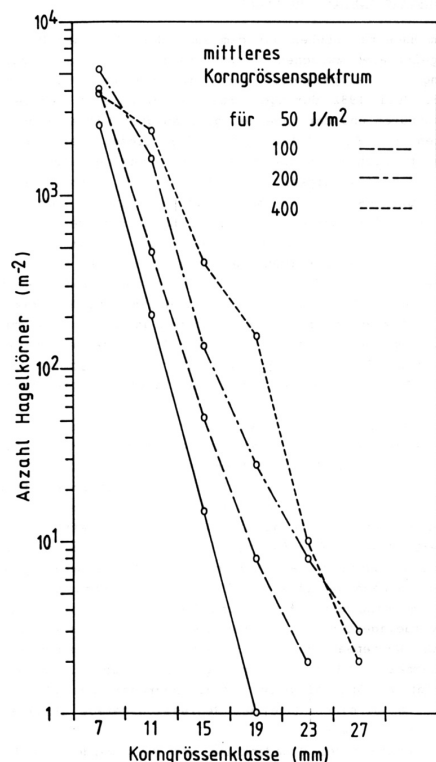


**Figure 1.3.** Distributions of mean hailstone size spectra for four classes of hail kinetic energy:  $50 \text{ Jm}^{-2}$  (331 cases),  $100 \text{ Jm}^{-2}$  (82),  $200 \text{ Jm}^{-2}$  (21) and  $400 \text{ Jm}^{-2}$  (6) of several hailfalls during Grossversuch IV in central Switzerland (1976-1983). The x-axis displays six classes of hailstone sizes and the y-axis shows numbers of hailstones on a logarithmic scale. For higher hail kinetic energy values (up to  $950 \text{ Jm}^{-2}$ ) only a limited number of spectra were available from the hailpads and did not allow the calculation of mean distributions. Over all spectra, 81% of the cases reveal a hail kinetic energy of  $< 26 \text{ Jm}^{-2}$  and only 0.6% had energies  $> 425 \text{ Jm}^{-2}$ . (after Schiesser, 1988)

Beside hailpads, *hail spectrometers* have been used to record hailstone size distributions during special experiments (e.g., Federer and Waldvogel, 1978). Hail spectrometers consist of a  $40 \times 40 \text{ cm}$  large moving platform where falling hailstones are recorded by an automatic camera over a time period of 30 seconds until the platform has been saturated by hailstones and changes automatically, exposing its fresh under-side surface. After film development, hailstones can be counted and measured, providing an overview of the hailstone spectra.

Both hailpads and hail spectrometers have considerable disadvantages that make them hardly usable on an operational basis: the costly manpower that is necessary to maintain the measuring devices, saturation of pads during very intense hailfall and the lack of time resolution. On the other hand, remote sensing techniques are a promising alternative to ground measurements of hailfalls, providing an overall temporal and spatial coverage of hailfalls.

### 1.3.2 Satellite Measurements of Hail

Satellite data provide information on cloud top temperatures that are estimated from infrared (IR) measurements, cloud top mean vertical growth rates derived from the rate of decrease of cloud top temperature and cloud-anvil expansion rates (e.g., Collier and Lilley, 1994). Visible (VIS) satellite data give an estimate of the optical thickness of a cloud and in combination



with IR images, low (warm) clouds can be distinguished from high (cold) clouds. Observations in spatial and temporal variations of convective cloud systems on IR satellite images have shown that storm severity correlates to the rate of change in cloud top temperature (e.g., Negri, 1977). A strong relationship exists between the onset of large hail (> 25 mm) and cloud top temperatures on IR satellite images becoming colder than the environmental tropopause temperature (Reynolds, 1980).

The potential of the use of METEOSAT images for the detection and prediction of hail in Switzerland was investigated by Bauer-Messmer and Waldvogel (1997). A necessary but not sufficient condition for the occurrence of hail is that a threshold in visible images must be exceeded, leading to a forecasting time from the first appearance of a characteristic signature to the occurrence of hail of about 90 min. IR data yield an even better detection criterion than VIS data, suffer however the drawback of appearing simultaneously or even after the onset of hail. Initially high false alarm ratios (81%) could be reduced to 60%, using additional meteorological measurements like sounding data. Many nowcasting systems use satellite images to identify developing thunderstorms and to predict hailfalls, but contain no direct information on intensities of hailfalls and hailstone spectra.

### 1.3.3 Radar Measurements of Hail

The purpose of radar-based remote sensing of hailstorms mainly is the identification of the dynamical structure of hail cells and the assessment of storm cell propagation modes. Radars provide near-ground information of hailfalls and much research has been done, both to identify hail in thunderstorms and quantify intensities of hailfall. An overview of radar-based identification of meteorological targets and operating principles of different types of radars is given in Atlas (1990) and Rinehart (1999) and is only briefly treated in the following.

Weather radars are based on the interaction of emitted electromagnetic wave pulses with hydrometeors or other atmospheric inhomogeneities. Most meteorological radars operate in the 3 cm (X-band), 5 cm (C-band) and 10 cm (S-band) wavelength band. Conventional (non-Doppler) radars measure the amplitude of the received power, whereas Doppler radars provide additional information on the phase, comparing the change in phases of the transmitted and received signals to determine the Doppler frequency shift (motion of particle towards or away from the radar).

When a cloud particle intercepts with electromagnetic waves, some of the energy is absorbed and some scattered backward in the direction of the antenna that is normally used for both transmitting and receiving. The amount of back-scattered energy depends on the dielectric properties of the scatter (refractive index) and the ratio of the wavelength to the size of the scatter. As energy propagates through the air or through precipitation, a loss in wavelength occurs, which is most pronounced for shorter wavelengths. The attenuation for 3.2 cm wavelength is about six times greater than at 5 cm and 40 times greater than at 10 cm

wavelength. The radar equation (Sauvageot, 1982) relates the received power ( $p_r$ ) to a knowledge of transmitted power, the radar system, the radar range and characteristics of the meteorological targets and is written as:

$$p_r = C \cdot \frac{|K|^2 z}{r^2} \quad (1.1)$$

$C$  is the radar constant that depends on the transmitted power, the antenna gain and the wavelength.  $|K|^2$  depends mainly on the target material (water or ice) and to a lesser extent to the temperature and wavelength of the signal.  $z$  is the radar reflectivity factor and  $r$  the distance between the radar and the cloud volume under investigation. For round precipitation particles with diameters significantly smaller than the wavelength (e.g., rain drops), Rayleigh scattering is assumed whereas  $z$  is proportional to the sixth power of the sum of particles written as:

$$z = \sum n_i \cdot D^6 \quad (1.2)$$

where  $n_i$  is the total number of target diameters and  $D$  the target diameter. As a result, the reflectivity for a single target of 19 mm in diameter is approximately 1000 times greater than for a single 6 mm target. The reflectivity factor  $z$  (measured in  $\text{mm}^6\text{m}^{-3}$ ) is usually converted into logarithmic units (decibels or dBZ) to reduce the large magnitude range:

$$Z = 10 \log_{10}(z) \quad (1.3)$$

where a  $z$  equal  $10^5 \text{ mm}^6\text{m}^{-3}$  becomes a  $Z$  of 50dBZ. The scale of precipitation ranges from 10dBZ (drizzle) up to 80dBZ (hail). Clouds show a large variety of different drop size distributions that vary with the storm type, the height within the cloud and the location. In order to determine precipitation rates with a radar, the echo intensity or the radar reflectivity factor  $Z$  has to be related to rainfall intensities  $R$  on ground. This  $Z$ - $R$  relationship depends on the elevation angle of the radar beam, the size of the radar volume, the distance to the radar and changes of aggregation states of precipitation. As it is impossible to know the exact drop size distributions for every measured cloud, a constant size distribution is often assumed, whereas the most commonly used empirical relationship between reflectivity ( $Z$ ) and rain rate ( $R$ ) is:

$$Z = a \cdot R^b \quad (1.4)$$

where the constants  $a$  and  $b$  depend on the precipitation situation and process; for convective precipitation the constants can be defined as  $a=460$  and  $b= 1.5$  (Waldvogel, 1972).

Radar measurements of thunderstorms that contain hail cause some particular problems. A major problem is that the term  $|K|^2$  in the radar Eq. (1.1) strongly depends on the material of the target and cannot precisely be defined, as hailstorms always contain ice particles along with liquid water that vary over time and space. In addition, the reflectivity of hail depends not only on its size but also on the state of its surface (wet or dry) and the amount of water enclosed in the hailstone. Dry hailstones produce a lower reflectivity than wet hailstones at

the same size. A final complication for hail is that it is often large enough that Rayleigh scattering conditions do not apply anymore and Mie scattering becomes relevant. One consequence of hail in the Mie scattering region is that the back-scattered cross-sectional area of a hailstone can increase as it melts and gets smaller. This effect might not be detectable with a radar, however, because the radar pulse volume is usually large enough that a large number of individual hailstones will be contributing to the received power at the same time; the effects of an individual hailstone would be less important because of the large number of stones present.

Radars used for meteorological applications usually display precipitation rates (e.g., in mm per hour) and measure in a *Plan Position Indicator* (PPI) mode where the radar beam measures at a constant angle about a horizontal plane in a regular time interval (e.g., 10 min). *Range Height Indicators* (RHI) are performed when the radar scans in a vertical plane at constant azimuth angle, providing a cross-section through a thunderstorm. Sector-volume scans can be obtained moving the radar antenna several times in the PPI mode between two azimuth angles, each time with another elevation angle. Sector-volume scan measurements can be converted into *Constant Altitude Plan Position Indicators* (CAPPI) displaying radar reflectivity at a given horizontal storm level and temporal resolution. The combination of PPIs, RHIs and CAPPIs give a good three-dimensional overview of storm structures. Doppler radars provide in addition to PPIs, RHIs and sector-volume scans, measurements of the radial component of horizontal particle movements from which the horizontal air flow can be reconstructed and many storm features like areas of rotating air masses (vortex signatures) and diverging or converging flows can be visualized.

#### 1.3.4 Radar-Based Criteria for the Detection of Hail

In addition to the quantitative use of meteorological radars for the measurement of rainfall, much research has been done to distinguish radar signals of hailstones from those of rain drops. Hailstorms have mostly been measured with *single-wavelength* radar techniques where the wavelength of one radar is used to sample a given volume with alterations in elevations and azimuths. On some occasions, *multi-wavelength* radar measurements have been performed using two or more radars of different wavelengths to view the same cloud volume in space and to detect the presence of hail (e.g., Atlas and Ludlam, 1961). Additionally, various polarization methods have been used to detect hail in thunderclouds. Polarization means restriction of the emitted or received electromagnetic wave to a specific direction, e.g., horizontally or vertically. Most operational radars are *single-polarization* radars where the emitted and received wave is measured horizontally. Additionally, *dual-polarization* techniques have been used to determine the kind of particles (e.g., hail or rain), their shapes and sizes in thunderstorms, particularly using differences between horizontal and vertical polarization ( $Z_{DR}$ ) according to a detected particle (e.g., Höller et al., 1994; Smyth et al.,

1999). As the operational implementation of dual-polarization techniques is rare up to now, hail detection methods still have to rely on single-polarization radar data in general.

Using a single-polarization radar, one of the most straight forward methods to distinguish hail from rain is based on maximum reflectivities measured on PPIs and/or CAPPIs. Since reflectivity increases exponentially with larger diameters of scattering particles, large hailstones produce stronger echoes than rain drops. Geotis (1963) found a strong relationship between maximum hailstone size and radar reflectivity. *Reflectivity thresholds* of  $> 55\text{dBZ}$  are generally considered to be associated to hail and hail cells can be discriminated from nonhail cells by the time-integrated  $55\text{dBZ}$  area (e.g., Waldvogel and Federer, 1976). Fig. 1.4 shows typical dimensions of radar reflectivity contours within a vertical cross-section of a hail-producing thunderstorm cell.

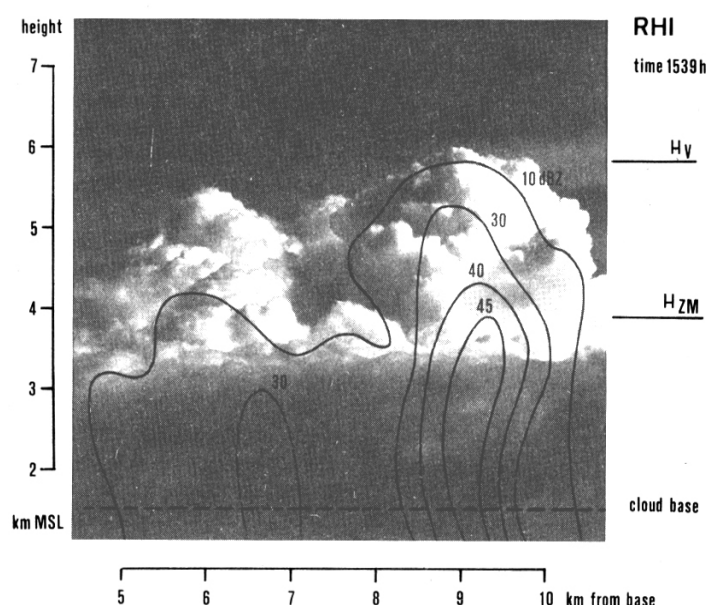


**Figure 1.4.** Photograph of a growing hail-producing convective cell on 5 September, 1978 over central Switzerland. The reflectivity contours of 10, 30, 40 and  $45\text{dBZ}$  are superimposed and the height (km MSL) indicated to the right.  $H_V$  is the radar cloud top and  $H_{ZM}$  the top of the maximum reflectivity. (after Waldvogel et al., 1979)

Waldvogel et al. (1979) proposed a hail detection method that uses the maximum altitude at which a reflectivity of  $45\text{dBZ}$  ( $H_{45}$ ) is found. When this strong reflectivity extends to  $1.4\text{ km}$  above the daily  $0^\circ\text{C}$  isotherm, the presence of hail has been shown to be very likely. Applying the  $H_{45}$  criteria on a large sample of thunderstorms in Switzerland, all hail cells were detected early in their evolution, whereas 30% of the cells identified as severe never actually produced hail at ground. The current hail detection algorithm (Witt et al., 1998) for the WSR-88D radar network in the USA, is based on the  $H_{45}$  hail criteria of Waldvogel et al. (1979) where a height difference of  $1.4\text{ km}$  corresponds to 0% and of  $6\text{ km}$  to 100% hailfall probability. Reflectivity-based hail detection criteria have been combined with other data that indicate

increasing or decreasing storm intensity; e.g., Auer (1994) combined high radar reflectivity levels (37-54dBZ) at low storm level with cloud top temperatures (between  $-5^{\circ}\text{C}$  and  $-55^{\circ}\text{C}$ ) from both satellite and sounding data to detect hail-prone thunderstorms.

In some studies, *Vertically Integrated Liquid Water* (VIL) has been used for the detection of hailstorms (e.g., Lenning et al., 1998). Via conversion of reflectivity to liquid water content and subsequent vertical integration of this water content, three-dimensional radar data are converted to a plan position indicator of the amount of liquid water present in a vertical column above a certain position. At present, there is no overall agreement on the best VIL threshold for the detection of hail. The minimum VIL correlates well to ground reports of severe hail but varies greatly from storm to storm, depending on air mass characteristics including vertical temperature and moisture profiles. The advantage of using VIL densities (ratio of the VIL value and the radar echo top height) as suggested by Amburn and Wolf (1997) instead of just VIL, is still disputed.

Among others, Holleman et al. (2000) tested above single-polarization methods for the detection of hail in the Netherlands and showed that the  $H_{45}$  method of Waldvogel et al. (1979) performed best.

### 1.3.5 Hail Kinetic Energy: Radar vs. Hailpad Data

One of the principle aims of measuring hail by radar is to obtain measurements as accurate as possible of the hailfall intensity of which the amount of hail damage on ground can be deduced. Verifications of hailfalls measured at the same time by radar and ground-based networks (hailpads) have therefore received major attention in hailstorm research. Waldvogel et al. (1978a) derived a relationship between 10 cm radar reflectivity ( $Z$ ) and the flux of kinetic energy at a measuring point ( $\dot{E}$ ) by analyzing a large number of time-resolved hailstone size distributions measured with hail spectrometers. The semi-empirical  $Z$ - $\dot{E}$  relations from different hailstorms showed a surprisingly similar behavior and energy values were within 25% of ground-measured energy values at a given measuring point. The  $Z$ - $\dot{E}$  relationship can be written as:

$$\dot{E} = 5 \cdot 10^{-6} \cdot Z^{0.84} \quad (1.5)$$

where  $\dot{E}$  is given in  $\text{Jm}^{-2}\text{s}^{-1}$  and the radar reflectivity  $Z$  in  $\text{mm}^6\text{m}^{-3}$ . The  $Z$ - $\dot{E}$  relationship is based on the assumption that hailstones are Rayleigh scatters and although this is a crude simplification, the effects caused by this simplification are thought to be averaged out when the time or area integrals of hailfalls are considered. To distinguish hail signals from rain signals, Waldvogel et al. (1978b) suggested to apply the “cutting method” where reflectivities  $> 55\text{dBZ}$  are attributed to hail and reflectivities  $\leq 55\text{dBZ}$  to rain, a technique that is based on experience with hail observations in Switzerland. Further rain-hail attribution methods can be found in Waldvogel et al. (1980). With above  $Z$ - $\dot{E}$  relationship, hail kinetic energy has been

derived from time- and/or space-integrated radar data and been compared to ground-truth data from hailpad networks.

In order to obtain the total amount of hail kinetic energy ( $E_{KIN}$ ) of a particular area,  $\dot{E}$  has to be integrated over the complete time span ( $t_0 \rightarrow t_1$ ) during which radar reflectivity values are measured at a particular radar element:

$$E_{KIN} = \int_{t_0}^{t_1} \dot{E}(t) dt \quad (1.6)$$

$E_{KIN}$  is given in  $Jm^{-2}$ . An example of the agreement between hail kinetic energy deduced from hailpads and radar data using above procedure is given in Fig. 1.5 for a severe hailstorm on 15 July 1982 (Schmid et al., 1992). The radar values of hail kinetic energy have been determined for locations just vertically above each hailpad site and a comparison between the two figures shows a valuable agreement between the two data samples with a cross-correlation coefficient of 0.66.

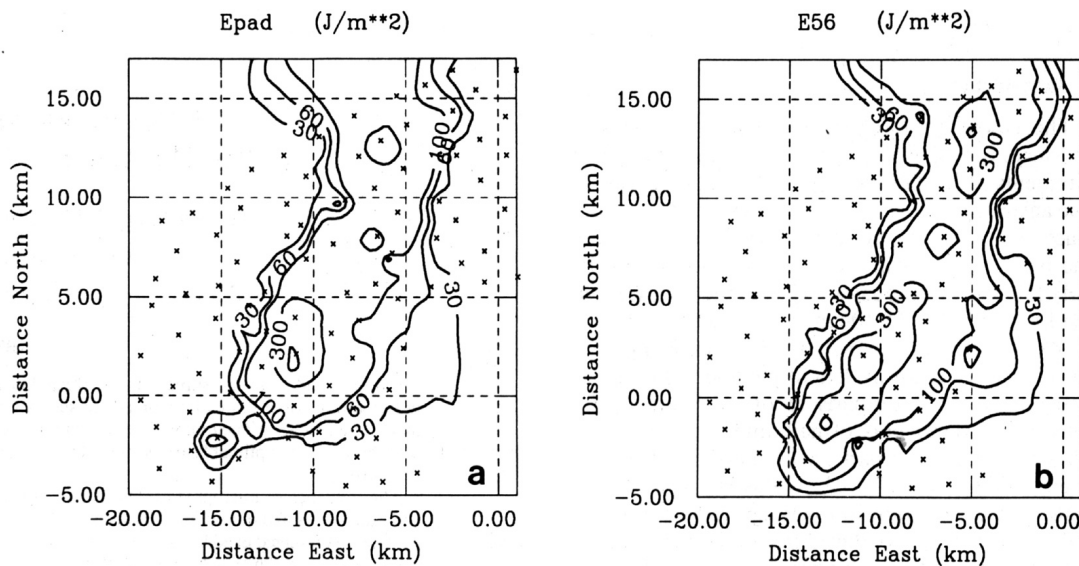


**Figure 1.5.** Pattern of hail kinetic energy from a severe hailstorm on 15 July 1982 over central Switzerland derived from a) a hailpad network (crosses) and b) a 10-cm radar. Isolines of constant hail kinetic energy are drawn using the same objective procedures in both figures. (after Schmid et al., 1992)

An important aspect of point-to-point comparisons of hail kinetic energy calculated from radar and hailpad measurements is that downdrafts displace falling hailstones through advection which can lead to a reduced correlation between the data. Waldvogel et al. (1980) and Schmid et al. (1992) showed that correlation coefficients between patterns of radar- and ground-measured patterns of hail-intensity parameters improved considerably, if the radar pattern is shifted against ground, at least when the transport of hail has a strong unidirectional component. Schiesser (1990) proposed a procedure where each radar measuring point is shifted in such a way that the length of the shift vector is proportional to the height of radar measurements above ground.

If the flux of hail kinetic energy ( $\dot{E}$ ) is integrated not only over the time of hailfall ( $t_0 \rightarrow t_1$ ) as in Eq. (1.6) but also over the area of hailfall ( $s_0 \rightarrow s_1$ ), global hail kinetic energy ( $E_{TOT}$ ) is obtained:

$$E_{TOT} = \int_{t_0}^{t_1} \int_{s_0}^{s_1} \dot{E}(x, y, t) dx dy dt \quad (1.7)$$

$E_{TOT}$  has been shown to agree reasonably well with corresponding hailpad data for both large storms (Waldvogel et al., 1978b; Schmid et al., 1992) and medium to small storms (Waldvogel and Schmid, 1983), as long as the radar scans below the 0°C isotherm and within 40 km of the radar. For many applications,  $\dot{E}$  is integrated over the entire storm duration and per radar element (e.g.,  $0.5 \times 0.5$  km) providing for every surface unit a column of vertically-integrated hail kinetic energy ( $E_{KINPIX}$ ).

Due to the good overall agreement between radar- and ground-measured patterns of hail intensity, hail kinetic energy has been used as a response variable in the statistical evaluation of hail suppression experiments such as Grossversuch IV in Switzerland. Furthermore, the semi-empirical relationship between the kinetic energy flux of the hailstones and the radar reflectivity is used in the current version of the operational WSR-88D Hail Detection Algorithm in the US (Witt et al., 1998) to estimate the probability of severe hail (Section 1.5).

### 1.3.6 Hail Kinetic Energy: Radar vs. Hail Damage Data

Only a few studies investigated the correlation between radar- or hailpad-derived hail kinetic energy and the amount of hail damages on ground. A few attempts have been undertaken to estimate hail damage to crops with the help of various hail parameters (e.g., kinetic energy, hail mass, maximum diameters or numbers of hailstones) measured by hailpads.

Katz and Garcia (1981) examined the relationship between hailpad measurements and the amount of hail damage to wheat crops at four different maturity stages in north-eastern Colorado and south-western Nebraska. Hailfall variables considered as predictors of losses in crop yield included hailpad-derived kinetic energy, momentum, hail mass and numbers of hailstones  $> 12.7$  mm in diameter. Katz and Garcia (1981) showed that kinetic energy appeared to be the best overall predictor of hail damage to crops, whereas mean hailstone diameters and numbers of hailstones did not predict crop damage as accurately. The nonlinear relationship between kinetic energy and percentages of damaged crop, was found to be best described by a logistic function that has the following form:

$$y_i \cong \frac{e^{(\beta_0 + \beta_1 x_i)}}{1 + e^{(\beta_0 + \beta_1 x_i)}} \quad (1.8)$$

where  $y_i$  represents the hail damage proportion,  $x_i$  the corresponding value of kinetic energy for an observation  $i$ , whereas  $\beta_0$  and  $\beta_1$  are parameters that have to be estimated from the data as described in Katz and Garcia (1981).

Wojtiw and Ewing (1983; 1986) related radar-derived hail kinetic energy to amounts of hail damage to cereal crops of similar maturity stages in Canada. In Switzerland, Schiesser (1990) investigated point-to-point relationships between radar-derived hail kinetic energy aloft and hail damage to crops on ground at the resolution of a single field. Respecting the drift of hailstones from radar measuring to ground level, the cross-correlation coefficient between radar-measured hail kinetic energy and percentages of damage to corn crops increased from 0.68 (no shift) to 0.86 in the investigated storm case. Using a logistic curve (Eq. 1.8), Schiesser (1990) established crop-hail loss curves for nine crop types (Fig. 1.6), allowing predictions of hail damages above 20% directly from radar measurements.

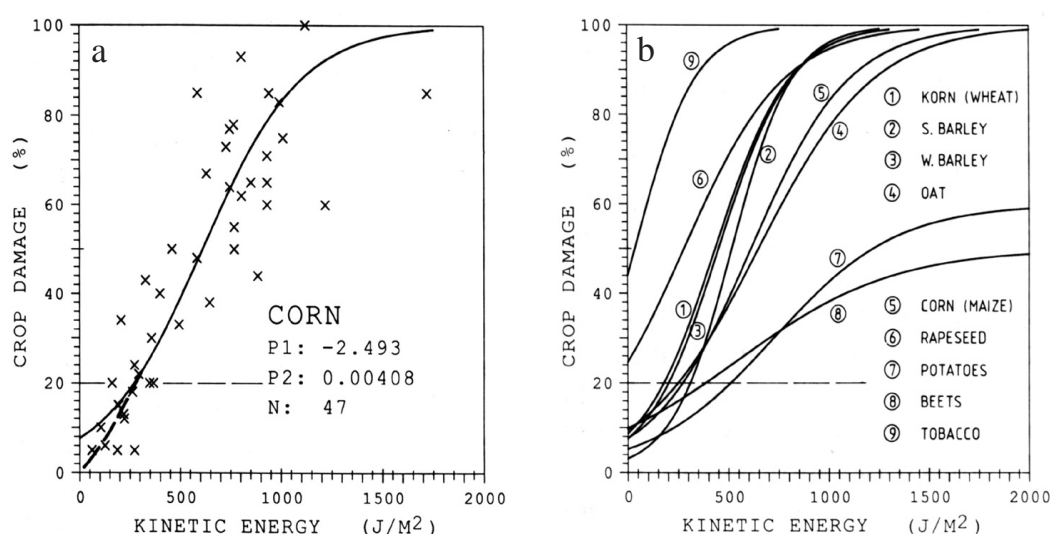


**Figure 1.6.** Damage curves established for the severe "Ruswil" hailstorm of 15 July 1982 in central Switzerland for a) corn crop (maize) with a scatter diagram of 72 observations and the corresponding damage curve (logit function, solid); the dashed curve is an assumed correction if damage estimates < 8% were available and b) corresponding damage curves for nine different crop types. At the time of storm occurrence, most crops were near maturity. Note that potatoes and beets are least vulnerable to hailfall (flat damage curve) as most of the insured crop is in ground, whereas tobacco leaves reveal the highest vulnerability to hailfall (steep damage curve). (after Schiesser, 1990)

Based on the good agreement between hail kinetic energy and the extent of hail damage to crops, Schiesser suggested that the damage functions can be used in real time to transform measured radar values into percentages of damage to a given crop type at a particular maturity stage as soon as a severe hailstorm has passed over an area of interest.

Up to present, no studies have been published on the relationship between radar-derived hail kinetic energy and the extent of hail damage to infrastructure, which is probably due to the fact that property insurance data are not generally available. However, the use of hail kinetic energy as a hailfall intensity variable is promising, regarding applications for the insurance industry. Relationships between radar-derived hail kinetic energy and the amount of hail damage to automobiles are presented in Chapter 2. In Chapter 3, the use of hail kinetic energy



to predict the extent of hail damages on residential buildings in Switzerland is discussed and compared for several severe hailstorms.

### 1.3.7 Radar Data in Switzerland

In Switzerland, the Swiss Meteorological Institute has operated a radar network of two non-Doppler C-band radars located at La Dôle (near Geneva) and Albis (near Zurich) between 1979-1995 (Joss and Lee, 1995); radar locations are shown in Fig. 4.1. In 1993 a third C-band Doppler radar was installed on Monte Lema (near Locarno, Fig. 4.1) and in 1994 the two existing radars at La Dôle and Albis were replaced by a new generation of Doppler C-band radars (Joss et al., 1998). Since 1995, all three radars are integrated into a network that covers the whole of Switzerland and different operational radar products are available. *OVERVIEW* radar images contain full information of the reflectivity that is updated very 5-min and consist of 12 images, each one corresponding to one height level, within a range of heights between 1-12 km. *TODAY* is a composite image of all three radars and shows three projections (horizontal map of reflectivity, west-east and north-south cross sections); the pixel size in the horizontal is  $2 \times 2$  km and in the vertical 1 km whereas each pixel contains the maximum radar reflectivity  $Z$  in each vertical column or horizontal strip. For display, reflectivity is converted into a rainfall rate  $R$  through the relation  $Z = 316 \cdot R^{1.5}$  and rain rates are color-coded in seven intensity steps on a logarithmic scale ranging from  $0.0-0.3 \text{ mmh}^{-1}$  (corresponds to  $< 17\text{dBZ}$ ) to  $\geq 100 \text{ mmh}^{-1}$  ( $\geq 55\text{dBZ}$ ); one image is produced every 5 min.

For non-operational research purposes, the Institute for Atmospheric Science ETH (LAPETH) has been operating a Doppler C-band radar at H  nggerberg (near Zurich, Fig. 4.1) since 1990 (Li et al., 1995). For radar operations, IRIS software (developed by Sigmet Inc.) is used for the storage of radar data and the creation of various radar products. The ETH radar is mainly operated if thunderstorms are within the 120 km detection range and allows automatic collection of PPIs and RHI. Additionally, sector-volume scans can be performed every 5 min, whereas ranges in azimuth, distance and altitude of the volumes to be scanned are interactively entered by a radar operator. For narrow sectors ( $30-45^\circ$ ), 15 scans are performed whereas it is only nine or less scans for sectors broader than  $90^\circ$ . For storms in medium distance from the radar (40-80 km), the horizontal resolution is as high as  $0.25 \times 0.25$  km with an altitude resolution of 1-1.5 km. Using a nearest-neighbor algorithm, sector-volume scan reflectivity observations are converted into CAPPIs with a 0.5-km vertical and a  $0.5 \times 0.5$  km horizontal resolution. For most the investigations of this thesis, CAPPIs and PPIs from the ETH radar have been used; a CAPPI is shown in Fig. 4.2, whereas Fig. 3.5 displays several PPIs. Characteristics of the ETH radar and the measuring program for thunderstorm situations are given in Table 1.1.

**Table 1.1.** Specifications of the ETH C-band Doppler radar and the measuring program for thunderstorm situations. (after Schmid et al., 1997)

Quantity	Specification
Frequency	5.66 GHz
Wavelength	5.3 cm
Peak power output	250 kW
Pulse length	0.5 and 0.3 $\mu$ s
Pulse repetition frequency (PRF)	250 to 1200 Hz
PRF for single PRF mode	1200 Hz
PRF for 3:2 Dual PRF mode	1200/800 Hz
PRF for 4:3 Dual PRF mode	1200/900 Hz
Unequivocal Doppler range for single PRF mode	$\pm 16 \text{ ms}^{-1}$
Unequivocal Doppler range for 3:2 Dual PRF mode	$\pm 32 \text{ ms}^{-1}$
Unequivocal Doppler range for 4:3 Dual PRF mode	$\pm 48 \text{ ms}^{-1}$
Antenna beam width	1.6° circular
Polarization	linear horizontal
Range	120 km
Scanning program	2 PPIs every 10 min RHIs every 5 min Sector-volume scans every 5 min

## 1.4 Hail Damage Assessment and Risk Response

Severe hailstorms are capable of inducing a large amount of damage to both agriculture and infrastructure. Losses from severe thunderstorms are essentially a function of the relationship between the built environment and the occurrence of a meteorological hazard such as tornadoes, hailfalls, flash floods, downbursts and lightning. In hail-prone areas, insurance against hail damage has a long tradition, relieving the financial burden on individual victims and taxpayers by spreading financial losses among a broad group of policy holders. Successful insurance businesses are based on the premise that individual contributions and risks can be pooled into a far less risky insurance portfolio (i.e., an entity of insured risks). Often, insurance companies purchase reinsurance to reduce their financial commitment to a single major risk and to protect themselves against important variations in the loss experience of entire portfolios.

Since the mid-1980s, the property industry has been facing a dramatic increase in hail damage claims and in the US, property losses from hail have reached US\$ 1.2 billion per year and are now in the range of annual crop losses (Changnon, 1999). The last two decades have seen a series of very damaging hailstorms that have generated major losses in numerous urban areas around the world including the Munich hailstorm in 1984 (MunichRe, 1984), the 1990 Denver, the 1987 Edmonton and the 1991 Calgary storms (Charlton et al., 1995) and two hailstorms in 1990 and 1999 over Sydney, Australia (Andrews and Blong, 1997; Yeo et al., 1999) that all caused insured losses over US\$ 500 million. As storm exposure is a direct function of exposure and material values are still increasing in expanding metropolitan areas,

insured hail losses will keep raising even without possible enhancement of thunderstorm activity that can result from a warmer climate.

In order to be able to cover major losses from severe hailfall events, both the insurance and reinsurance industry have established methods to identify hail damage-prone areas and to determine risk-based premiums with rating systems.

#### 1.4.1 Hail Damage Assessment

The amount of hail damage to an insurance portfolio is basically a function of two factors: (1) the *frequency* of hailfalls, reflected in the number of days with hail damage occurrence (called haildays) and/or hail reports from weather stations and (2) the *intensity* of hailfalls depending on the number of hailstones, the maximum and/or average hailstone sizes and wind gusts that accelerate falling hailstones and increase the damage amount.

The type and nature of an insured unit at risk from hailfall has a major influence on the loss amount. The extent of hail damage to crops varies with the crop type and susceptibility to hailfall, the maturity of the crop as a function of the season and can vary within an insured portfolio from year to year as a result of rotational crop planting. The amount of hail damage to a property portfolio depends on the type of buildings insured, and the density of exposed risks, whereas the exposure of a motor portfolio varies both in space and time as a result of the mobility of the insured units. While the extent of hail damage to crops is more dependant on the number of hailstones (typically diameters > 6 mm), the amount of hail damage to a property or motor portfolio is more determined by the maximum hailstone size (typically > 20 mm) rather than by the number of hailstones per surface unit.

#### 1.4.2 Response to Hail Risk

The response to hail risk varies between the crop and property insurance as a function of experiences from past severe hailfalls and loss data. Crop-hail insurers typically use a mix of hailday frequencies (seasonal averages and/or extremes) and average loss statistics to define risk areas and to establish risk-dependent premium rates. Additionally, long time series of annual days of hail losses provide an area-related indication of return frequencies of hailfalls. The property industry often lacks long hail loss records and uses a mixture of climatological data (regional hailday frequencies from crop insurers) coupled with a measure of hailstone sizes considered to be critical to the insured property target, to establish an accurate premium rating system. Constantly increasing insured losses have created a great concern about future maximally possible losses within the property-casualty and crop insurance industry and lead to various corporate efforts to improve the understanding of hail risk and to find relationships between hailfall and damage intensities.

*Laboratory studies* aimed to measure hail damage as a function of the impact of hailstones using ice propelled against a selected building surface or a crop's leaf, to provide guidance on

various hail characteristics that induce damage (Sections 2.2 and 3.2). Based on results of simulated hail damage studies, new building codes have been suggested under risk prevention guidelines.

Several *field studies* of individual severe hailfalls were conducted to compare the amount of hail damage to different buildings types and structures to hailfall intensity (mainly maximum hailstone diameters). In some studies (Sections 2.2 and 3.2), the extent of hail damage to a particular type of building (e.g., residential or commercial) and part of the building (exterior or interior structures) or car panels have been related to maximum hailstone diameters reported by the public. Some of these studies provided empirical relationships between hailfall intensity as a function of maximum hailstone diameters and the amount of induced damage.

*Insurance pricing models* exist for many natural hazards (e.g., earthquakes or hurricanes) but little work has concentrated on models that are able to reproduce past hail damages and estimate future potential losses. This is probably due to the fact that there is no simple physical relationship between hailfall intensity measured from storm parameters (e.g., spatial extent, wind gusts, precipitation rates) and the amount of damage to infrastructure. Furthermore, only a small number of hailfalls have been recorded (e.g., from hailpads) in a way that hailfall intensity can be related to damage extents. Pricing models generally use a damage-intensity relationship that is based on: (1) the *hazard* that deals with the intensity and frequency per location and (2) the *vulnerability* that quantifies the number and monetary amount at a given hazard intensity. Determining vulnerability from claims data (including numbers and amounts) and combining that information mathematically with the hazard probability for a geographic area, a loss curve can be derived to determine the total cost of a severe event. Fig. 1.7 shows how a loss curve can be established for wind gusts using past claim data and a probability curve. From the loss curve, possible maximum losses (PML) can be generated for a given area and portfolio of interest and insurance companies can calculate premiums and limits above which they require reinsurance.

One of the key issues in determining hail damages from a physical hail loss model is that entire spatial variabilities of hailfalls are rarely measured and if they are measured, the data quality from ground-based networks or public records of hailfall intensity (e.g., the number and maximum diameters of hailstones) is hardly systematic (Section 1.3.1). The lack of systematically collected hailfall data and the complexity of hailfalls complicate the establishment of a relationship between hailfall intensity and the initiated hail damage amount. Based on a reasonably large number of ground-measured hailstorms, the Natural Hazard Research Centre (NHRC) developed a hail loss model for the Australian insurance market to estimate hail losses to cars and buildings in the areas of Sydney and Brisbane (Kuhnel, 2000). The NHRC model uses an empirical relationship that is based on maximum hailstone sizes reported by the public and hail damage extents per postcode area (Kuhnel,

personal communication). The use of ground-based measurements and/or reports of hailfall intensity has however limitations and limits the use of many severe hailstorms where hailstones have not been reported but considerable hail damages occurred.

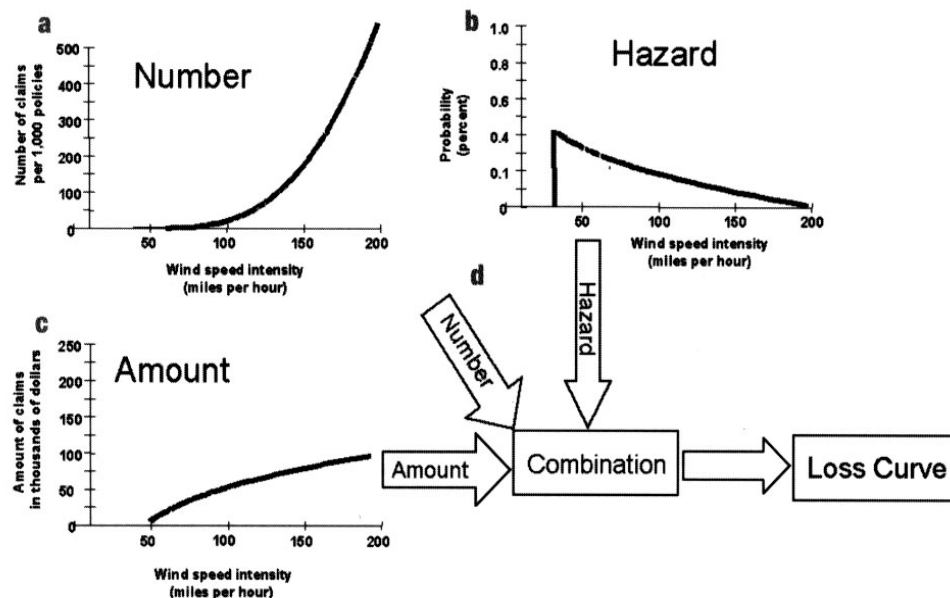


**Figure 1.7.** Schematic Overview of the establishment of a loss curve for wind speeds (> 25 mph) involving: a) numbers of past claims per policy unit, b) amounts of past claims expressed in a monetary unit (US\$) and c) a probability curve based on the percentage of days per year that a geographical area (e.g., community or district) is likely to experience a given wind intensity; in the example wind gusts over 25 mph are shown. (after Thomas, 2000)

On the other hand, weather radar provide highly resolved storm data and with a valuable relationship between a radar-derived hailfall variable (e.g., reflectivity, hail kinetic energy or VIL) and the extent of hail damage to infrastructure, radar-based hail loss curves could be used to simulate future hail damage scenarios. Chapter 2 shows a radar-based method of how a loss curve for the amount of hail damages to automobiles can be established from hail kinetic energy. The same method is used in Chapter 3 to link radar-derived hail kinetic energy of several severe hailstorms to the amount of hail damages to residential and agricultural buildings in Switzerland.

### 1.4.3 Hail Damage Data in Switzerland

Switzerland is one of the regions within Europe that is mostly affected by hailfalls (Collier and Liley, 1994) and both crop and property insurers have a long experience with hail damage claims. The prealpine areas of central Switzerland and the southern part of canton Ticino experience the most hail damage on the long-term average; for a more detailed discussion see Schiesser et al. (1997).

Hail damages to crops have been insured for more than 120 years and since the 1920s, the Swiss Hail Insurance (SHV) is the only company that covers agricultural values against hailfall in Switzerland. During the last 20 years, annual damage claims reached on the average CHF 45 million varying between CHF 11-101 million (SHV, 1999). Crop damage is routinely appraised by trained loss adjusters and once the damage extent is determined, only damages that are over a 8% franchise and a 4% deductible (insured's participation on the damage) are reimbursed to the farmer. Hail damage data are available from the SHV on a daily yes/no basis for every Swiss community since the 1950s. Crop-hail insurance data depend on the variety of the cultures planted over time on a particular field and the insurance participation, which in turn depends on economic and political factors. At the resolution of a single field, the name and address of the insured farmer, date and time of a particular hailfall, kind of crop planted, insured amount of the expected yield and the damage (in percent of the expected yield) are available.

Over the last 20 years, the Swiss building insurers have been facing increasing losses from hailfall (Section 3.2) and highest insured losses when hailstorms moved over densely populated urban areas. Building insurance against elementary damage including hailfall is compulsory in 19 out of 26 cantons. In cantons where building insurance is obligatory, policies are issued by monopolistic non-profit orientated cantonal building insurance companies, whereas in the other cantons, insurance coverage is available from several private companies. Policies cover both exterior (e.g., roofs, walls, windows) and interior building structures (e.g., ceilings, floors, plaster, electrical devices) and can sometimes be expanded to the land and its belongings around the insured building. Insurance costs vary with the canton, the community and the type of building (e.g., residential, commercial agricultural or industrial). Hail damages to buildings are assessed by insurance agents and recompensation of losses range from reinstatement costs up to the full compensation of the new building value in the case of a total loss. Building insurance companies keep records of every settled claim and commonly aggregate their data daily per building category and Swiss community. Fig. 3.1 shows an example of community-resolved hail damage amounts on residential buildings.

Some private insurance companies cover motor vehicles (e.g., automobiles, vans, motor bikes) against hail damage in Switzerland. The last 10 years have seen a series of urban hailstorms that caused insured losses to motor vehicles that surmounted corresponding damages to buildings and agriculture (Section 2.2). Insurance premiums for automobiles are initially based on the new value of the vehicle to be insured and vary with increasing age, numbers and amounts of claimed damages, which in turn has an influence on the deductible. On days when a large number of insured cars were damaged through hailfall, insurance companies organize "drive through" facilities where agents directly determine the damage amount and losses are directly paid to the insured. Motor insurers aggregate daily claims data of policy holders by community where the damaged vehicle is matriculated. Fig. 2.1 reveals

the spatial distribution of numbers of hail-damaged cars after the passage of a severe hailstorm.

## 1.5 Prediction of Hailfall

Forecasting thunderstorm initiation is commonly made from stability indices gained from radio sounding data on a daily yes/no basis. As hail events tend to be short-lived (a few tens of minutes) and usually affect only a few hundred square kilometers, forecasting that hailfall will occur at a given location several hours in the future is currently not possible. The accurate parameterization of convection and the prediction of thunderstorms occurrence in general and large hail in particular with operational numerical weather models, is still a fundamental topic of research (e.g., Dudhia, 1996).

Satellite and radar images have been integrated into *nowcasting* systems that describe the present weather situation and extrapolate it up for a few hours, assuming no significant change in the general behavior of the forecasted precipitation pattern (Wilson et al., 1998). Satellite images may give warning times of up to two hours for discovering hailstorms (e.g., Bauer-Messmer and Waldvogel, 1997), but the exact location of hail on ground has to be determined by radar images which is only possible when a thunderstorm cell has already developed towards the mature stage where precipitation produces a characteristic radar echo. Nowcasting systems use cell tracking algorithms that are based on pattern recognition carried out either applying cross correlation or a tracking of mass centroids. *Mass Centroid Techniques* derive the displacement vector between two consecutive radar scans from the distance of the mass centers of two corresponding radar echoes. The centers are assumed to be representative for individual convective storms and a cell identification problem occurs with cells splitting and/or merging during storm propagation. *Cross Correlation Techniques* use the correlation coefficient as a test criterion to detect similar patterns of radar echoes in consecutive radar scans. An initial tracking area is compared to all possible tracking areas within the consecutive scan. A displacement vector is found using the maximum correlation coefficient and is then extrapolated. There are a number of operational nowcasting systems, primarily based on extrapolation of radar echoes and forecasting initiation and dissipation of precipitation areas; e.g., SCIT (Storm Cell Identification and Tracking, Johnson et al., 1998) or COTREC (COntinuity of TREC vectors, Li et al., 1995).

In the US, the National Severe Storm Laboratory (NSSL) has been developing a series of severe weather detection algorithms that are based on WSR-88D radar data and have been implemented into operational nowcasting systems such as SCIT (Witt et al., 1998). The current WSR-88D hail detection algorithm estimates the probability of hail (any size), the probability of severe-size hail (diameter > 19 mm) and maximum expected hail size for each detected storm cell. In order to estimate the probability of severe hail, a semi-empirical

relationship between the kinetic energy flux of the hailstones and the radar reflectivity (Waldvogel et al., 1978a,b) is used. A severe hail index (SHI) is then calculated by vertically integrating the kinetic energy flux weighted by a reflectivity-based and temperature-based gating function (Witt et al., 1998). Subsequently, a SHI warning threshold is calculated from the height of the freezing level using an empirical relationship. Finally, the probability of severe hail is calculated from the obtained SHI and this warning threshold using again an empirical relationship. The current lead time for a particular area threatened by a large cell (about 100 km<sup>2</sup> haled area) is about 30 min (Stumpf, 2000).

In order to improve the ability of nowcasting systems to detect hail-prone thunderstorms to increase warning lead time of severe weather occurrence and reduce false alarm ratios, much research has been devoted to the integration of additional operationally available data that contain information on the stage of the lifecycle of a convective cell and its movement. One of these data that reveal a large potential to support nowcasting systems are lightning location data from lightning detection networks that can: (1) improve the prediction of thunderstorm propagation and changes in storm intensity (mainly cell growth and decay) and (2) identify in real time relevant lightning rates that precede the occurrence of severe weather. Due to the vast complexity of storm electrification and distributions of lightning rates (Section 1.6), the use of lightning location data for operational detection and prediction of severe storms is still under research.

## 1.6 Lightning Activity in Severe Thunderstorms

Lightning discharges are part of the complex dynamical and microphysical interactions in thunderstorms. Due to the relatively rare occurrence of severe thunderstorms, studies that investigated the electrical nature of storms have been spotty and only since the improvement of lightning location techniques, lightning histories of severe storms could be entirely assessed. From a large body of lightning studies of severe thunderstorms it results that lightning activity varies with the storm type, the storm environment, the location and the season. Detailed descriptions of storm electrification mechanisms, lightning discharge process and electrical characteristics of different storm types can be found in Uman (1987) and MacGorman and Rust (1998), from which a large part of this chapter is taken.

### 1.6.1 Lightning Discharges

Lightning is a transient, high current discharge and several terminologies that are employed are briefly introduced in the following. Discharges occurring within the cloud are called *intracloud* (IC) lightning and a discharge from the cloud base to the ground is a *cloud-to-ground* (CG) lightning. In most storms, ICs outnumber CGs with a ratio of 1:5 in non-severe storms, whereas in severe thunderstorms, this ratio can exceed 100 with a runaway of IC



lightning. CG discharges lower either negative (–CG) or positive (+CG) charge to the ground and of all CGs, –CGs typically consist of 90%. The apparent flickering of many CG flashes results from the fact that they are often composed of multiple events called *strokes*. Occasionally, lightning discharges occur from cloud to clear air, and very rarely, flashes are initiated from tops of tall towers, or mountains and propagate (unlike CGs) upwards towards the cloud base.

CG flashes are typically initiated deep within the thundercloud where dynamical and microphysical processes cause electrical charge separation (Section 1.6.2). The majority of CG flashes begin with an IC discharge that is called a *preliminary breakdown*. After about a tenth of a second, a negatively charged channel (a *stepped leader*) appears below cloud base and propagates downward in a series of intermittent steps. The electrical charge distribution between cloud and ground and the intensity of the electric field that develops between the front of the leader and the ground, causes upward-moving discharges called *streamers*. As one of the streamers connects with the leader (usually < 100 m above ground), the electrical circuit is closed and when the leader channel connects to the ground potential, charge starts flowing to the ground and a current wave propagates up the newly completed channel. This process is called *return stroke* and is perceived as the bright flash. Return strokes usually last tens to 100 milliseconds (ms) with peak currents in the order of 30 kA attained in 1 ms. Once the current finishes flowing through the leader-created channel and after a pause (10-150 ms), another leader (a *dart leader*) can propagate down the previous return stroke channel and initiate a *subsequent return stroke*. In roughly 30-50% of all CG flashes, the dart leader propagates down just a portion of the previous return stroke channel and then forges a different path to ground; in these cases, the flash actually strikes ground in several places. A –CG flash can consist of 10 up to 50 strokes, whereas a +CG flash often has a single stroke characterized by a long-lasting (tens to 100 ms) continuing current.

CG lightning discharges emit characteristic electromagnetic fields that are operationally measured by lightning detection networks, determining time, location, polarity and either the number of CG flashes and their multiplicity (number of strokes in a flash) or individual CG strokes. Fig. 1.8 shows three of the main impulses that are typically radiated by a CG flash and recorded at a lightning receiver.

Lightning detection systems are based on different location techniques: (1) *Magnetic Direction Finder* (MDF) systems use the ratio of two perpendicular magnetic field components, to determine the angle to the CG lightning from the magnetic field measured at least at two different receivers. CG strike locations are thereafter determined by triangulation. (2) *Time-of-Arrival* (ToA)-based systems rely on measurements of the time-of-arrival of a radio pulse at several receivers that are precisely synchronized. Since radio signals propagate close to the speed of light, a constant difference in the arrival time at two stations defines a hyperbola and multiple stations provide multiple hyperbolas whose intersections define the

source location of CG lightning discharges. *Lightning Positioning and Tracking Systems* (LPATS) are based on wide-band ToA-receivers and are suitable for locating lightning sources at medium and long ranges using the hyperbolic location method. (3) *Hybrid-systems* (e.g., the US National Lightning Detection Network, Cummins et al., 1998) use a combination of the MDF- and ToA-lightning locating methods. All lightning location methods rely on theoretical and/or empirical models that describe the shapes of the electric and magnetic fields that are produced by return strokes at different distances and can produce together with field propagation effects considerable site errors. The performance of a lightning detection system depends on the configuration and numbers of receivers used, while the detection efficiency drops with range.

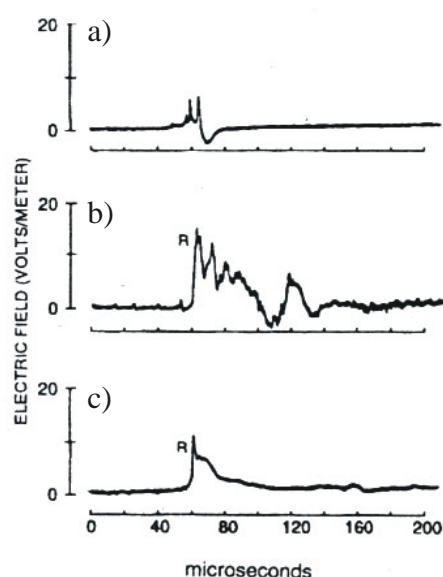


**Figure 1.8.** Electric field impulses that were radiated by a CG flash from a) a preliminary breakdown within the cloud, b) the first return stroke and c) a subsequent return stroke. The small pulses that precede the first return stroke in b) were produced by the final steps of the stepped leader, just before the onset of the connecting discharge and the return stroke. (after Cummins et al., 1998)

As different types of lightning detection systems are currently in operation and performances can vary greatly even within the same network, results from studies that relate lightning activity to storm characteristics can show non-conformities, especially when CG flash rates are compared to CG stroke rates.

### 1.6.2 Thunderstorm Electrification Processes

Many different theories have been established to explain the electrical charge separation and the formation of charge layers within a thunderstorm. While considerable progress is being made in laboratory experiments, field studies and cloud discharge models, a concise theory has not yet emerged.

The electrical charge structure of thunderstorms has long been assumed to be either a vertical *dipole* (positive above negative charge layer) or a *tripole* with a lower positive charge region added below the dipole. However, recent studies revealed that charge structures of severe thunderstorms are more complex than the tripole model. Stolzenburg et al. (1998a,b,c)

analyzed electric field soundings through convective regions of mesoscale convective systems (MCS), isolated supercells and isolated air mass storms and revealed the complexity of electrical charge regions that differ between updraft and downdraft regions (Fig. 1.9). Dimensions and heights of different charge regions vary with the type of convection, the size and strength and relative position of the updrafts and downdrafts.

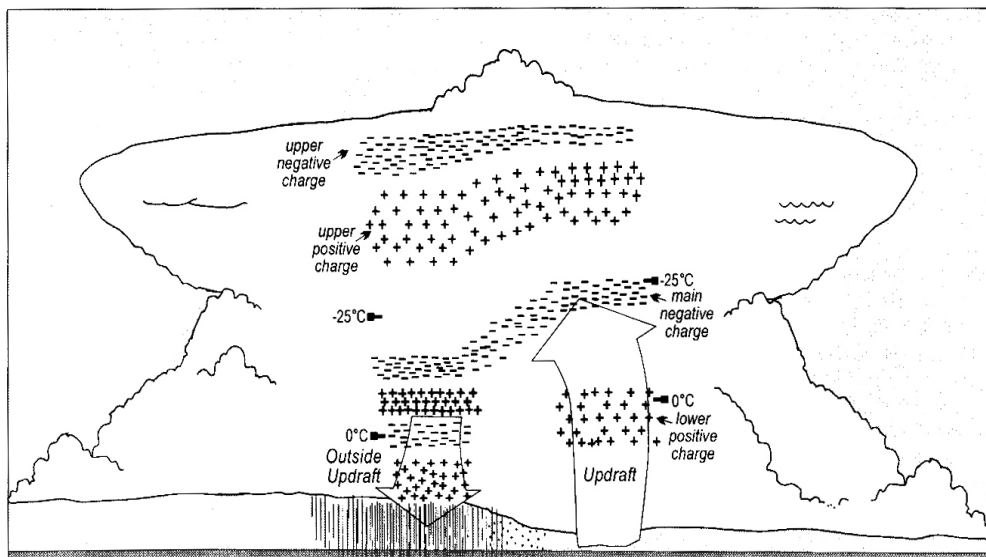


**Figure 1.9.** Schematic of the basic charge structure in the convective region of a thunderstorm. Four charge regions are shown near the updraft and six charge regions are shown outside the updraft within the convective precipitation region. Densities of the plus (minus) signs in the cloud correspond roughly to the typical charge density in each positive (negative) charge region, as estimated from most common features of 49 balloon soundings of electric fields of MCS convective regions, isolated supercells and New Mexican air mass storms. Horizontal and vertical scales and heights of features shown vary with the type of convection, the size, strength and relative positions of the updraft and downdraft. The classical tripole model is clearly represented as the lowest three of the four charge regions in the convective updrafts and are also contained within the six charge regions identified in the downdraft regions. (after Stolzenburg et al., 1998c)

Several mechanisms are thought to be responsible for thunderstorm electrification, of which the most commonly used are briefly introduced below; for a more detailed discussion of different thunderstorm electrification processes see Saunders (1993), Stolzenburg et al. (1998c) and MacGorman and Rust (1998).

- The *non-inductive collisional charging of ice crystals and graupel* (Jayaratne et al., 1983) has been used to explain the tripole charging structure in updraft regions. At temperatures colder than the charge reversal temperature (varying from  $-10^{\circ}$  to  $-20^{\circ}\text{C}$ , depending primarily on the liquid water mixing ratio), the smaller ice particles obtain a net positive charge and may compose the upper positive charge region. The graupel charge negatively and may compose the main negative charge region. The lower positive charge region at mid- to low-storm level may be the result of the same process occurring as graupel were found to charge positively and ice crystals negatively below the charge reversal temperature (Jayaratne et al., 1983). The initial charging structure depends to a major

extent on the horizontal and vertical distribution of updraft speed (particularly above the lower boundary of the mixed phase region), the volume in which particle interactions occur, the resident time of graupel in the mixed phase region, on subsequent trajectories of particles and possibly on the way a storm's environment influences its microphysics. Besides, other non-inductive mechanisms, such as depositional-growth charging of ice crystals and melting charging may also contribute to charge separation.

- *Inductive charge transfer mechanisms* rely on the existing vertical electric field to induce polarization charges in particles so that when a smaller particle bounces off the underside of a larger particle, the oppositely charged particles separate and their charges enhance the electric field (e.g., Saunders, 1993). When the electric field is positive, as it is in low- to mid-levels in updraft regions, falling graupel retain positive charge, while the ascending droplets carry away negative charge that could explain the formation of lowest charge regions.
- In the *screening layer formation process*, negative ions in the clear air are attracted downward in the cloud in the presence of a positive electric field at the cloud boundary. Once these negative ions attach to particles at the cloud boundary, a negative (uppermost) charge layer may form.
- With the *convective charging mechanism*, charges from the surrounding clear air move into the cloud where they attach to cloud particles and are distributed in the cloud by convective motion (updrafts, downdrafts, outflows). This mechanism may account partly for the lower positive charge region in the updrafts, if predominantly positive ions are swept up by the storm's inflow and become attached to hydrometeors in the updraft.

Based on several field studies, laboratory experiments and thunderstorm-lightning models, it has commonly been agreed that there is no typical electrical structure in thunderstorms and that none of above mechanisms can completely explain thunderstorm electrification. MacGorman and Rust (1998) concluded that storm electrification is probably a combination of several mechanisms, whereas non-inductive charging plays a key role.

### 1.6.3 Observation of CG Lightning Activity in Severe Thunderstorms

There have been many attempts to determine whether a severe thunderstorm is producing lightning, examining radar-determined storm characteristics including storm height, formation and location of precipitation and the rate of storm growth. Reviews of the partly controversy results of a large number of lightning observations of both severe and non-severe thunderstorms (e.g., MacGorman and Rust, 1998), revealed that factors that govern flash rates and types are still not completely understood. Some of the most convincing relationships between lightning rates and storm characteristics and the occurrence of severe weather are introduced in the following.

Studies that related radar-determined storm characteristics to lightning observations have shown that taller storms tend to have larger flash rates and that maximum CG flash rates occur approximately when the storm height peaks (e.g., Watson et al., 1995). Buechler and Goodman (1990) found that lightning was imminent when reflectivity values of 40dBZ reached the  $-10^{\circ}\text{C}$  temperature height and radar echo tops exceeded 9 km in 15 storms. Hondl and Eilts (1994) noted that CG lightning occurred 5-25 min after the first 10dBZ echo was observed at the  $-10^{\circ}\text{C}$  isotherm in 22 Florida storms.

Since vigorous growth of storm tops is closely linked to updraft strength, many studies claimed that the speed and structure of updrafts may affect the intensity and timing of thunderstorm electrification (e.g., Solomon and Baker, 1994; Zisper and Lutz, 1994). Increases in vertical storm growth and updrafts have been found to correlate with increasing flash rates; e.g., Mazur et al. (1986) noted that the trend in maximum CG flash densities were similar to trends in maximal heights of 40dBZ reflectivity.

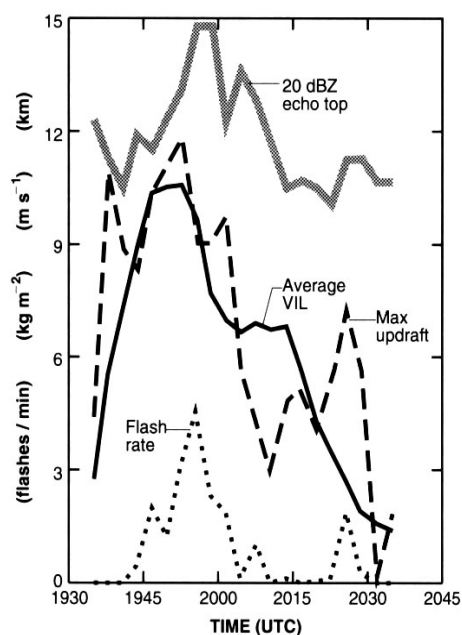


**Figure 1.10.** Total CG flash rates relative to the maximum height of 20dBZ, maximum updraft velocity and average Vertically Integrated Liquid Water (VIL) in a Florida storm. (after MacGorman and Rust, 1998)

The dependence of CG lightning rates on convective strength is related to the observations by several investigators that days with greater conditional instability or greater CAPE tended to produce storms with higher flash rates (e.g., Petersen et al., 1996). Fig. 1.10 shows CG flash rates in relation to several storm variables.

When CG flash rates have been examined relative to radar reflectivity structures, they have often tended to peak at mature storm phase as the reflectivity core descended to middle and lower storm levels (e.g., Williams et al., 1989; Reap and MacGorman, 1989). Most often, CG strikes were found to be near or inside reflectivity contours of 20 or 30dBZ and are densest in regions of high reflectivity (40-50dBZ) that are related to high densities of precipitation particles (Mazur et al., 1986; Reap and MacGorman, 1989; Holle et al., 1994; Petersen et al.,

1996). CG flash rates have been observed to peak prior (10 min) or during convective rainfall and decrease more rapidly from peak values than rainfall (e.g., Watson et al., 1994). Locations of  $-CG$  discharges often cluster in areas of largest reflectivity echoes, whereas  $+CG$  strike points are generally more randomly scattered and normally intensify during dissipating storm phase, showing generally lower densities than  $-CG$  strikes. Fig. 1.11 shows  $-CG$  and  $+CG$  strike locations relative to radar reflectivity cores of a severe Oklahoma storm that produced severe hailfall and a tornado.

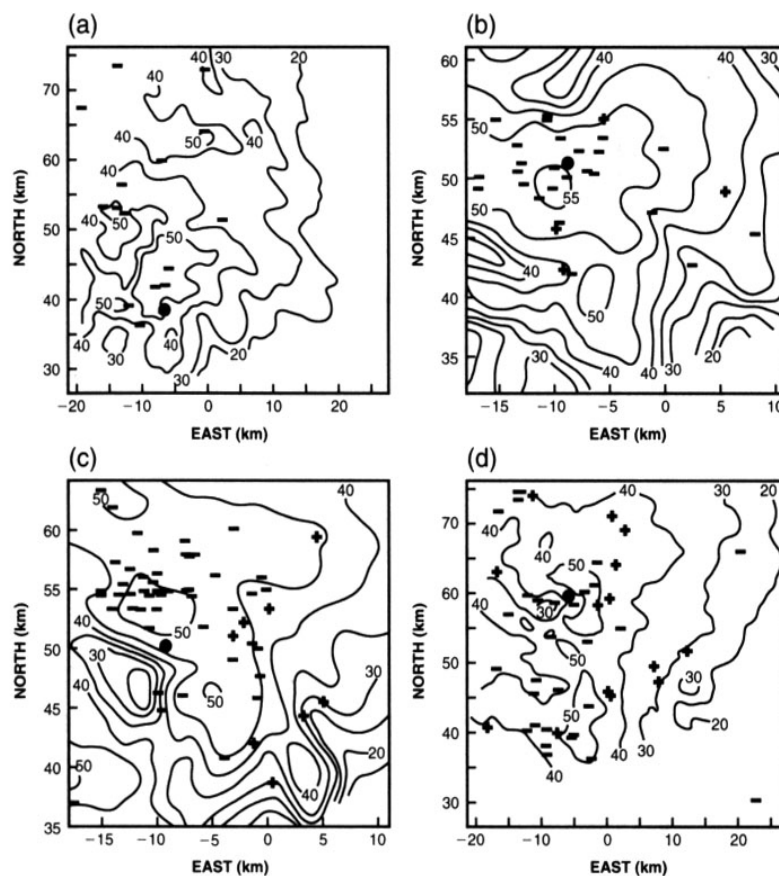


**Figure 1.11.** CG lightning strike location superimposed on radar reflectivity (in dBZ contours) for the 3-km level during four periods of the Edmond storm of 8 May, 1986 in Oklahoma with a) 1802-1806 CST, b) 1814-1817 CST, c) 1824-1827 CST and d) 1834-1838 CST. Minuses indicate strike points of  $-CG$  flashes and pluses strike locations of  $+CG$  flashes. The large dot marks the center of a mesocyclone out of which a tornado developed in time steps b) and c). Note that the distance scale of a) and d) is different from b) and c). (after MacGorman and Nielson, 1991)

Most severe storms produce a majority of  $-CG$  flashes (e.g., Knapp, 1994) and when storms produce  $+CG$  flashes, the percentage is normally small. However, in some storms, the majority of CG flashes can be positive either in the whole storm or during some stage (e.g., Fig. 1.11d) or in some component of the storm; for more details see Section 4.2. Although many severe and tornadic storms do not have large numbers of  $+CG$  flashes, evidence suggests that many storms that produce relatively high flash rates and densities of  $+CG$

flashes also produce severe weather including large hail and tornadoes. Some studies (e.g., Seimon, 1993; MacGorman and Burgess, 1994; Stolzenburg, 1994) suggested that when tornadic storms are dominated by +CG flashes, tornado touchdown occurs after the peak of +CG flash rate and before or near the time when –CG became dominant. Only a few studies examined the relationship between CG flash rates and the occurrence of downbursts and hailfall; for a summary of studies dealing with lightning and hailfall see Section 4.2.

The reason why +CG flashes outnumber –CG flashes for extended periods of time (> 30 min) during the mature phase of some severe storms is not fully understood but often hypothesized to be the result of dynamical and microphysical interactions within the thunderstorm. While, CG flashes lower mostly negative charge to ground during the developing stage of severe storms (mainly as a result of strong updrafts that favor the formation of a large negative charge region under intensive non-inductive graupel-ice collisions), the increase of +CG flashes towards mature and dissipating storm phase is mostly explained by the presence of an enhanced positive charge region in the lower part of the storm (MacGorman and Nielson, 1991; MacGorman and Burgess 1994). The formation of a lower positive charge center can be the result of: (1) a horizontal displacement of updrafts and precipitation during mature storm phase that tilt the dipole and (2) during mature storm phase (i.e., when rain and hail mass fluxes are rapidly increasing at ground), the descent of large numbers of graupel particles in regions below the charge reversal temperature to warmer temperatures (0°C to –15°C) causes graupel to charge positively and create an enhanced positive charge layer that easily explains the predominantly positive charge lowered to ground. While some observations support above hypothesis, some investigations reveal CG lifecycles that can not be fully. MacGorman and Rust (1998) stated that there are still too few data to support or reject any hypothesis that explains the cause of predominately +CG flash activity in severe thunderstorms.

The combination between data of lightning detection systems and radars has been suggested by many studies (e.g., Zisper and Lutz, 1994; Hondl and Eilts, 1994) but as there is still a large number of disagreements between CG lightning rates and the occurrence of severe weather, lightning data could more successfully be used to track thunderstorms (e.g., Finke, 1999; Steinacker et al., 2000) and to detect developing thunderstorms before characteristic radar reflectivity features are available. However, the integration of CG lightning location data into operational nowcasting systems is still a topic of research.

In Chapter 4, CG lightning rates are linked to hailfall intensity (determined from radar-derived hail kinetic energy) of a large sample of hail cells that occurred over the Swiss Mittelland. Based on a reliable relationship between peaks of –CG stroke and hailfall intensity, the results suggest that real-time –CG stroke rates could be used in the future to improve nowcasting of severe hailfalls.

### 1.6.4 CG Lightning Data in Switzerland

In Switzerland, the telecommunication company Swisscom operated a Lightning Positioning and Tracking System (LPATS) between 1989 and 1997 (Rubinstein et al., 1994). Since 1997, the six Swisscom receivers (for location see Fig. 4.1) have been integrated into the Siemens LPATS that covers now Germany and Switzerland. The Swiss LPATS used time-of-arrival (ToA) technology to determine the location of lightning originated pulses and has the capacity of recording simultaneously vertical electric field waveforms detected at up to six receivers. In order to test lightning detection accuracies, Swisscom operated two lightning measuring stations at St. Chrischona (near Basel) and Hohen Peissenberg (near Munich), where CG discharges were constantly measured and been compared to the detection accuracy of the Swiss LPATS. During the time of operation, the Swiss LPATS had an estimated detection efficiency of 70% and a measured lightning location accuracy of 0.2-0.5 km (Rubinstein et al., 1994). Inaccuracies in CG stroke measurements occurred with desensitized receivers during periods of high CG lightning activity and entire system breakdowns when several severe thunderstorms occurred simultaneously over a given region (Section 4.4.2).

Bayernwerk has been operating an LPATS in Southern Germany (Fister et al., 1994) since 1992. As the Bayernwerk system covers a large part of northern Switzerland and has a similar network configuration as the Swiss detection network, lightning location measurements are helpful to evaluate the relative detection efficiency of the Swiss LPATS and to determine days with reduced performance (Section 4.4.2). Since recently, METEORAGE has been maintaining a lightning location system that covers a large part of central Europe (including France, Switzerland, Germany and Austria) and delivers CG flash location measurements with indications of stroke multiplicities. Compared to the Swiss LPATS, the METEORAGE detection system locates CG flashes (and not individual strokes) and utilizes less and different receivers.

## 1.7 Introducing the Three Articles

The first of the following articles is entitled “The use of weather radars to estimate hail damage to automobiles: An exploratory study in Switzerland”. In previous studies, a good relationship was found between hail kinetic energy ( $E_{\text{KINPIX}}$ ) calculated from hailpads and from radar measurements (e.g., Waldvogel et al., 1978a,b; Schmid et al., 1992) so that  $E_{\text{KINPIX}}$  can be taken as a valuable hailfall intensity variable. Furthermore, Schiesser (1988; 1990) found a good correlation between  $E_{\text{KINPIX}}$  and the extent of hail damage to various types of crops and used logistic functions to predict the amount of hail damage to crops from a given hail kinetic energy. In this article we try to relate amounts of hail damage to automobiles to  $E_{\text{KINPIX}}$  that was calculated for several severe hail cells that occurred over the Swiss Mittelland (1992-1998). The constant movement of the cars at risk from hailfall as well as



changing temporal and spatial exposures, complicate a direct attribution of damage claims to hailfall intensity ( $E_{\text{KINPIX}}$ ). As insurance companies attributed damage claims to the community where hail-damaged vehicles are registered, locations of damage claims are irregularly scattered in space. In this article we develop a method to resolve attribution problems, transforming both insurance and radar data on a regular grid so that the data are directly comparable. Disposing of a sample of 12 severe hailstorms, the challenge of this article is to find a link between radar-measured hailfall intensity ( $E_{\text{KINPIX}}$ ), a mean damage per car and the amount damaged in relation to the sum insured.

The second article deals with “Hailfall: The relationship between radar-derived hail kinetic energy and hail damage to buildings”. For a selected number of days where ETH radar measurements were available, we obtained hail damage claims to residential and agricultural buildings from several cantonal building insurance companies. As for hail damage claims on automobiles (article 1), corresponding data from building insurers are aggregated by Swiss community and are therefore irregularly scattered in space. Furthermore, the vulnerability of a building towards hailfall depends on the structure that varies with the type of building. Using the hailfall-damage attribution method established in article 1, damage claims are triangulated on a regular grid, so that damage amounts become comparable to radar-derived hailfall intensity ( $E_{\text{KINPIX}}$ ). The challenge of this article is to investigate the possibility to use logistic functions to predict the mean cost of a hail-damaged building and a total loss ratio (actual damage in relation to the total sum insured of all buildings) of residential and agricultural buildings. In order to verify and calibrated the established damage functions, we use two additional radar-measured hail cells and damage claim data.

If a relationship exists between hailfall intensity ( $E_{\text{KINPIX}}$ ) and the amount of hail damage to automobiles and buildings, we imagine that the established damage functions could be used to assess present hail losses and to predict the approximate amount of expected losses after the passage of a severe hailstorm. Following calibrations of the damage functions with further radar-measured hailstorms and damage claim data, we believe that the curves could be used to calculate worst case scenarios (possible maximum losses), shifting several past severe hailstorms over an insurance portfolio of interest. Based on a large number of radar-measured hailstorms and several modifications of these storms (stochastic modeling), a large number of potential losses could be calculated for exposed risks, providing several damage distributions. This might be of interest for the (re)insurance industry.

The last of the three articles is on “Cloud-to-ground lightning activity in relation to the radar-derived hail kinetic energy in Switzerland”. A large number of studies that examined the electrical lifecycles of severe thunderstorms, revealed a close link between the occurrence of CG flashes (mainly +CGs), large hailfall and tornadoes. Using radar-derived hail kinetic energy ( $E_{\text{KINPIX}}$ ) as a hailfall intensity variable, we aim to investigate the relevance of a link between hailfall intensity and both +CG and –CG stroke rates for a large sample of Swiss

hailstorms. As the study region contains prealpine areas, shielding of low-level radar measurements through the relief are first identified and corrected. Hail cells that first showed low numbers of CG strokes were initially thought to be a special type of storm, but analyzing reports of lightning receivers revealed inaccuracies in the performance of the lightning detection network. Following data correction, the challenge of this article is then to find a link between temporal and spatial peaks of  $\pm$ CG stroke rates and radar-derived hailfall intensity ( $E_{\text{KINPIX}}$ ) and to discuss the resulting difference in the evolution of  $-$ CG and  $+$ CG stroke rates in terms of dynamical and microphysical processes that lead to storm electrification.

Based on a good relationship between temporal and spatial maxima in  $-$ CG stroke rates and hailfall intensity, we believe that once the established relationships have been tested on an independent sample of storms, operationally measured  $-$ CG stroke rates could be used in the future to: (1) support radar-based nowcasting systems and increase warning lead times of severe hailstorms and (2) to determine spatial hailfall patterns ( $E_{\text{KINPIX}}$  distributions) following two methodological approaches described in Chapter 5.

## Chapter 2

### The use of weather radars to estimate hail damage to automobiles: An exploratory study in Switzerland

(reproduced as accepted for publication in *Atmospheric Research* with changes in section numbers, acknowledgement and references at the end of the thesis)

#### 2.1 Abstract

As the first of its kind, this study presents damage functions between two damage variables of hail-damaged automobiles and radar-derived hail kinetic energy for a total of 12 severe hailstorms that have occurred over the Swiss Mittelland (1992-1998). Hail kinetic energy is calculated from C-band Doppler radar CAPPIs at low storm level (1.5 km MSL) and is integrated per radar element ( $E_{\text{KINPIX}}$ ) for entire hail cells. Hail damage claim data were available per Swiss community on a daily basis and transformed (Delaunay triangulation) along with  $E_{\text{KINPIX}}$  to a regular  $3 \times 3$  km grid, thereafter allowing cross-correlation between the variables.

The results show nonlinear relationships between  $E_{\text{KINPIX}}$  and both loss ratios and mean damages per hail-damaged car, differing between high hail season storms (15 June-15 August) and storms that occurred during the low season (before and after). A weighted logistic function provides correlation coefficients between  $E_{\text{KINPIX}}$  and loss ratios of 0.71 (0.79) for high (low) season storms and 0.76 (0.40) for mean damages of high (low) season hailstorms. Maximally possible loss ratios reach 60% (40%) in high (low) season storms with maximum mean damages of CHF 6000 (CHF 3000) and average values around CHF 3100 (CHF 2100). Seasonal differences in hailfall intensities are discussed in terms of atmospheric conditions favoring convective activity and the likelihood of higher numbers of large hailstones ( $> 20$  mm in diameter) that induce more severe damage to cars during the high storm season. The results suggest that radar-derived hail kinetic energy could be used by insurance companies in the future to (1) assess hail damage to cars immediately after a storm

has passed over a radar observation area and (2) to estimate potential maximal hail losses to car portfolios for parts of central Europe.

## 2.2 Introduction

Past experience has shown that severe hailstorms can cause substantial damage and significant losses to insured property, especially if hailstorms move over densely populated areas. In urban hailstorms, hail damage to motor vehicles can consist of a large proportion of the total insured losses; e.g., around 55% in the case of the 1984 Munich hailstorm (MunichRe, 1984), 50% for the 1990 Denver hailstorm (Charlton et al., 1995) and 43% following the 1990 Sydney storm (Andrews and Blong, 1997). In Switzerland, the insurance industry has been facing a growing number of claims due to hailfall damage to property during the last 10 years. Among the most costly hailstorms in Switzerland is the squall line of 21 July 1992 that moved over the city of Basle and induced a total damage of CHF 65 million (US\$ 40 million at current rate) of which 77% was attributable to more than 10,000 hail-damaged motor vehicles (Haase-Straub et al., 1994). As accumulated material values are constantly increasing, storm exposure and damage claims are also expected to raise, independent of a possibly enhancing storm activity as, e.g., partly identified in Switzerland (Schiesser et al., 1997) and France (Dessens, 1995) through time series of hail damage claims on agriculture.

Studies of hail damage to crops and property have revealed that the amount of damage to a target at risk from hailfall is basically a function of: (1) the frequency of severe hailstorms analyzed through historical hail data such as aggregated damage claims provided by crop-hail insurers and (2) the intensity of hailfalls as a function of maximum and/or average hailstone sizes, numbers of hailstones per surface unit and wind that causes hailstones to fall at inclined angles (Changnon, 1999). The magnitude of a hailstorm is often defined in terms of maximum hailstone sizes that were found in an area affected by hailfall (e.g., a postcode area, a community or a district). Maximum hailstone diameters are occasionally provided by meteorological observers and/or the public and are often referred to objects of known or assumed sizes. However, several studies (e.g., Changnon, 1971; Charlton et al., 1995) have shown that hailstone sizes are frequently overestimated by the public. During special field experiments (e.g., NHRE, Foote and Knight, 1979; Grossversuch IV, Federer et al., 1986), dense networks of hailpads have been used to derive hailstone spectra (numbers of hailstones per diameter class) from indentations on the hailpad surfaces. Although hailpads provide probably the most reliable ground-truth information on fine-structures of spatial hailfall variability, networks are costly to maintain on a larger scale and hailstone spectra are usually not available on an operational basis.

On the other hand, the use of weather radar devices for hail detection and quantitative measurements of hailfalls are a promising alternative to ground-measurements with the

advantage to dispose of a unique resolution in time and space. If radars are used, hail cells can be distinguished from nonhail cells by the time-integrated 55dBZ reflectivity area (Geotis, 1963), which gives, however no quantitative result of hailfall intensity. In order to quantify the effects of weather modification experiments (e.g., Federer et al., 1986), considerable effort has been undertaken to find a radar-based variable that reproduces hailfall intensity. One radar-derived hailfall intensity variable that showed valuable results in relation to both ground measurements of hailfalls and hail damage to crops is hail kinetic energy. Waldvogel et al. (1978a) established a point-to-point relationship between S-band radar reflectivity and hail parameters deduced from time-resolved hailstone spectra, a relationship that has been used thereafter to calculate the hail kinetic energy for entire hail cells (Waldvogel et al., 1978b; Waldvogel and Schmid, 1983; Husson and Pointin, 1989). Schmid et al. (1992) found a significant correlation between ground- and radar measured patterns of hail kinetic energy and Wojtiw and Ewing (1986) and Schiesser (1990) revealed good correspondences between patterns of radar-derived hail kinetic energy and amounts of hail damage to crops. Radar-derived hail kinetic energy represents the total volume of hailfall received per surface unit and is used in the current NSSL severe weather detection algorithm (Witt et al., 1998) to estimate the probability of severe hail from radar data provided by the US WSR-88D radar network.

Although costs of hail damage to motor vehicles often represent an important portion of the total loss, only a few attempts have been undertaken to relate hailfall intensity to the amount of hail damage to motor vehicles. This is probably due to the fact that the cost of hail damage to motor vehicles is primarily of interest to insurance companies and published results are not publicly available. Laboratory studies (e.g., Di Constanzo et al., 1996; Shi et al., 1997) have shown that the most significant effect of hail damage to cars is plastic deformation of panels (denting) and failure by cracking of windscreens and plastic components. A dent is defined as a permanent deformation deeper than 0.1 mm (Shi et al., 1997) and dent resistance of car panels is a function of the strength, thickness and curvature of the steel that depends on the car type and age. The size, density and shape of a hailstone, as well as its impact angle and velocity, determine the impact energy and the extent of deformation. Based on studies of hail damage to buildings, Changnon (1977) suggested that damage to structures is more highly correlated to maximum hailstone sizes rather than to numbers of hailstones per surface unit. Waldvogel (1980) deduced from an experiment where natural hailstones were thrown from a 40 m height to a car panel, that only hailstones with diameters  $> 20$  mm caused visible dents. Similarly, Yeo et al. (1999) showed that the most severe damage to cars was induced from hailstones of 50 mm in diameter, whereas stones  $< 30$  mm caused little damage following the severe 1999 Sydney hailstorm. Horizontal wind velocities (e.g., in gust fronts or downbursts) add to the impact energy of a hailstone (often assumed to be proportional to the hailstone diameter) so that hailstones that are below a damage-inducing threshold diameter of e.g., 20 mm (Waldvogel, 1980), could produce a visible dent on a car panel.

Besides the impact energy and various hailstone parameters, the overall amount of hail damage depends on various additional factors (e.g., summarized in Leigh, 1998) including: (1) numbers, densities and values of exposed vehicles within a storm track; (2) spatial and temporal exposures of vehicles that vary with the time of the day and the day of the week; (3) the constant mobility of the cars (especially cars used for commuting and transportation) means that the location where a hail damage has occurred is not necessarily identical to the location where the damage claim is settled; insurance companies often attribute damage claims to administrative area where the car is matriculated; (4) the proportion of fully exposed vehicles (nonsheltered) in relation to nonexposed vehicles (sheltered); (5) the dentability and the reparability costs of different car panel types and (6) the insured value of a unit risk as well as premium-related deductibles (insured's participation on the damage). Furthermore, the threshold damage amount at which it becomes more economic to replace a panel rather than to repair it, is difficult to determine as it depends on numbers and depths of the induced dents, the panel thickness (thin panels are more difficult to repair using traditional panel beating techniques), the panel type (color and type of paint) as well as on the car type and model (Leigh, 1998). The overall claim is further determined by the accessibility of the damaged panel from the inside of the car. As a result, complexities and interactions of the above factors can lead to nonconformities in the locations of the claimed hail damage relative to the storm track and hailfall intensity.

This paper links for the first time radar-derived hail kinetic energy of entire hail cells to hail damage claim data of an entire car portfolio covered by a leading casco and liability insurer. From a sample of 12 severe hail cells that contain a majority of the recent most damaging hailstorms over the Swiss Mittelland (1992-1998), a complete set of radar and hail damage information is available in order to compare spatial coherence between both variables. Section 2.3 provides a description of the data that are analyzed with methods presented in Section 2.4. In Section 2.5, main results including damage functions are shown and discussed in Section 2.6. The paper is thereafter concluded in Section 2.7.

## **2.3 Data**

### **2.3.1 Insurance Data**

Hail damage claim data were available through Winterthur Insurance, a leading casco and liability insurer which covers around 23% of insured motor vehicles in Switzerland. Obligatory casco insurance covers cars against elementary damage including hailfall. Insurance policies are based on the official value of a car (sum insured), which in turn depends on the car type and model and decreases nonlinearly with increasing age of the insured car. Once hail damage has occurred, the damaged vehicle is examined by a trained loss adjuster and the damage cause as well as the estimated damage amount are registered per

policy holder and attributed to the community where the car was matriculated. After a damage amount has been settled, the claim above a certain deductible (defined in the policy) is paid to the insured. A large majority (98%) of the policies issued by Winterthur Insurance contain no deductible so that hail damage claims can be taken as the actual amount of damage and do not have to be adjusted.

For the present study, the following data were available on a daily basis for every hail-damaged car that has been insured by Winterthur Insurance: the postcode of the community where the car was matriculated and the claim was attributed, the approximate location where the damage occurred, the damage claim, the sum insured (value of the car in the year of the claim), the initial value (purchase cost of the car) as well as the number of year risks. Year risks represent the number of exposed policies on a monthly basis as a proportion of the year; e.g., a car that is insured from June of one year throughout May of the following year, reveals a year risk equal to 7/12 in the first year and 5/12 in the following year. However, the number of policies that were exposed in a particular month or day were not available in the present case. On days with severe thunderstorm occurrence and available radar data (Section 2.3.2), insurance data of individual cars were integrated per community where the car was matriculated and geo-referenced by coordinates representing the center of the community. Fig. 2.1 displays numbers of hail damage claims reported to Winterthur Insurance that occurred per community (polygons) following the 10 August 1994 hailstorm over the Swiss Mittelland.

**Table 2.1.** Overview of investigated hail cells and amounts of hail damages on cars insured by Winterthur Insurance (1992-1998) including numbers of damaged cars and claimed damages on a daily basis as well as per hail cell. Proportions of mean damages and loss ratios above a certain level are listed separately.

Storm	Cell	Number of Damaged Cars		Claimed Damage				Loss Ratio <sup>a</sup>	
		Cars Day	Cars Storm	Cars Day	Cars Storm	Number ≤ CHF 4'000	Number > CHF 4'000	≤ 50%	> 50%
[Date]	[UTC]			[CHF mio]	[CHF mio]	[%]	[%]	[%]	[%]
920601	1828	194	110	0.384	0.195	95	5	98	2
920721	1648	7907	857	26.946	2.498	79	21	87	13
920820	1618	1006	678	2.536	1.688	89	11	92	8
930519	1523	537	373	1.101	0.754	89	11	93	7
930705	1429	*5921	1902	*17.402	6.205	72	28	81	19
	1624		384		0.970	84	16	87	13
940602	1653	3861	3229	7.915	6.511	95	5	91	9
940718	1218	898	650	2.673	1.978	74	26	83	17
940806	1553	2187	297	6.585	0.886	78	22	89	11
940810	1208	2493	1285	9.059	5.018	60	40	80	20
950722	1403	451	169	1.089	0.429	76	24	86	14
980721	1303	2550	1933	10.111	7.459	60	40	81	19

\* daily total including several investigated hail cells

<sup>a</sup> calculated from damages as a percentage of sums insured

### 2.3.2 Radar Data

Radar data were provided by the C-band Doppler radar (Joss and Lee, 1995) that has been operating by the Swiss Federal Institute of Technology (ETH) at H  nggerberg, Zurich since 1990. During the National Research Program 31 on “climate changes and natural disasters” in Switzerland (1992-1996) and the following years, more than 200 hail cells were measured with the ETH-radar at a detection range of 120 km that covers a large part of the Swiss Mittelland (Fig. 2.1). In the following, hail cells were distinguished from nonhail cells by the time integrated 55dBZ reflectivity area (e.g., Federer et al., 1986) that lasts at least over 30 min (Schiesser et al., 1997). For most hail cells, manually performed sector-volume scans were available and converted into Constant Altitude Plan Position Indicators (CAPPIs) showing a 0.5-km vertical and a  $0.5 \times 0.5$  km horizontal resolution. For this study, CAPPIs were generated at two storm levels: at 2 km above the daily 0  C isotherm where hailstones grow and at low storm-level on 1.5 km MSL (0.9 km above radar) close to the surface where hailfall occurs. In situations where storms moved over mountainous terrain and CAPPI reflectivities at the lower storm-level were shielded by the relief, upper-level CAPPIs were used for correction according to a radar profile given in Schmid and Waldvogel (1986). On individual CAPPIs, entire hail cells are approximated for each time step (5 min) by a circle centered on the cell core containing reflectivities  $\geq 30$ dBZ using a method previously described in Hohl and Schiesser (2001). The splitting of one cell into two or more cells and the opposite case, the merger of two or more cells into one cell, are treated as one cell only.

Waldvogel et al. (1978a) investigated the relationship between radar reflectivity measured with an S-band radar and the kinetic energy flux determined from 175 hailstone spectra obtained from hail spectrometer measurements. The semi-empirical relationship between the radar reflectivity factor  $Z$  ( $\text{mm}^6\text{m}^{-3}$ ) and the vertical flux of kinetic energy  $\dot{E}$  (at a particular point) can be written as:

$$\dot{E} = 5 \cdot 10^{-6} \cdot Z^{0.84} \text{ [Jm}^{-2}\text{s}^{-1}\text{]} \quad (2.1)$$

The relevance of above  $Z$ - $\dot{E}$  relationship for C-band radar measurements (as used in the present study) has been investigated in Schiesser et al. (1999). The study showed that hail kinetic energy which was calculated from CAPPIs performed from C-band ETH radar measurements in the investigated storm case agreed reasonably well to amounts of hail damage to crops (cross-correlation coefficient of 0.73). Furthermore, the obtained distributions of hail kinetic energy and damage amounts as well as the relationship between these variables appeared to be similar to equivalent data from a hail cell that has been measured (Schiesser, 1990) with the same S-band radar used in Waldvogel et al. (1978a). However, the use of a C-band radar has the disadvantage that the radar beam is more attenuated by high precipitation areas so that high radar reflectivity measurements can be lower compared to S-band radar measurements. As in the case of the present study, a particular emphasis has been put on the assessment of nonattenuated hail cells, the above  $Z$ - $\dot{E}$



relationship has been considered appropriate to calculate the flux of kinetic energy from C-band radar reflectivity.

Since the radar reflectivity factor  $Z$  is radar-specific and varies over the time, a small error in  $Z$  produces a difference in the flux of hail kinetic energy ( $\dot{E}$ ) and once  $\dot{E}$  is integrated over the time and surface of hailfall, a systematic error can occur. In order to assess and correct variations of  $Z$ , ETH radar reflectivity measurements have constantly been calibrated with corresponding measurements of a Joss-Waldvogel distrometer (Joss and Waldvogel, 1967). A distrometer transforms the vertical moment of an impacting raindrop into an electric pulse whose amplitude is a function of the drop diameter. A conventional pulse height analysis yields the size distribution of the precipitation particles and a reflectivity factor can be calculated out of the sums of particles to be compared with a factor directly obtained from radar measurements. During the period of investigation (1992-1998), ETH radar measurements were calibrated on the average three times a year and revealed an overall increase of  $Z$  in the range of +1.5dBZ.

In the following, the flux of kinetic energy was calculated from radar reflectivity measured at low level CAPPIs, using the  $Z$ - $\dot{E}$  relationship in Eq. (2.1). To obtain the entire hail kinetic energy per surface unit ( $E_{KINPIX}$ ),  $\dot{E}$  is integrated over the entire storm duration ( $t_0 \rightarrow t_1$ ) and per radar element ( $s_0 \rightarrow s_1$ ) at a  $0.5 \times 0.5$  km resolution:

$$E_{KINPIX} = \int_{t_0}^{t_1} \int_{s_0}^{s_1} \dot{E}(x, y, t) dx dy dt \quad [\text{Jm}^{-2}] \quad (2.2)$$

In this study, the “cutting method” (i.e., all reflectivity values  $> 55\text{dBZ}$  are attributed to hail and those  $\leq 55\text{dBZ}$  to rain) is used for the calculation of  $E_{KINPIX}$ ; other different attribution methods are discussed in Waldvogel et al. (1980). The “cutting method” was also used by Schiesser (1990) and lead to good relationships between hailfall and damage to crops. In the following, the area covered by radar pixels that contain  $E_{KINPIX}$  is considered to represent the area of hailfall and the value of  $E_{KINPIX}$  the intensity of hailfall. However, as hail kinetic energy represents the volume of hailfall per surface unit, a volume that contains a large number of small hailstones can produce the same energy as a volume of a few large stones.

From a previous study (Hohl and Schiesser, 2001), 60 radar-measured hail cells were available, of which 12 cells were selected. Eight of the analyzed cells occurred on one of the 15 days (1992-1998) where damage claims from more than 1000 cars were reported to Winterthur Insurance (Winterthur Insurance, 2000). On days, where several hail cells induced damages to cars (e.g., 920721 or 930705 in Table 2.1), storm tracks were only analyzed if damage was clearly attributable to a specific storm as identified from radar measurements.

## 2.4 Methods

Methods of how radar-derived hail kinetic energy is related to hail damage claims are first presented and illustrated for one hail cell (Fig. 2.1). Spatial integration of radar and damage data as well as cross-correlation methods are described and illustrated in the following (Fig. 2.2).

### 2.4.1 Attribution of Hailfall Intensity and Damage Claims

Complexities in relating hailfall intensity to damage claims of entire car portfolios result mainly from changes in spatial and temporal exposures through the constant mobility of the units at risk. In order to compare hailfall intensities and damage amounts on the radar scale, the following simplification and assumptions were necessary. (1) Radar-derived hail kinetic energy ( $E_{\text{KINPIX}}$ ) is considered as the hail intensity response variable. (2) Wind velocity measurements (e.g., Doppler velocities) were not available and hailfall is therefore assumed to be constant from one direction over the entire storm duration. (3) The area of hailfall is approximated by a storm box (Fig. 2.1) containing all radar elements that reveal  $E_{\text{KINPIX}}$ . (4) Hail-damaged cars are attributed to the community where they were matriculated, assuming first a quasi-nonmobility of the units at risk. (5) A community is considered to be affected by hailfall if its center is located in the area of hailfall (storm box) and at least five hail damage claims were reported. First analyzes have shown that communities that are within an approximated storm box show considerably higher numbers of hail-damaged cars than communities outside the box (Fig. 2.1). Winterthur Insurance (1997) conducted a study where car exposure has been assessed through traffic counts in urban and suburban areas in Switzerland, showing that 15% of the cars were moving whereas 85% were parked (40% of them in the open) during the afternoon (15-16 UTC). The 15% of cars estimated to be on mobility during hailfall is similar to the five damage claims per community that represent on the average 20% of the total claims. (6) As  $E_{\text{KINPIX}}$  and damage variables are compared on the radar scale and no information was available on hail damage severity to cars, panel dentabilities of different car types are assumed to be comparable.

For communities that fulfill above criteria, three damage variables were calculated: a damage extent (numbers of damaged cars / numbers of year risks), a loss ratio (total damage / sums insured) and a mean damage per insured car (total damage / numbers of damaged cars).

### 2.4.2 Cross-Correlation and Storm Shifting Method

In order to perform a direct point-to-point analysis of the locations of damage claims that are irregularly scattered over the communities (Fig. 2.1) relative to hailfall intensity ( $0.5 \times 0.5$  km resolution), the data were transformed to a regular grid. Depending on the spatial continuity of nonregularly spread data, various methods can be used to obtain regularly gridded data points (e.g., Bailey and Gatrell, 1996). In the present case, Delaunay triangulation is applied,

transforming the hail damage variables to a regular  $3 \times 3$  km grid. This resolution is accurate since one grid point approximately covers one community in the Swiss Mittelland with a mean surface of  $10 \text{ km}^2$ . The main advantage of averaging damage variables per community and triangulating the data on a regular grid is that differences in the sums insured and damages that are produced by individual cars are mostly removed. In correspondence with the damage variables,  $E_{\text{KINPIX}}$  values were transformed to the same grid, which, however, involves a loss in the fine-structures of hailfalls. Reproductivity of characteristic features of storm and damage variables on a  $3 \times 3$  km grid appeared to be equally precise as on a  $2 \times 2$  km or  $1 \times 1$  km grid, containing, however, a lower amount of data points. Fig. 2.2 shows triangulated  $E_{\text{KINPIX}}$  and loss ratios on a  $3 \times 3$  km grid for the hailstorm that occurred on 10 August 1994 with clearly discernible spatial correspondence between the data.

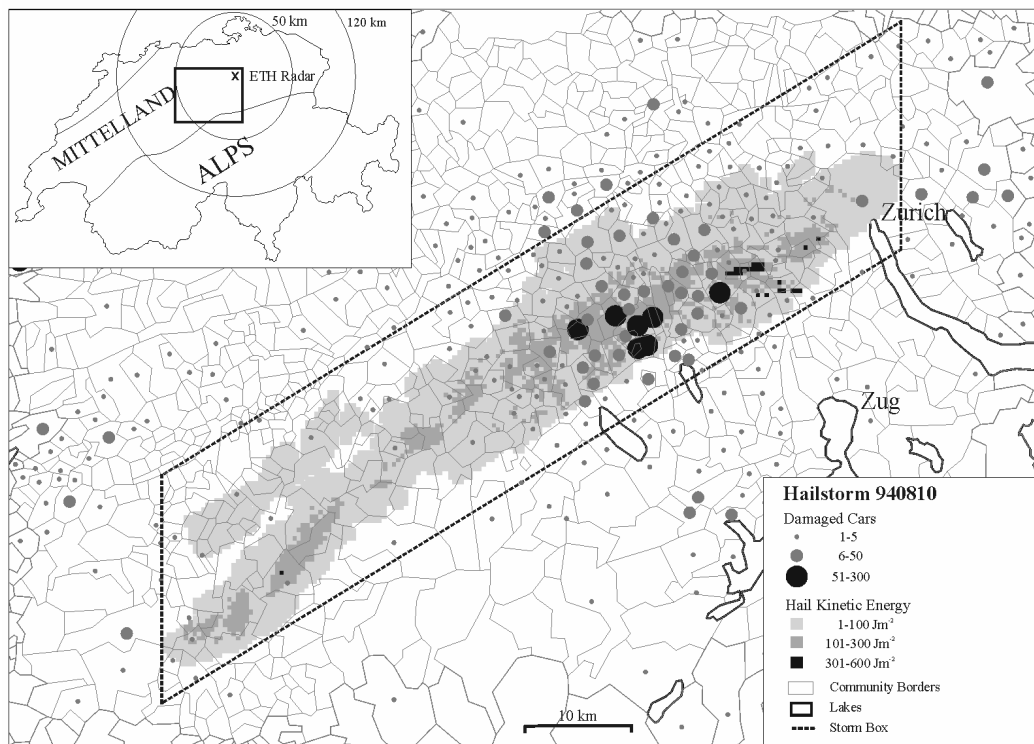


**Figure 2.1.** Overview of Switzerland (top left) with geographically distinct regions of the Mittelland and the Alps, the location of the ETH-radar (cross), the 50 and 120 km detection range (circles) and the area of enlargement over central Switzerland (square). The enlarged area displays radar-derived hail kinetic energy in three intensity levels (grey shaded squares) and numbers of hail-damaged cars per Swiss community in three intensity levels (grey shaded circles) for the hailstorm that occurred on 10 August 1994. The storm box (dotted) designs the area of hailfall in which hail kinetic energy and hail damage variables are cross-correlated. Major cities are indicated and lakes are given in as bold outlines.

Cross-correlating radar-derived hail kinetic energy at low storm level and vertically underlying extents of hail damage to crops, Wojtiw and Ewing (1986) and Schiesser (1990) showed that correlation coefficients improved considerably applying a shift vector to the energy field against ground. This improvement is mainly due to displacements of hailstones

that fall from radar-measuring level to ground and are diverged through downdrafts in the cell core. In this study, a constant unidirectional shift vector of 3 km (one grid width) in one direction is applied to the entire  $E_{\text{KINPIX}}$  field, neglecting, however, the different fall distances between a radar-measurement point and the underlying damage as well as terminal velocities of hailstones that determine the fall time. The final shift vector is composed of a vertical component determined by the fall speed of hailstones and a horizontal component resulting from wind velocities in or near the downdraft region of the hail cell. As shown in Mezeix and Admirat (1978) and Matson and Huggins (1980), falling hailstones of 10 mm (20 mm) in diameter reach terminal fall speeds of  $10 \text{ ms}^{-1}$  ( $15 \text{ ms}^{-1}$ ). Horizontal wind components in severe hailstorms vary typically between 10 and  $25 \text{ ms}^{-1}$  with maximum gusts of  $50 \text{ ms}^{-1}$  in the downdraft region (e.g., Browning, 1977; Houze et al., 1993). A 3 km horizontal shift of the  $E_{\text{KINPIX}}$  field against ground implies, in the present case, the descent of a 10 mm hailstone (terminal fall speed of  $10 \text{ ms}^{-1}$ ) from 1.5 km MSL (radar measuring level) to 0.4 km MSL (ground) with a horizontal wind component between 20 and  $30 \text{ ms}^{-1}$ ; at a given horizontal wind component, fall distances decrease, however, with increasing hailstone diameters. In the following, an individual optimal shift vector is first determined for every damage variable and thereafter combined into an unidirectional vector that agrees best to all variables.

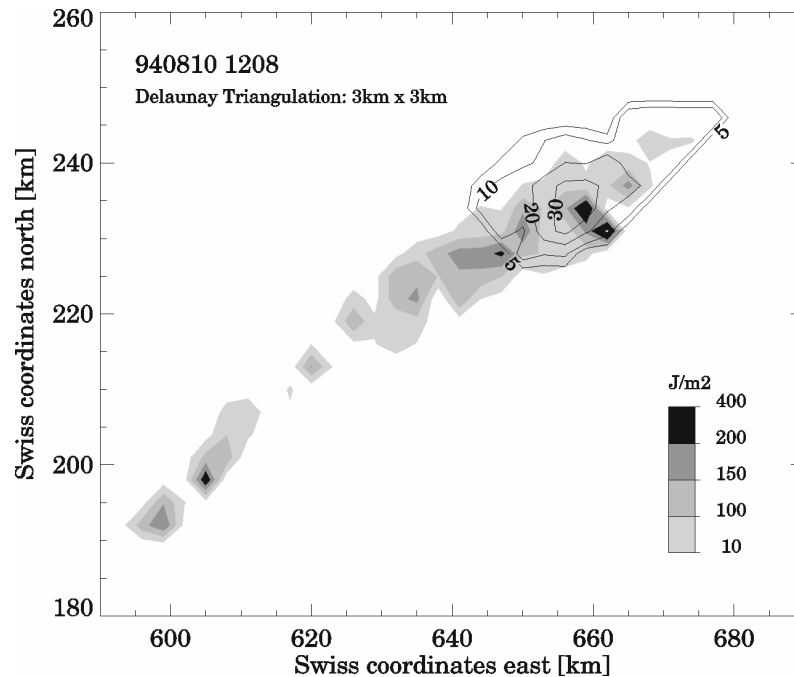


**Figure 2.2.** Same storm as in Fig. 2.1 but with triangulated hail kinetic energy ( $E_{\text{KINPIX}}$ ) in four intensity scales (grey shades) and triangulated loss ratios (labeled isolines in percent) on a regular  $3 \times 3$  km grid before storm shifting (see Section 2.5.3). Swiss coordinates are used.

## 2.5 Results

Hail cells are first compared on storm scale and trends in the agreement between hailfall variables and amounts of damage presented. The shifting of storm fields and the resulting cross-correlation coefficients between hailfall intensity ( $E_{\text{KINPIX}}$ ) and two damage variables are given thereafter. In the following,  $E_{\text{KINPIX}}$  is presented in relation to loss ratios, mean damages and damage extents. Table 2.1 provides an overview of numbers and amounts of claimed hail damages, both per day and investigated hail cell. Table 2.2 lists hailfall variables including storm heights, distributions of  $E_{\text{KINPIX}}$ , surfaces of hailfall as well as estimations of maximum hailstone diameters. Cross-correlation coefficients between patterns of  $E_{\text{KINPIX}}$  and both loss ratios and mean damages as well as corresponding shifting vectors are shown in Table 2.3. Individual hail cells are distinguished according to the date and initial time (UTC) of occurrence.

### 2.5.1 Storm Scale Analyzes

The investigated hail cells caused losses ranging from CHF 0.2 million (110 cars damaged) up to CHF 7.5 million attributable to 1923 cars (Table 2.1). Of all storms, cell 940602 1653 produced the highest number of damaged cars and induced a total damage of CHF 6.5 million. On days where several hail cells occurred, daily insured losses reached up to CHF 27 million. All hail cells developed between mid-day (first cell 1208 UTC) and early evening (last cell 1828 UTC), typically propagating from southwest to northeast (Table 2.2). Most storms produced hail streaks of 22-125 km in length, while one cell (940602 1653) traveled over 200 km and initiated several damage tracks with lengths over 50 km. The surface of hailfall was determined from the sums of radar elements containing  $E_{\text{KINPIX}}$  and range in the present cases from 114 to 2295 km<sup>2</sup> (Table 2.2). Eight of the investigated hail cells were previously classified as supercells (e.g., Schiesser et al., 1997; 1999) that are well known to generate large and long-lasting updraft regions in which hailstones can grow large enough to cause important damage on ground.

Waldvogel et al. (1979) showed that a thunderstorm cell is very likely to initiate hailfall if the maximum 45dBZ radar reflectivity height ( $H_{45}$ ) is at least 1.4 km above the daily 0°C isotherm which is typically around 3-4 km MSL in summer. Additionally, Schiesser (1998) revealed that hail cells with  $H_{45} > 9$  km MSL produced hailstones larger than 20 mm, measured on ground-based hailpads. In all present cells,  $H_{45}$  heights range from 10 to 14 km (Table 2.2) and exceed both the 0°C isotherm and the 9 km threshold level. For some of the hail cells, maximum hailstone diameters were available from newspaper reports (Table 2.2). Additionally, maximum hailstone diameters were estimated from highest radar reflectivity measurements according to an empirical relationship given in Schiesser (1998). The present hail cells produced largest hailstones which ranged between 30 and 50 mm in diameter and reveal differences in estimated and reported maximum hailstone sizes in some cases (e.g.,

930705 1429 in Table 2.2). The apparent differences in hailstone sizes could be due to usual over-estimations of hailstone sizes by the public (Changnon, 1971; Charlton et al., 1995) and/or potential underestimation of maximum hailstone sizes measured on hailpads (Smith and Waldvogel, 1989) which are linked to radar reflectivity.

**Table 2.2.** Storm variables calculated for the investigated hail cells including mean movement, area of hailfall (surface of radar elements with  $E_{KINPIX}$ ), distributions of hail kinetic energy ( $E_{KINPIX}$ ) and hailfall duration as well as maximum hailstone sizes. Note that  $E_{KINPIX}$  values are before triangulation.

Storm	Cell	Mean	H <sub>45</sub>	A <sub>55</sub>	E <sub>KINPIX</sub> [Jm <sup>-2</sup> ]				Hailfall Duration [min]			dBZ	Max Hailstone	
		Movement	Max	TOT	Max	< 200	200-600	> 600	Max	≤ 5	> 5	Max	Diameter	
													est. <sup>a</sup>	rep. <sup>b</sup>
[Date]	[UTC]	[°/km/s <sup>-1</sup> ]	[km]	[km <sup>2</sup> ]	[Jm <sup>-2</sup> ]	[%]	[%]	[%]	[min]	[%]	[%]	[dBZ]	[mm]	[mm]
920601	1828	217/51/11	11	315	480	76	24	0	10	73	27	65.8	35	
920721	*1648	227/65/12	11	641	426	98	2	0	12	93	7	65.5	35	30
920820	*1618	207/87/10	12	746	673	71	28	1	15	65	35	68.2	37	
930519	1523	211/35/6	11	378	1222	39	47	14	25	32	68	66.7	36	
930705	*1429	178/72/14	13	810	612	84	16	0	10	81	19	68.5	35	50
	*1624	214/76/14	11	345	448	92	8	0	7	98	2	71.2	41	30
940602	*1653	215/218/23	10	2295	326	91	9	0	7	99	1	69.5	39	
940718	1218	199/63/10	10	235	453	94	6	0	7	99	1	67.5	37	
940806	1553	234/22/4	13	114	1809	44	23	33	35	38	62	69.0	39	50
940810	*1208	209/90/14	11	1003	520	96	4	0	8	97	3	71.5	42	
950722	*1403	219/125/17	14	896	412	85	15	0	13	73	27	66.7	36	
980721	*1303	239/60/12	11	517	821	68	27	5	20	53	47	67.7	37	50

\* supercell thunderstorm

<sup>a</sup> estimated from measured maximum radar reflectivity (dBZ) according to Schiesser (1998)

<sup>b</sup> reported in newspapers

The investigated hail cells reveal a certain relationship between storm variables and hailfall intensity, particularly regarding propagation velocities that determine both the duration of hailfall and  $E_{KINPIX}$  through the volume of hail received per surface unit. In the present cells, hail kinetic energy tends to decrease nonlinearly with increasing propagation velocity and differences are most pronounced if cells with highest and lowest velocities are compared. (1) Cells that reveal lowest average propagation velocities (930519 1523 at  $6 ms^{-1}$ ; 940806 1553 at  $4 ms^{-1}$ ) produced low proportions of  $E_{KINPIX} < 200 Jm^{-2}$  but high proportions above  $600 Jm^{-2}$  with high maximum  $E_{KINPIX}$  (Table 2.2). On the other hand, fast moving hail cells (940602 1653 at  $23 ms^{-1}$ ; 950722 1403 at  $17 ms^{-1}$ ) generate hailfalls that tend to induce  $E_{KINPIX}$  spectra that have the highest proportions in the low ( $E_{KINPIX} < 200 Jm^{-2}$ ) and small proportions in the middle and upper range ( $E_{KINPIX} > 600 Jm^{-2}$ ) along with lower maximum  $E_{KINPIX}$  measured at one radar element (Table 2.2). (2) For slow moving cells, maximum hailfall per radar element lasted 25 (930519 1523) and 35 min (940806 1553) while around two-thirds of the surfaces were affected by hailfalls that lasted over 5 min (Table 2.2). Cells that show high propagation velocities tend to generate hailfalls that lasted maximally 7 (940602 1653) and 13 min (950722 1403), with a majority of radar elements that received hailfalls that lasted less than 5 min.

### 2.5.2 The Influence of Seasonal Hailfall Intensity on Damage Variables

Comparing cell-specific distributions of mean damages and loss ratios above a certain damage threshold (Table 2.1) it appears that one group of cells produced lower percentages of mean damages over CHF 4000 and correspondingly lower amounts of loss ratios that are above the 50% level. The same distinction between these two groups of storms results from statistical relationships between hailfall intensity ( $E_{\text{KINPIX}}$ ) and both loss ratios and mean damages (Section 2.5.4 and 2.5.5). Since hail damage on motor vehicles occurs mainly from the impact of large hailstones (e.g.,  $> 20$  mm in diameter as suggested in Waldvogel, 1980), the apparent differences in loss ratios and mean damages between the two groups of cells can be the result of differences in proportions of large hailstones, which produced, on the average, higher damage to cars.

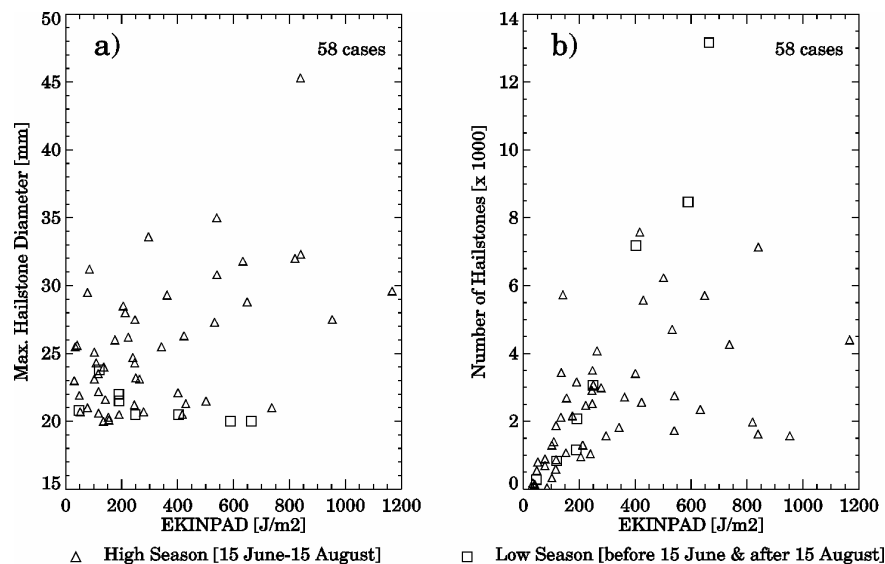


**Figure 2.3.** Hailpad measurements of 15 days with hailstorm occurrence (1977-1983), available from Grossversuch IV conducted in the Swiss Mittelland (Federer et al., 1986). The figure depicts relationships between hailpad-derived kinetic energy ( $E_{\text{KINPAD}}$ ) and a) the maximally measured hailstone diameters for pads with at least one stone of 20 mm in diameter from high season storms (50 cases, triangles) and low season storms (8 cases, squares) and b) the number of hailstones recorded per hailpad (with at least one stone of 20 mm in diameter) for high season storms (50 cases, triangles) and low season storms (8 cases, squares).

There is evidence that hailstorms which occur during the peak hail season (typically during mid-summer months when convective instability and vertical storm development are highest) produce hailfalls that are characterized by a high percentage of large hailstones. In the present study, the distinction of storms that occurred during the high season (defined here from 15 June to 15 August) and a low season (before and after) lead to best results. The present classification is based on some general reflections on seasonal differences in storm environments (Section 2.6) and is supported by findings of some previous studies that are discussed in the following. (1) Prodi (1974) investigated hailfall frequencies over the Po-valley in northern Italy (1968-1972) from reports of ground-based observers and showed that

the frequency of small hailstones decreased from April to August, whereas largest hailstones ( $> 30$  mm in diameter) occurred mostly during August. (2) Schiesser (1998) investigated 58 hailpad-derived hailstone spectra that were available from Grossversuch IV (Federer et al., 1986) in central Switzerland (1977-1983). Comparing maximum heights of 45dBZ radar reflectivity ( $H_{45}$ ) and hailpad-derived hailstones  $> 20$  mm in diameter, Schiesser (1998) showed that largest hailstones were mostly produced by storms with  $H_{45} > 9$  km that occurred most frequently in July and August. This finding is supported by the fact that the 50 most severe haildays in Switzerland (1920-1994) that produced the highest daily number of hail damage claims to crops (Radar Meteorology Group, 1995), occurred in 64% during storms of the high season (15 June-15 August). (3) A reanalysis of the data investigated in Schiesser (1998) shows that maximum hailstone diameters were significantly larger during the high hail season (15 June-15 August) with average sizes of 26 mm (20-45 mm), than during the low season (before and after) with sizes averaging around 21 mm (20-23 mm) as shown in Fig. 2.3a. Measured hailstones averaged around 2490 (4526) stones per hailpad for storms that occurred during the high (low) season (Fig. 2.3b). The data show a significant difference in both maximum hailstone sizes and numbers according to the hailstorm season: e.g., a hailpad revealing a kinetic energy ( $E_{KINPAD}$ ) of  $600 \text{ Jm}^{-2}$  can receive around 4000 hailstones per pad in the high season with maximum diameters of 30 mm, whereas a low season hailstorm can reveal the double amount of hailstones with maximum sizes of 20 mm. (4) Above differences in the seasonal distribution of numbers and diameters of hailstones are partly confirmed by a recent study of Giaiotti et al. (2001), where monthly percentile average distributions of hailstones are analyzed from 3408 hailpads on the plain of Friuli-Venezia Giulia, northern Italy (1988-1998). The study revealed that numbers of large hailstones were relatively smaller in April and May than during the following months (June-September). On the other hand, highest numbers of hailstones were mainly produced in the months of June and September.

Although the present hail season classification is somewhat arbitrary and more quantitative criteria are needed (Section 2.6), differences in damage amounts can be reasonably explained, dividing hail cells into high and low season storms. Comparing loss ratios of the four low season storms, the data show that proportions of the loss ratios that are over the 50% threshold level (i.e., half of the sum insured if a car is damaged) are below 10% (Table 2.1). Moreover, the eight cells that occurred during the high season tend to generate proportionally higher loss ratios that reach 50% and more, varying between 11% and 20%. Correspondingly, proportions of hail damage claims over CHF 4000 vary between 16 and 40% among high season storms (Table 2.1) and are higher than proportions of damages induced by low season storms (5-11%).



### 2.5.3 Shifting and Correlation Analyses

For every hail cell, cross-correlations between data pairs of  $E_{\text{KINPIX}}$  and damage variables have been calculated, first with underlying damage variables (no shift) and secondly applying a shift of the  $E_{\text{KINPIX}}$  field against ground. Correlation coefficients between  $E_{\text{KINPIX}}$  and loss ratios ranged initially from  $-0.31$  to  $0.79$  (no shift) and improved overall after storm shifting, varying between  $0.26$  and  $0.93$  (Table 2.3). Cross-correlation coefficients between  $E_{\text{KINPIX}}$  and mean damages improved correspondently, ranging from  $-0.12$  to  $0.89$  after appropriate storm shifting (Table 2.3); in one cell (950722 1403), the coefficient remained negative after shifting, whereas in a further case (920721 1648) no correlation is obtained since the two data pairs are vertically aligned (Fig. 2.4d). In most hail cells, hailstones fell from the 1.5-km radar measuring level to ground towards north ( $0^\circ$ ) and northeast ( $45^\circ$ ) and best results are achieved by applying a horizontal shifting of 3 and 4.3 km (Table 2.3). For two storms, no shifting was required since correlation coefficients decreased with shifting. The fallout of hail from low storm-level to ground from north or northeast has also been noticed in similar studies conducted in the Swiss Mittelland (e.g., Schiesser, 1990; Schmid et al., 1992).

After storm shifting, a complete set of data pairs containing  $E_{\text{KINPIX}}$  as well as damage extents (178 pairs), loss ratios (133 pairs) and mean damages (74 pairs) are available to analyze point-to-point relationships.

**Table 2.3.** Cross-correlation coefficients for the relationships between  $E_{\text{KINPIX}}$  and both, loss ratios and mean damages before and after storm shifting. The average shift vectors are listed additionally and numbers of data pairs are indicated separately for each damage variable.

Storm	Cell	Correlation Coefficients Shift						Shift Vector
		loss ratio			mean damage			
		no	yes	pairs	no	yes	pairs	
[Date]	[UTC]							[°/km]
920601	1828	0.78	0.78	6	0.64	0.64	4	none
920721	1648	-0.08	0.46	6	*0.00	*0.00	2	0/3.0
920820	1618	0.53	0.74	17	0.37	0.78	11	45/4.3
930519	1523	0.11	0.81	12	0.53	0.73	5	315/4.3
930705	1429	-0.12	0.51	32	-0.26	0.54	16	45/4.3
	1624	0.12	0.32	8	-0.02	0.53	3	0/3.0
940602	1653	-0.31	0.73	22	-0.19	0.77	3	34/4.3
940718	1218	0.14	0.93	3	0.39	0.50	5	0/3.0
940806	1553	0.67	0.74	5	0.55	0.89	5	0/3.0
940810	1208	0.23	0.26	11	0.59	0.62	11	0/3.0
950722	1403	0.79	0.79	4	*-0.12	*-0.12	4	none
980721	1303	0.01	0.53	7	0.05	0.78	5	45/4.3
Total	12 cells			133			74	

\* for explanation see Section 2.5.3. and Fig. 2.4d

### 2.5.4 Hailfall Intensity vs. Loss Ratios

The relationship between hail kinetic energy and hail damage is inherently nonlinear as amounts of hailfall smaller than some level may result in no damage while, on the other hand, amounts of hailfall greater than some other level can still result in no more than a maximally possible damage. Katz and Garcia (1981) and Schiesser (1990) showed that the nonlinear relationship between hail kinetic energy and hail damage to crops is best described by a logistic function that has the following general form:

$$y_i \cong \frac{e^{(\beta_0 + \beta_1 x_i)}}{1 + e^{(\beta_0 + \beta_1 x_i)}} \quad (2.3)$$

where  $y_i$  represents the hail damage proportion,  $x_i$  the corresponding value of the hailfall variable (here  $E_{KINPIX}$ ) for an observation  $i$ , while  $\beta_0$  and  $\beta_1$  are parameters that have to be estimated by the data as follows:

$$L(y_i) = \ln\left(\frac{y_i}{1 - y_i}\right) = \beta_0 + \beta_1 x_i \quad (2.4)$$

$L(y_i)$  is the natural logarithm (or *logit*) of the ratio of proportion damaged to proportion non-damaged and is a linear function of the hailfall variable. Since  $L(y_i)$  depends on the proportion of damage and is therefore not a constant function, a weighted regression analysis of  $L(y_i)$  vs.  $x_i$  has been performed according to the method used in Katz and Garcia (1981). Hail damage values must strictly be above 0% and below 100%, since otherwise the *logit* transformation given in Eq. (2.4) is undefined. As  $E_{KINPIX}$  data points without underlying damage were excluded from the analysis and low loss ratios (< 10%) are difficult to obtain (since reparability costs of car panels are, independent of the number of dents, above a minimal level), the logistic curve is not defined at lowest values and has to be assumed. Katz and Garcia (1981) suggested that one way to predict values at low scale by the logistic function is to fit the curve through  $x=0$  and  $y=0$  replacing the hailfall variable  $x_i$  in Eq. (2.3) by the natural logarithm of  $x_i$ . As loss ratios within a car portfolio hardly reach 100% (total damage) but approximate a lower maximally possible ratio, the logistic curve can be adjusted for maximum values, assuming a possible maximum damage ratio ( $y_{max}$ ) and replacing  $y_i$  in Eq. (2.4) by  $y_i/y_{max}$ . In the present case,  $y_{max}$  was estimated to reach 60% (40%) for storms during the high (low) season (Fig. 2.4a,b).

From the available data pairs, damage functions are calculated for eight high season storms (76 pairs) and four low season hailstorms (57 pairs). Weighting of data on the middle part modifies the shape of the logistic curve (slightly steeper) and provides correlation coefficients of 0.71 for high season storms and 0.79 for storms that occurred during the low season. The difference in loss ratios from high and low season storms is further illustrated in Fig. 2.4c.

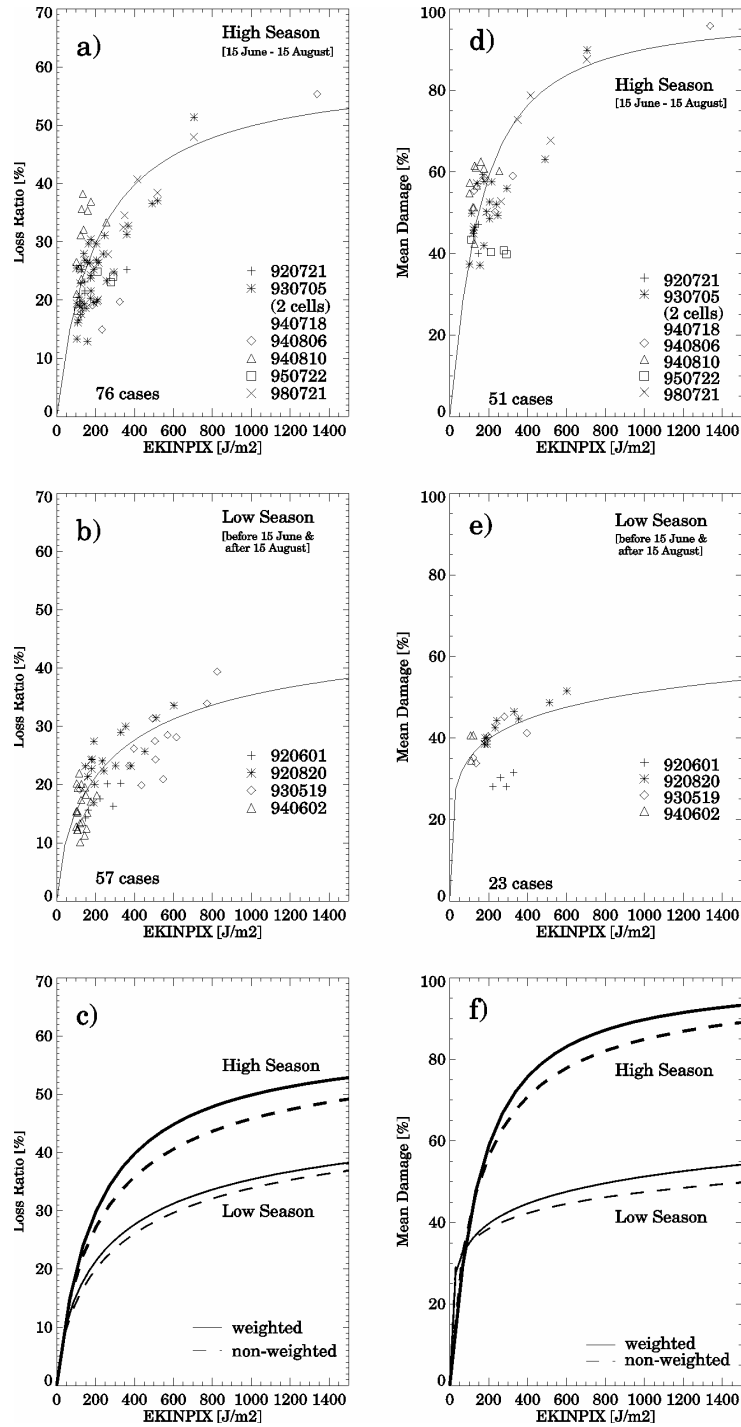


**Figure 2.4.** Relationship between hail kinetic energy ( $E_{KINPIX}$ ) and a) loss ratios of high season storms (76 cases) with a weighted logistic function providing a correlation coefficient of  $r=0.71$ ; b) same as a) but for low season storms (57) cases with a correlation coefficient of  $r=0.79$ ; c) loss ratios of high season storms with weighted (solid) and non-weighted logistic function (dashed) for high season storms (thick) and low season storms (thin); d) the mean damage per car as a percentage of the maximally possible mean damage (CHF 6000) for high season storms (51 cases) with a weighted logistic function providing a correlation coefficient of  $r=0.76$ ; e) the same as d) but for low season storms (23 cases) with a correlation coefficient of  $r=0.40$ ; e) same as c) but for mean damages. Note that different storms are depicted by different symbols.

### 2.5.5 Hailfall Intensity vs. Mean Damages

In accordance with loss ratios, mean damages also reveal seasonal dependence. Maximum mean damages reach CHF 6000 per car in the case of high season storms (taken as 100% in Fig. 2.4d,e) and around CHF 3000 for storms that occurred during the low hailstorm season (Fig. 2.4e). Mean damages average CHF 3100 (US\$ 1900 at current rate) during the high season, whereas it is CHF 2100 (US\$ 1300) for low season hailstorms. The average mean damage per high season storm is comparable to the mean damage of DM 3300 (US\$ 1700) that occurred after the 12 July 1984 Munich hailstorm (MunichRe, 1984), which qualifies under the present definition as a high season storm. From all investigated hail cells, the 1992 Basle storm (920721 1648) produced the highest average mean damage per car with CHF 5900 (US\$ 3700). In comparison to the 1984 Munich and the 1992 Basle storm, the 1999 Sydney hailstorm produced a considerably higher average mean damage per car that reached US\$ 5300 (PartnerRe, 1999). Beside differences in exposure and vulnerability of cars, differences in the amount of damage is partly explained by hailfall intensity: both the 1984 Munich and the 1992 Basle storm produced hailstone sizes that reached 50 mm in diameter (MunichRe, 1984; Haase-Straub et al., 1994), whereas the 1999 Sydney cell produced hailstones that were larger than 65 mm (Yeo et al., 1999) with a maximum of 110 mm (Buckley et al., 2001).

As for the loss ratios, a weighted logistic curve has been fitted to the mean damages with the maximally possible mean damage set to 100% in order to be able to calculate the ratio of proportions damaged to proportion nondamaged. The resulting correlation coefficient reaches 0.76 for storms of the high season (Fig. 2.4d), but is considerably lower (0.40) for low season storms as values of the high intensity scale are missing in the data sample. Seasonal dependence of mean damages (Fig. 2.4e) is even more pronounced than in the loss ratios previously discussed.

### 2.5.6 Hailfall Intensity vs. Damage Extents

Analyzes have shown that damage extents (numbers of damaged cars / numbers of year risks) do not directly relate to hailfall intensity ( $E_{KINPIX}$ ). This is due to the fact that numbers of damaged cars per community do not directly reflect the degree of hail damage, which is better quantified by loss ratios and mean damages where only hail-damaged cars are compared. Furthermore, mobility and sheltering factors are more difficult to estimate when damaged cars are related to nondamaged cars. A further point is that the density of matriculated cars per average community surface (not available for this study) has a strong influence on the relationship between damage extents and overlying storm intensities ( $E_{KINPIX}$ ).

## 2.6 Discussion

The investigated hail cells have revealed some interesting relationships between hailfall intensity ( $E_{\text{KINPIX}}$ ) and the amount of hail damage to cars, particularly in the case of loss ratios and mean damages per car. Key findings are discussed in the following and put in a larger context:

1. Pre-defined assumptions on hailfall intensity ( $E_{\text{KINPIX}}$  as a hail intensity response variable) and area (storm box), risk exposure (damaged cars attributed to the community where they were matriculated), risk mobility (only communities with  $> 5$  damage claims considered as affected by hailfall), vulnerability of cars (comparable dentability of different car models and types) as well as storm shifting (hailfall direction assumed to be overall constant in one direction) have lead to good agreements between  $E_{\text{KINPIX}}$  and both loss ratios and mean damages per car. The comparisons between hailfall intensity and damage variables on the radar scale made averaging and triangulation of radar as well as damage variables necessary, with the disadvantage of losing some of the fine-structures of spatial hailfall variability.
2. In correspondence with hail kinetic energies of hailfalls that have been analyzed in previous studies of (e.g., Schiesser, 1990; Schmid et al., 1992), the investigated hail cells produced hailfalls that are typically characterized by a majority of radar elements containing low  $E_{\text{KINPIX}}$  and a small proportions of energies that are in the mid and upper-range of the spectra (Table 2.2). As no hailstone spectra were available for the present study and due to the fact that  $E_{\text{KINPIX}}$  does not directly resolve individual hailstone sizes, differences in amounts of damage to cars (that result from impacts of hailstones above a certain threshold diameter size) cannot directly be explained through propagation velocities, energy spectra and hailfall duration. The fact that some of the hail cells reveal both higher amounts of damage (Table 2.1) and higher loss ratios as well as mean damages (Fig. 2.4a-d), than others is best explained by a classification of the hail cells into high season storms (15 June-15 August) and low season storms (before and after).

The development of severe thunderstorms is mainly the result of the interaction between large scale processes that develop a suitable thermodynamic structure and mesoscale processes that initiate convection (e.g., Carlson et al., 1980; Doswell, 1987; Branick et al., 1988). Giaiotti et al. (2001) explained seasonal differences in hailfall intensities in northern Italy in terms of differences in equivalent potential temperature, convective available potential energy (CAPE) at lower levels and heights of both the  $0^{\circ}\text{C}$  isotherm and the  $0^{\circ}\text{C}$  dew point temperature. In Switzerland, Huntrieser et al. (1994) showed that the occurrence of extremely severe convective storms is linked to mesoscale conditions characterized by wind shear speeds  $> 5 \text{ ms}^{-1}$  (0-6 km height), a large temperature gradient between 850 and 500 hPa and high CAPEs with average values of  $1200 \text{ Jkg}^{-1}$ . The present analyzes of hailpad-derived hailstone distributions (Fig. 2.3a,b) suggested that numbers of large

hailstones ( $> 20$  mm in diameter) tend to be higher during the mid-summer months (June–August), which is confirmed by findings of prior studies (Prodi, 1974; Schiesser, 1998; Giaioti et al., 2001). On storm scale, several studies revealed good correlations between storm intensity and hailfall severity, particularly between maximum hailstone diameters and maximum updraft velocity (e.g., Johns and Doswell, 1992), cloud temperature at the level of maximum updraft (e.g., Dennis and Musil, 1973) as well as strengths of divergent outflows at upper storm level (Witt and Nelson, 1991). Houze et al. (1993) and Schmid et al. (1997) have investigated thunderstorm environments in Switzerland and have shown that supercell storms contain a large potential to produce hail damage on ground. The enhanced convective activity during mid-summer explains that most (72%) of the supercells that have been measured with the ETH radar between 1991 and 1998 (Schiesser et al., 1997) occurred during July and August. This agrees with the present finding that six of the eight investigated supercells occurred during the peak hail season (15 June – 15 August).

The limited number of analyzed hail cells makes a seasonal distinction somewhat arbitrary, but once more storm and damage data are available, the classification of cells into high and low season storms could be improved, using thunderstorm indices. One possibility that might lead to valuable results is the use of a thunderstorm index called “SWISS” (combined stability and wind shear index for thunderstorms in Switzerland) that has been developed for the forecasting of severe thunderstorm activity in Switzerland (Huntrieser et al., 1997).

3. Defining first boundary conditions of the logistic function and weighting data pairs at the mid-range, both loss ratios and mean damages are reasonably well predicted from hailfall intensity ( $E_{\text{KINPIX}}$ ). Since hail damages are mostly above a minimal damage threshold level that is determined by a minimal cost of reparability, damage variables at low intensity scale are difficult to obtain. Correspondingly, highest  $E_{\text{KINPIX}}$  and damage values are rare and the logistic function predicts high losses only after a maximal possible damage level has been determined from the data. The scatter around the obtained damage functions is in some cases considerable (Fig. 2.4a-d) and can be influenced by various errors such as: (1) inaccurate radar measurements (e.g., limited spatial and temporal resolution or shielding of the radar beam); (2) horizontal wind velocities (not reproduced by hail kinetic energy) that additionally increase the amount of damage; (3) sheltering factors; (4) different vulnerability (dentability) of cars towards hailfall; (5) different reparability costs and/or (6) inaccuracies in both damage assessment and estimates by insurance agents as well as nonclaimed hail damage. It is at the moment not possible to perform a variance estimation on each of these sources of error since more comparisons between radar-measured storms and hail damage data must be conducted first. Once additional damage claim data are available, the categorization of damage claims according to the car type (and eventually the car model), the insured value of the damaged cars as well as vulnerability to hailfall as a function of the ages of the damaged cars, would certainly reduce the scatter and improve the damage functions.

Combining the four damage functions obtained from the present data, approximate damage amounts can be calculated from a given hailfall intensity ( $E_{\text{KINPIX}}$ ) and a known (or assumed) number ( $n$ ) of exposed cars that reveal a proportion ( $p$ ) of the total sum insured. In the case of a high season storm, a grid point revealing an  $E_{\text{KINPIX}}$  of  $1000 \text{ Jm}^{-2}$  would induce a damage equal to 50% of a proportion  $p$  of the sum insured (Fig. 2.4a) on an underlying grid element of a car portfolio. In a low season storm, the damage induced from a hail kinetic energy of  $1000 \text{ Jm}^{-2}$  would be lower, reaching around 35% (Fig. 2.4b). For the same hailfall intensity still, the resulting loss would approximately be equal to the number  $n$  of exposed cars times 90% of the maximally possible mean damage of CHF 6000 in the case of a high season storm (Fig. 2.4d) and 50% for a low season storm (Fig. 2.4e). According to Winterthur Insurance (1997), the number of exposed cars ( $n$ ) would be around 40% (i.e., the proportion of cars estimated to be parked in the open) of the number of all insured cars per area during the afternoon (15-16 UTC), whereas the proportion of exposed cars rise to 65% during later evenings.

## 2.7 Conclusion

As the first of its kind, the present study examined the relationship between radar-derived hail kinetic energy integrated per radar element ( $E_{\text{KINPIX}}$ ) and three damage variables calculated from hail-damaged cars insured by Winterthur Insurance in Switzerland (1992-1998) and revealed the following key results.

(1) As shown in prior studies,  $E_{\text{KINPIX}}$  is a valuable parameter for hailfall intensity, revealing the total hail volume received per surface unit. Average cell propagation velocities determine the distribution of  $E_{\text{KINPIX}}$  as well as the duration of hailfall to a certain degree. (2) Assumptions on exposure, mobility and vulnerability of hail-damaged cars (factors that are otherwise hardly assessable) allowed comparisons between damage variables and  $E_{\text{KINPIX}}$  on a regular  $3 \times 3 \text{ km}$  grid. (3) Cross-correlation coefficients between entire storm fields (area of  $E_{\text{KINPIX}}$ ) and underlying damage variables improved considerably if an unidirectional drift of the hailstones between the radar measuring level and ground is considered. (4) Both loss ratios and the mean damages per car are considerably higher during the high season (15 June-15 August) than during the low season (before and after). Seasonal differences in hailfall intensities and resulting amounts of damage have been discussed in terms of synoptic and mesoscale processes as well as storm structure that justify the present classification of hail cells into low and high season storms to a certain degree. The availability of further storm and damage data as well as the use of thunderstorm indices will certainly improve the classification of hail cells. (5) Logistic functions that were fitted to the data, provided correlation coefficients between  $E_{\text{KINPIX}}$  and loss ratios of high (low) season storm of 0.71 (0.79) and of 0.76 (0.40) for mean damages. No direct link was found between  $E_{\text{KINPIX}}$  and the

number of hail-damaged cars relative to totals of year risks, mainly as a result of differences in spatial risk exposure.

The availability of additional radar measurements and claimed hail damage to motor vehicles from additional severe hail cells, will not only allow to verify but also to improve the established damage functions through variance estimates. Conducting a case study where damage claims of individual cars are available per location where the damage occurred (and are not aggregated per community where the claim has been settled), and are directly compared to radar-derived hail kinetic energy on the radar scale (resolution of  $0.5 \times 0.5$  km), would definitely improve the damage functions and reduce the scatter around the curves. The distinction of damage claims according to the damage severity (e.g., dented panels and/or broken windows), car models and ages, is another way to reduce the scatter around the damage curve. The use of the present damage curves could be of interest for insurance companies in order to: (1) estimate the extent of hail damage to an insured car portfolio immediately after a storm has passed over a combined radar observation area and to (2) evaluate possible maximum losses (PML), shifting a given storm surface (area of  $E_{KINPIX}$ ) over an insurance portfolio of interest. An appropriate PML determination is of major interest for a car insurer to calculate accurate insurance premiums according to area-related exposures and to purchase reinsurance cover to be able to handle the highest losses. Using the present damage functions to calculate a PML for insurance purposes, a distinction between high and low season storms is probably not relevant, as the high season damage function automatically produces the highest damage. If both radar and hail damage claim data from car-insurers are available for days where large parts of central Europe were affected by severe hailstorms, mesoscale convective systems (MCS) could be analyzed and car-hail damage functions be established accordingly.



## Chapter 3

### Hailfall: The relationship between radar-derived hail kinetic energy and hail damage to buildings

(reproduced as submitted to *Atmospheric Research* with changes in section numbers, acknowledgement and references at the end of the thesis)

#### 3.1 Abstract

Relationships between radar-derived hail kinetic energy and hail damage to residential and agricultural buildings are presented for nine hail cells that occurred over the Swiss Mittelland (1992-1999). Hail kinetic energy ( $E_{\text{KINPIX}}$ ) was calculated from C-band Doppler radar CAPPIs at a height of 1.5 km and daily hail damage claim data were available per Swiss community through several cantonal building insurance companies. In order to derive point-to-point relationships, hailfall and damage variables were triangulated on a  $2 \times 2$  km grid and cross-correlation coefficients were then calculated for entire hail cells.

The results show that high season hailstorms (15 June-15 August) produced higher mean damage than low season storms (before and after) and weighted logistic damage functions produced correlation coefficients of 0.83 (0.86) for high (low) season storms over residential buildings and 0.79 (0.88) over agricultural buildings. The relationship between  $E_{\text{KINPIX}}$  and total loss ratios (damage in relation to total sums insured) reveals no seasonal difference in hailstorm intensities and nonweighted logistic functions yield correlation coefficients of 0.85 (0.84) for residential (agricultural) buildings. The comparison between actual and predicted losses showed that nonweighted functions overestimated actual damage and that altered damage functions (flatter slope gradients) predicted damages that are in the range of the actual losses. Damage functions are calibrated using  $E_{\text{KINPIX}}$ , total loss ratios and actual losses from two independent hail cells. One hail cell showed that damage induced through rainfall that followed hailfall multiplied the final loss considerably. The valuable agreement between radar-measured hailfall intensity and total loss ratios suggests that the established damage

functions could be used by insurance companies to derive possible maximal hail losses to a building portfolio of interest.

### 3.2 Introduction

Severe hailstorms are capable of inducing large amounts of damage to infrastructure, especially when they move over densely populated areas (urban hailstorms). As property values at risk are constantly increasing in growing urban areas, storm exposure and hail losses are expected to raise correspondingly, independently to a possible increase in storm activity as identified in certain regions (e.g., Dessens, 1995; Schiesser et al., 1997; Changnon and Changnon, 2000). In the US, the number of thunderstorm events that caused losses over US\$ 50,000 have been increasing since the 1990s (Etkin and Myers, 2000) and property losses from hail have reached US\$ 1.2 billion annually and are now in the range of annual crop hail losses (Changnon, 1999). Total losses from some of the most devastating hailstorms reached US\$ 0.9 billion in the 1990 Denver hailstorm, US\$ 1.1 billion following the 1995 Dallas storm (Hill, 1996), US\$ 0.8 billion following the 1999 Sydney hailstorm (PartnerRe, 1999) and around US\$ 0.5 billion in the case of the 1984 hailstorm over Munich, Germany (MunichRe, 1984).

In the Swiss cantons where building insurance is obligatory, insured hail damage to buildings have been increasing over the last decade, averaging yearly at CHF 45 million (US\$ 28 million at current rate) ranging from a minimal amount of CHF 5 million (1990) up to CHF 95 million in 1992 (VKF, 1999). Highest insured losses occurred in situations when hailstorms moved over densely populated areas; e.g., a squall line that moved over Switzerland on 21 July 1992, induced total hail damage of CHF 100 million (Haase-Straub et al., 1994), and a single supercell storm that produced severe hailfall over the city of Lucerne on 21 July 1998, caused hail damage to buildings that amounted to CHF 72 million (GVL, 1998). On 5 July 1999, a mesoscale convective system (MCS) produced several hail cells that moved one after the other over canton Berne and induced important hail damage to buildings that reached some CHF 50 million (GVB, 1999).

The amount of hail damage to a property insurance portfolio (entity of insured risks) is basically a function of (1) the frequency of hailfalls, reflected in the number of days with hail damage occurrence (haildays) and/or reports from weather stations; (2) the intensity of hailfalls that depends on the number of hailstones, the maximum and/or average hailstone sizes and the wind gusts that accelerate falling hailstones and increase the damage amount and (3) the vulnerability and exposure of a building towards hailfall. Constantly increasing insured losses have created a great concern about future losses within the property-casualty industry and lead to various efforts to improve the understanding of hail risk. Analyses of historical hail data, laboratory simulations of hail damage to building structures, as well as

field studies of individual hailstorms have brought a deeper insight into the complexity between hailfall intensity and resulting amounts of hail damage. However, as the relationship between hailfall intensities and the amount of induced damages to buildings is primarily of interest to insurance companies, only a few studies have been published on this topic.

Historical records of hail losses from crop-insurers, and/or measurements of hailfall by weather stations and observers, have been combined to reveal long-term trends in the frequency and intensities of hailfalls for a given area (e.g., Paul, 1991; Schiesser et al., 1997; Changnon and Changnon, 2000). Laboratory studies aimed to measure hail damage as a direct function of the impact of natural and artificially produced hailstones that are propelled against building materials, to reveal how hailstone sizes and different impact energies relate to impact resistance and the amount of caused damage (e.g., Paterson and Sankaran, 1994; Render and Pan, 1995; Mahinfalah and Skordahl, 1998). Most experiments revealed that the amount of damage varies with the age of a particular building material (weathering increases vulnerability to hailfall), the hailstone size, the velocity and angle under which a hailstone impacts a building surface. Based on structural responses of different building materials from laboratory studies, guidelines for the use of more hail-resistant building materials have been established.

In field studies of severe hailstorms, the amount of hail damage to different building types and structures are mostly compared to the maximum size of reported or measured hailstones that represent the intensity of hailfall per area. The extent of hail damage to building structures has been shown to be more highly correlated with maximum hailstone sizes than with numbers of hailstones per surface unit and hailstones with diameters  $> 19$  mm must fall before serious property losses occur (e.g., MunichRe, 1984; Changnon et al., 1997). From a severe hailstorm that induced important damage to buildings in Alberta, Canada, Charlton et al. (1995) revealed that the amount of damage from impacts of hailstones  $> 50$  mm in diameter is considerably higher for residential buildings (tiled roofs) than for commercial buildings (graveled tar roof). Following the 1999 Sydney hailstorm, Leigh (1999) deduced from a public survey that impacts of hailstones  $< 30$  mm in diameter did not break roof tiles, whereas stones  $> 50$  mm caused substantial damage and stones  $> 70$  mm caused roof damage to all buildings. Charlton (1998) showed from field observations of hail-damaged shingles on residential buildings and measured hailstone sizes, that densities of reshingling in residential areas increased with maximally measured hailstone diameters and that the resistance of asphalt shingles to hail damage decreased considerably through weathering. Andrews and Blong (1997) analyzed the scale of hail damage to buildings caused by different damage agents in the 1990 Sydney hailstorm and found that: (1) while hail damage was widespread in the hail streak, a majority of claims were concentrated typically in a small area; (2) hailfall caused most damage (80%) to exterior building surfaces, whereas roof and window glass together constituted up to 50% of the total damage; (3) heavy rain that occurred during and/or followed hailfall induced considerable damage to building contents and reached up to 20% of

the total damage and (4) buildings constructed out of fibro, timber and aluminum reveal a higher damage potential than brick dwellings. Schiesser et al. (1999) correlated amounts of hail damage to buildings with radar measurements and showed that severe downdrafts that occur along with hailfall can increase overall damage to building surfaces in an area.

Apart from hailfall intensity and hailstone parameters, the amount of hail damage over a given area is further determined by factors including: (1) building exposure which is a function of numbers, densities and values of insured buildings in a given area; (2) the extent of shielding of a building from direct impacts of hailstones (e.g., through trees or other buildings); (3) building structures: the type and age of a specific building structure determines the vulnerability towards of hailfall; (4) the maintenance of the building structure, especially the replacement of weathered structural components which reduces vulnerability to potential hailfall; (5) reparability and replacement costs of hail-damaged building structures that depends on the type of building structure, the extent and size of the damage as well as the accessibility of the part of the damaged building; (6) insurance specific issues such as inclusions or exclusions of special risks in elementary insurance or deductibles (insured's participation on the damage); (7) the damage agent that determines the part of the damage to the exterior and interior building structure: e.g., insured losses from hailfall increase considerably once exterior building structures have been damaged to such an extent that interior structures are exposed to rainfall that follows hailfall and (8) esthetical reasons can lead to the full replacement of a partly damaged part of a building (e.g., a roof or aluminum blinds) and increase the overall damage. As a result, the complex composition of building structures, the spatial variability of hailfall and hardly assessable influences through other factors, can lead to nonconformities if damage claims are related to hailfall intensities.

In most studies where hailfall intensities are related to the amounts of damaged building structures, ground-based measurements of hailstone spectra from hailpad networks and/or human observers have been used. Although public reports of maximum hailstone sizes provide a crude overview of hailfall distributions, reported hailstone sizes are often over-estimated (e.g., Changnon, 1971; Charlton et al., 1995) and hardly provide complete information of the entire hailstone spectra. Hailpad measurements probably provide the best ground-truth data of hailfalls, but large hailpad networks are only conducted during special field experiments (e.g., NHRE, Foote and Knight, 1979; Grossversuch IV, Federer et al., 1986) and are therefore not operated on a regular basis. As an alternative to ground-measurements of hailfall intensity, weather radar measurements can be taken indirectly as a quantitative hailfall variable. Geotis (1963) showed that hail cells can be distinguished from nonhail cells by the time-integrated 55dBZ reflectivity area, which is however not a quantitative measure of hailfall intensity. One radar-derived hailfall variable that showed valuable results in relation to ground measurements of hailfalls and hail damage amounts to crops, is hail kinetic energy. Waldvogel et al. (1978a) established a point-to-point relationship between S-band radar reflectivity and time-resolved hailstone spectra that has been used to

calculate the hail kinetic energy for entire hail cells (e.g., Waldvogel et al., 1978b; Waldvogel and Schmid, 1983). A significant relationship was found between radar- and ground-measured patterns of hail kinetic energy (e.g., Schmid et al., 1992), extents of hail damage to crops (e.g., Wojtiw and Ewing, 1986; Schiesser, 1990; Visser, 2000) and average amounts of hail damage to automobiles (Hohl et al., 2001). Radar-derived hail kinetic energy is a direct function of the volume of hailfall received per surface unit but does not directly resolve hailstone sizes at a given radar element. In the current severe weather detection algorithm of the National Severe Storm Laboratory (NSSL), radar-derived hail kinetic energy is used in order to estimate the possibility of severe hailfall (Witt et. al., 1998).

This paper aims to link the radar-derived hail kinetic energy of entire hail cells to amounts of claimed hail damage to residential and agricultural buildings in Switzerland. From a sample of nine severe hail cells that occurred over the Swiss Mittelland (1992-1999), a complete set of radar and hail damage information is available for cross-correlation between both variables. Section 3.3 gives an overview of radar and insurance data that are analyzed and cross-correlated with methods that are presented in Section 3.4. Main results including damage functions and the verifications of actual damage amounts with the established damage functions are shown in Section 3.5. Section 3.6 discusses different aspects of two damage variables and radar-derived hail kinetic energy for both residential and agricultural buildings. The paper is concluded in Section 3.7.

## 3.3 Data

### 3.3.1 Radar Data

Radar data were provided by the C-band Doppler radar (Li et al., 1995) operated at the Swiss Federal Institute of Technology (ETH) at H nggerberg, Zurich since 1990 (Fig. 3.1). In the last ten years, more than 200 hail cells have been measured over the Swiss Mittelland within the 120 km standard detection range of the ETH radar. Following Waldvogel et al. (1979), Federer et al. (1986) and Schiesser et al. (1997), hail cells were distinguished from nonhail cells through the time-integrated 55dBZ reflectivity area that lasts at least for 30 min during the mature storm phase. From manually performed sector volume scans, Constant Altitude Plan Position Indicators (CAPPIs) are generated per 5-min time step at two standard levels with a horizontal resolution of  $0.5 \times 0.5$  km: at 2 km above the daily 0 C isotherm (3-4 km MSL in summer) where hailstones grow and at low storm level on 1.5 km MSL (0.9 km above radar) close to ground where hailfall occurs. A radar profile (Schmid and Waldvogel, 1986) was used to correct attenuated low level CAPPI reflectivities from upper level CAPPIs as well as when the radar beam was shielded by the relief.

For every time step, hail cells were approximated on CAPPIs at a 1.5-km height by a circle circumscribing reflectivities  $\geq 30$ dBZ according to a method described in Hohl and Schiesser

(2001). The splitting of one cell into two or more cells and the opposite case, the merger of two or more cells into one cell, are treated as one cell only. Waldvogel et al. (1978a) related radar reflectivity measured with an S-band radar to the flux of kinetic energy (determined from 175 hailstone spectra) and showed that the semi-empirical relationship can be written as:

$$\dot{E} = 5 \cdot 10^{-6} \cdot Z^{0.84} \text{ [Jm}^{-2}\text{s}^{-1}] \quad (3.1)$$

where  $Z$  is the radar reflectivity factor ( $\text{mm}^6\text{m}^{-3}$ ) and  $\dot{E}$  the flux of kinetic energy. Schiesser et al. (1999) found a valuable agreement between radar-derived hail kinetic energy and amounts of hail damage to crops for one storm that has been measured by an S-band radar (Schiesser, 1990) as used in Waldvogel et al. (1978a), and a comparable storm where hail kinetic energy was derived from ETH C-band Doppler radar measurements (as used in the present study). Since the radar reflectivity factor  $Z$  varies over time, a small error in  $Z$  produces a difference in the flux of kinetic energy ( $\dot{E}$ ) that can lead to systematic errors, especially if  $\dot{E}$  is integrated over the time and surface of a hailfall. In order to be able to correct variations of  $Z$ , ETH radar measurements are constantly calibrated with corresponding measurements from a Joss-Waldvogel distrometer (Joss and Waldvogel, 1967); for a more detailed description of the radar-distrometer calibration procedure see Hohl et al. (2001). Over the period of investigation (1992-1999), the radar reflectivity factor  $Z$  of the ETH radar increased overall by +1.5dBZ.

In the following analysis, hail kinetic energy was calculated from 1.5-km level CAPPI reflectivities, using the  $Z$ - $\dot{E}$  relationship given in Waldvogel et al. (1978a). To obtain the entire hail kinetic energy per surface unit ( $E_{\text{KINPIX}}$ ), the flux of  $\dot{E}$  is integrated first over the entire storm duration ( $t_0 \rightarrow t_1$ ) and secondly per radar element ( $s_0 \rightarrow s_1$ ) at a  $0.5 \times 0.5$  km resolution:

$$E_{\text{KINPIX}} = \int_{t_0}^{t_1} \int_{s_0}^{s_1} \dot{E}(x, y, t) dx dy dt \text{ [Jm}^{-2}] \quad (3.2)$$

Waldvogel et al. (1980) examined several radar-reflectivity thresholds and methods to distinguish rain from hailfall signals. In the present study, the 55dBZ threshold criteria (i.e., reflectivities  $> 55\text{dBZ}$  are attributed to hail and those  $\leq 55\text{dBZ}$  to rain) has been used, since this threshold lead to good results for hailfalls that have produced considerable damage to crops (Schiesser, 1990). The area covered by radar elements that contain  $E_{\text{KINPIX}}$  is considered to represent the area of hailfall while specific values of  $E_{\text{KINPIX}}$  are taken as a measure of hailfall intensity. Since  $E_{\text{KINPIX}}$  represents the entire volume of hailfall received per surface unit over the time, a volume that contains a large number of small hailstones can produce the same hail kinetic energy as a volume of a few large stones.

For most of the hail cells that were measured with the ETH radar (1992-1999) and where insurance data were available (Section 3.3.2),  $E_{\text{KINPIX}}$  has been calculated from CAPPI reflectivities. For one hail cell (990705 1534 in Table 3.1) where CAPPI reflectivities were only partly available, radar reflectivities of 10-min ETH Plan Position Indicators (PPIs) were

used to calculate  $E_{\text{KINPIX}}$  using the same method as for CAPPIs. As the use of PPIs involves an increase of radar measuring heights with distance away from the radar, PPI reflectivities were reduced to a 1.5-km standard level using a radar profile given in Schmid and Waldvogel (1986). Several comparisons between storms where hail kinetic energy has been calculated from both CAPPI and PPI reflectivities, revealed that resulting  $E_{\text{KINPIX}}$  values were overall comparable, whereas highest energies were in some cases lower than when calculated from PPI reflectivities.

**Table 3.1.** Storm variables of the analysed hail cells including storm types, mean movements, areas of hailfall, maximum hailfall durations and distributions of hail kinetic energies ( $E_{\text{KINPIX}}$ ). The first six cells are used to establish a point-to-point relationship between  $E_{\text{KINPIX}}$  and damage variables, whereas cell 990705 1534 is only used for comparison. The last two cells are taken to verify and calibrate the established damage functions in Section 3.5.5.

Storm	Time	Storm Type	Mean Movement	$A_{55}$ TOT	Hailfall Duration	$E_{\text{KINPIX}}$ [ $\text{Jm}^{-2}$ ]				
						MAX	< 200	200-400	400-600	> 600
[Date]	[UTC]		[°/km/ms <sup>-1</sup> ]	[km <sup>2</sup> ]	[min]	[Jm <sup>-2</sup> ]	[%]	[%]	[%]	[%]
920601	1828-1953	isolated	217/51/11	315	10	480	76	23	1	0
920721	*1558-1623	group MCS	234/20/13	291	6	280	97	3	0	0
930519	1523-1723	isolated	211/35/6	378	25	1222	40	29	18	13
930520	1203-1408	isolated	250/65/8	531	19	1069	76	15	6	3
940823	1648-1758	group	252/56/11	500	13	498	68	30	2	0
980721	*1306-1431	isolated	239/60/12	518	20	821	71	19	8	2
990705	†1534-2114	group MCS	212/97/13	2166	16	532	83	16	1	0
920721	1333-1523	group MCS	210/53/7	596	9	1016	71	23	4	2
940810	1218-1353	isolated	209/90/14	1002	8	520	91	8	1	0

† cell combined from four individual hail cells that moved over the same area

\* supercell thunderstorm

### 3.3.2 Hail Damage Claim Data

In Switzerland, building insurance against elementary damage including hailstorms is compulsory in 19 out of 26 cantons (political districts), where policies are issued by monopolistic and nonprofit orientated cantonal building insurance companies. Insurance against elementary damage covers both exterior building structures (e.g., roofs, walls and windows) and interior building elements (e.g., ceilings, insulation, floors, plaster and electrical installations). Insurance premiums are generally calculated according to the new building value (sum insured) and contain deductibles (participation of the insured on the damage) that vary with the type of insured building, averaging around CHF 200 per year. Building insurance policies are issued for buildings often categorized into residential, agricultural, public, commercial and industrial buildings, and proportions of each building type can vary considerably between urban and rural communities. Damaged buildings are examined by trained loss adjusters who record the cause of damage, the parts of the building damaged and the overall costs of compensation. If hail is the cause of damage, additional damages (e.g., through wind and water) are mostly attributed to hailfall and reported as hail damages. Once the damage has been repaired by an appointed company, the building insurance compensates the loss ranging from reinstatement costs up to full compensation of the new building in case of a total loss. If partly damaged buildings parts are fully replaced

due to esthetic reasons, the building insurance company covers not the full but only a certain minimal cost of replacement. Insurance companies distinguish between gross losses and net losses (deductibles subtracted) and often provide claim data for the year when the damage occurred but sums insured at current values. In order to compare losses of several hailfall events, damages of different years are adapted to the current year, using a Switzerland-wide building cost index.

**Table 3.2.** Overview of hail damage claims available from cantonal building insurance companies. Numbers, total amounts of hail damages and proportions of claims over and under CHF 6000 are listed for residential and agricultural buildings. The first six cells are used to establish a point-to-point relationship between hailfall intensity and damage variables, whereas cell 990705 1534 is only used for comparison. The last two cells are taken to verify and calibrate the established damage functions in Section 3.5.5.

Storm	Time	Residential Buildings				Agricultural Buildings			
		Number	Claimed damage			Number	Claimed damage		
			Total	≤ 6000	> 6000		Total	≤ 6000	> 6000
[Date]	[UTC]		[CHF mio]	[%]	[%]		[CHF mio]	[%]	[%]
920601	1828-1953	224	0.697	98	2	43	0.191	92	8
920721	1558-1623	527	1.418	89	11	69	0.332	85	15
930519	1523-1723	882	3.305	94	6	355	1.883	90	10
930520	*1203-1408	8	0.017	100	0	8	0.022	100	0
940823	1648-1758	242	0.905	100	0	17	0.042	100	0
980721	1306-1431	7993	54.639	81	19	625	3.548	88	12
990705	†1534-2114	4221	20.316	90	10	1324	15.367	84	16
920721	1333-1523	9174	27.683	92	8	74	1.096	90	10
940810	1218-1353	331	9.761	89	11	436	1.200	78	13

† cell combined from four individual hail cells that moved over the same area

\* maximum hailfall intensity occurred outside the area where damage claim data were available

For the present study, damage claims on residential and agricultural buildings were available from the cantonal building insurance company of canton Berne (1992-1999). Residential buildings include single and multiple-story dwellings with or without a part of the building used for commercial reasons (e.g., shops or offices in the basement). Agricultural buildings consist of farm buildings (e.g., stalls and barns) as well as residential farm buildings. For a selected number of days where ETH radar measurements of severe hail cells were available, the building insurance companies of the following cantons provided claims and exposure data: Aargau, Basle Land and Lucerne. All building insurance companies provided the following community-aggregated data for both residential and agricultural buildings: the date when the damage occurred, numbers of damaged buildings (numbers of claims), total net hail damage amounts, sums insured of the damaged buildings and sums insured of all insured buildings (total sums insured). For a few days with severe hailstorm occurrence (1992-1999), the building insurance company of canton Berne provided coordinates, claimed damages and sums insured for every individual damaged residential building in the canton. In order to relate damage claims to hailfall intensity, damage data on community level were geo-referenced by coordinates representing the center of a community and damages to individual buildings were integrated and averaged per radar element at a resolution of  $0.5 \times 0.5$  km.



Both radar and damage claim data were available for a total of nine hail cells: six cells over canton Berne, one cell over canton Basle Land, a cell over canton of Lucerne and a further cell over the combined area of canton Aargau, Berne and Lucerne. In cases where storms moved out of a canton where insurance data were available into a neighboring canton and/or back in the same canton (e.g., cell 940823 1648 in Fig. 3.1), only the part of the storm with corresponding damage data could be analyzed. On days where several hail cells moved over the Swiss Mittelland, hail streaks were only investigated if locations of damage claims were clearly attributable to either one hailstorm or the other. The storm of 5 July 1999 consists of a special case: as four hail cells moved one after the other over the same area, hail kinetic energies ( $E_{\text{KINPIX}}$ ) of the four hail streaks were combined into one single storm (990705 1534 in Table 3.1) and related to the available claim information.

### 3.4 Methods

Methods of relating radar-derived hail kinetic energy to damage variables are first described and illustrated. Spatial integration of radar and damage data as well as cross-correlation methods is presented thereafter. Various characteristics and limitations in the establishment of damage functions between hailfall intensity ( $E_{\text{KINPIX}}$ ) and amounts of damage are introduced in the following sections. An iterative procedure of how damage functions were calibrated and verified from actual losses is shown thereafter.

#### 3.4.1 Cross-Correlation of Storm Intensity and Hail Damage Variables

Complexities in relating hailfall intensity to hail damage claims on buildings arrive from differences in spatial variability and intensity of hailfalls as well as from variable exposures of building structures. In order to compare claimed damages to hailfall intensity on the radar scale, some simplifications and assumptions were necessary. Radar-derived hail kinetic energy ( $E_{\text{KINPIX}}$ ) is considered as the hailfall intensity response variable. As accurate wind velocity measurements (e.g., Doppler velocities) were not available, hailfall has been assumed to be constant from one direction over the entire storm duration and the additive impact of hailstones from wind were neglected. Since buildings could only be grouped into residential and agricultural buildings and no information was available on details of building structures and materials, all buildings were assumed to be equally exposed and susceptible to hailfall over the time and area. Since insurance companies attribute wind and/or water damages that occurred during a thunderstorm to “damage induced through hail”, communities were only analyzed if the following criteria were fulfilled. (1) The community center lies within the hail streak that is approximated by a storm box containing  $E_{\text{KINPIX}}$ . Fig. 3.1 shows for two hailfalls that the highest numbers of hail-damaged residential buildings occurred in the area of highest  $E_{\text{KINPIX}}$  in center of the storm box. (2) The community contains at least five damage claims for

residential and two claims for agricultural buildings which limits the possibility that proportionally high numbers of claims with water and/or wind damage are included in the data.

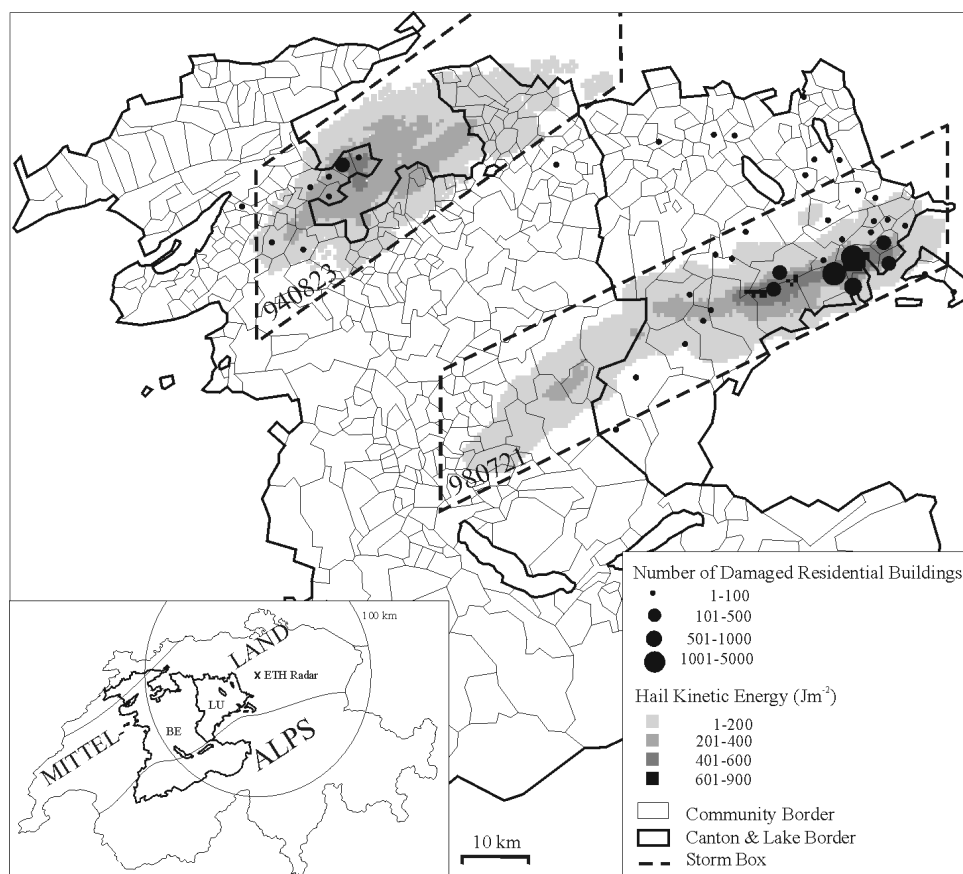


**Figure 3.1.** Overview of Switzerland (lower left) with geographically distinct regions of the Mittelland and the Alps, the location of the ETH radar (cross) at Höggerberg near Zurich with a detection range of 100 km (circle) and the cantons of Berne (BE) and Lucerne (LU) from where most hail damage claim data were available. The enlargement shows borders of the communities contained in canton Berne and Lucerne (outlined), canton and lake borders (bold outlined) as well as radar-derived hail kinetic energy in four intensity levels (grey shades) and numbers of hail-damaged residential buildings (proportional circles) for two hail cells that occurred on 23 August 1994 and 21 July 1998 (labeled). For the hailstorm of 23 August 1994, damage claim data were available from canton Berne only, whereas in the case of the 21 July 1998 storm, corresponding data were only provided by the building insurance company of canton Lucerne. Storm boxes (dashed) design the area of hailfall in which hail kinetic energy and damage variables are cross-correlated.

For communities that fulfilled the above criteria, two damage variables were calculated for residential and agricultural buildings: a mean damage per building (total damage / number of damaged buildings) and a total loss ratio (total damage / total sums insured of all buildings). Damages to individual geo-referenced residential buildings were averaged per radar element ( $0.5 \times 0.5$  km) and a mean damage determined from the available data. In order to perform a direct point-to-point analysis of the locations of damage claims in relation to hailfall intensities, both radar and insurance data were transformed to a regular grid. Of the various

methods that can be applied to grid nonregularly spread data points (e.g., Bailey and Gatrell, 1996), Delaunay triangulation has been used in the present study to transform  $E_{\text{KINPIX}}$  and damage variables to a  $2 \times 2$  km grid. On this resolution, typical features of  $E_{\text{KINPIX}}$  and damage variables are accurately reproduced and a typical community of the Swiss Mittelland with an average surface of  $10 \text{ km}^2$  contains two grid points. Fig. 3.2 shows triangulated hail kinetic energy ( $E_{\text{KINPIX}}$ ) in relation to triangulated mean damages of two hail cells with clear spatial correspondence between the data.

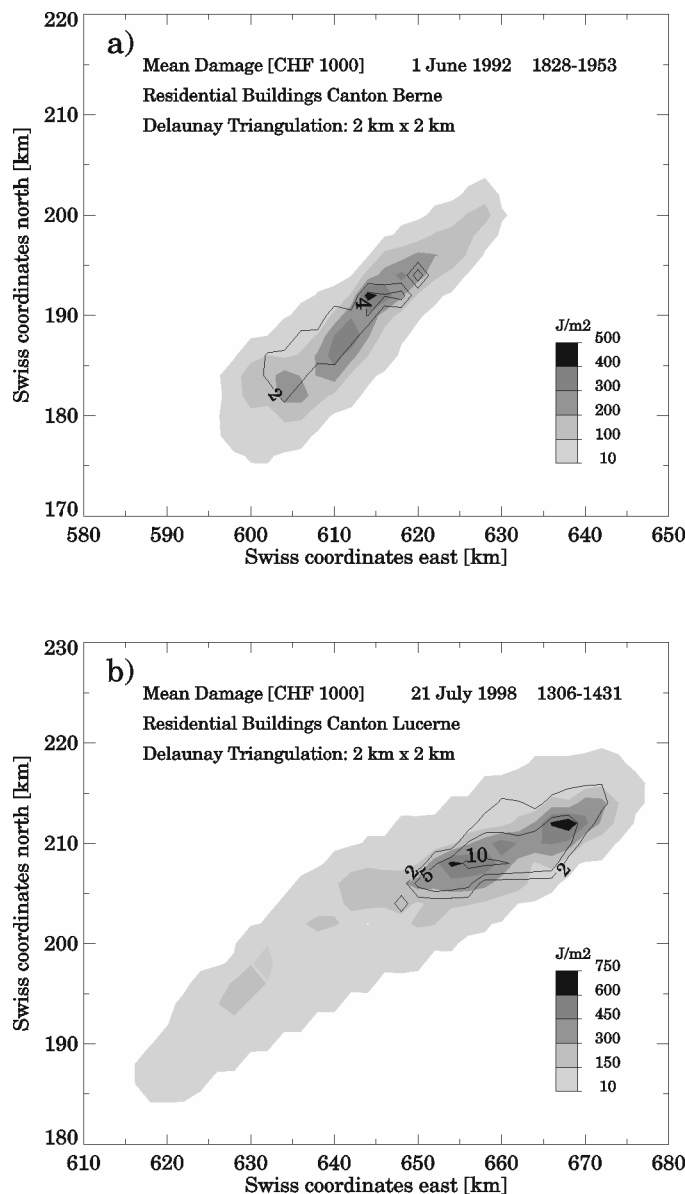


**Figure 3.2.** Radar-derived hail kinetic energy ( $E_{\text{KINPIX}}$ ) in four intensity levels (grey shades) and mean damages to residential buildings (labeled isolines in CHF 1'000) as triangulated on a  $2 \times 2$  km grid within the hailfall area (storm box) for a) the hail cell on 1 June 1992 and b) the hailstorm that occurred on 21 July 1998. Cross-correlation coefficients between  $E_{\text{KINPIX}}$  and mean damages reached in a) 0.26 and improved to 0.48 after storm shifting (Section 3.5.2), whereas corresponding coefficients improved from 0.66 to 0.74 for the storm in b). Note that  $E_{\text{KINPIX}}$  intensity levels are different in the two figures. Swiss coordinates (km units) are used in both figures.

An important aspect of point-to-point comparisons between hail kinetic energy at the radar-measuring level and damage to ground is that downdrafts displace falling hailstones through advection which in turn leads to lower correlation coefficients between ground and radar measurements. Schmid et al. (1992) showed for hailpad measurements and Schiesser (1990)

for hail damage extents to crops, that shifting of the radar-measuring field against ground increases correlation coefficients between radar-derived hail kinetic energy and ground measurements considerably. In this study, entire  $E_{\text{KINPIX}}$  fields are shifted by one grid width (2 km), assuming that the advection of hail has a strong component in one favored direction during the whole duration of hailfall. However, the use of a regular shift vector neglects terminal velocities of hailstones that determine the fall time and different fall distances between a radar-measuring point and damage on ground. The fall distance ( $d$ ) of individual hailstones can be determined as follows (Schiesser, 1990):

$$d = \frac{H_R - H_G}{V_T} \cdot u \quad [\text{km}] \quad (3.3)$$

where  $u$  is the mean horizontal wind speed,  $H_R$  the radar measuring level and  $H_G$  the ground level, while  $V_T$  is the terminal velocity for a mean hailstone diameter ( $D$ ); values for  $u$  can be found e.g., in Browning (1977) and the relationship between  $V_T$  and  $D$  is given in Matson and Huggins (1980). In the present case, a 2-km shift is applied to triangulated community-aggregated damage variables, and a gradual 0.5-km shift has been applied to damage data averaged per radar element. A shift at the radar measuring level of 2 km (one grid width) implies for this study a falling of a 20 mm hailstone ( $V_T=15 \text{ ms}^{-1}$ ) from  $H_R=1.5 \text{ km}$  to  $H_G=0.4 \text{ km}$  with  $u=20 \text{ ms}^{-1}$ . Hail cell-specific shift vectors are determined separately for every damage variable and are then combined into a final vector that agrees best for both mean damages and total loss ratios.

### 3.4.2 Damage Functions

The relationship between hailfall intensity and amounts of hail damage is typically such that a relatively high number of low damages occur together with a small number of damages that reach maximal damage levels. Since amounts of hailfalls smaller than a particular level may result in no damage and amounts of hailfall greater than a characteristic damage-inducing level can result in no more than 100% loss, the relationship is inherently nonlinear. Katz and Garcia (1981) showed that the nonlinear relationship between hailpad-derived kinetic energy and crop damage is best described by a logistic function. In addition, logistic damage functions provided valuable results between radar-derived hail kinetic energy and the predicted damage to crops (Schiesser, 1990) and amounts of damage to automobiles (Hohl et al., 2001). The logistic function has the following general form:

$$y_i \cong \frac{e^{(\beta_0 + \beta_1 x_i)}}{1 + e^{(\beta_0 + \beta_1 x_i)}} \quad (3.4)$$

where  $y_i$  represents proportion of hail damage,  $x_i$  the corresponding value of hailfall intensity for an observation  $i$ . The parameters  $\beta_0$  and  $\beta_1$  have to be estimated by the data using the following relationship given in Katz and Garcia (1981):

$$L(y_i) = \ln\left(\frac{y_i}{1-y_i}\right) = \beta_0 + \beta_1 x_i \quad (3.5)$$

$L(y_i)$  is the natural logarithm of the ratio of proportion damaged to proportion nondamaged and is a linear function of the hailfall variable. As the variance of  $L(y_i)$  is not a constant function, a weighting method described in Katz and Garcia (1981) can be applied. Since the logistic function requires damage values that are strictly greater than 0% and less than 100% (otherwise Eq. (3.5) is not defined), boundary conditions need to be determined first. Following Katz and Garcia (1981), and Schiesser (1990), the minimum and maximum constraints were determined in the present case as follows: (1) hailfall intensities ( $E_{\text{KINPIX}}$ ) that produced no damages to buildings were excluded from the analysis; (2) in order to predict damage values at low scale, the logistic function is fitted through  $x=0$  and  $y=0$ , replacing the hailfall variable  $x_i$  in Eq. (3.4) by  $\ln(x_i)$  and (3) to determine the upper boundary, the logistic function is adjusted for maximal damage values, assuming a possible maximal damage level ( $y_{\text{max}}$ ) that is set to 99% replacing  $y_i$  in Eq. (3.5) by  $y_i/y_{\text{max}}$ . Damage functions are calculated in the following with those pairs of observations, which are obtained using the optimal shift vector as presented in the previous section.

Katz and Garcia (1981) stated that the functional form of a logistic curve that predicts losses from hailfall accurately, is difficult to determine from observations alone. As hailfalls generally show distributions of kinetic energies that are dominated by a large number of low values, weighting of a logistic function alone cannot produce damage curves that reproduce all damages to a satisfying degree. Recalculating actual damage from analyzed hail cells is only one way to calibrate damage functions and gain some information about prediction accuracies of damage amounts, which is essential in perspective of practical applications. In the following, three gradually altered damage functions are used to recalculate the overall total damage to agricultural and residential buildings, using four of the analyzed cells and two independent cells that were not used to calculate the damage functions.

### 3.5 Results

First, analyzed hail cells are briefly described, comparing storm variables and amounts of damages to both residential and agricultural buildings. Table 3.1 gives an overview of storm variables including storm types, mean movements, hailfall surfaces, maximum hailfall duration and distributions of hailfall intensities ( $E_{\text{KINPIX}}$ ) of all investigated cells. Table 3.2 displays numbers and damages to residential and agricultural buildings per hail cell. In the following, results of cross-correlation analyzes between patterns of shifted hail kinetic energy and mean damages as well as total loss ratios are presented and summarized in Table 3.3. Relationships between radar-derived hailfall intensity ( $E_{\text{KINPIX}}$ ) and two damage variables as well as characteristics of fitted logistic damage functions are given thereafter. The following

section compares actual hail losses and damage predicted by several damage functions for a selected number of hail cells listed in Table 3.4. The hail cells that occurred on 5 July 1999 over canton Berne are separately discussed in the last section. Individual hail cells are distinguished according to the date and initial time (UTC) of occurrence.

### 3.5.1 Storm Variables

Using a radar-based criteria (Schiesser et al., 1995), the present hail cells were classified into three storm organization types, determined at the moment of occurrence: (1) five isolated cells; (2) one cell embedded in a group organization (bounded 40dBZ region with more than one cell that reveals peak echoes  $> 47\text{dBZ}$  and extents  $< 100\text{ km}$  in one direction at mature storm phase) and (3) three cells that occurred in a mesoscale convective storm system (multiple enclosed contours of 40dBZ reflectivity are separated from each other and arranged in an area of reflectivity  $\geq 25\text{dBZ}$  that extents  $> 100\text{ km}$  at time of maximum extent). Two of the analyzed hail cells (Table 3.1) were previously classified as supercell thunderstorms (Schiesser et al., 1997; Schiesser et al., 1999). Hail cells developed around mid-day (first cell 1203) and early evening (last cell 1828) and typically propagated from southwest to northeast ( $225^\circ$ ) with average propagation velocities of  $6\text{--}14\text{ ms}^{-1}$  (Table 3.1). Storm track lengths ranged from  $20\text{--}97\text{ km}$  while hailfall areas (determined from the number of radar elements containing  $E_{\text{KINPIX}}$ ) varied from  $291\text{--}1002\text{ km}^2$ ; cell 990705 1534 shows with a size of  $2166\text{ km}^2$  the largest hailfall area as it was combined out of four different cells that moved over the same area. As noticed in a previous study (Hohl et al., 2001), a certain link between cell propagation velocity, hailfall duration and distributions of hail kinetic energies also exists in the present cells. In comparison to fast moving cells (e.g., 920721 1558 at  $13\text{ ms}^{-1}$ ; 940810 1218 at  $14\text{ ms}^{-1}$ ), slow moving cells (e.g., 930519 1523 at  $6\text{ ms}^{-1}$ ; 930520 1203 at  $8\text{ ms}^{-1}$ ) tend to produce low proportions of  $E_{\text{KINPIX}} < 200\text{ Jm}^{-2}$  but higher proportions of  $E_{\text{KINPIX}} > 600\text{ Jm}^{-2}$  along with higher maximal  $E_{\text{KINPIX}}$  and longer maximal hailfall duration per radar element (Table 3.1).

The investigated hail cells produced hail damage to residential buildings that ranged from CHF 0.017 million (eight buildings damaged) up to CHF 54.639 million which resulted from 7993 hail-damaged buildings (Table 3.2). In comparison, numbers and amounts of hail damage to agricultural buildings are proportionally lower, with losses that varied between CHF 0.022 million (eight buildings damaged) and CHF 15.367 million (1324). Comparing percentages of hail damage claims over CHF 6000, it appears that some storms produced higher proportions for both residential and agricultural buildings (Table 3.2). As hail damage to buildings occur mainly from impacts of large hailstones (e.g., Charlton et al. 1995; Changnon et al., 1997), differences in damage amounts can be the result of differences in proportions of large hailstones that produced on the average higher damages to building structures. The fact that storms that occur during the peak hail season (typically in mid-summer when vertical storm development and convective activity are most enhanced) tend to

produce more severe hailfalls in terms of hailstone sizes has been shown in Prodi (1974) and Giaioti et al. (2001) for Northern Italy, Reuter and Aktary (1995) and Smith et. al. (1998) for Alberta and Schiesser (1998) for Switzerland. Comparing radar-derived hail kinetic energy to amounts of hail damage to automobiles for 12 hail cells in Switzerland, Hohl et al. (2001) showed that differences in mean damage amounts were best explained if cells were grouped into high season storms (15 June-15 August) and storms that occurred during the low season (before and after). Furthermore, Hohl et al. (2001) showed from hailpad-derived hailstone spectra which were available from Grossversuch IV in central Switzerland (Federer et al., 1986), that high season storms produced lower numbers of hailstones but larger maximum diameters than low season storms for a given hailpad-derived hail kinetic energy.

Grouping the present hail cells into high (15 June-15 August) and low (before and after) season storms shows that the five high season storms produced proportions of mean damages over CHF 6000 that ranged between 10-19% for residential buildings and between 10-16% for agricultural buildings (Table 3.2). On the other hand, the four cells that occurred during the low season (before 15 June and after 15 August) induced lower proportions of mean damages over CHF 6000 with percentages varying between 0-6% (0-10%) for residential (agricultural) buildings (Table 3.2).

### 3.5.2 Storm Shifting and Cross-Correlation Analyses

In order to respect the drift of falling hailstones from radar measuring level to ground, storm surfaces (area of  $E_{KINPIX}$ ) were shifted at radar measuring level against ground. Only four of the present hail cells fulfilled the assessment criteria for agricultural buildings (i.e., at least two buildings have to be damaged per community), while all cells contained residential building data (Table 3.3).

**Table 3.3.** Cross-correlation coefficients between hail kinetic energy ( $E_{KINPIX}$ ) and mean damages as well as total loss ratios for residential and agricultural buildings before (no shift) and after storm shifting. Numbers of obtained data pairs are separately listed for each damage variable. Average shift vectors indicate the direction and distance of storm shifting that produced the best correlation coefficients for all damage variables. Note that the table includes only cells that are used to establish damage functions between point-to-point observations.

Storm	Time	Correlation Coefficients Shift												Shift Vector
		Residential Buildings						Agricultural Buildings						
		mean damage			total loss ratio			mean damage			total loss ratio			
		no	yes	pairs	no	yes	pairs	no	yes	pairs	no	yes	pairs	
[Date]	[UTC]													[°/km]
920601	1828-1953	0.26	0.48	18	0.01	0.42	18	0.18	0.55	25	0.06	0.45	25	90/2.0
920721	1558-1623	0.07	0.21	21	0.25	0.62	21	0.49	0.58	16	0.28	0.42	16	0/2.0
930519	1523-1723	0.33	0.47	24	0.15	0.40	24	0.16	0.41	30	-0.08	0.37	30	225/2.8
930520	1203-1408	0.01	0.41	6	-0.36	0.69	6	-	-	-	-	-	-	90/2.0
940823	1648-1758	0.59	0.75	5	0.54	0.58	5	-	-	-	-	-	-	90/2.0
980721	1306-1431	0.66	0.74	39	0.11	0.43	39	0.24	0.78	40	0.45	0.67	40	90/2.0
Total	6 cells			113			113			111			111	

- no values; i.e., less than two agricultural buildings were damaged per Swiss community

Correlation coefficients between  $E_{KINPIX}$  and mean damages of residential (agricultural) buildings ranged from 0.07-0.66 (0.16-0.49) and improved after storm shifting to values of 0.21-0.75 (0.41-0.78) as shown in Table 3.3. For total loss ratios of residential (agricultural) buildings, cross-correlation coefficients that ranged from -0.36 to 0.54 (-0.08 to 0.45), improved after storm shifting to values between 0.40-0.69 (0.37-0.67). Hailfalls occurred most frequently from the east ( $90^\circ$ ) with a drift of 2 km between radar measuring and ground level (Table 3.3) and are similar to hailfalls analyzed in previous investigations (e.g., Schiesser, 1990; Schmid et al., 1992; Hohl et al., 2001). After storm shifting, 113 pairs of  $E_{KINPIX}$  and mean damages and total loss ratios of residential buildings as well as 111 corresponding data pairs for agricultural buildings are available in order to analyze point-to-point relationships between hailfall intensity and damage variables and to derive logistic damage functions.

### 3.5.3 Radar-Derived Hail Kinetic Energy vs. Mean Damages

Comparing hailfall intensity and mean damages to both residential and agricultural buildings of the six hail cells used to establish the damage functions (Table 3.3), a seasonal difference appears between storms of the high (15 June-15 August) and low season (before and after). On the average, high season storms produced mean damages of CHF 4800 (CHF 5300) per residential (agricultural) building, whereas the average amount is lower in the case of low season storms with values around CHF 3200 (CHF 3800) for residential (agricultural buildings). The resulting average mean damage of CHF 4800 (US\$ 3000) to residential buildings is similar to mean damages of US\$ 3000 calculated from damage claims on residential buildings after the 1991 Calgary hailstorm (Charlton et al., 1995), provided that costs of living are comparable. In comparison, the 1999 Sydney hailstorm produced mean damages of some US\$ 6500 on residential dwellings and are twice as high as typical mean damages induced by a Swiss hailstorm (PartnerRe, 1999). This could be due to the fact that (1) the 1999 Sydney storm produced high proportions of hailstones over 50 mm in diameter (Yeo et al., 1999) up to maximum diameters of 110 mm (Buckley et al., 2001), whereas most of the severe Swiss storms induce hailstones with maximum diameters of 50 mm (e.g., Hohl et al., 2001) and (2) residential buildings in Australia show some building components (e.g., shingles) that are not commonly used in Switzerland (tiles prevail) and that could be more sensitive to hailfall.

As expected, the relationship between hailfall intensity and mean damages is nonlinear with damages that increase rapidly from low  $E_{KINPIX}$  to reach a maximum amount of damage at highest  $E_{KINPIX}$ . Low hail damages (e.g., below CHF 1200 equal to 10% in Fig. 3.3a,b) are difficult to obtain, since damage claims are mostly higher than a minimal amount above which reparability and/or replacement becomes economical.



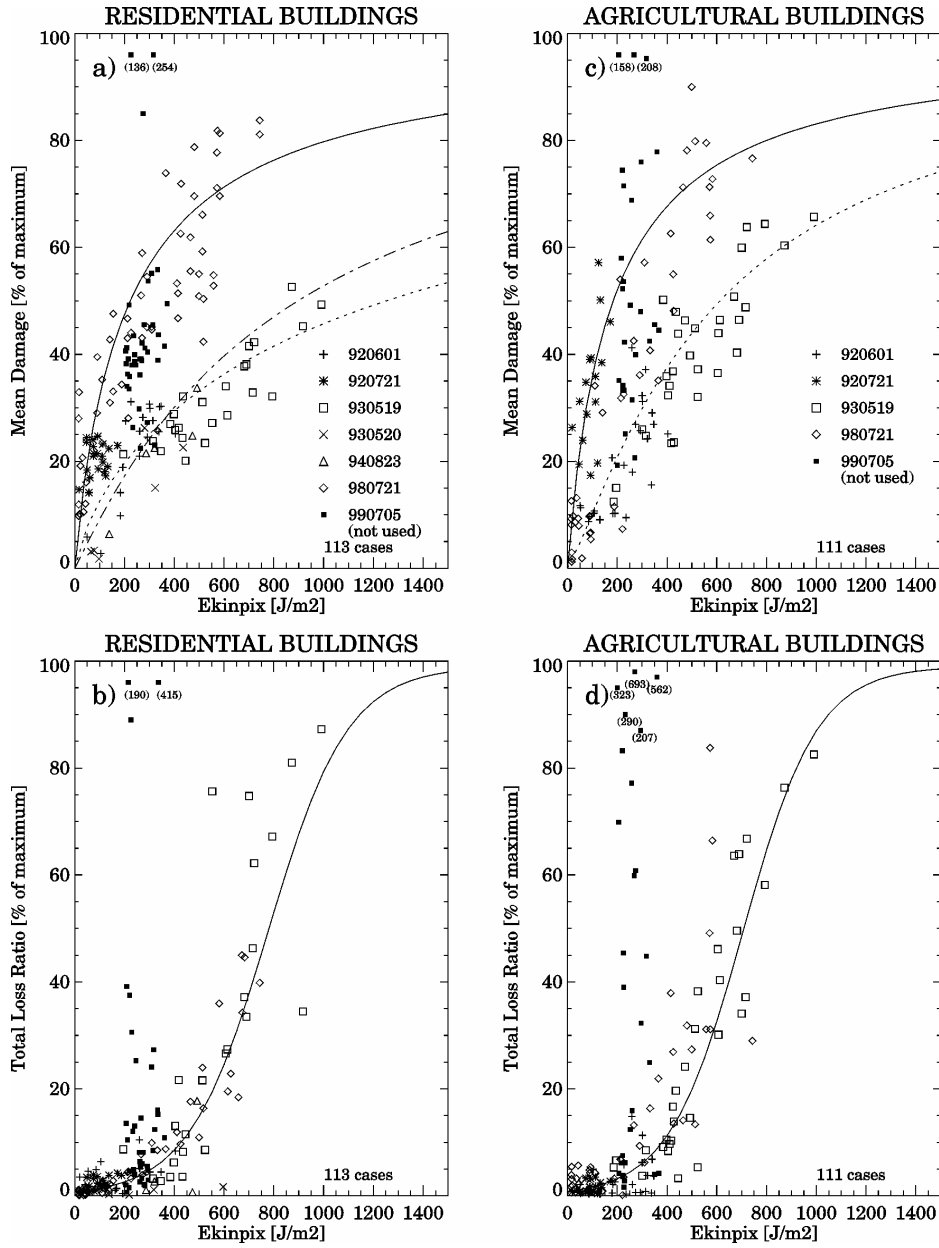


**Figure 3.3.** Relationship between triangulated radar-derived hail kinetic energy ( $E_{KINPIX}$ ) and triangulated damage variables for residential buildings including a) mean damages displayed as percentages of a maximum possible mean damage with weighted logistic damage functions calculated for two high season storms (outlined, correlation coefficient of 0.83) and four low season storms (dotted, 0.87). For low season storms, a third logistic damage function (dashed dotted) describes the relationship between  $E_{KINPIX}$  and mean damages of individual residential buildings that were averaged per radar element with a correlation coefficient of 0.86. b) Total loss ratios presented as percentages of a maximum possible value with a non-weighted logistic damaged function (outlined) that provides a correlation coefficient of 0.85. Corresponding relationships between  $E_{KINPIX}$  and damage variables for agricultural buildings are given in c) for mean damages with a weighted logistic damage function for two high season storms (outlined, correlation coefficient of 0.79) and two low season storms (dotted, 0.88) and d) for total loss ratios with a non-weighted logistic damage function that yields a correlation coefficient of 0.84. Since the hail cell 990705 reveals a special case (Section 3.5.6), observations are only shown for  $E_{KINPIX} > 200 \text{ Jm}^{-2}$  and data points not used to calculate logistic damage functions. Different symbols depict different cells that are separately labeled.

In order to fit a logistic damage function to the data, a maximum possible mean damage was determined for high season storms at CHF 11,000 for residential buildings and at CHF 12,000 in the case of agricultural buildings (taken as 100% in Fig. 3.3a,c). In comparison, low season storms produced lower maximum mean damages that reach approximately CHF 7000 (CHF 8000) for residential (agricultural) buildings. For residential buildings, a weighted logistic function for observations at mid-scale, provides a correlation coefficient between  $E_{\text{KINPIX}}$  and mean damages of 0.83 (0.86) for high (low) season storms. A corresponding damage function yields a correlation coefficient of 0.79 (0.88) between  $E_{\text{KINPIX}}$  and mean damages to agricultural buildings for high (low season storms). Generally, seasonal differences in hailfall and damage intensities are more pronounced for residential than for agricultural buildings where some data points could belong to storms of either season. As hail damage claims of individual residential buildings were additionally available for three of the present low season storms, a weighted logistic damage function was calculated and provided a correlation coefficient of 0.86 between  $E_{\text{KINPIX}}$  and mean damages that were both averaged per  $0.5 \times 0.5$  km radar element (Fig. 3.3a, dashed dotted). A comparison with the logistic function derived from community-aggregated mean damages for low season storms (Fig. 3.3a, dotted), reveals an overall good correspondence with some differences in slope parameters between the two damage functions. The valuable agreement between the two damage functions shows that triangulated amounts of damage claims per community reproduce spatial damage variability to a satisfying degree. Cell 990705 1534 produced the overall highest mean damages (Fig. 3.3a,c) and reveals a special case that is discussed separately in Section 3.5.6.

### 3.5.4 Radar-Derived Hail Kinetic Energy vs. Total Loss Ratios

A seasonal difference in amounts of hail damage does not result for total loss ratios (Fig. 3.3b,d), which can be explained by the fact that (1) a total loss ratio reaches maximally a few percent as it reflects the proportion of community-aggregated hail damage claims to the total sum insured of all buildings of a certain type within the same community and (2) as the difference between the average mean damage produced by low season storms in relation to a high season storm is for both residential and agricultural buildings, around CHF 500 (Section 3.5.3), it is too small to be reproduced in the total loss ratio. In the following, total loss ratios are considered for one storm season only. The average mean total loss ratio reaches around 0.156% for residential buildings and is similar to the 0.180% calculated from damage claims of residential buildings produced by the 1990 Sydney hailstorm (Andrews and Blong, 1997). In comparison with residential buildings, the average mean total loss ratio for agricultural buildings is slightly higher at 0.224%.

The statistical relationship between hailfall intensity and total loss ratios is characterized by a majority of observations at low scale ( $E_{\text{KINPIX}} < 400 \text{ Jm}^{-2}$ , total loss ratios  $< 10\%$ ) and relatively few data points with  $E_{\text{KINPIX}}$  and amounts of damage at the upper scale. As total loss ratios involve both damaged and nondamaged buildings (reflected in the total sum insured),

damage amounts remain small at low  $E_{\text{KINPIX}}$  values and increase nonlinearly to reach a maximal possible damage level that has been set as 100% (Fig. 3.3b,d) in order to calculate a logistic damage function. Nonweighted logistic functions provide correlation coefficients of 0.85 for residential (Fig. 3.3b) and 0.84 for agricultural buildings (Fig. 3.3d); resulting parameters of the nonweighted logistic function are given in Table 3.4. For a given hailfall intensity, total loss ratios of agricultural buildings are slightly higher than for corresponding values of residential buildings. As already noted for mean damages (Section 3.5.3), cell 990705 1534 produced total loss ratios that are considerably higher than corresponding values of all other cells; this storm case is therefore discussed in more detail in Section 3.5.6.

### 3.5.5 Calibration of Damage Functions for Total Loss Ratios

Since hailfalls typically produce distributions of hail kinetic energies ( $E_{\text{KINPIX}}$ ) that are characterized by a large number of small and a small number of high  $E_{\text{KINPIX}}$  values (Table 3.1, Fig. 3.3), it is difficult to fit a logistic damage function to the observations and to derive an accurate weighting procedure. As enough data are available in the present case, three functions have been derived from the initially nonweighted logistic damage functions (Fig. 3.3b,d), altering the parameters  $\beta_0$  and  $\beta_I$  that define the functions in Eq. (3.4). Damages are calculated from the available hailfall intensity ( $E_{\text{KINPIX}}$ ) at individual grid elements and integrated over the entire area of hailfall for four cells that were used to establish the initial damage function and for an additional two cells available for calibration. Predicted damages are then compared to the actual total amounts of hail damage to residential and agricultural buildings (Table 3.4) to reveal the most accurate functional form of the logistic damage function.

**Table 3.4.** Overview of actual and predicted hail damage amounts (in CHF million) from four cells used to establish the damage functions and two independent cells for residential and agricultural buildings. Actual losses are compared to losses predicted by the damage function obtained from the observations (a, e) and functions with gradually altered parameters (b-d, f-h) that are listed below. Damage functions that predict damages that are closest to actual losses are indicated in bold and prediction errors listed for every hail cell.

Storm	Time	Residential Buildings							Agricultural Buildings						
		Hail Damage [CHF mio]							Hail Damage [CHF mio]						
		actual	calibrated				error		actual	calibrated				error	
[Date]	[UTC]		a)	b)	c)	d)	[%]		e)	f)	g)	h)	[%]		
920601	1828-1953	0.697	4.374	3.642	1.654	<b>0.924</b>	+35	0.191	2.224	1.858	0.837	<b>0.464</b>	+142		
920721	1558-1623	1.418	4.758	4.354	1.768	<b>0.795</b>	-43	0.332	1.339	1.243	0.497	<b>0.216</b>	-35		
930519	1523-1723	3.305	23.146	16.040	10.746	<b>11.764</b>	+255	1.883	16.855	11.725	9.724	<b>8.450</b>	+348		
980721	1306-1431	54.639	118.275	79.914	52.504	<b>57.477</b>	+5	3.548	10.056	7.877	4.025	<b>3.040</b>	-14		
920721	1333-1523	27.683	40.667	31.897	25.319	<b>24.206</b>	-12	1.096	5.413	4.631	2.328	<b>2.063</b>	+88		
940810	1218-1353	9.761	18.355	16.623	14.697	<b>12.190</b>	+24	1.200	6.625	4.786	3.867	<b>2.806</b>	+133		

a) as obtained from observations (Fig. 3.3b) with  $\beta_0 = -4.82478$  and  $\beta_I = 0.00645030$ .

b) same  $\beta_0$  as in a) with  $\beta_I = 0.00545030$ .

c) with  $\beta_0 = -5.82478$  and same  $\beta_I$  as in a).

d) same  $\beta_0$  as in c) with  $\beta_I = 0.00745030$ .

e) as obtained from observations (Fig. 3.3d) with  $\beta_0 = -4.74966$  and  $\beta_I = 0.00669465$ .

f) same  $\beta_0$  as in e) with  $\beta_I = 0.00569465$ .

g) with  $\beta_0 = -5.74966$  and same  $\beta_I$  as in e).

h) same  $\beta_0$  as in g) with  $\beta_I = 0.00769465$ .

Compared to actual losses, the initial nonweighted damage functions (Fig. 3.4, outlined) produce damages to residential (agricultural) buildings that are between two to eight times (three to eleven times) higher (Table 3.4a,e). The large differences between actual and predicted losses mainly appear as nonweighted functions cannot reproduce the large numbers of observations at low intensity levels with  $E_{\text{KINPIX}} < 400 \text{ Jm}^{-2}$  (84% of entire spectra in Fig. 3.4) in proportion to the few points at high intensity levels of  $E_{\text{KINPIX}} > 600 \text{ Jm}^{-2}$  (10%). Lowering the parameter  $\beta_l$  by 0.001 defines a logistic function that shows an overall flatter slope (Fig. 3.4, dotted) and produces considerably lower predicted damages (Table 3.4b,f). Altering the parameter  $\beta_0$  of the logistic function by one unit (Fig. 3.4, dashed), reduces the predicted damages further and high losses (980721 1306; 920721 1333) are in the range of the observed losses (Table 3.4c,g). Small losses are accurately predicted for cell 920721 1158 but are still overestimated for other cells by factor four (920601 1828) up to factor five (930519 1523). Overall, the best agreement between actual and predicted damages occurs with an alteration of both  $\beta_0$  (one unit) and  $\beta_l$  (by 0.001) that provides a logistic damage function that increases most flat at low levels and reaches a most steep slope at higher intensity levels (Fig. 3.4, dashed-dotted).

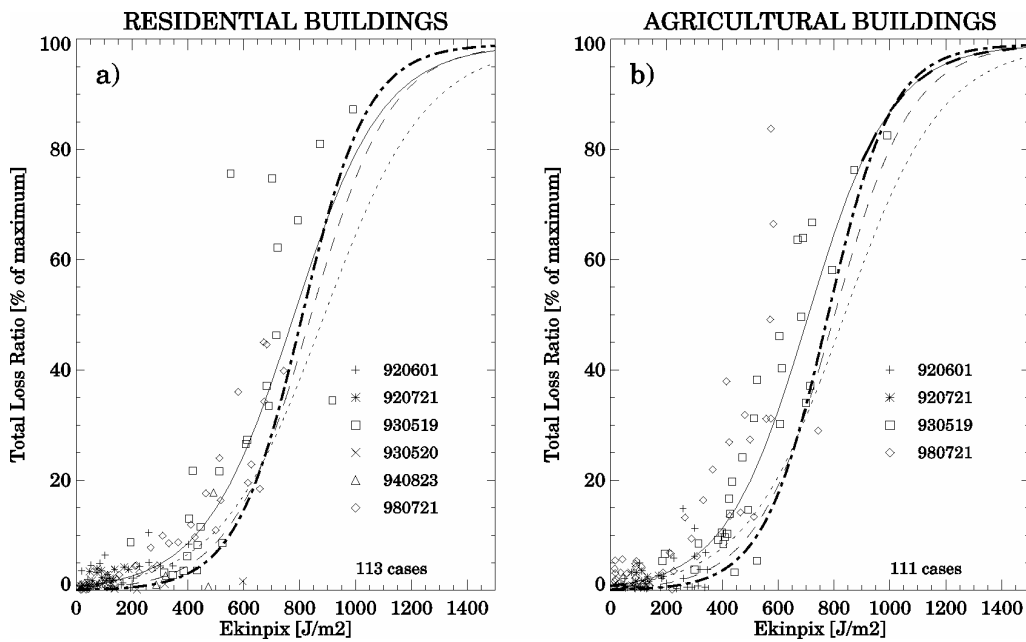


**Figure 3.4.** Relationship between triangulated radar-derived hail kinetic energy ( $E_{\text{KINPIX}}$ ) and triangulated total loss ratios (as percentages of a maximum possible value) of six hail cells for a) residential buildings and b) for agricultural buildings. Both figures contain four nonweighted logistic damage functions calculated from the observations (outlined, same as in Fig. 3.3b,d) and determined with an altered slope parameter  $\beta_l$  (dotted), an altered intercept  $\beta_0$  (dashed) and both an altered slope and intercept (dashed dotted). Parameters  $\beta_0$  and  $\beta_l$  that define the logistic damage functions are listed in Table 3.4. Different cells are distinguished by labeled symbols.

As a result, highest losses are equally well predicted as in the previous step (with altered  $\beta_0$  only) with relative prediction errors of damages to residential buildings in the range of +5% (980721 1158), -12% (920721 1333), and +24% (940810 1218) as shown in Table 3.4. While

some of the small damages are now similar to the actual losses, others are either underestimated (920721 1558) or overestimated with a relative prediction error of +255% (930519 1523). Similarly, highest losses to agricultural buildings (980721 1306) are accurately reproduced whereas other damages are overestimated by +88% (920721 1333) up to 348% (930519 1523) as listed in Table 3.4. Although more altered damage functions would need to be calculated to determine the most accurate functional form, the present function (altered  $\beta_0$  and  $\beta_1$ ) reproduces the highest damages to a satisfying degree, which is of major interest, regarding practical applications for insurance purposes.

### 3.5.6 The hailstorm of 5 July 1999

The synoptic situation and storm environments of 5 July 1999 were ideal for the development of severe thunderstorms in Switzerland (Huntrieser et al., 1997; Schiesser et al., 1997). Radar images of the Swiss radar composite (available through the Swiss Meteorological Institute) and analyses of METOSAT images reveal that the hail cells that moved over the Swiss Mittelland are part of a larger storm system over central Europe that shows characteristic features of a mesoscale convective system (MCS). The MCS developed in the early afternoon over eastern France and western Switzerland before an approaching cold front by merging of individual rain areas of several convective cells. The initial group organization of the MCS turned into a line organization of convective cells and moved as a squall line into southern Germany, followed by a large area of stratiform rainfall. MCSs that show a line organization of convective cells, are well known to produce severe hail, heavy rainfall and strong winds over a large area (e.g., Schiesser et al., 1995).

Plan Position Indicators (PPIs) performed by the ETH radar (Fig. 3.5) show that the MCS consisted of several hail cells (radar reflectivities > 51dBZ) that moved one after the other over the western part of Switzerland. Individually identified hail cells developed at 1600 UTC (Fig. 3.5a), 1610 (not shown), 1720, 1730, 1750 and 1755 (all in Fig. 3.5b,c) and storm tracks crossed each other several times over the same area in canton Berne. Following the passage of the MCS, several precipitation systems with embedded convective cells entered Switzerland from France and produced rainfalls that lasted over the night (Fig. 3.5d-f) until the early morning of 6 July.

Over canton Berne, the combined hail cell produced hail damage claims of CHF 20.316 million to residential and CHF 15.367 million to agricultural buildings (Table 3.1). Average mean damages reached CHF 6000 (CHF 9000) for residential (agricultural) buildings are higher than mean damages produced by the other cells (Section 3.5.3). The highest community-related damage reached CHF 8.146 million for residential buildings (40% of total damage); for location see Fig. 3.5. Damage claims in the neighboring community amounted to a further CHF 3.494 million for residential buildings (17% of total damage) and CHF 5.283 million (34%) for agricultural buildings.

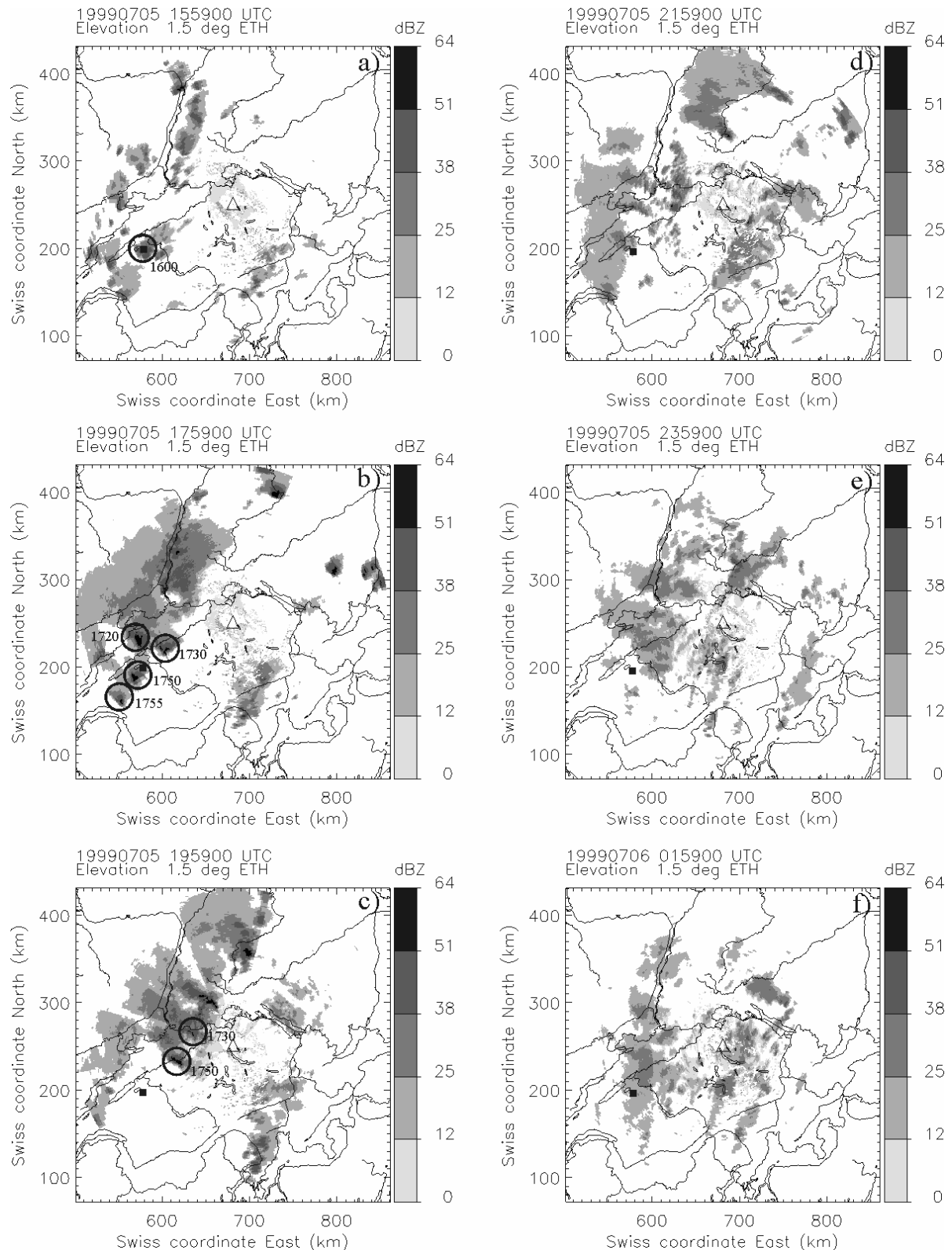


**Figure 3.5.** Plan Position Indicators (PPIs) of radar reflectivity (grey shades in five intensity levels) performed by the ETH C-band Doppler radar (location indicated by a triangle) of hail cells that occurred as part of a mesoscale convective system (MCS) over Switzerland on 5 July 1999; for orientation and country borders see

Figure 3.1. The figure includes a sequence of six PPIs over a total of 12 hours with a) at 1559 UTC (1759 LST) with the arrival of the MCS and a first hail cell (radar reflectivity  $> 51\text{dBZ}$ ) that developed at 1600 (circle) over canton Berne where insurance data were available and propagated towards northeast in the following; a further hail cell developed at 1610 (not shown) and followed the track of cell 1600; b) at 1759 UTC with four hail cells that developed at 1720 (cell did not directly move over canton Berne), 1730 and 1750 and propagated over canton Berne towards northeast; cell 1755 did not reach canton Berne and decayed shortly after development; c) at 1959 UTC with cell 1730 at decaying stage and cell 1750 that moved further northeast out of canton Berne; d) at 2159 UTC when all hail cells have decayed and a first precipitation system (reflectivities  $< 38\text{dBZ}$ ) that entered the western part of Switzerland from France; e) at 2359 UTC and f) at 0159 UTC on 6 July when further precipitation systems moved over the northwestern part of Switzerland; rainfall ceased over canton Berne in the early morning hours of 6 July 1999. The location of the community where the highest total hail damage amount to residential buildings has been recorded is indicated in the figures by a square. Scales, radar detection ranges (maximum 180 km), radar elevation angles ( $1.5^\circ$ ) and radar reflectivity levels (1-64dBZ) are the same in all figures. Swiss coordinates (km units) are used in all figures.

The cell 990705 1534 qualifies as a high season storm and while most mean damages are in the range of values produced by the other high season storms (Fig. 3.3a,c), maximum mean damages reach 254% (corresponds to CHF 30,000 in Fig. 3.3a) for residential and 208% (CHF 25,000 in Fig. 3.3c) for agricultural buildings. Correspondingly, the cell 990705 1534 produced total loss ratios (Fig. 3.3b,d) that are generally higher than ratios of all other cells with maximum values of 415% (693%) of residential (agricultural buildings).

From the amount of induced damage relative to hailfall intensity ( $E_{\text{KINPIX}}$ ), it becomes relevant that the actual damages of the four different hail cells that were combined into cell 990705 1534 cannot be considered as proportionally additive to the final loss. As several cells propagated over the same areas of canton Berne, it is very likely that a first storm induced an initial damage through hailfall and/or strong wind gusts so that a second cell increases the damage, mainly through hail and/or water damage to interior building structures (e.g., ceilings, wall papers). Furthermore, as several precipitation systems followed the hail-bearing MCS, long-lasting rainfalls increased the damage to the exposed internal building structures additionally. In addition, flooded basements and cellars of several hail-damaged buildings added to the final damage amount.

The fact that numerous communities were hit by several hail cells and following precipitation systems, partly explains the finding that hail kinetic energies of  $200\text{--}400\text{ Jm}^{-2}$  produced mean damages of up to CHF 30,000 (Fig. 3.3a,c) and total loss ratios that are six times higher than for other cells (Fig. 3.3b,d). On the other hand, there is a possibility that  $E_{\text{KINPIX}}$  values might have been underestimated to a certain extent since hail kinetic energy was calculated from PPI reflectivities which were measured at a large distance from the radar (up to 120 km) as opposed to CAPPI reflectivities used for all other cells.

### 3.6 Discussion

The present study on the relationship between radar-derived hailfall intensity ( $E_{\text{KINPIX}}$ ) and amounts of damage to residential and agricultural buildings involved several simplifications and assumptions including hailfall intensity ( $E_{\text{KINPIX}}$ ), hailfall area (storm box), hailfall direction (unidirectional), building exposure (only communities with a defined number of claims are analyzed), building structure (assumed to be comparable) as well as damage amounts (comparable reparability costs and insurance conditions). The investigation of radar and damage claim data from a total of nine hail cells that occurred over the Swiss Mittelland (1992-1999), revealed interesting relationships which are discussed in the following.

1. Distribution of radar-derived hail kinetic energies ( $E_{\text{KINPIX}}$ ) showed that most radar elements contain energies at the low scale ( $< 200 \text{ Jm}^{-2}$ ) that consist of 40-97% of the entire spectra (Table 3.1). As  $E_{\text{KINPIX}}$  represents the time-integrated hail volume received per radar element,  $E_{\text{KINPIX}}$  spectra are to some extent influenced by the propagation velocity of a hail cell. Although not enough data are available for general conclusions, slow moving cells tend to produce higher proportions of  $E_{\text{KINPIX}} > 600 \text{ Jm}^{-2}$  and longer maximum hailfall durations per radar element (Table 3.1). Since radar-derived hail kinetic energy does not directly resolve hailstone spectra and a  $E_{\text{KINPIX}}$  value can either be produced by a large number of small hailstones or a small number of larger stones, hail kinetic energies cannot directly be related to damage amounts. Although somehow arbitrary, the classification of hail cells into high and low season storms reflects distributions of hailfall intensities and resulting amounts of damage. Hohl et al. (2001) showed from hailpad-derived hailstone spectra (available from Grossversuch IV, Federer et al., 1986), that high season storms (defined from 15 June to 15 August) tend to produce for a given  $E_{\text{KINPIX}}$  lower numbers of hailstones but larger maximum diameters than storms that occurred during the low season (before and after); this finding is partly confirmed by a study of hailfalls in Northern Italy by Giaioti et al. (2001). The present study revealed that for both residential and agricultural buildings, high season storms (15 June-15 August) produced higher proportions of damage claims above CHF 6000 than low season (before and after) storms (Table 3.2). Comparisons of point-to-point relationships between  $E_{\text{KINPIX}}$  and two damage variables revealed that a seasonal classification of hail cells was necessary for mean damages (Fig. 3.3a,c), but not for total loss ratios (Fig. 3.3b,d) where seasonal differences in damage amounts are too small to be reproduced. Once more storm data are available, the seasonal classification of hail cells that is necessary to distinguish mean damages either storm season, could be improved using storm indices (e.g., CAPE) such as analyzed in Huntrieser et al. (1997) for Switzerland.
2. As shown in Katz and Garcia (1981), Schiesser (1990) and Hohl et al. (2001), logistic functions also lead to good results between hailfall intensity and damage amounts to residential and agricultural buildings in the present study. Since hail damage claims are



mostly above a minimal cost of reparability (e.g., CHF 1000), weighted logistic damage functions have been fitted through  $x=0/y=0$  and a maximum possible damage, assuming from the nature of hailfalls that the data should contain a certain percentage of damage at low and high values. In most cases, a clear difference occurs between amounts of mean damages produced by low relative to high season storms. The valuable agreement between logistic functions calculated from both community-aggregated mean damages and mean damages to individual buildings (Fig. 3.3a), shows at least for residential buildings, that a triangulation of community-aggregated data reproduces spatial damage variability to a satisfying degree.

For total loss ratios where the majority of observations reveal  $E_{\text{KINPIX}} < 400 \text{ Jm}^{-2}$  and ratios  $< 10\%$  (Fig. 3.3b,d), weighting of the logistic damage functions provided no satisfying results. For a selected number of hail cells, nonweighted logistic damage functions (Fig. 3.4) produced predicted damages that are between two to eleven times higher than the actual losses (Table 3.4). In order to respect proportions of low and high damages, parameters of the nonweighted damage functions are altered (Fig. 3.4), whereas a function with both altered  $\beta_0$  and  $\beta_1$  produced damage amounts that are closest to the occurred losses. High damages are accurately predicted (at least for residential buildings with average errors around 14%), whereas small damages are overestimated by up to five times (e.g., 930519 1523 in Table 3.4d,h). As mentioned earlier, proportions of  $E_{\text{KINPIX}}$  at different intensity levels have a direct influence on the predicted damage amounts. The damage functions that produce the best results (altered  $\beta_0$  and  $\beta_1$ ) reveal the flattest slope gradient at low intensity levels and the steepest gradient at higher levels and predict damages for hailfalls that reveal between 71-97% of  $E_{\text{KINPIX}} < 200 \text{ Jm}^{-2}$  (Table 3.1) to a satisfying degree. However, the same damage function fails to reproduce damages for the cell 930519 1523 which induced lower proportions of low ( $E_{\text{KINPIX}} < 200 \text{ Jm}^{-2}$ ) but higher proportions of high ( $E_{\text{KINPIX}} > 600 \text{ Jm}^{-2}$ ) hail kinetic energy (Table 3.1). Further alteration of the established functions (with e.g., a smaller  $\beta_1$ ) would eventually reduce the predicted damage for cell 930519 1523, but increase the predicted losses of other cells that reveal  $E_{\text{KINPIX}}$  distributions with lower proportions at high intensity levels on the other hand. The three alterations used in the present study to calibrate the damage functions give only a brief overview of how the most accurate functional form of a logistic damage function could be found. Once more insurance and storm data are available, a large number of iterations could be calculated and the ratios between predicted damages to the occurred losses would identify the form of a damage function that could be used for practical applications.

3. Although the established logistic damage functions yield valuable correlation coefficients, the scatter around the curves is in some cases considerable and could be influenced by various errors such as: (1) inaccurate radar measurements (e.g., attenuation of the radar beam by precipitation areas); (2) wind velocities that are not reproduced by  $E_{\text{KINPIX}}$  and can additionally increase the impact of hailstones adding to the final damage amount; (3)

building exposure, structure and vulnerability towards hailfall as well as reparability and/or replacement costs and (4) inaccuracies in the settlement of the final damage amount and variations of the indexed damages according to a Swiss-wide building cost index. It is at the moment not possible to compute variance estimates of each of the sources of errors, since more comparisons between radar measurements and hail damage must be conducted first. The classification of damage claims from buildings that consist of traditional building materials (e.g., tiles, wood) or new materials (e.g., glass, aluminum), would certainly reduce the scatter and improve the damage functions. The availability of insurance and claim data for a spatially consistent area (e.g., for all of the Swiss cantons) would not only reduce the bias that occurs when community-aggregated data are triangulated between areas where no information is available, but also allow the assessment of large storms and entire storm systems..

4. From comparisons between proportions of damages above CHF 6000 (Table 3.2), average mean damages (Section 3.5.3), total loss ratios (Section 3.5.4) and point-to-point relationships between  $E_{KINPIX}$  and mean damages (Fig. 3.3a,c), results that damage amounts are consistently higher for agricultural than for residential buildings. While sums insured of damaged residential and agricultural buildings are on the average in a comparable range, differences in total loss ratios (Fig. 3.3b,d) result from higher average claims induced on agricultural buildings. A combination of several factors could be responsible for the fact that damage amounts are higher for agricultural buildings. (1) Agricultural buildings are often isolated and therefore fully exposed to hailfall, whereas the high spatial density of residential buildings could provide a certain sheltering from impacts of hailstones. (2) Agricultural buildings reveal larger exposed surfaces, so that a hail damage to a building that reveals the same sum insured as a typical residential building produces a higher total loss ratio. (3) Due to the large exposed surfaces of agricultural buildings, replacement costs are on the average higher than for residential buildings, especially if cranes and/or scaffoldings need to be built before the damaged surfaces can be assessed. The role of above factors on the total damage outcome can only be verified once more storm and insurance data are available.
5. Analyzes of the hail cell 990705 1534 have shown that damage-inducing hail cells occurred within a mesoscale convective system (MCS) and that damage amounts of individual cells (that were combined into cell 990705 1534) are not directly additive to the final loss amount. While the use of PPI reflectivities for cell 990705 1534 might have involved an underestimation of  $E_{KINPIX}$ , the high amounts of damage are mainly the result of a combination of several cells that moved over the same area and the arrival of several precipitation systems following the hail-bearing MCS. As a result of the interaction between damage induced by hail and rainfall, relationships between  $E_{KINPIX}$  and both mean damages and total loss ratios reflect the combined damage potential of hail and rainfall in comparison to damage of hailfall alone as in all other cells. A better knowledge of the damage agent that

caused the claimed hail damage (e.g., hail alone or in combination with water and/or wind) would be helpful to separate storms according to their damage potential. Once more detailed claims and radar data as well as finely resolved precipitation measurements are available, it would not only be possible to determine the damage-adding influence of rainfall but also to establish a damage function for hailfall in combination with wind and/or rainfall. In Switzerland, MCSs that produced several hail-bearing cells occur occasionally and are well known to produce the highest daily hail damages (Schiesser et al., 1995). However, cases where several hail cells have moved one after the other over the same area and are followed by several precipitation systems are rare and can be considered as worst cases from a damage perspective.

### 3.7 Conclusion

The present investigation showed that radar-derived hail kinetic energy relates well to the amounts of hail damage to residential and agricultural buildings calculated for a total of 9 hail cells that occurred over the Swiss Mittelland (1992-1999). Several assumptions and simplifications of hailfall intensity, wind velocities and building exposure as well as building structures were necessary before hailfall intensities could be related to damage variables. Radar-derived hail kinetic energy ( $E_{\text{KINPIX}}$ ) has been integrated for entire hail cells and reveals the volume of hailfall received per surface unit which is related to hail damage. The available radar measurements (per  $0.5 \times 0.5$  km resolution) and damage data (community resolution) were triangulated on a  $2 \times 2$  km grid and the best shift vector between  $E_{\text{KINPIX}}$  values at radar measuring level (1.5 km MSL) and ground determined. The following key findings result from the presented study:

- Differences in storm intensity, mean damages and proportions of claims > CHF 6000 are best explained if hail cells are grouped into high (15 June-15 August) and low (before and after) season storms.
- Weighted damage functions provide correlation coefficients between  $E_{\text{KINPIX}}$  and mean damages of residential buildings that reach 0.83 (0.86) for high (low) season storms and amount to corresponding coefficients 0.79 (0.88) for agricultural buildings.
- As weighting of the logistic damage functions appeared to be difficult for total loss ratios, a nonweighted function has been fitted to the data and provided correlation coefficients of 0.85 for residential and 0.84 for agricultural buildings.
- Compared to actual losses, the nonweighted damage functions predicted damages that are consistently overestimated whereas differences between simulated and occurred damages decreased if three gradually altered functions (flatter slope gradients) were used.
- The finding that damages are in most cases higher for agricultural than for residential buildings results from the fact that agricultural buildings are more exposed to hailfall,

show larger exposed surfaces, are therefore more costly to repair and are generally less well maintained than residential buildings.

- Damage amounts for hail cells that moved as part of a mesoscale convective system over the same area and were followed by several precipitation systems were considerably higher and the relationship between  $E_{KINPIX}$  and amount of hail damage from this cell is therefore not comparable to damages induced from other hail cells, where hailfall prevailed.

Although logistic damage functions produced valuable correlation coefficients, the scatter around the curves is in some cases considerable and could be improved in future studies if the following data are available: (1) high resolution wind velocity measurements (e.g., Doppler radar velocities) so that the fall direction of hail could be improved; (2) aggregated damage claim data for a consistent area and on a finer resolution (e.g., per  $1 \times 1$  km grid) or even per individually geo-referenced building; (3) details of claims settlements and costs divided into pure damage costs and costs for damage assessment and reparability; (4) classifications of damages according to the damaged building parts and (5) the proportion of different damage agents (hail, wind and water) on the amount of damage. Future studies with improved damage information will not only help to verify but also to improve the established damage functions.

The valuable relationship between total loss ratios and hail kinetic energy directly derived from radar measurements reveals some interesting applications for the property insurance industry in (1) estimating the extent of hail damage to an insured building portfolio immediately after a storm has passed over a combined radar observation area and (2) evaluating possible maximum losses (PML) to an insured building portfolio. For an insurance company, PMLs are the basis of calculating accurate premiums and to determine the insurers retention above which reinsurance cover is purchased in order to be able to handle highest losses. Once more studies have confirmed the validity of the present damage functions and additional data are available, maximum losses within a portfolio could be calculated for entire hail cells in two ways: (1) The damage function for mean damages predict an average mean damage for a given hailfall intensity ( $E_{KINPIX}$ ) that can be related to a known (e.g., from experience) or assumed number of buildings that are likely to be damaged per insured area and storm season (high or low season storms). (2) The damage functions established for total loss ratios provides a predicted proportion of damage relative to the total sum insured per insured area for every hailfall intensity. Based on known total sums insured, radar-measured past severe hailstorms can be shifted over a portfolio of interest and predicted damages be calculated, with the highest simulated damage considered as a PML. In a further step, a large number of hailstorms could be gradually derived from radar-measured hail cells (e.g., changes in intensity) and a large number of simulated damages could be obtained for a given portfolio. Attributing a return period to all individual simulated damages, complete information on the relationship between intensity and frequency of hailstorms would be available.

## Chapter 4

### Cloud-to-ground lightning activity in relation to the radar-derived hail kinetic energy in Switzerland

(reproduced as published in *Atmospheric Research* with changes in section numbers, acknowledgement and references at the end of the thesis)

#### 4.1 Abstract

First of its kind, this study presents relationships between radar-derived hail kinetic energy at low storm-level (1.5 km MSL) and cloud-to-ground (CG) lightning stroke rates for 41 hail cells of various intensities that occurred over the Swiss Mittelland (1992-1995). Hail kinetic energy is calculated from C-band Doppler radar Constant Altitude Plan Position Indicators (CAPPIs), and locations of positive and negative CG strokes attributed to hail cells, which are approximated for every time step (5 min) by a circle including reflectivities  $\geq 30\text{dBZ}$ . Inaccuracies of CG stroke and radar measurements were corrected to obtain a complete data set.

The results show that negative CG stroke totals are in good linear correspondence with total amounts of hail kinetic energy ( $E_{\text{KINTOT}}$ ) with a correlation coefficient of 0.95.  $E_{\text{KINTOT}}$  correlates to temporal (0.88) and spatial locations of negative CG stroke peaks (0.84) relative to maximally expected hailfall (peaks in hail kinetic energy): in 66% of the cases, negative CG stroke rates peaked on the average 22 min and 19 km prior to maximal hailfall. Totals of positive CG stroke rates are in no direct correspondence with  $E_{\text{KINTOT}}$ . Temporal-spatial locations of positive CG stroke peaks reveal large variances with a tendency for weak isolated hail cells to occur on the average 10 min before and 3.5 km after maximal hailfall, whereas peaks of positive CG strokes lag maximal hailfall up to 30 min and 45 km in strong, large isolated cells. The study suggests that negative CG stroke rates could be used in the future to support and improve nowcasting operations for severe hailstorms in central Europe.

## 4.2 Introduction

Much research has been done to understand the role of cloud-to-ground (CG) lightning in relation to severe weather occurrence, recently reviewed by MacGorman and Rust (1998). Since the availability of coherent ground-based lightning location systems, the quality of CG lightning data has improved and many studies noticed a close link between CG lightning and severe weather.

Numerous studies analyzed the structure and organization of severe thunderstorms in terms of ratios between negative (–CG) and positive CG lightning (+CG). It results that although many severe tornadic storms are dominated by –CG flash rates (e.g., MacGorman and Nielson, 1991; Knapp, 1994), some severe storms that reveal high +CG flash rates also produce severe weather. Situations where +CG flashes are elevated and can dominate –CG flash rates, have recently been summarized by Carey and Rutledge (1998): (1) the anvil region of severe storms (e.g., Rust et al., 1981); (2) the trailing stratiform region of mesoscale convective systems (MCS) (e.g., Rutledge et al., 1990; Engholm et al., 1990; Stolzenburg, 1990) and (3) in MCS that produce large hail (> 2 cm in diameter) and sometimes tornadoes during at least 30 min of the mature phase (e.g., Branwick and Doswell, 1992; Curran and Rust, 1992; Seimon, 1993; MacGorman and Burgess, 1994; Stolzenburg, 1994).

A large number of studies on CG lightning in severe storms have examined tornadic storms (mostly in relation to elevated +CG flash rates), whereas relatively few investigations addressed the relationship between CG lightning activity and hailfall; some recent results are summarized in the following. Rust et al. (1985) and Reap and MacGorman (1989) found that large hail is more likely to occur in storms that have high densities of +CG flashes. Changnon (1992) analyzed 48 hail streaks in Illinois and noticed that –CG flash rates typically increased until hail damage began, decreased (but remained large) during damage and decreased more rapidly after hail damage ceased. In 15 severe Oklahoma supercell storms examined by MacGorman and Burgess (1994), large hail was reported during periods when +CG flashes dominated and a decrease of reported hailstone diameters was noticed after dominant positive polarity switched to negative. However, Carey and Rutledge (1998) found that broad peaks in +CG flash rates lag relative maxima in the fallout of large hail up to 30 min in two Colorado supercell storms. Most recently, Williams et al. (1999) investigated CG flash activity of severe Florida thunderstorms and observed abrupt increases in flash rates 5–20 min prior to microburst, hailfall and tornado occurrence. It becomes clear that there are both, similarities and differences in the temporal and spatial evolution of CG lightning activity in relation to maximal hailfall, which is thought to be the result of differences in dynamical and microphysical processes in severe thunderstorm clouds.

In studies where CG lightning activity is compared to hailfall, the location of maximal hailfall has been determined in various ways: (1) surface reports by the public (e.g., MacGorman and Burgess, 1994; Williams et al., 1999) and from national weather services (e.g., Stolzenburg,

1994); (2) reports from storm chasing teams (e.g., Carey and Rutledge, 1998); (3) derived from loss amounts of insured hail-damaged agricultural values (e.g., Changnon, 1992) and (4) combinations of several methods in relation to radar measurements. The advantage of radar for hail detection and measurements is the unique resolution in space and time. If radars are used, hail cells can be distinguished from non-hail cells by the time-integrated 55dBZ reflectivity area (Geotis, 1963; Federer et al., 1986). A radar reflectivity-based criteria for spatial hailfall intensity is the hail kinetic energy developed and used to quantify the effects of weather modification experiments (e.g., Federer et al., 1986). Waldvogel et al. (1978a) established a relationship between S-Band radar reflectivity and hail parameters deduced from time-resolved hailstone spectra, a relationship that has been used thereafter to calculate the hail kinetic energy for entire hail cells (Waldvogel et al., 1978b; Waldvogel and Schmid, 1983; Husson and Pointin, 1989). Schmid et al. (1992) found a good correlation between ground- and radar-measured patterns of hail kinetic energy and Wojtiw and Ewing (1986) as well as Schiesser (1990) revealed good correspondences between patterns of radar-derived hail kinetic energy and intensities of hail damage to crops. Since directly derived from radar measurements, the hail kinetic energy is a good alternative to ground-based reports of hailfall intensity with the advantage to cover large coherent areas.

This paper links, for the first time, CG lightning activity to radar-derived hail kinetic energy patterns close to ground. From 41 hail cells of various intensities that occurred over the Swiss Mittelland (1992-1995), a complete set of radar and lightning information is available to compare the temporal and spatial patterns of both variables. Section 4.3 provides a description of the data, of which some showed inaccuracies and were corrected according to methods presented in Section 4.4. Section 4.5 presents the main results that are discussed and put in common context in Section 4.6. The paper is concluded in Section 4.7.

## 4.3 Data

### 4.3.1 Radar

Radar data are available from the network of two non-Doppler C-band radars (Joss and Lee, 1995) maintained by the Swiss Institute of Meteorology (SMI) until 1995; thereafter a network with three Doppler radars has been operated (Fig. 4.1). Plan Position Indicators (PPIs) are used to monitor thunderstorm propagation over a large area ( $500 \times 400$  km) and to determine the type of cell organization within a larger synoptic context. Further radar data are provided by the C-band Doppler radar (Li et al., 1995) operated by the Swiss Federal Institute of Technology (ETH) at Höggerberg, Zurich, since 1990 (Fig. 4.1). The ETH radar delivers 10-min standard PPIs and Range Height Indicators (RHIs) as well as 5 min manually performed sector-volume scans when thunderstorms are within 80-100 km of the radar. Sector-volume scans have a vertical resolution of 1-1.5 km with 15 scans for narrow sectors

(30°-45°) and nine or less for sectors wider than 90°. Sector-volume scan reflectivity observations are converted into Constant Altitude Plan Position Indicators (CAPPIs) with a 0.5-km vertical and a  $0.5 \times 0.5$  km ( $480 \times 480$  radar elements) spatial resolution using a nearest-neighbor algorithm. During the National Research Program 31 (NRP31) on “climate changes and natural disasters” (1992-1996) in Switzerland, more than 200 hail cells were measured both with the SMI radars and the ETH radar (Schiesser et al., 1997). Overviews of the radar-measured hail cells during NRP31 are given in several reports of the Radar Meteorology Group (1993, 1994, 1995, 1997). During the NRP31, convective cells were defined as hail cells if the succession of the 55dBZ contour lasts at least 30 min. Most of the hail cells produced hail damage to agriculture, available from daily hail damage reports of the Swiss Hail Insurance. For the present study, hail cells from the NRP31 data base were analyzed if the following criteria were fulfilled: (1) the mature phase of a hail cell (radar echoes with reflectivities  $> 55$ dBZ) is entirely within the study area and complete ETH sector-volume scans exists at least for 40 min; (2) in order to avoid concentric rings of missing data at upper-level CAPPIs close to the radar, a minimal distance of 10 km between the radar and the cell is respected; (3) the cell is directly exposed to the radar beam in order to exclude major attenuation through precipitation areas between the radar and the cell and (4) interruptions of sector-volume scan measurements are not exceeding one time step (5 min). These criteria were fulfilled by some 60 hail cells of which 41 hail cells of various intensities that occurred on 22 summer days (May-September 1992-1995) were analyzed in this study. Additionally, five rain cells (55dBZ contour lasts less than 30 min) were analyzed in comparison with the hail cells.

#### 4.3.2 CG Lightning

Lightning data were available from two independently operated Lightning Positioning and Tracking Systems (LPATS) that provide the time of a CG stroke (one flash consists of several strokes), the location, the peak current and the polarity of charge lowered to ground. In Switzerland, Swisscom operated an LPATS (Rubinstein et al., 1994) between 1989-1998 with a network configuration of six receivers (Fig. 4.1). The Swiss LPATS had an estimated detection efficiency of over 70% (Rubinstein et al., 1994) and a measured lightning location accuracy in the range of 0.2-0.5 km (Montandon, 1991); this location error is small compared to the typical diameter of hail cells ( $> 20$  km). Additionally, Bayernwerk has been operating an LPATS in Southern Germany (Fister et al., 1994) since 1992, whose lightning detection area covers a large part of Northern Switzerland. In the coverage region of both LPATS, a region (46.5°-48°N and 7°-10°E) has been defined (Fig. 4.1) in which CG lightning detection efficiencies of the two systems are compared. In relation to the Swiss LPATS, the South German system detects generally fewer CG strokes, since the area designed here for performance evaluation lies at the border of the network configuration. The performance



evaluation of two independently operated LPATS is unique in this study, since network performance is often assumed to be throughout constant.

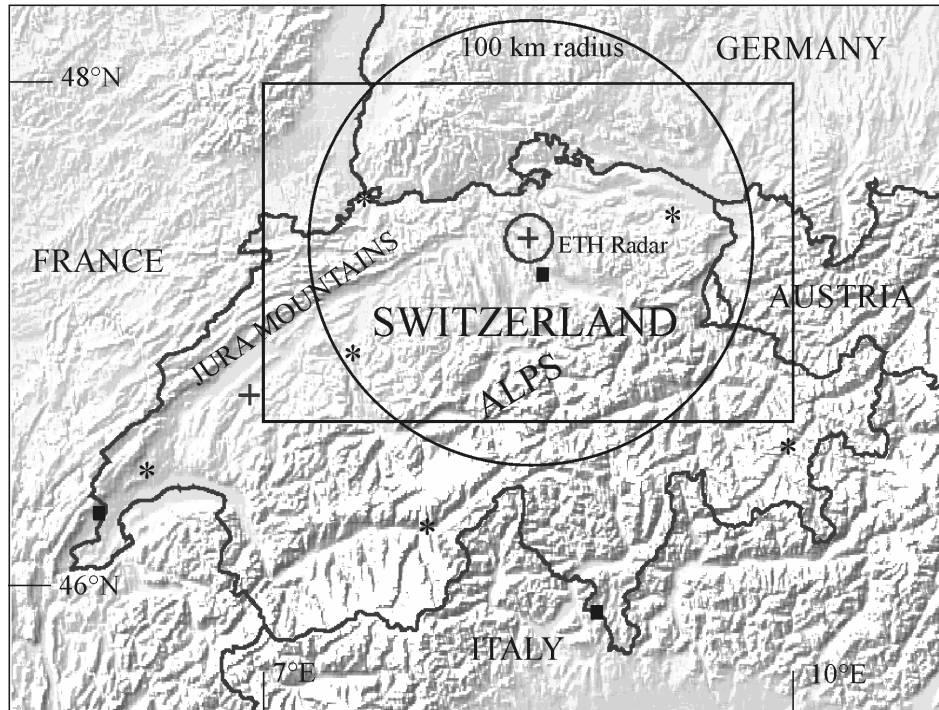


**Figure 4.1.** Overview of Switzerland and the neighboring border regions. Orography is shown in relief and major mountain chains are labeled. The circle shows the 100-km detection range of the ETH radar located at H nggerberg, Zurich, that designs the study area. Stars mark locations of lightning receivers of the Swiss LPATS and the cross indicates the sounding station of Payerne. Squares mark positions of SMI radars and the rectangle over Northern Switzerland designs the area determined for evaluation of CG stroke detection efficiencies from the LPATS of Switzerland and South Germany.

## 4.4 Method and Data Correction

Methods of hail cell assessment, the calculation of hail kinetic energy and the cell-related attribution of CG lightning strokes are described below and illustrated (Figs. 4.2 and 4.3). Correction methods of non-accurate radar measurements and lightning records are given thereafter. Individual hail cells are distinguished according to the date and initial time (UTC) of occurrence and are listed in Table 4.1.

### 4.4.1 Radar and Lightning Data Analyzes Method

From 5-min sector-volume scans performed with the ETH radar, CAPPIs are calculated on two standard levels: (1) at 2 km above the daily 0 C isotherm (typically around 3-4 km MSL in summer) where hailstones grow and (2) at low storm level on 1.5 km MSL (0.9 km above radar) close to the surface where hailfall occurs. For every time step, the location of radar

elements with reflectivities  $\geq 30\text{dBZ}$  around the cell core are selected from displayed CAPPIs. Within that area, the half distance between the maximal distant 30dBZ signatures (in the west-east and north-south extension) are taken to determine the mean radius of a circle that is centered on the core echo and contains reflectivities  $\geq 30\text{dBZ}$  (Fig. 4.2). This method is similar to other studies where the 30dBZ area was shown to contain a majority of CG lightning locations (e.g., Reap and MacGorman, 1989; Holle et al., 1994; Petersen et al., 1996), but is unique in that changes in cell evolution are respected. Different cells on the same CAPPI are easily distinguishable and the cell with the most intensive echo has been assessed. The splitting of one cell into two or more cells and the opposite case, the merger of two or more cells into one cell, are treated as one cell. Only in one case where two cells developed close to each other and merged shortly to continue as two individual cells, both cells (9208211508 and 9208211513 in Table 4.1) were assessed individually (including the case of merging and the splitting into two new cells) and have been considered as one large cell (9208211453 in Table 4.1) before the merger, following the more intense cell thereafter.

The hail kinetic energy is calculated from CAPPI reflectivities captured within the encircled 30dBZ cell area, using the relation between the radar reflectivity factor  $Z$  ( $\text{mm}^6\text{m}^{-3}$ ) and the vertical flux of the kinetic energy  $\dot{E}$  (at a particular point) given in Waldvogel et al. (1978a) as:

$$\dot{E} = 5 \cdot 10^{-6} \cdot Z^{0.84} \quad [\text{Jm}^{-2}\text{s}^{-1}] \quad (4.1)$$

To obtain the entire hail kinetic energy of each time step, the flux of  $\dot{E}$  is integrated over the considered time interval (here, 5 min) and the area with reflectivities indicating a hail signal:

$$E_{\text{KIN}} = \int_{t_0}^{t_1} \int_{s_0}^{s_1} \dot{E}(x, y, t) dx dy dt \quad [\text{GJ}] \quad (4.2)$$

Integrated over the total storm area ( $s_{\text{TOTAL}}$ ) and duration ( $t_{\text{TOTAL}}$ ), the total amount of hail kinetic energy ( $E_{\text{KINTOT}}$ ) is calculated. Different attribution methods of hail signals to reflectivities larger than a certain dBZ threshold are discussed in Waldvogel et al. (1980). In this study, the “cutting method” is used, i.e., all reflectivity values  $> 55\text{dBZ}$  are attributed to hail and those  $\leq 55\text{dBZ}$  to rain. Comparisons between radar measurements and hailpad data have shown that this threshold lead to good results for hailfalls that produce considerable damage to crops (Schiesser, 1990).

Lightning counts were performed, overlying the encircled cell areas on the 1.5-km level CAPPI with daily CG stroke locations from the Swiss and South German LPATSS. Lightning strokes were distinguished according to their polarity into  $-CG$  and  $+CG$  strokes and summed up over 5-min intervals; i.e., 2.5 min before and after the moment the sector-volume scan was completed. The temporal evolution of hail kinetic energy and CG stroke rates per time step (5 min) are shown in Fig. 4.3 for two different hail cells. Absolute 5-min maxima of hail kinetic energy ( $E_{\text{KINMAX}}$ ) and CG stroke rates ( $\pm CG_{\text{MAX}}$ ) were determined and the time that elapsed between  $E_{\text{KINMAX}}$  and  $\pm CG_{\text{MAX}}$  calculated.

**Table 4.1.** Overview of investigated hail cells (total 41) and rain cells (total 5) between 1992-1995.

Storm	Time	Cell Type	Super Cell	Duration	Distance	Direction	Speed	Ekintot	Ekimax	Ekinpix	Atot55	-CGTOT	+CGTOT	DECELL	HAIL
[Date]	[UTC]			[min]	[km]	[°]	[ms <sup>-1</sup> ]	[GJ]	GJ/5min	Jm <sup>-2</sup>	[km <sup>2</sup> ]	total	total	[%]	damage reported
920601	1138-1218	isolated		40	14.7	203	6	2.1	0.17	199	73	2	0	32	11
	1828-1953	isolated large		85	50.7	217	11	55.9 †	1.85 †	480 †	1525	423	7	32	21
920721	1333-1523	isolated	x	110	52.8	210	7	93.9	1.72	1016	2603	203	42 *	35	14
	1433-1548	isolated		75	56.4	222	11	76.5 †	2.00 †	601 †	2424	356 *	27 *	35	53
	1533-1613	isolated		40	29.4	207	11	43.4	1.82	526	1232	221 *	55 *	35	5
	1648-1818	line	x	90	65.4	227	12	81.8	2.50	426	1004	469	209	35	31
920729	1643-1838	isolated		115	85.2	226	8	40.1	1.14	1555	1052	99	95	41	0
920803	1333-1448	isolated		75	58.4	221	12	8.8	0.36	241	401	78	8	47	42
	1813-1938	isolated		85	53.3	201	12	64.3 †	2.22 †	787 †	1334	383	60	47	38
920821	1453-1743	isolated large	x	170	142.9	190	13	371.7 †	5.97 †	1405 †	10822	2026	170	31	10
	1513-1718	isolated large	x	125	98.9	189	12	286.8 †	5.57 †	1328 †	7976	1158	130	31	10
	1508-1708	isolated large	x	120	119.3	190	15	235.8 †	5.12 †	1363 †	6324	1103	83	31	10
930519	1523-1723	isolated		120	34.6	211	6	129.6 †	2.59 †	1222 †	4284	313	65	15	13
	1758-1913	isolated		75	31.0	244	7	40.9	1.07	972	1690	133	5	15	40
930520	1203-1408	isolated		125	65.3	241	8	75.2	1.66	1069	2438	248	17	18	22
930526	1503-1638	isolated		95	50.2	219	8	63.8 †	2.14 †	578 †	2345	224	116	36	25
930705	1339-1439	isolated	x	60	47.2	195	14	57.8	1.91	546	1933	296 *	74 *	218	20
	1429-1554	isolated	x	85	71.8	178	16	89.7	2.03	612	2942	387 *	43 *	218	56
	1624-1734	isolated	x	70	76.3	214	17	31.3 †	1.16 †	448 †	837	160 *	40 *	218	10
930730	1509-1634	isolated		85	71.1	222	14	47.1	1.75	544	1409	202	106	48	19
930805	1438-1533	isolated		55	28.1	208	9	19.6	0.78	438	717	29 *	6 *	75	225
	1543-1653	isolated		70	54.2	206	12	46.3	1.92	692	1419	190 *	8 *	75	124
	1743-1908	isolated		85	50.3	207	9	23.1	0.78	520	751	59 *	15 *	75	77
930822	1648-1758	group		70	93.5	213	21	72.2 †	2.90 †	268 †	2617	396	256	92	108
940517	1323-1503	isolated		100	59.6	214	9	30.5	0.65	617	1261	6	0	36	25
	1618-1728	isolated		70	43.1	226	7	4.5 †	0.37 †	376 †	236	63	18	36	29
	1903-2118	isolated large	x	135	121.3	211	14	75.1	1.82	477	1849	648	88	36	16
940602	1653-1913	isolated large	x	140	218.4	215	23	127.9	2.80	326	5107	606	240	84	55
940608	1158-1253	isolated		55	38.0	232	7	6.9	0.33	356	285	1	1	30	0
	1603-1713	isolated		70	65.2	214	13	5.6	0.17	135	275	32	11	30	0
940704	1408-1538	isolated		90	38.5	225	6	0.4	0.04	67	24	0	0	71	0
	1548-1658	group		70	37.8	183	8	9.4	0.58	195	486	86	50	71	1
	1943-2108	group		85	44.0	197	7	19.4	0.60	573	685	33	0	71	68
940706	1538-1718	group		100	43.0	236	7	33.7	0.95	738	972	71	18	74	109
940718	1218-1333	isolated		75	62.8	199	10	19.7	0.73	453	554	47	10	94	86
940731	1143-1308	isolated		85	47.1	234	5	31.9	0.81	928	1122	15	12	94	146
940806	1413-1523	isolated		70	22.1	270	4	10.8	0.47	422	488	42	33	234	6
	1553-1723	isolated		90	21.8	234	4	96.7	2.04	1809	2563	430 *	108 *	234	981
	1823-1938	isolated		75	37.1	224	4	66.6 †	2.33 †	1084 †	2277	271 *	68 *	234	2557
940810	1208-1353	isolated	x	105	89.9	209	14	87.8	2.10	520	2431	196	56	22	1
950722	1403-1558	line	x	115	124.6	219	17	111.2 †	2.81 †	412 †	7454	280	316	6	4
Rain Cells															
920526	1053-1153	isolated		60	25.8	203	7	0		0	0	0	0	36	11
920601	1228-1323	isolated		55	22.1	189	7	0		0	0	6	0	32	10
	1233-1323	isolated		50	18.9	224	6	0		0	0	0	0	32	15
930803	1218-1258	isolated		40	14.7	196	6	0.2		12	2	0	0	28	32
940629	1238-1338	isolated		60	34.0	210	10	0.3		23	1	0	0	34	43

♦ Correction of length of either radar or CG stroke data

† Extrapolation of kinetic hail energy at the lower storm-level

\* Estimation of the total CG stroke rate according to detection efficiencies from both LPATS used

- Missing values

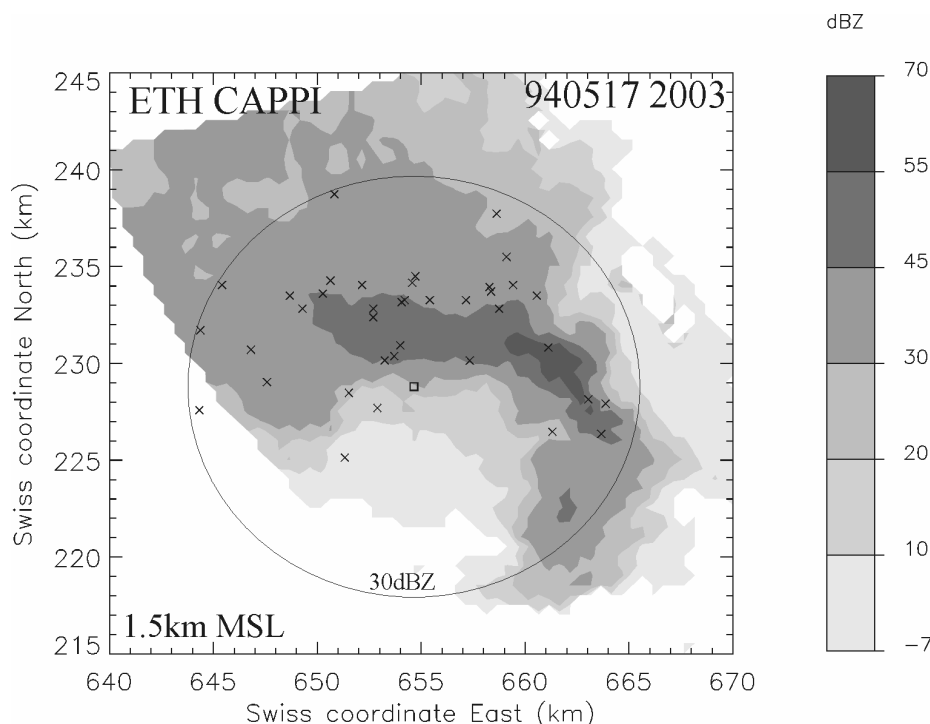


**Figure 4.2.** CAPPI at low storm-level (1.5 km MSL) derived from the ETH radar with radar reflectivities (grey shades) and CG stroke locations (crosses) of a hail cell observed on 17 May 1994 at 2003 UTC. Areas of reflectivities  $> 55\text{dBZ}$  (darkest shades) are attributed to hailfall. The extent of the hail cell is approximated by a circle of a mean radius determined from maximally distant locations of  $30\text{dBZ}$  reflectivities.

Integrated over the time of convective activity, the total numbers of CG strokes ( $\text{CG}_{\text{TOT}}$ ) and  $\pm\text{CG}_{\text{TOT}}$  are obtained and allow comparison with the total amount of hail kinetic energy ( $E_{\text{KINTOT}}$ ). Spatial maxima of hail kinetic energy ( $E_{\text{KINPIX}}$ ) are calculated by integration per radar element ( $0.5 \times 0.5 \text{ km}$ ). Similarly, the spatial maxima of CG strokes ( $\pm\text{CG}_{\text{PIX}}$ ) per four radar elements ( $1 \times 1 \text{ km}$ ) are derived and the distances between  $E_{\text{KINPIX}}$  and  $\pm\text{CG}_{\text{PIX}}$  determined. In the following,  $E_{\text{KINTOT}}$  is taken as a measure for storm intensity and  $E_{\text{KINMAX}}$  (temporal peak) as well as  $E_{\text{KINPIX}}$  (spatial peak) associated to maximally expected hailfall, based on the good agreement between maximal values of hail kinetic energy and maximal hail damage on crops (Wojtiw and Ewing, 1986; Schiesser, 1990).

#### 4.4.2 Data Correction Methods

In a statistical analysis, it is important to obtain as many accurate sample pairs as possible. Since both radar and CG stroke measurements show obvious inaccuracies, some data were corrected in order to improve the data base; Table 4.2 gives an overview of corrected and non-corrected data.

Three different types of corrections were applied on the data: (1) The use of radar to measure convective cells over mountainous regions has some limitations such as inadequate radar reflectivity measurements at low levels due to shielding of the radar beam by the topography or attenuation by strong precipitation systems. Several storms analyzed in this study moved

over mountainous areas and low-level CAPPIs show significantly smaller precipitation areas than CAPPIs at higher levels. Schmid and Waldvogel (1986) dealt with this problem and investigated S-Band radar measurements of 154 severe convective cells in Switzerland, establishing a radar profile that allows extrapolation of radar reflectivities on ground level from measurements aloft. After several pre-studies, the profile was found to be applicable on C-Band radar reflectivities and used here to correct attenuated low-level reflectivities. (2) Since sector-volume scans are performed on real-time by an operator, measurements are occasionally not complete, especially when several severe cells develop simultaneously over a large area. When either the beginning and/or end of a cell has not been measured, the hail kinetic energy values were derived from PPIs of the same cell and estimated thereafter for the missing time steps. Coordinates of missing circles were estimated in the same way and CG stroke counts performed thereafter. (3) Inaccuracies in CG lightning measurements with LPATS occur with desensitized receivers during periods of high CG lightning activity and entire system breakdowns (Rubinstein and Montandon, 1996).

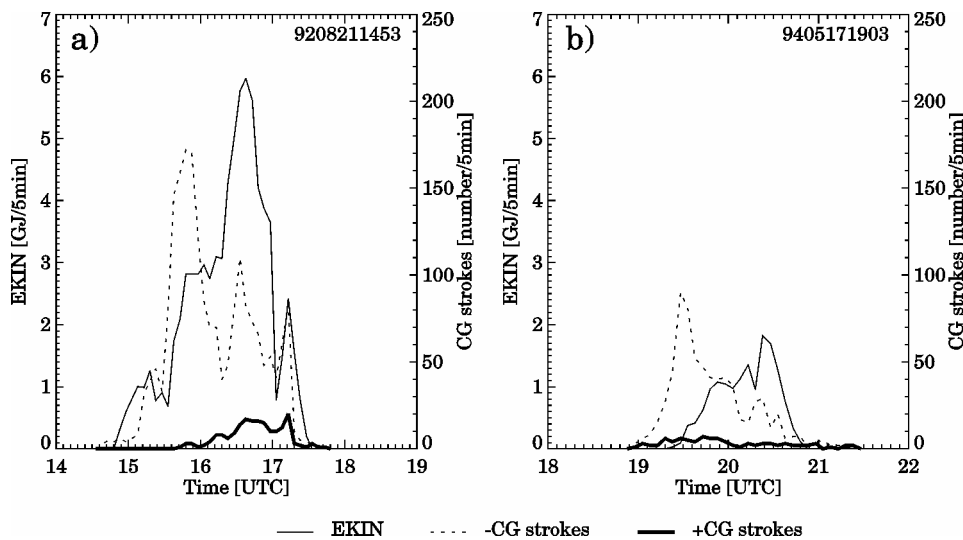


**Figure 4.3.** Temporal evolution of hail kinetic energy (EKIN) at low storm level (1.5 km MSL) relative to -CG strokes and +CG strokes for two large isolated supercell storms: a) observed on 21 August 1992 and b) on 17 May 1994. Values are given in 5-min intervals and the same Y scales are used in both figures.

Compared to the Swiss LPATS, the South German network shows an average daily stroke detection efficiency ( $DE_{DAY}$ ) of 45% and a cell-related detection efficiency ( $DE_{CELL}$ ) of 36% within the area designed for network performance comparison (Fig. 4.1). For eight storms,  $DE_{DAY}$  and/or  $DE_{CELL}$  are significantly higher (Table 4.1) which goes back to system breakdowns of the Swiss LPATS in the range of several minutes (up to 30 min), relevant from status receiver reports. In these situations, CG stroke counts were corrected, using the average  $DE_{DAY}$  and initially measured proportions of  $DE_{CELL}$  ratios. For three other storms that occurred on the same day (9207211333, 9207211433 and 9207211533 in Table 4.1), non-

accurate CG stroke rates were corrected according to likely detection efficiency values given in Montandon (1992).

**Table 4.2.** Overview of data with corrections.

Total	Corrections							
	none	Radar				Lightning		
		none	extrapolation	length	both	estimated	length	both
41	19	25	13	4	1	11	4	2

## 4.5 Results

Hail cells are first compared on storm scale and variables of interest briefly described. The relation between the hail kinetic energy aloft and close to ground is presented thereafter. In the following, correspondences between hail kinetic energy and total CG stroke rates are given and temporal-spatial relationships between  $\pm$ CG stroke peaks and maximally expected hailfall presented. Table 4.1 gives an overview of investigated hail and rain cells and Table 4.3 summarizes the major relationships between the main variables.

### 4.5.1 Storm Scale Analyzes

All hail cells occurred during the hail season in Switzerland, typically lasting from May to September (Schiesser et al., 1997), and were initiated around mid-day (first cell 1138) and the early evening (last cell 1943) with a maximum of occurrence (11 cases) around 1500 (Table 4.1). The average storm duration is around 88 min, during which a medium distance of 63 km was covered. Most of the hail cells entered the study area from south, south-west or west with an average propagation direction from 210°.

In this study, hail cells were classified according to the type of cell organization within a larger storm context into: (1) 29 isolated cells; (2) six large isolated cells (dimension of precipitation area > 100 km during mature storm phase); (3) four cells embedded in a group organization (bounded 40dBZ region contains more than one cell with peak echoes > 47dBZ over the mature phase of storm development; Schiesser et al., 1995) and (4) two cells in a line organization (two or more cells are more or less perpendicular arranged to the direction of storm movement with a length-to-width ratio around 3:1; Schiesser et al., 1995). A total of 12 hail cells (Table 4.1) were classified as being supercells according to a previous investigation by Schiesser et al. (1997) including the present data. Reports from the Swiss Hail Insurance show that 34 cells initiated hail damage to agriculture in at least one Swiss community lying in the storm track (Table 4.1). For some hail cells, newspaper reports are available describing the initiated storm and hail damages with occasional information on maximal hailstone sizes found on ground. Maximal hailstone diameters range for the reported cases from 2 cm (one case), 3 cm (two cases), 4 cm (one case) up to 5 cm (five cases) as indicated in Table 4.1. For

5 cells, hail damage on agriculture have not been reported and damage information is missing for two cells: one moved over German territory and one cell propagated entirely over mountainous area with few or no insured agricultural values (missing values in Table 4.1).

Besides, a weak relationship appears between the type of cell organization and the velocity of cell movement: velocities generally increase from isolated ( $66\% \leq 11\text{ms}^{-1}$ ) to large isolated cells ( $\geq 11\text{ms}^{-1}$ ) and cells organized in lines ( $\geq 11\text{ms}^{-1}$ ).

#### 4.5.2 Hail Kinetic Energy at Upper and Lower Storm-Level

The total amount of hail kinetic energy ( $E_{\text{KINTOT}}$ ) at upper (2 km above daily  $0^\circ\text{C}$  isotherm) and lower storm level (1.5 km MSL) are in good linear agreement (correlation coefficient of 0.95).  $E_{\text{KINTOT}}$  at low level is about twice as high as at upper level, due to the melting of frozen water, graupel and hailstones (wet surfaces) below the  $0^\circ\text{C}$  isotherm producing higher radar reflectivities at lower level. Lag times between maxima of hail kinetic energy ( $E_{\text{KINMAX}}$ ) aloft and lower level increase non-proportionally (square-root function) with storm intensity ( $E_{\text{KINTOT}}$ ), ranging from 5 to 30 min with an average of 12 min. This finding supports the fact that strong and long-lasting updraft regions increase with storm intensity ( $E_{\text{KINTOT}}$ ) and generate larger hailstones (higher radar reflectivities and hail kinetic energy) that remain longer at upper storm level until they fall out and reach ground (temporally delayed  $E_{\text{KINMAX}}$ ). In agreement with findings of prior studies (e.g., Schiesser, 1990),  $E_{\text{KINTOT}}$  corresponds with maximal values of hail kinetic energy ( $E_{\text{KINMAX}}$  and  $E_{\text{KINPIX}}$  in Table 4.3), radar reflectivity surfaces (e.g.,  $\geq 30\text{dBZ}$ ,  $\geq 45\text{dBZ}$  and  $\geq 55\text{dBZ}$  in Table 4.3) and maximal height of radar echo volumes (e.g.,  $20\text{dBZ}$  and  $45\text{dBZ}$  in Table 4.3).

#### 4.5.3 Total Hail Kinetic Energy vs. Total CG Stroke Rates

Differences in ratios of –CG and +CG flashes are in the literature often associated with specific storm types (for review: see MacGorman and Rust, 1998). In the present data, +CG stroke ratios consist on the average of: (1) 21% for isolated cells showing lowest absolute +CG and –CG stroke rates; (2) 11% for large isolated; (3) 24% for cells organized in groups and (4) 42% for cells in line structures with one case (9507221403) where +CG strokes dominate with 53%. These proportions are similar to ratios found in other studies: e.g., Knapp (1994) revealed that 202 out of 264 tornadic storms produced less than 30% +CG flashes. In some studies, supercell storms were found to generate a majority of +CG lightning (e.g., MacGorman and Burgess, 1994; Carey and Rutledge, 1998), which was relevant in the present data for one supercell storm organized in a line (9507221403 in Table 4.1). In the following, –CG and +CG stroke counts are treated separately in relation to the hail kinetic energy:

(1) The total amount of –CG strokes ( $-\text{CG}_{\text{TOT}}$ ) increases linear with  $E_{\text{KINTOT}}$ . If all hail cells (the three most intensive hail cells are omitted), a significant correlation coefficient of 0.95

(0.79) results (Fig. 4.4a). A large majority (93%) of the hail cells produced less than 700 –CG strokes and 150 GJ, whereas the three most intensive hail cells reveal 1100-2000 –CG strokes and 230-370 GJ of hail kinetic energy. Most isolated cells (90%) and 75% of cells within a group organization are below threshold values of 250 –CG strokes and 50 GJ, while all large isolated cells and cells organized in lines are above that threshold. Supercells were identified above 160 –CG strokes and 31 GJ and consist half of the hail cells above these values; most (83%) supercells contain more than 200 –CG strokes and 58 GJ. The high correlation between –CG<sub>TOT</sub> and E<sub>KINTOT</sub> implies a linear agreement between –CG<sub>TOT</sub> and total reflectivity surfaces  $\geq 55$  dBZ (A<sub>TOT55</sub> in Table 4.1) with a linear correlation coefficient of 0.86, surfaces  $\geq 45$  dBZ (0.77) and areas  $\geq 30$  dBZ (0.74). Weakest hail cells (e.g., 9206011138 or 9407041408) and rain cells (Table 4.1) reveal low or no –CG<sub>TOT</sub> and E<sub>KINTOT</sub>; however, a fixed limit in terms of hail kinetic energy and –CG stroke rates could not be determined.

**Table 4.3.** Overview of correlations between E<sub>KINTOT</sub> and important variables

	Max. dBZ Height		dBZ Surfaces			Hail Kinetic Energy			CG Strokes			Temporal Relation		Spatial Relation	
	20 dBZ	45 dBZ	$\geq 30$ dBZ	$\geq 45$ dBZ	$\geq 55$ dBZ	E <sub>KINTOT</sub> aloft	E <sub>KINMAX</sub> 1.5km	E <sub>KINPIX</sub> 1.5km	CG <sub>TOT</sub>	-CG <sub>TOT</sub>	+CG <sub>TOT</sub>	-CG	+CG	-CG	+CG
E <sub>KINTOT</sub> 1.5km MSL	0.56	0.63	0.74	0.77	0.86	0.95	0.94	0.64	0.95	0.95 <sup>a</sup> 0.79 <sup>b</sup>	-	0.88	-	0.84	-

<sup>a</sup> Linear correlation with all data (41 cases)

<sup>b</sup> Linear correlation without the three strongest hail cells (38 cases)

(2) +CG stroke counts show no consistent relationship with storm intensity (E<sub>KINTOT</sub>) as shown in Fig. 4.4b. Although +CG stroke rates of cells organized in groups and lines tend to increase more rapidly with E<sub>KINTOT</sub> than large isolated cells, reasons for such disparities cannot successfully be explained by different types of cell organization. Supercells contain more than 40 +CG strokes and 31 GJ hail kinetic energy and reveal some 55% of the cells above that threshold. (3) Peaks in –CG stroke rates (5-min values) are more pronounced and occur generally prior to the more broad peaks of +CG strokes (Fig. 4.3a,b).

#### 4.5.4 Temporal-Spatial Relation between Hail Kinetic Energy and CG Stroke Rates

Temporal (lag times between E<sub>KINMAX</sub> and  $\pm$ CG<sub>MAX</sub>) and spatial behaviors (lag distances between E<sub>KINPIX</sub> and  $\pm$ CG<sub>PIX</sub>) are examined in the following. Both, lag times and distances were calculated at low storm level from non-corrected lightning counts; in total 29 hail cells were retained in relation to –CG and 26 cases for +CG strokes. Temporal and spatial locations of CG stroke rates are referred to the location of hail kinetic energy peaks; i.e., lag times and lag distances are in Figs. 4.5-4.7 positive (negative) if  $\pm$ CG stroke peaks occur before (after) the maximally expected hailfall (maxima in hail kinetic energy), and zero at temporal and spatial correspondence.



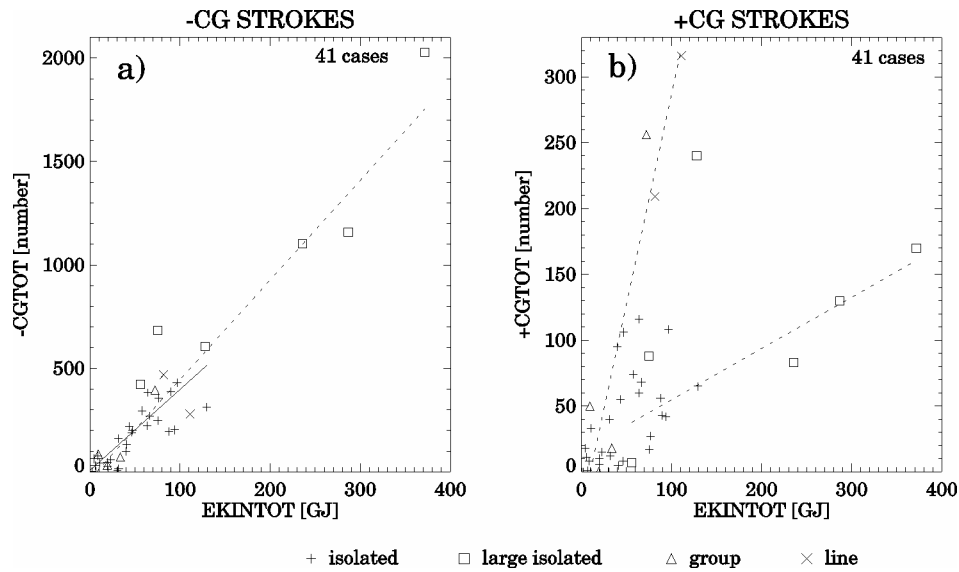


**Figure 4.4.** a) Relationship between the total amounts of hail kinetic energy (EKINTOT) at low storm-level (1.5 km MSL) and totals of –CG strokes (–CGTOT) with the dashed (solid) line indicating the linear regression of all cases (38 cases) with a correlation coefficient  $r = 0.95$  ( $r = 0.79$ ) significantly different from zero at the 1% level. b) Relationship between EKINTOT and +CGTOT with dashed lines indicating trends for large isolated cells (five out of six cases) and cells organized in groups and lines (six cases). Data points are stratified according to the type of cell organization.

For –CG strokes, storm intensity ( $E_{\text{KINTOT}}$ ) is a good function of the lag time (Fig. 4.5a) and is best described by a square-root function (correlation coefficient of 0.88). In the majority of hail cells (90%), –CG stroke rates peaked on average 26 min before the maxima of hail kinetic energy (positive values in Fig. 4.5a) and occurred only in one case 10 min after maximally expected hailfall (negative values). Stratified according to the type of cell organization, lag times range for isolated cells from 0 to 35 min (average 17 min), 0–25 min (10 min) for cells in groups, 25–35 min (30 min) for cells organized in lines and from 25 to 65 min (52 min) for large isolated cells. The good correlation between  $E_{\text{KINTOT}}$  and the lag times indicates a relation between dynamic mechanisms in the cell core and –CG lightning generation, a finding that results also if highest spatial –CG stroke rates are linked to maxima of hail kinetic energy ( $E_{\text{KINPIX}}$ ).

The lag distance, i.e., the gap that is covered from the area of maximal –CG stroke rates to  $E_{\text{KINPIX}}$ , is in good nonlinear (square-root function) correspondence (correlation coefficient of 0.84) with  $E_{\text{KINTOT}}$  (Fig. 4.5b). The data reveal in 66% hail cells that –CG strokes peaked 3–38 km (average 19 km) prior to  $E_{\text{KINPIX}}$ . On the other hand, in 34% of the cases (with on exception only weak isolated cells), –CG strokes were maximal between 1 and 18 km (average 8 km) after  $E_{\text{KINPIX}}$  was reached (negative values in Fig. 4.5b). Seen in a temporal-spatial context (Fig. 4.7a), it appears that two-thirds of the hail cells (including all large isolated and cells organized in lines) produced highest –CG stroke rates temporally and spatially before maximally expected hailfall whereas only one hail cell showed the opposite

case. In some isolated cells,  $-CG$  stroke maxima temporally preceded but spatially followed the peak in hail kinetic energy.

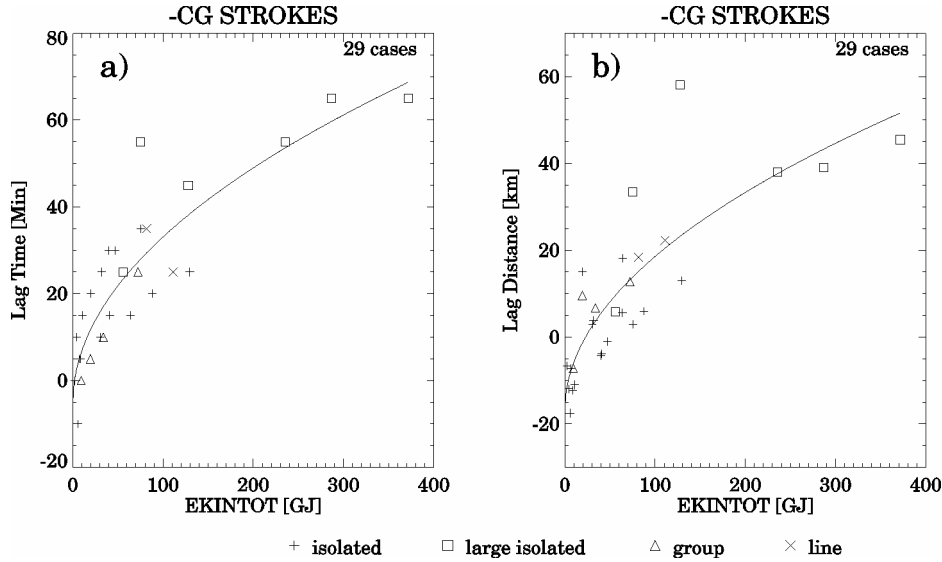


**Figure 4.5.** Relationship between total amounts of hail kinetic energy ( $E_{KINTOT}$ ) at low storm-level (1.5 km MSL) and  $-CG$  strokes for: a) lag times calculated between  $E_{KINMAX}$  and  $-CG_{MAX}$  (29 cases) with nonlinear (square-root function, solid line) correlation coefficient  $r = 0.88$  and b) the lag distances calculated from  $E_{KINPIX}$  and  $-CG_{PIX}$  (29 cases) with nonlinear (square-root function, solid line) correlation coefficient  $r = 0.84$ . Data points are stratified according to the type of cell organization.

Lag times between peaks in  $+CG$  stroke rates and maximally expected hailfall are in no direct correspondence with  $E_{KINTOT}$  (Fig. 4.6a). In 69% of the cases,  $+CG$  stroke peaks occurred on the average 22 min (5-60 min) before and in 27% 18 min (5-30 min) after the maxima in energy. Lag times increase with  $E_{KINTOT}$  for most types of cell organization but decreases for large isolated cells. Similar tendencies are also relevant from comparisons between lag distances and  $E_{KINTOT}$  (Fig. 4.6b): in 62% of the hail cells, maximal  $+CG$  stroke rates occurred on the average 14 km (3-37 km) prior and in 38% on the average 20 km (4-45 km) following maximally expected hailfall. Large isolated cells reveal a special case: while storm intensity ( $E_{KINTOT}$ ) increases,  $+CG$  stroke rates peak increasingly after maxima of hail kinetic energy. Figure 4.7b shows the temporal-spatial behavior of  $+CG$  stroke rates: (1) isolated cells show tendencies for  $+CG$  stroke rates to peak (temporally and spatially) before or after the maximal hail kinetic energy; (2) cells organized in groups and lines show no clear trend; (3) weak large isolated cells show temporal-spatial peaks prior to maximal energy and (4) highest  $+CG$  stroke rates peak for stronger large isolated cells following maxima in hail kinetic energy.

The results reveal differences in the temporal-spatial evolution of  $\pm CG$  strokes, discussed in the next section in terms of different microphysical and dynamical processes in the updraft cores depending storm intensity.

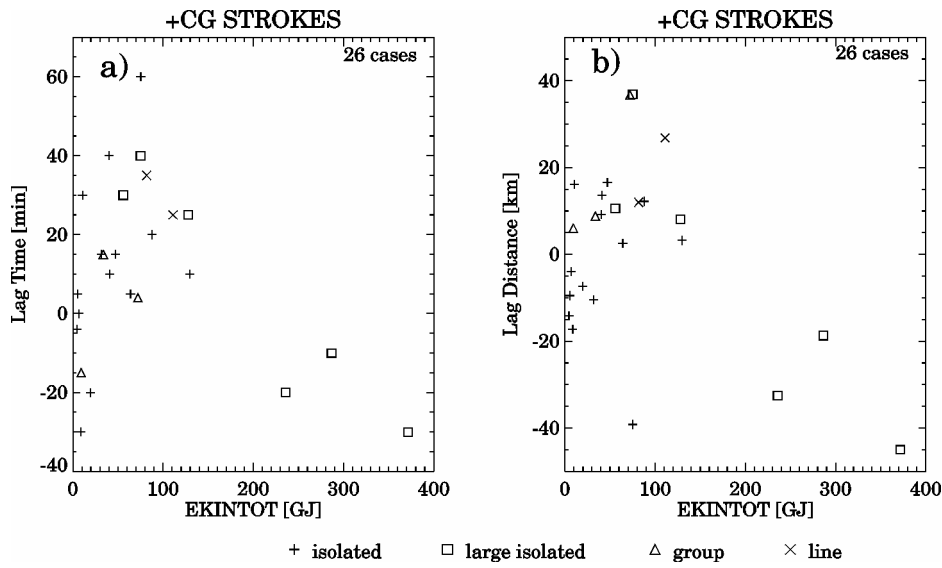


**Figure 4.6.** same as Fig. 4.5 but for +CG strokes (26 cases); no correlations were calculated.

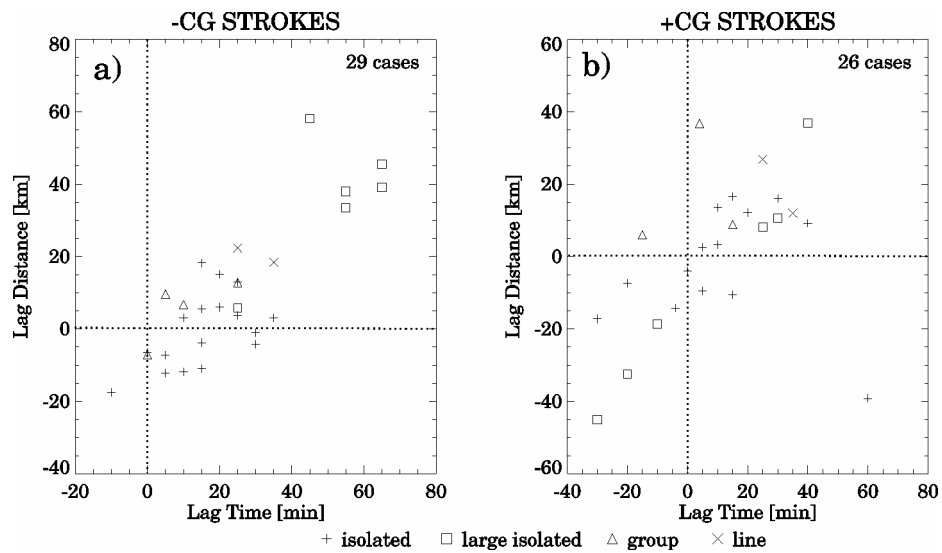


**Figure 4.7.** Temporal-spatial correspondences between lag times and lag distances for a) –CG strokes (29 cases) and b) +CG strokes (26 cases). Positive (negative) values of lag times and lag distances reveal that highest  $\pm$ CG stroke rates occurred before (after) peaks of hail kinetic energy. Data points are stratified according to the type of cell organization.

## 4.6 Discussion

The 41 examined hail cells have revealed some interesting relationships between storm intensity, CG stroke totals and temporal as well as spatial locations of highest CG stroke rates in relation to maximally expected hailfall (peaks of hail kinetic energy). In the following, key findings are briefly discussed and put in a common context:

1. Storm intensity, defined here through the total amount of hail kinetic energy ( $E_{KINTOT}$ ), shows dependence on dynamical processes in the thundercloud: as convective depth (maximal altitude of 20dBZ and 45dBZ) increases, an increase of (1) maximal reflectivity, (2)  $E_{KINMAX}$ , (3) lag times between  $E_{KINMAX}$  aloft (2 km above 0°C isotherm) and at low storm level (1.5 km MSL) and (4) maximally expected hailfall ( $E_{KINPIX}$ ) occurs. Several studies reveal that since strong convective regions have by definition strong updrafts and high reflectivity echoes produced by large numbers of hydrometeors aloft, enhanced graupel-ice collisions aloft are favorable for the production of lightning in the most active region of convective storms (e.g., Reap and MacGorman, 1989; Holle et al., 1994; Petersen et al., 1996). The comparison of CG stroke activity and hail kinetic energy in the core region of the present hail cells showed that –CG stroke rates increase linear to storm intensity ( $E_{KINTOT}$ ) whereas no coherent relationship is found between +CG stroke rates, which cannot fully be explained through stratification of different types of cell organization. The increase of CG lightning activity (shown here for  $CG_{TOT}$  and  $-CG_{TOT}$ ) with storm height and radar reflectivity surfaces has been shown e.g., in Keighton et al. (1991) and Watson et al. (1995).
2. Convective strength and storm intensity are thought to play an important role in the determination of locations of highest  $\pm$ CG stroke rates relative to maximally expected hailfall. Major differences were found between temporal-spatial evolution of –CG and +CG strokes. Since only a few other studies examined the temporal-spatial relation between CG lightning activity and maximal hailfall, the present results can only conditionally be compared, partly as different lightning detection techniques were used. Changnon (1992) noticed in 48 cases that –CG flashes began typically around 10 min (2–21 min) before first hail, increased until hail damage began and decreased during hailfall to end around 8 min after last hail damage. The examined hailstorms were non-supercell storms and probably of weak intensity as only –CG flashes (often associated with non-severe storms) were recorded and maximal hail damage to crops was limited to small areas. Some agreement is found between the storms analyzed by Changnon (1992) and weak hail cells ( $E_{KINTOT} < 30$  GJ) of this study, where –CG strokes peaked on the average 6 min before and 5 km after maximally expected hailfall. Analyzing severe storms that formed near a dryline in Oklahoma, Shafer (1990) found that the location of high densities of –CG flashes occurred roughly with the location of large hail reports and high values of vertically integrated liquid water (VIL). However, Carey and Rutledge (1996) noticed that the maximal number of –CG flashes immediately followed the peak in large hail in non-severe thunderstorms, a finding that was confirmed in a later study (Carey and Rutledge, 1998) for a supercell storm that was dominated by +CG flashes. The present results are in disagreement with Carey and Rutledge (1996, 1998) since –CG stroke rates preceded maximally expected hailfall in 38 out of 41 hail cells (including large isolated supercells, e.g., 9208211453 in Fig. 4.3a).

Some studies reveal that +CG flash rates of severe thunderstorms are in close relation to hailfall. Carey and Rutledge (1995) analyzed a severe multicell storm that produced large hail and noticed that +CG flash rates increased 5-10 min before large hail was detected. This is in agreement with the present data, although +CG strokes peaked in the majority of severe non-supercell storms 19 min prior to maximal expected hailfall. In a further study, Carey and Rutledge (1998) examined two supercell storms that showed highest +CG flash rates 20-35 min after a majority of large hailstones ( $\geq 2\text{cm}$ ) reached ground. This finding is partly in coherence with the present finding in that highest +CG stroke rates occurred on the average 20 min after maximal energy in the three most intensive large isolated supercell storms (e.g. 9208211453 in Fig. 4.3a), but is, however, non-consistent with five weaker supercells showing highest +CG rates on the average 30 min prior to maximally expected hailfall.

3. Although the present data set is by far not large enough for explaining the behavior of maximal CG lightning rates in relation to hailfall, a few interpretations are justified. The present results, particularly the close link between temporal-spatial locations of –CG stroke peaks relative to maximally expected hailfall, supports the hypothesis of many investigators that convective updrafts are favorable for the production of lightning through non-inductive graupel-ice interactions aloft (e.g., Jayaratne et al., 1983; Williams 1989; Baker and Dash, 1994); other important processes that lead beside non-inductive graupel-ice interactions to electrification are discussed e.g., in Stolzenburg et al. (1998). In severe convective thunderstorms, graupel and hailstones grow aloft through aggregation of supercooled water droplets and are thought to gain negative charge (while ice crystals charge positively) in the mixed-phase region at temperatures from  $-10^{\circ}\text{C}$  to  $-20^{\circ}\text{C}$  (e.g., Jayaratne et al., 1983; Keith and Saunders, 1990), forming the main negative charge region aloft. The dimensions and velocities of vertical updrafts are thought to determine the intensity and timing of electrification (e.g., Solomon and Baker, 1994); as a result, –CG flashes were often found inside or near reflectivity cores (within 20dBZ and 30dBZ contours). The present findings support these hypothesis since temporal-spatial locations of –CG lightning rates relative to maximal hail kinetic energy, increase with storm intensity ( $E_{\text{KINTOT}}$ ): strong vertical updrafts must enhance non-inductive graupel-ice collisions aloft, generate more elevated –CG lightning rates and as the particles remain longer in the updraft cores until descent, lag times and lag distances between –CG stroke peaks and maximal hailfall increase in relative consistence with the type of cell organization. On the other hand, it has been hypothesized (e.g., MacGorman and Burgess, 1994; Carey and Rutledge, 1998) that when graupel and hailstones descend in regions with temperatures warmer than  $0^{\circ}\text{C}$  to  $-10^{\circ}\text{C}$ , they can obtain positive charge (while ice crystals charge negatively) resulting in the formation of a lower positive charge center and be one of the reasons why +CG discharges can dominated –CG lightning rates. The evolution between first elevated –CG stroke rates in developing severe storms and increasing +CG lightning activity during mature storm phase (when graupel and

hailstones descend to middle and low storm level) seems to be confirmed in most of the present data (e.g., Fig. 4.3a,b), since +CG stroke peaks generally occur closer to temporal and spatial maxima of expected hailfall than –CG stroke peaks. However, the fact that equally intense supercell and non-supercell storms show temporal and spatial peaks in +CG stroke rates both, before and after maximal hailfall (Fig. 4.6a,b), cannot be explained in this way and remains speculative. From more comprehensive studies with extensive storm data, we would expect a close relationship between mean updraft velocities (not quantifiable for the present data) and locations of temporal-spatial CG lightning peaks relative to maximal hailfall.

## 4.7 Conclusion

First of its kind, the present study examined temporal-spatial relationships between  $\pm$ CG stroke peaks and maximal hailfall for 41 hail cells with the following results:

- As shown in prior studies, the total amount of hail kinetic energy ( $E_{\text{KINTOT}}$ ) is a good parameter of storm intensity.
- $E_{\text{KINTOT}}$  shows good linear correspondence with totals of –CG stroke counts (correlation coefficient of 0.95) but reveals no direct relationship regarding +CG stroke totals, although hail cells were stratified according to the type of cell organization.
- Temporal and spatial locations of maximally expected hailfall correlate with temporal (0.88) and spatial (0.84) peaks of –CG strokes. Most hail cells (66%) show –CG stroke peaks on the average 22 min (0-65 min) and 19 km (3-58 km) prior to maximally expected hailfall.
- Locations of +CG stroke peaks reveal large variance relative to maximally expected hailfall. +CG strokes in weak cells tend to peak on the average 10 min before and 3.5 km after maxima in hail kinetic energy, whereas +CG stroke peaks in strong large isolated cells lag maximally expected hailfall up to 30 min and 45 km.
- The influence of storm intensity ( $E_{\text{KINTOT}}$ ) on lag times and lag distances between highest  $\pm$ CG stroke rates and maximal hailfall is thought to be in close relation with convective updraft strength, associated and discussed in favor of the non-inductive graupel-ice electrical charging mechanism that leads to cloud electrification.
- The evaluation of CG stroke detection efficiencies from two independent Lightning Positioning and Tracking Systems (LPATS) allowed identification of important measuring inaccuracies and considerably improved the CG lightning data set.

Similarities and disagreements in the details of both, the evolution of –CG and +CG stroke rates, between the present data and a few other studies reveal the complexity of the electrical nature of severe storms in relation to hailfall. More comprehensive studies will make lightning data an independent and promising tool for improvement of short-term forecasting

of severe hailfall. Through the short lag times between observations and operational availability, CG lightning data alone could be used for detection of severe convective cells, especially in mountainous regions where the topography hinders the use of radar or furthermore, over areas where radar devices are not available. The present study consists in a small step in this direction. If more research is based on the relationship between –CG stroke rates and hailfall, shown here to be in good agreement, –CG strokes could be used in conjunction with other operational devices to improve nowcasting of hailstorms in central Europe. As spatial extents of hail damage to agriculture were shown to be in good correlation with radar-derived hail kinetic energy patterns, –CG strokes could be related to hail damage and directly be used for nowcasting purposes and evaluations of hail damage potentials.





## **Chapter 5**

### **The determination of hailfall areas with cloud-to-ground lightning location data**

#### **5.1 Introduction**

Many studies have revealed a close relationship between cloud-to-ground lightning (CG) activity and storm intensity (Section 1.6.3). Since the recent improvement of lightning detection networks, CG lightning location data can be considered as storm markers, useful for weather nowcasting in combination with radar measurements (e.g., Goodman, 1991; Baker et al., 1995; Cheze and Sauvageot, 1997) and/or satellite observed radiances (e.g., Toracinta et al., 1996; Mohr et al., 1996). Long-term averages of spatial lightning distributions have been used to relate lightning and storm activity to certain orographic features (e.g., Watson et al., 1994; Finke and Hauf, 1996) and to a synoptic pattern (Reap, 1994). Disposing of daily measured CG lightning rates, the spatial-temporal behavior of lightning patterns can be described applying correlation methods that are commonly used for cloud tracking in radar meteorology (Section 1.5). Finke (1999) used an empirical autocorrelation function to describe spatial and temporal densities of lightning location data and to derive spatial sizes of electrically active thunderstorms in south Germany. Based on CG lightning densities and radar reflectivities, Steinacker et al. (2000) proposed an automatic tracking algorithm where a Gaussfilter is used to identify different scales and movement directions of convective systems in Austria.

As locations of CG lightning discharges are highly variable in time and space, lightning data are often reduced to a few basic features before they are related to radar and/or satellite measurements that reveal characteristics of storm motion. Furthermore, the relationship between lightning cluster sizes and cloud sizes as seen by radars depends on vertical distributions of water and ice particles that change during the evolution of a thunderstorm (Jameson et al., 1996). As radar-determined thunderstorm structures show a typical evolution with lightning activity from early development to the fallout of precipitation at mature storm

phase, only a combination of both lightning and radar data reflects the entire lifecycle of a thunderstorm.

In Chapter 4, relationships between both negative (–CG) and positive CG (+CG) lightning rates, and radar-derived hail kinetic energy have been analysed for 41 hail cells that moved over the Swiss Mittelland (1992–1995). The results revealed that –CG stroke peaks are (independent of the type of thunderstorm) more closely correlated with maximal radar-derived hailfall intensity than +CG stroke peaks. Based on these relationships, the present chapter introduces some methodological approaches and concepts of how entire hailfall areas could be derived from –CG lightning location measurements alone. In Section 5.2, patterns of –CG strokes are first cross-correlated with fields of radar-derived hail kinetic energy for a part of the hail cells that have been investigated in Chapter 4. Cross-correlation coefficients between patterns of –CG stroke and hailfall intensities are shown together with highest –CG stroke and hailfall intensities in Table 5.1. Section 5.3 introduces an existing method of how CG location data can be attributed to individual hail cells and presents two methods that could be used to derive hailfall areas from hail cell-specific lightning data. Some general ideas and approaches for further studies that might lead to practical applications are discussed in Section 5.4.

## 5.2 Cross-Correlation between –CG Stroke and Hailfall Patterns

From the 41 hail cells that have been investigated in Chapter 4 (Table 4.1), time- and area-integrated radar-derived hail kinetic energy and CG stroke rates are available to analyze spatial cross-correlations between to data. First, –CG stroke locations were integrated per  $2 \times 2$  km surface (–CG<sub>PIX</sub> thereafter), whereas hail kinetic energies of 16 individual radar elements (resolution  $0.5 \times 0.5$  km) were averaged over the corresponding  $2 \times 2$  km surface (E<sub>KINPIX</sub> thereafter). The comparison of –CG stroke and hailfall patterns at a  $2 \times 2$  km resolution has the advantage that spatial distributions of –CG stroke rates become more pronounced relative to radar-derived hail kinetic energy. On the other hand, the averaging of hailfall intensity over 16 radar elements has the disadvantage that some of the fine-scales in the spatial variability of hailfalls are not resolved. Fig. 5.1 shows the spatial relationship between –CG stroke rates and E<sub>KINPIX</sub> for the hail cell that occurred over central Switzerland on 1 June 1992. Both patterns show similar distributions and reveal a valuable spatial correspondence.

From the available sample of 41 hail cells (Table 4.1), only cells that fulfilled the following criteria were analyzed: (1) an accurate detection efficiency of the Swiss lightning location network has to be guaranteed during the entire lifecycle of a hail cell and cases where lightning receivers were desensitized or entire system breakdowns occurred, were not considered (11 cells; Section 4.4.2); (2) a hail cell produced a maximal E<sub>KINPIX</sub>  $> 100 \text{ Jm}^{-2}$  and at least two –CG<sub>PIX</sub> per  $2 \times 2$  km surface; eight cells (e.g., 940704 1408 in Table 4.1) did not

fulfill this criteria and (3) in order to keep hail cell structures simple, four cells that split and/or merged over their lifecycle (e.g., 920821 1453 in Table 4.1) were not considered for the present analyzes. Of the 41 hail cells, a total of 18 cells fulfilled above assessment criteria and are used in the following for analyzes of spatial cross-correlation between –CG stroke and hailfall distributions.

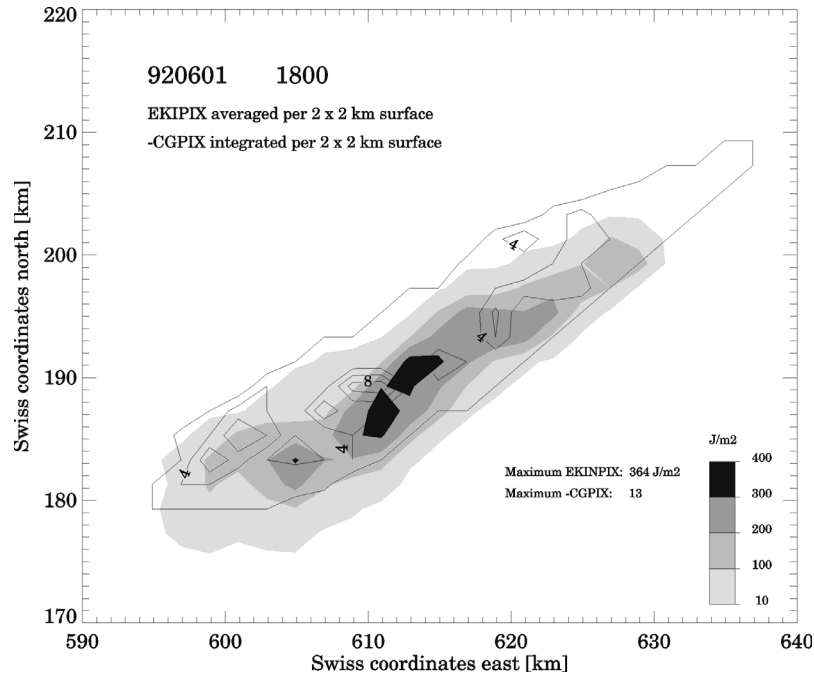


**Figure 5.1.** Spatial patterns of radar-derived hail kinetic energy (grey shades) and –CG strokes (labeled isolines) for a hail cell that occurred over central Switzerland on 1 June 1992. Note that radar-derived hail kinetic energy has been averaged per  $2 \times 2$  km surfaces and –CG stroke rates been integrated over the corresponding  $2 \times 2$  km surfaces. Swiss coordinates (km units) are used.

The cross-correlation procedure involves several separate steps. First, maxima of  $-CG_{PIX}$  and  $E_{KINPIX}$  are determined within the  $2 \times 2$  km surfaces. For every hail cell, the entire lightning pattern is shifted over the hailfall area (area of  $E_{KINPIX}$ ) according to the previously determined distance between spatial peaks of –CG strokes and hail kinetic energy (*lag distance* in Chapter 4). As  $E_{KINPIX}$  is only available at low radar-measuring height (1.5 km MSL) and falling hailstones are displaced by horizontal wind velocities before reaching ground, a certain error might occur when  $E_{KINPIX}$  is related to CG stroke locations that are measured at ground level. Additionally, the lag distance represents a direct line between the peak in –CG strokes and maximal hailfall intensity and does not necessarily respect the complex propagation tracks of some storm cells. Therefore, lightning patterns are displaced by the cell-specific lag distance, positioned over the maximum in  $E_{KINPIX}$  and an algorithm is used to shift the –CG stroke patterns by a maximum of four grid points (8 km) in the four cardinal directions relative to the hailfall surface. For every shifting step, cross-correlation coefficients are calculated between the data. After shifting, cross-correlation coefficients

improved in most cases and reached values between 0.33 and 0.66 (Table 5.1). For two hail cells, no shifting has been applied and as only two data points were available for two other cells, coefficients of 1.00 resulted (Table 5.1).

**Table 5.1.** Overview of the 18 investigated hail cells with average propagation velocities, surfaces of hailfall ( $A_{TOT}$ ), lengths of main axes that define the hailfall area, total amounts of radar-derived hail kinetic energy ( $E_{KINTOT}$ ), maximum hail kinetic energy averaged per  $2 \times 2$  km surface ( $E_{KINMAX}$ ), total numbers of –CG strokes ( $-CG_{TOT}$ ), maximum –CG stroke rates per  $2 \times 2$  km surface ( $-CG_{MAX}$ ), lag distances, data pairs and cross-correlation coefficients.

Storm	Time [UTC]	Speed [ms <sup>-1</sup> ]	$A_{TOT}$ <sup>a</sup> [km <sup>2</sup> ]	Main Axis [km]	$E_{KIN}$ TOT [GJ]	$E_{KIN}$ MAX [Jm <sup>-2</sup> ]	–CG TOT	–CG MAX	Lag Distance		Pairs	Correl. Coeff.
									X	Y		
920601	1828-1953	6.1	315	40	55.9	364	423	13	0	0	39	0.43
920721	1648-1818	12.1	424	70	81.8	253	469	11	16	10	9	0.49
920729	1643-1838	14.0	305	55	40.1	291	99	7	0	2	6	0.43
920803	1333-1448	12.2	191	50	8.8	362	78	11	18	18	10	0.45
930519	1523-1723	6.1	373	40	129.6	853	313	9	0	-4	50	0.39
	1758-1913	6.5	204	30	40.9	233	133	4	0	-2	6	0.60
930520	1203-1408	8.1	531	45	75.2	696	248	15	0	0	32	0.49
930526	1503-1638	8.4	377	60	63.8	474	224	15	6	4	28	0.66
930730	1509-1634	13.9	406	60	47.1	432	202	15	0	2	19	0.49
930822	1648-1758	20.8	857	80	72.2	215	396	10	12	12	15	0.33
940517	1618-1728	7.2	61	15	4.5	207	63	6	-6	-8	2	1.00
	1903-2118	13.5	733	80	75.1	244	648	8	18	18	35	0.49
940602	1653-1913	22.8	2296	210	127.9	141	606	4	50	32	9	0.52
940704	1943-2108	7.3	206	50	19.4	178	33	3	-2	-2	2	1.00
940706	1538-1718	6.8	223	35	33.7	324	71	3	8	8	8	0.37
940718	1218-1333	9.5	236	50	19.7	178	47	3	20	-4	3	0.60
940810	1208-1353	14.3	1003	100	87.8	233	196	5	2	0	13	0.47
950722	1403-1558	13.5	897	80	111.2	288	280	9	20	10	14	0.45
Total:		18 cells									300	

<sup>a</sup>  $A_{TOT}$  is determined from the sums of individual radar elements ( $0.5 \times 0.5$  km) that contain hail kinetic energy

The average propagation velocity of a hail cell has previously been shown to influence the distribution of hail kinetic energy as well as durations of hailfall per given surface (Section 2.5.1): in comparison to slower moving cells (velocity  $< 10$  ms<sup>-1</sup>), fast propagating cells ( $> 15$  ms<sup>-1</sup>) tend to produce hailfalls that are characterized by higher proportions in the low ( $E_{KINPIX} > 200$  Jm<sup>-2</sup>) and smaller proportions of the middle to upper range of hail kinetic energy ( $E_{KINPIX} > 600$  Jm<sup>-2</sup>). Regarding lightning activity, updraft strengths (e.g., Solomon and Baker, 1994) as well as the propagation velocity (e.g., MacGorman and Rust, 1998) were found to have a certain influence on the distributions of –CG discharges. This becomes partly relevant from the present hail cells (Table 5.1) where slow moving cells with propagation velocities  $< 10$  ms<sup>-1</sup> (e.g., 920601 1828; 930520 1203) tend to produce higher maximum hail kinetic energy and –CG stroke rates along with shorter lag distances (X and Y shift) than fast moving cells at velocities  $> 20$  ms<sup>-1</sup> (e.g., 940602 1653; 930822 1648). Due to the complex interactions between storm dynamics and thunderstorm electrification, the above relationship

between propagation velocity and –CG lightning activity can only be considered as a general trend, which has to be confirmed by further studies.

The valuable correlation between spatial patterns of –CG rates and hailfall intensities reveals a certain link between storm intensity and –CG lightning activity and is the basis for two methodological approaches that are presented in the next section. Both approaches describe methods of how CG lightning location data could be used to derive entire areas of hailfall, which in turn could be related to hail damage areas to predict initiated damage amounts to a car and/or building portfolio with previously established methods (Chapter 2 and 3).

### 5.3 Methodological Approaches

In order to derive areas of hailfall from CG lightning observation alone, a first step would be the attribution of daily measured –CG lightning stroke locations to a specific hail cell. Although the actual lightning distribution varies due to the random character of thunderstorm initiation, there are many characteristic features in the structure of lightning distributions, which is confirmed through visual inspections of plotted lightning locations relative to thunderstorm tracks.

Finke (1999) suggested a method to extract parameters, which are representative for storms in a considered time period and geographical region by a space- and time-depending density function. Due to the highly variable and complex distribution of CG lightning data, it appears more reasonable to focus on relative positions of lightning locations in time and space. An empirical correlation function provides an averaging and supports the extraction of the dominating structures and properties of the lightning activity. As a result, the complexity of the primary lightning distribution can be reduced to a few basic features of the correlation function pattern. In order to reduce preliminary attribution errors, it is essential to evaluate the daily detection efficiency of the lightning location network that is used. The correlation function given in Finke (1999) enables the classification of the type of lightning and storm activity (isolated vs. system) and the derivation of mean parameters characterizing the size and propagation properties of the storms. The spatial correlation for selected time lags provides information on the shape and mutual position of the clouds, while a radial-temporal correlation represents the temporal evolution of the lightning clusters. Finke (1999) revealed that the correlation function can be applied on lightning data from other regions, while resulting patterns will differ according to the specifics of storm size and movement. Since south German thunderstorms are in their structure comparable to Swiss storms (e.g., distances between storm systems, sizes of cells or spatial-temporal evolution cycles), above correlation function could be used for applications in Switzerland (Finke, personal communication). The fact that both the south German LPATS used by Finke (1999) and the Swiss LPATS, function

according to the same lightning location method (Section 4.3.2) and record locations of CG strokes (and not CG flashes), would further facilitate the use of above correlation function for lightning events in Switzerland. Although complex in its implementation, the correlation function given in Finke (1999) could be applied to the present CG lightning data, mainly to attribute –CG stroke locations to a particular hail cell and/or storm system. Distributions of –CG stroke locations could then be integrated over the entire area assigned to a hail cell and be integrated over a regular grid (e.g.,  $2 \times 2$  km). However, the performance of the correlation function would need to be tested first, particularly for cells that show a pulsing development and/or merged and split several times during their lifecycles. In order to derive a hailfall intensity per given surface and/or for entire areas of hailfall from –CG stroke rates, two possible approaches that could be used are discussed in the following.

### 5.3.1 Relationship between Individual Surfaces

One of the most straight forward method to find a link between patterns of –CG strokes and hailfall intensities, is the analysis of the correspondence of spatially cross-correlated individual surfaces, which could be combined to build up entire areas of hailfall. Based on the data of 18 hail cells (Table 5.1) where entire patterns of –CG strokes have been cross-correlated with areas of hailfall at a  $2 \times 2$  km resolution, the spatial relationship between surfaces of –CG stroke rates and hail kinetic energy ( $E_{\text{KINPIX}}$ ) is investigated in the following.

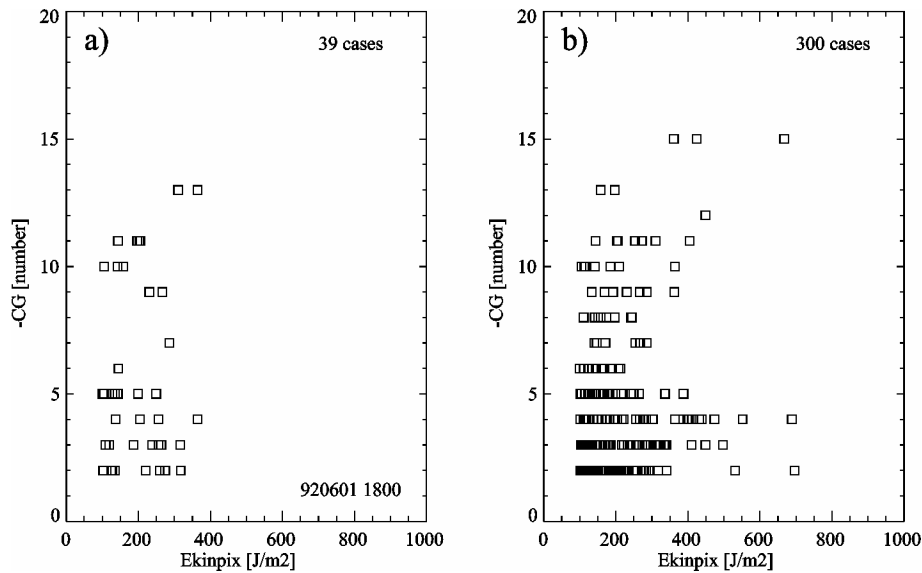


**Figure 5.2.** Relationship between individual surfaces ( $2 \times 2$  km) of cross-correlated radar-derived hail kinetic energy ( $E_{\text{KINPIX}}$ ) and numbers of –CG strokes for a) a hail cell that occurred over central Switzerland on 1 June 1992 (39 cases) and b) 18 hail cells (300 cases).

Corresponding pairs of –CG stroke and  $E_{\text{KINPIX}}$  observations are first determined per hail cell (Fig. 5.2a) and are then combined for all storms (Fig. 5.2b) with the following results. (1) Due

to the nature of hailfalls, a majority of the data pairs show hail kinetic energies at the low to medium scale ( $E_{\text{KINPIX}} < 400 \text{ Jm}^{-2}$ ) and relatively few observations at higher levels ( $E_{\text{KINPIX}} > 600 \text{ Jm}^{-2}$ ) and (2) –CG lightning activity is characterized by most observations with  $< 5$  strokes per  $2 \times 2 \text{ km}$  surface. Moreover, a stratification of the observations according to average propagation velocities of the hail cells did not lead to a more clear relationship between individual surfaces. As a result of the influence of storm dynamics on storm electrification, the variability in the distributions of –CG stroke locations and hailfall surfaces cannot be reproduced by a simple function. Disposing of a large number of additional hail cells, a more complex stratification including average propagation velocities, storm types and updraft velocities would possibly lead to more statistically significant relationships between –CG stroke and hailfall intensities.

### 5.3.2 Relationship between Entire Surfaces

This more generalized approach is based on the concept that CG lightning activity increases with storm intensity, parameterized through extents of radar-derived surfaces of hailfall, storm heights and maximum updraft strengths. The idea is to determine the complete spatial distributions of hailfalls from a given –CG stroke pattern using some of the relationships established in Chapter 4.

As shown in Chapter 4, the relationships between spatial peaks of –CG stroke and hailfall intensities ( $E_{\text{KINPIX}}$ ) relative to global hailfall intensity ( $E_{\text{KINTOT}}$ ) can be used to determine the following storm variables. (1) The total hail kinetic energy ( $E_{\text{KINTOT}}$ ) can be derived from the total number of –CG strokes that fall into the time-resolved area of radar reflectivities  $\geq 30\text{dBZ}$ , using the linear relationship given in Section 4.5.3; e.g., a thunderstorm that produced 400 –CG strokes would receive an  $E_{\text{KINTOT}}$  of 80 GJ. (2) From the estimated  $E_{\text{KINTOT}}$ , the lag distance (i.e., the distance between the peaks of –CG strokes to the maximum of hailfall intensity) can be derived according to a nonlinear function given in Section 4.5.4; e.g., a storm that contains an  $E_{\text{KINTOT}}$  of 80 GJ would reveal a lag distance of around 10 km. (3) Using the approximate lag distance, the location of the –CG stroke peak can be shifted in the propagation direction (determined from the occurrence of the first and last –CG strokes and the covered distance) and indicates the location where the maximal hailfall intensity could be expected for a particular hail cell. Changnon (1992) examined hail clusters relative to locations of CG lightning clusters and revealed that areas of highest hailfall intensities were mostly within the general storm propagation direction.

Time-integrated areas of radar-derived hail kinetic energy have been shown to reveal a structure of concentric ellipses (e.g., Waldvogel et al., 1978a,b; Schmid et al., 1992). The spatial distribution of radar-derived hailfall areas typically show a decrease in intensities from the center of the ellipse towards the edges of the hailfall area (Figs. 3.2 and 5.1). The structure of radar-determined hail kinetic energy ( $E_{\text{KINPIX}}$ ) can be explained by the fact that hailfall

starts only with developing downdrafts at mature storm phase and is therefore low during thunderstorm development and the decaying phase. The concentric and elongated structures of radar-derived hailfall areas can be described by an ellipse model as a function of the lengths of two axes that define the ellipse.

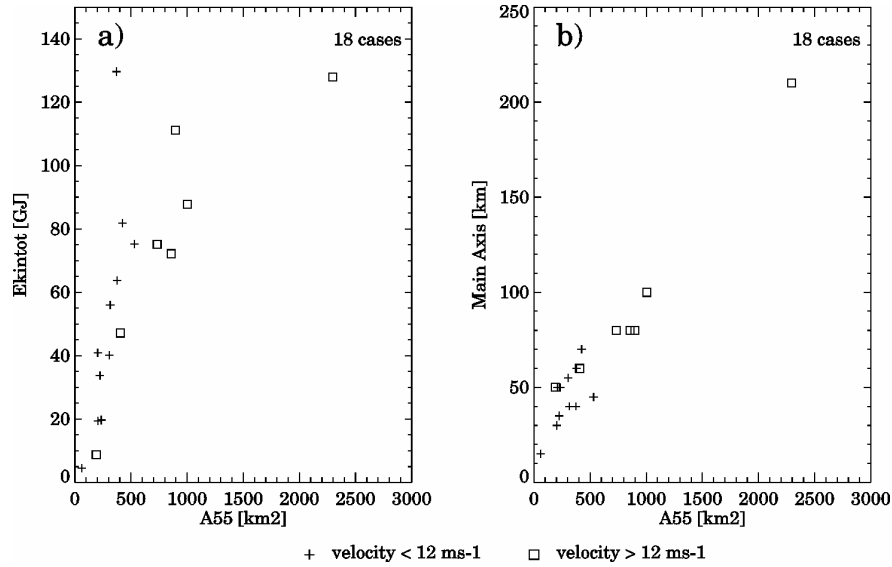


**Figure 5.3.** Relationship between sizes of hailfall areas (A55 as sums of radar elements that contain hail kinetic energy) and a) total hail kinetic energies (Ekintot) and b) the lengths of the main axes that define hailfall areas of hailfall for the examined 18 hail cells. The observations are stratified according to the average propagation velocity.

The examination of the present 18 hail cells has revealed a nonlinear relationship between the surface of hailfall (i.e., the area covered by radar elements that contain hail kinetic energy) and the total amount of total hail kinetic energy ( $E_{KINTOT}$ ) as shown in Fig. 5.3a. A linear relationship exists between the sizes of hailfall surfaces and the lengths of the main axes that describe the hailfall areas (Fig. 5.3b). Storm dynamics are reproduced in mean propagation velocities: faster moving cells (velocities  $> 12 \text{ ms}^{-1}$ ) show larger hailfall surfaces and corresponding  $E_{KINTOT}$  than slower propagating storms ( $< 12 \text{ ms}^{-1}$ ). Above relationships can be used to determine the geometry of the hailfall area (surface and length of main axis) from the total amount of hail kinetic energy ( $E_{KINTOT}$ ); e.g., a hail cell that produced an  $E_{KINTOT}$  of 80 GJ covers (on the average) a surface of hailfall of  $700 \text{ km}^2$  with a main axis of approximately 70 km in length. However, the average propagation velocity has a direct influence on the distribution of hailfalls, mainly on the size of a hailfall surface and the length of the main axis, a relationship that has to be further investigated. Given a cell-specific total number of -CG strokes as well as the position of -CG stroke peak, a combination of the present relationships can be used to determine  $E_{KINTOT}$ , the lag distance and through that the location of the maximum of hail kinetic energy, the total surface of hailfall and the approximate length of the main axis that determines the area of hailfall. With the availability



of more hail cells, geometries of hailfall areas could be examined more consistently, stratifying hail cells according to certain propagation velocities.

The next step in determining areas of hailfall from spatial distributions of –CG strokes would consist in the distribution of hail kinetic energy around the peak value. A storm that produced 400 –CG strokes and propagated at  $8 \text{ ms}^{-1}$  over the entire lifecycle, would reveal an  $E_{\text{KINTOT}}$  of 80 GJ that has to be distributed around the peak value at a location that can be determined from the pattern of –CG strokes (lag distance) over a surface of  $700 \text{ km}^2$ . In this particular case the distribution of hail kinetic energy can be taken from the model storm 940517 1903 (Table 5.1). An idealized storm model would contain gird elements (e.g.,  $2 \times 2 \text{ km}$ ) with hail kinetic energy that decreases in intensity with increasing distance from the centre of a structure described as a concentric ellipse. In order to dispose of several generalized models that predict hailfall areas from the amount of  $E_{\text{KINTOT}}$  and the average propagation velocity, a large data set of radar-measured storms and corresponding –CG lightning information is needed. If a valuable relationship exists between different models of a certain storm type, it would be possible to interpolate between different models; e.g., the distribution pattern of hail kinetic energy of a storm that produced an  $E_{\text{KINTOT}}$  of 100 GJ could be derived through geometrical parameters (ellipse model) from similar storms that initiated 80 GJ and 120 GJ, whereas the energy distribution of a storm that initiated 100 GJ at a propagation velocity of  $15 \text{ ms}^{-1}$  could be estimated from a comparable storm that moved at  $10 \text{ ms}^{-1}$ .

As radar-derived hailfall areas can show asymmetric structures, the geometry of hail kinetic energy patterns could more accurately be described by an ellipse model used in Schmid (1988) to approximate 5-min PPI radar reflectivity contours. This (more sophisticated) ellipse model needs six input parameters: the maximum radar reflectivity, a gradient parameter, two center-of-mass coordinates and two shape parameters. The determination of each parameter and the equations of the ellipse model can be found in Schmid (1988). In a future study, the present 18 hail cells could be expressed in a mathematical formula using above ellipse model, so that 18 cells would be available as model storms for a certain total hail kinetic energy ( $E_{\text{KINTOT}}$ ).

## 5.4 Outlook and Possible Applications

From Section 5.3 appears that numerous further studies have to be conducted before CG lightning location data can be attributed to individual hail cells and before entire areas of hailfalls could be determined from CG lightning location data alone. The valuable agreement between patterns of –CG strokes and kinetic hail energy (cross-correlation coefficients in Table 5.1) and the already existing method of Finke (1999) to attribute CG lightning location

data to individual thunderstorm cells, are certainly encouraging for further studies that go in this direction.

The availability of additional storm parameters (e.g., updraft strengths) would certainly improve the understanding of spatial hailfall patterns in relation to distributions of –CG lightning locations. The present data set as well as the relationships between peaks of CG lightning and maximum hailfall intensity (Section 4.5.4) and between hailfall surfaces, (sizes and lengths of main axes) and total kinetic hail energy (Section 5.3.2), could be used for further studies. The availability of additional radar and CG lightning data would facilitate the analysis of spatial hailfall and CG lightning patterns which might lead to some practical applications. The use of an ellipse model to describe distributions of both hailfall and –CG stroke areas could be a successful approach and lead to a general model that allows the determination of entire hailfall areas directly from –CG lightning observations.

The possibility to use –CG lightning locations to derive entire areas of hailfall opens up some interesting applications for the future. (1) Weather radars reveal at the moment the only possibility to detect hail-bearing thunderstorms, to monitor hailfalls at real time and to determine areas of hailfalls shortly after the passage of a hailstorm. Once hailfall areas can directly be derived from CG lightning location measurements, hailfall surfaces can be determined for regions where radar measurements are not available or for mountainous regions where radar beams are shielded. However, as a method that uses CG lightning data to derive areas of hailfalls would essentially rely on a general (statistical and/or mathematical) model, the resolution and prediction accuracies of areas affected by hail would be lower than when determined by radars. (2) Operational weather radars measure mainly precipitation rates and do in most cases not provide intervals of high radar reflectivities (e.g.,  $> 55$  dBZ) which are essential for the accurate detection and determination of hail and hailfall areas. The determination of hail-affected areas by operational radars could therefore be supported by CG lightning information. (3) Hailfall areas and amounts of hail damage to agriculture and infrastructure is of vital interest to the insurance industry. Radar-derived hail kinetic energy has been shown to be a physical measure of hailfall intensity and can be considered as a damage response variable (Chapter 2 and 3). However, the availability of radar-measured hailstorms is temporally and spatially limited and accurate measurements are difficult to obtain, especially for a larger area where data have to be retrieved from a radar network. On the other hand, CG lightning location data are widely available and could potentially be used to determine hailfall areas over a large scale. Once a CG lightning-derived hailfall area has been determined, the relationship between hailfall intensity (hail kinetic energy) and the amount of damage (Chapter 2 and 3) can be used to estimate hail damage potentials. The availability of a complete set of radar measurements, CG lightning information, hail damages on infrastructure for several severe thunderstorms and a method to determine hailfall areas directly from CG lightning observations, would show how accurately CG lightning-

determined hailfall areas would correspond to damage patterns. If hail damage areas are of interest on a large scale (e.g., central Europe), it would be possible to use CG lightning location data from the recently established European lightning composit to determine hailfall areas not only for individual storm cells but also for entire storm systems (e.g., mesoscale convective systems).

Until it will finally be possible to derive hailfall areas from CG lightning location data alone, much research has to be devoted to understand the relationship between CG lightning distributions and hailfall patterns in order to find an accurate way to describe the spatial distributions between the data.



# References

## Chapter 1

- Atlas, D. (ed.), 1990: *Radar in Meteorology*. Amer. Meteor. Soc., Boston, 806 p.
- Atlas, D. and Ludlam, F.H., 1961. Multi-wavelength radar reflectivity of hailstorms. *Quart. J. Roy. Meteor. Soc.* 87, 523-34.
- Amburn, S.A. and Wolf, P.L., 1997. VIL density as a hail indicator. *Wea. Forecasting* 12, 473-78.
- Andrews, K.E. and Blong, R.J., 1997. March 1990 hailstorm damage in Sydney, Australia. *Natural Hazards* 16, 1-13.
- Auer, A.H. Jr., 1994. Hail recognition through the combined use of radar reflectivity and cloud-temperatures. *Mon. Wea. Rev.* 122, 2218-21.
- Bauer-Messmer, B. and Waldvogel, A., 1997. Satellite data based detection and prediction of hail. *Atmos. Res.* 43, 217-31.
- Borland, S.W., 1977. Hail suppression: Progress in assessing its costs and benefits. In G.B. Foote and C.A. Knight (eds.) *Hail: A Review of Hail Science and Hail Suppression*. Meteor. Monogr. 16, Amer. Meteor. Soc., Boston, 155-75.
- Burgess, D.W. and Lemon, L.R., 1990. Severe thunderstorm detection by radar. In D. Atlas (ed.) *Radar in Meteorology*. Amer. Meteor. Soc., Boston, 619-47.
- Browning, K.A., and Foote, G.B., 1976. Airflow and hail growth in supercell storms and some implication for hail suppression. *Quart. J. Roy. Meteor. Soc.* 102, 499-533.
- Browning, K.A., 1977. The structure and mechanisms of hailstorms. In G.B. Foote and C.A. Knight (eds.) *Hail: A Review of Hail Science and Hail Suppression*. Meteor. Monogr. 16, Amer. Meteor. Soc., Boston, 1-43.
- Buechler, D.E. and Goodman, S.J., 1990. Echo size and asymmetry: Impact on NEXRAD storm identification. *J. Appl. Meteorol.* 29, 962-69.
- Changnon, S.A., 1999. Data and approaches for determining hail risk in the contiguous United States. *J. Appl. Meteorol.* 38, 1730-39.
- Charlton, R.B., Kachman, B.M. and Wojtiw, L., 1995. Urban hailstorms: A view from Alberta. *Natural Hazards* 12, 29-75.
- Collier, C.G. and Lilley, R.B.E., 1994. Forecasting thunderstorm initiation in north-west Europe using thermodynamic indices, satellite and radar data. *Met. Apps.* 1, 75-84.

- Cotton, W.R., 2000. An overview of mesoscale convective systems. In R. Jr. Pielke and R. Sr. Pielke (eds.) *Storms*. Volume II, Routledge Hazards and Disaster Series, Routledge, London, 3-27.
- Cummins, K.L., Krider, E.P. and Malone, M.D., 1998. The U.S. National Lightning Detection Network and applications of cloud-to-ground lightning data by electric power utilities. *IEEE Trans. Electromag. Compat.* 40, 465-80.
- Doswell, C.A. III and Burgess, D.W., 1993. Tornadoes and tornadic storms: A review of conceptual models. In *The Tornado: Its Structure, Dynamics, Prediction and Hazard*. AGU Monogr., No. 79, Amer. Geophys. Union, 161-72.
- Dudhia, J., 1996. Thunderstorms. Part 2: Storm types and associated weather. *Weather* 52, 2-6.
- Federer, B. and Waldvogel, A., 1978. Time-resolved hailstone analysis and structure of Swiss storms. *Quart. J. Roy. Meteor. Soc.* 104, 69-90.
- Federer, B., Waldvogel, A., Schmid, W., Schiesser H.H., Hampel, F., Schweingruber, M., Stahel, W., Bader, J., Mezeix, J.F., Doras, M., d'Aubigny, G., DerMegreditchian, G. and Vento, D., 1986. Main results of Grossversuch IV. *J. Appl. Meteorol.* 25, 917-57.
- Finke, U., 1999. Space-time correlations of lightning distributions. *Mon. Wea. Rev.* 127, 1850-61.
- Fister, V., von Rheinbaben H. and Zundl T., 1994. Analysis of the 1992 and 1993 lightning data in south Germany. *Preprints, 22nd Int. Conf. on Lightning Protection*, Budapest, 211-16.
- Foote, G.B. and Knight, C.A., 1979. Results of a randomized hail suppression experiment in northeast Colorado. Parts 1-9. *J. Appl. Meteorol.* 18, 1526-639.
- Geotis, S.G., 1963. Some radar measurements of hailstorms. *J. Appl. Meteorol.* 2, 270-75.
- Holle, R.L., Watson, A.I., Lopez, R.E., MacGorman, D.R. and Ortiz, R., 1994. The life cycle of lightning and severe weather in a 3-4 June 1985 PRE-STORM mesoscale convective system. *Mon. Wea. Rev.* 122, 1798-1808.
- Holleman, I., Wessels, H.R.A., Onvlee, J.R.A. and Barlag, S.J.M., 2000. Development of a hail-detection-product. *Phys. Chem. Earth (B)* 25, 1293-97.
- Höller, H., Bringi, V.N., Hubbert, J., Hagen, M. and Meischner, P.F., 1994. Life cycle and precipitation formation in a hybrid-type hailstorm revealed by polarimetric and Doppler radar measurements. *J. Atmos. Sci.* 51, 2500-22.
- Hondl, K.D. and Eilts, M.D., 1994. Doppler radar signatures of developing thunderstorms and their potential to indicate the onset of cloud-to-ground lightning. *Mon. Wea. Rev.* 122, 1818-36.
- Houze, R.A. Jr., 1993. *Cloud Dynamics*. Inter. Geophys. Series, Academic Press, San Diego, Vol. 53, 570 p.
- Houze, R.A. Jr., Smull, B.F. and Dodge, P., 1990. Mesoscale organization of springtime rain storms in Oklahoma. *Mon. Wea. Rev.* 118, 613-65.

- Houze, R.A. Jr., Schmid, W., Fovell, R.G. and Schiesser, H.H., 1993. Hailstorms in Switzerland: left movers, right movers and false hooks. *Mon. Wea. Rev.* 121, 3345-70.
- Huntrieser, H., Schiesser, H.H., Schmid, W. and Waldvogel, A., 1997. Comparison of traditional and newly developed thunderstorm indices for Switzerland. *Wea. Forecasting* 12, 108-25.
- Jayarathne, E.R., Saunders, C.P.R. and Hallett, J., 1983. Laboratory studies of the charging of soft-hail during ice crystal interactions. *Quart. J. Roy. Meteor. Soc.* 109, 609-30.
- Johns R.H. and Doswell, C.A. III, 1992. Severe local storms forecasting. *Wea. Forecasting* 7, 588-612.
- Johnson, J.T., MacKeen, P.L., Witt, A., DeWayne Mitchell, E., Stumpf, G.J., Eilts, M.D. and Thomas, K.W., 1998. The storm cell identification and tracking algorithm: An enhanced WSR-88D algorithm. *Wea. Forecasting* 13, 263-76.
- Joss, J. and Lee, R., 1995. The application of radar-gauge comparisons to operational precipitation profile corrections. *J. Appl. Meteorol.* 34, 2612-30.
- Joss, J., Schädler, B., Galli, G., Cavalli, R., Boscacci, M., Held, E., Della Bruna, G., Kappenberger, G., Nepsor, V. and Spiess, R., 1998. *Operational Use of Radar for Precipitation Measurements in Switzerland*. Final Report NRP31, vdf Hochschulverlag, ETH Zurich, Switzerland, 108 p.
- Katz, R.W. and Garcia, P.R., 1981. Statistical relationships between hailfall and damage to wheat. *Agricult. Meteorol.* 24, 29-43.
- Klemp, J.B. and Wilhelmson, R.B., 1978. Simulations of right- and left-moving thunderstorms produced through storm splitting. *J. Atmos. Sci.*, 1097-1110.
- Knapp, D.I., 1994. Using cloud-to-ground lightning data to identify tornadic thunderstorm signatures and nowcast severe weather. *Nat. Wea. Assoc. Digest* 19, 35-42.
- Kuhnel, I., 2000. Pricing hail losses: Extrapolation of past losses vs. stochastic modelling. *Natural Hazards Quart.* 6, 4 p.
- Lenning, F., Fuelberg, H.E. and Watson, A.I., 1998. An evaluation of WSR-88D severe hail algorithm along the Northeastern Gulf coast. *Wea. Forecasting* 13, 1029-44.
- Li, L., Schmid, W. and Joss, J., 1995. Nowcasting of motion and growth of precipitation over a complex orography. *J. Appl. Meteorol.* 34, 1286-1300.
- List, R., 1986. Properties and growth of hailstones. In E. Kessler (ed.) *Thunderstorm Morphology and Dynamics*. University of Oklahoma Press, Norman, 259-76.
- Lozowski, E.P. and Strong, G.S., 1978. On the calibration of hailpads. *J. Appl. Meteorol.* 17, 521-28.
- MacGorman, D.R. and Nielson, K.E., 1991. Cloud-to-ground lightning in a tornadic storm on 8 May 1986. *Mon. Wea. Rev.* 119, 1557-74.
- MacGorman, D.R. and Burgess, D.W., 1994. Positive cloud-to-ground lightning in tornadic storms and hailstorms. *Mon. Wea. Rev.* 122, 1671-97.

- MacGorman, D.R. and Rust, W.D., 1998. *The Electrical Nature of Storms*. Oxford University Press. 422 p.
- Macklin, W.C., 1977. The characteristics of natural hailstones and their interpretation. In G.B. Foote and C.A. Knight (eds.) *Hail: A Review of Hail Science and Hail Suppression*. Meteor. Monogr. 16, Amer. Meteor. Soc., Boston, 65-88.
- Mazur, V., Gerlach, J.C. and Rust, W.D., 1986. Evolution of lightning flash density and reflectivity structure in a multicell thunderstorm. *J. Geophys. Res.* 91, 8690-700.
- Mezeix, J.F. and Admirat, P., 1978. The measurement of hail at ground level. *Atmosph. Ocean* 16, 61-8.
- Miller, L.J., Tuttle, J.D. and Knight, C.A., 1988. Airflow and hail growth in a severe northern High Plains supercell. *J. Atmos. Sci.* 45, 736-62.
- Moller, A.R., Doswell, C.A. III, Foster, M.P. and Woodall, G.R., 1994. The operational recognition of supercell thunderstorm environment and storm structure. *Wea. Forecasting* 9, 327-47.
- MunichRe, 1984. *Hagel*. Münchner Rückversicherungsgesellschaft, Munich, Germany, 56 p.
- Negri, A.J., 1977. *Satellite Observations of Onset and Growth of Severe Local Storms*. Atmos. Sci. Pap. No. 278, Colorado State University, USA, 89 p.
- Nelson, S.P., 1987. The hybrid multicellular-supercellular storm: An efficient hail producer. Part II: General characteristics and implication for hail growth. *J. Atmos. Sci.* 44, 1960-72.
- Petersen, W.A., Rutledge, S.A. and Orville, R.E., 1996. Cloud-to-ground lightning observations from TOGA COARE: Selected results and lightning location algorithms. *Mon. Wea. Rev.* 124, 602-20.
- Reap, R.M. and MacGorman, D.R., 1989. Cloud-to-ground lightning: climatological characteristics and relationships to model fields, radar observations, and severe local storms. *Mon. Wea. Rev.* 117, 518-35.
- Rinehart, R.E., 1999. *Radar for Meteorologists*. 3rd edition, Rinehart Publications, Grand Forks, 428 p.
- Reynolds, D.W., 1980. Observations of damaging hailstorms from geosynchronous satellite digital data. *Mon. Wea. Rev.* 108, 337-48.
- Rubinstein, M., Montandon, E. and Ianoz, M., 1994. Analyzes of multi-station cloud lightning electric field pulses recorded with the Swiss LPATS network. *Preprints, 22nd Int. Conf. on Lightning Protection*, Budapest, 5 p.
- Saunders, C.P.R., 1993. A Review of thunderstorm electrification processes. *J. Appl. Meteorol.* 32, 642-55.
- Sauvageot, H., 1982. *Radarmétéorologie. Télédétection active de l'Atmosphère*. Edition Eyroles, Paris, France, 296 p.
- Schiesser, H.H., 1988. *Fernerkundung von Hagelschäden mittels Wetterradar*. Remote Sensing Series Vol. 14, University of Zurich, Switzerland, 199 p.



- Schiesser, H.H., 1990. Hailfall: The relationship between radar measurements and crop damage. *Atmos. Res.* 25, 559-82.
- Schiesser, H.H., Houze, R.A. Jr. and Huntrieser, H., 1995. The mesoscale structure of severe precipitation systems in Switzerland. *Mon. Wea. Rev.* 123, 2070-97.
- Schiesser, H.H., Waldvogel, A., Schmid, W. and Willemse, S., 1997. *Klimatologie der Stürme und Sturmsysteme anhand von Radar- und Schadendaten*. Schlussbericht NFP31. vdf Hochschulverlag, ETH Zurich, Switzerland, 132 p.
- Schiesser, H.H. and Waldvogel, A., 2000. Hailstorms. In R. Jr. Pielke and R. Sr. Pielke (eds.) *Storms*. Volume II, Routledge Hazards and Disaster Series, Routledge, London, 133-45.
- Schmid, W., Schiesser, H.H. and Waldvogel, A., 1992. The kinetic energy of hailfalls. Part IV: Patterns of hailpad and radar data. *J. Appl. Meteorol.* 31, 1165-78.
- Schmid, W., Schiesser, H.H. and Bauer-Messmer, B., 1997. Supercell storms in Switzerland: case studies and implications for nowcasting severe winds with Doppler radar. *Meteorol. Appl.* 4, 49-67.
- Seimon, A., 1993. Anomalous cloud-to-ground lightning in an F5-tornado-producing supercell thunderstorm on 28 August 1990. *Bull. Amer. Meteor. Soc.* 74, 189-203.
- SHV, 1999. *Geschäftsbericht 1999*. Schweizerische Hagel-Versicherungs-Gesellschaft, Zurich, Switzerland, 16 p.
- Smith, P.L., 1992. Hail suppression activity around the world. *Preprints, Symp. on Planned and Inadvertent Weather Modification*, Atlanta, Amer. Meteor. Soc., 28-34.
- Smith, P.L. and Waldvogel, A., 1989. On the determination of maximal hailstone sizes from hailpad observations. *J. Appl. Meteorol.* 28, 71-6.
- Smyth, T.J., Blackman, T.M. and Illingworth, A.J., 1999. Observations of oblate hail using dual polarization radar and implications for hail-detection schemes. *Quart. J. Roy. Meteor. Soc.* 125, 993-1016.
- Solomon, R. and Baker, M., 1994. Electrification of New Mexico thunderstorms. *Mon. Wea. Rev.* 122, 18787-88.
- Steinacker, R., Dorninger, F., Wölfelmaier, F. and Krennert, T., 2000. Automatic tracking of convective cells and cell complexes from lightning and radar data. *Meteorol. Atmos. Phys.* 72, 101-10.
- Stolzenburg, M., 1994. Observation of high ground flash densities of positive lightning in summertime thunderstorms. *Mon. Wea. Rev.* 122, 1740-50.
- Stolzenburg, M., Rust, W.D., Smull, B.F. and Marshall, T.C., 1998a. Electrical structure in thunderstorm convective regions. 1. Mesoscale convective systems. *J. Geophys. Res.* 103, 14059-78.
- Stolzenburg, M., Rust, W.D. and Marshall, T.C., 1998b. Electrical structure in thunderstorm convective regions. 2. Isolated storms. *J. Geophys. Res.* 103, 14079-96.
- Stolzenburg, M., Rust, D.W. and Marshall, T.C., 1998c. Electrical structure in thunderstorm convective regions. 3. Synthesis. *J. Geophys. Res.* 103, 14097-108.

- Stumpf, G.J., 2000. The National Severe Storms Laboratory severe weather detection algorithms. *Preprints, 1st Conf. Europ. Tornadoes and Severe Storms*, Toulouse, 2 p.
- Thomas, R., 2000. Insurance Pricing with GIS. *Geospat. Solutions*, Sept. 2000, 4 p.
- Uman, M.A., 1987. *The Lightning Discharge*. Int. Geophys. Series 39, Academic Press, Orlando, 370 p.
- Waldvogel, A., 1972. *Über den  $N_0$ -Sprung von Tropfenspektren*. Wiss. Mitt. Nr. 68, Eidg. Komm. zum Studium der Hagelbildung und der Hagelabwehr, Zurich, Switzerland, 94 p.
- Waldvogel, A. and Federer, B., 1976. Large raindrops and the boundary between rain and hail. *Preprints, 17th Conf. Radar Meteorology*, Seattle, Amer. Meteor. Soc., 167-72.
- Waldvogel, A. and Schmid, W., 1983. Single wavelength radar measurements of hailfall kinetic energy. *Preprints, 21st Conf. Radar Meteorology*, Edmonton, Amer. Meteor. Soc., 425-28.
- Waldvogel, A., Schmid, W. and Federer, B., 1978a. The kinetic energy of hailfalls. Part I: Hailstone spectra. *J. Appl. Meteorol.* 17, 515-20.
- Waldvogel, A., Federer, B. and Schmid, W., 1978b. The kinetic energy of hailfalls. Part II: Radar and hailpads. *J. Appl. Meteorol.* 17, 1680-93.
- Waldvogel, A., Federer, B. and Grimm, P., 1979. Criteria for the detection of hail cells. *J. Appl. Meteorol.* 18, 1521-25.
- Waldvogel, A., Federer, B. and Högl, D., 1980. On the correlation between hailpad and radar data. *Preprints, 19th Conf. Radar Meteorology*, Miami, Amer. Meteor. Soc., 493-98.
- Watson, A.I., Lopez, R.E., and Holle, R.L., 1994. Diurnal cloud-to-ground lightning patterns in Arizona during the southwest monsoon. *Mon. Wea. Rev.* 122, 1716-25.
- Watson, A.I., Holle, R.I. and Lopez, R.E., 1995. Lightning from two national detection networks related to vertically integrated liquid water and echo-top information from WSR-88D radar. *Wea. Forecasting* 10, 592-605.
- Williams, E.R., Weber, M.E. and Orville, R.E., 1989. The relationship between lightning type and convective state of thunderclouds. *J. Geophys. Res.* 94, 13213-20.
- Wilson, J.W., Crook, N.A., Mueller, C.K., Sun, J. and Dixon, M., 1998. Nowcasting thunderstorms: A status report. *Bull. Amer. Meteor. Soc.*, 2079-99.
- Witt, A. and Nelson, S.P., 1991. The use of single-Doppler radar for estimating maximum hailstone size. *J. Appl. Meteorol.* 30, 425-31.
- Witt, A., Eilts, M.D., Stumpf, G.J., Johnson, J.T., Mitchell, E.D. and Thomas, K.W., 1998. An enhanced hail detection algorithm for the WSR-88D. *Wea. Forecasting* 13, 286-303.
- Wojtiw, L and Ewing, C., 1983. The use of radar to estimate crop damage for hailstorms in Alberta, Canada. *Preprints, 21st Conf. Radar Meteorology*, Edmonton, Amer. Meteor. Soc., 435-41.
- Wojtiw, L and Ewing, C., 1986. The relationship of time-integrated radar reflectivity with hail crop damage. *Preprints, 23rd Conf. Radar Meteorology*, Snowmass, Amer. Meteor. Soc., 23-26.

- WMO, 1995. *Program on Physics and Chemistry of Clouds and Weather Modification Research: Meeting of Experts to Review the Present Status of Hail Suppression*. World Meteorological Organisation, WMP Report No. 26.
- Yeo, S., Leigh, R. and Kuhnel, I., 1999. The April 1999 Sydney hailstorm. *Natural Hazards Quart.* 5, 4 p.
- Zisper, E.J. and Lutz, K.R., 1994. The vertical profile of radar reflectivity of convective cells: A strong indicator of storm intensity and lightning probability? *Mon. Wea. Rev.* 122, 1751-59.

## Chapter 2

- Andrews, K.E and Blong, R.J., 1997. March 1990 hailstorm damage in Sydney, Australia. *Natural Hazards* 16, 1-13.
- Bailey, T.C. and Gatrell, A.C., 1996. *Interactive Spatial Data Analysis*. Longman, London, 413 p.
- Branick, M.L., Vitale, F., Lai, C.C. and Bosart, L.F., 1988. The synoptic and subsynoptic structure of a long-lived severe convective system. *Mon. Wea. Rev.* 116, 1335-70.
- Browning, K.A., 1977. The structure and mechanisms of hailstorms. In G.B. Foote and C.A. Knight (eds.) *Hail: A Review of Hail Science and Hail Suppression*. Meteor. Monogr. 16, Amer. Meteor. Soc., Boston, 1-43.
- Buckley, B.W., Leslie, L.M. and Wang, Y., 2001. The Sydney hailstorm of April 14, 1999: Synoptic description and numerical simulation. *Meteorol. Atmos. Phys.* 76, 167-82.
- Carlson, T.N., Richard, R., Anthes, A., Schwartz, M., Benjamin, S.G. and Baldwin, D.G., 1980. Analysis and prediction of severe storm environment. *Bull. Amer. Meteor. Soc.* 61, 1018-32.
- Changnon, S.A., 1971. Note on hailstone size distribution. *J. Appl. Meteorol.* 10, 168-70.
- Changnon, S.A., 1977. Scales of hail. *J. Appl. Meteorol.* 16, 626-48.
- Changnon, S.A., 1999. Data and approaches for determining hail risk in the contiguous United States. *J. Appl. Meteorol.* 38, 1730-39.
- Charlton, R.B., Kachmann, B.M. and Wojtiw, L., 1995. Urban hailstorms: a view from Alberta. *Natural Hazards* 12, 29-75.
- Dennis, A.S. and Musil, D.J., 1973. Calculations of hailstone growth and trajectories in a simple cloud model. *J. Atmos. Sci.* 30, 278-88.
- Dessens, J., 1995. Severe convective weather in the context of night time global warming. *Geophys. Res. Lett.* 22, 1241-44.
- Di Constanzo G.P., Matlock D.K. and Foley, R.P., 1996. *Effect of tensile properties on dent resistance of sheet steels*. SAE Technical Paper Series No. 960024.
- Doswell, C.A. III, 1987. The distinction between large-scale and mesoscale contribution to severe convection: A case study example. *Wea. Forecasting* 2, 3-16.

- Federer, B., Waldvogel, A., Schmid, W., Schiesser, H.H., Hampel, F., Schweingruber, M., Stahel, W., Bader, J., Mezeix, J.F., Doras, N., d'Aubigny, G., DerMegreditchian, G. and Vento, D., 1986. Main results of Grossversuch IV. *J. Appl. Meteorol.* 25, 917-57.
- Foote, G.B. and Knight C.A., 1979. Results of a randomized hail suppression experiment in northeast Colorado. Parts 1-9. *J. Appl. Meteorol.* 18, 1526-1639.
- Geotis, S.G., 1963. Some radar measurements of hailstorms. *J. Appl. Meteorol.* 2, 270-75.
- Giaiotti, D., Giancesini E. and Stel, F., 2001. Heuristic considerations pertaining to hailstone size distributions in the plain of Friuli-Venezia Giulia. *Atmos. Res.* 57, 269-88.
- Haase-Straub, S., Heimann, D., Hauf, T., Smith, R.K., 1994. *The squall line of 21 July 1992 in Switzerland and southern Germany – a documentation*. DLR-Forschungsbericht 94-18, 226 p.
- Hohl, R. and Schiesser, H.H., 2001. Cloud-to-ground lightning activity in relation to the radar-derived hail kinetic energy in Switzerland. *Atmos. Res.* 56, 375-96.
- Houze, R.A. Jr., Schmid, W., Forell, R.G. and Schiesser, H.H., 1993. Hailstorms in Switzerland: left movers, right movers and false hooks. *Mon. Wea. Rev.* 121, 3345-70.
- Huntrieser, H., Schiesser, H.H. and Waldvogel, A., 1994. The synoptic and mesoscale environment of severe convective activity in Switzerland. *Preprints, Int. Symp. Life Cycle of Extratropical Cyclones*, Bergen, Vol. III, 101-06.
- Huntrieser, H., Schiesser, H.H., Schmid, W. and Waldvogel, A., 1997. Comparison of traditional and newly developed thunderstorm indices for Switzerland. *Wea. Forecasting* 12, 108-25.
- Husson, D. and Pointin, Y., 1989. Quantitative estimation of hailfall intensity with a dual polarization radar and a hailpad network. *Preprints, 24th Conf. Radar Meteorology*, Tallahassee, Amer. Meteor. Soc., 318-21.
- Johns, R.H. and Doswell, C.A. III, 1992. Severe local storms forecasting. *Wea. Forecasting* 7, 588-612.
- Joss, J. and Waldvogel, A., 1967. Ein Spektograph für Niederschlagstropfen mit automatischer Auswertung. *Pure Appl. Geophys.* 68, 240-46.
- Joss, J. and Lee, R., 1995. The application of radar-gauge comparison to operational precipitation profile corrections. *J. Appl. Meteorol.* 34, 2612-30.
- Katz, R.W. and Garcia, R.R., 1981. Statistical relationships between hailfall and damage to wheat. *Agricult. Meteorol.* 24, 29-43.
- Leigh, R., 1998. *Hail damage to motor vehicles: an examination of economic costs*. Natural Hazards Research Center, Macquarie University, Sidney, Australia, 9 p.
- Matson, R.J. and Huggins A.W., 1980. The direct measurement of the size, shapes and kinematics of falling hailstones. *J. Atmos. Sci.* 37, 1107-25.
- Mezeix, J.F. and Admirat, P., 1978. The measurement of hail at ground level. *Atmosph. Ocean* 16, 61-68.
- Munich Re, 1984. *Hagel*, Münchner Rückversicherungsgesellschaft, Munich, Germany, 56 p.

- PartnerRe, 1999. *Sydney Hailstorm, April 14, 1999*. PartnerResearch, PartnerRe Reinsurance Company Ltd., Zurich, Switzerland, 4 p.
- Prodi, F., 1974. Climatologia della grandine nella Valle Padana (1968-1972). *Rivista Italiana di Geophysica*, 23, 283-90.
- Radar Meteorology Group, 1995. *Monitoring of severe hailstorms in Switzerland 1994*. LAPETH-33, Atmospheric Science ETH, Zurich, Switzerland, 243 p.
- Schiesser, H.H., 1990. Hailfall: the relationship between radar measurements and crop damage. *Atmos. Res.* 25, 559-582.
- Schiesser, H.H., 1998. *Wolkenparameter und Hagelkorngrößen von Hagelzellen mit Autoschadenpotential – Versuch einer Klimatologie anhand von Radardaten*. Projektskizze. Internal Report, Atmospheric Science ETH, Zurich, Switzerland, 10 p.
- Schiesser, H.H., Waldvogel, A., Schmid, W., Willemse, S. 1997. *Klimatologie der Stürme und Sturmsysteme anhand von Radar- und Schadendaten*. Schlussbericht NFP31. vdf Hochschulverlag, ETH Zurich, Switzerland, 132 p.
- Schiesser, H.H., Hohl, R. and Schmid, W., 1999. *Über die Beziehung Hagelfall-Gebäudeschäden: Fallstudie Luzern-Hagelsturm vom 21 Juli 1998*. Technical Report, Atmospheric Science ETH, Zurich, Switzerland, 37 p.
- Schmid, W. and Waldvogel, A., 1986. Radar hail profiles in Switzerland. *J. Climate and Appl. Meteorol.* 25, 1002-11.
- Schmid, W., Schiesser, H.H. and Waldvogel, A., 1992. The kinetic energy of hailfalls. Part IV: Patterns of hailpad and radar data. *J. Appl. Meteorol.* 31, 1165-78.
- Schmid, W., Schiesser, H.H. and Bauer-Messmer, B., 1997. Supercell storms in Switzerland: Case studies and implications for nowcasting severe winds with Doppler radar. *Meteorol. Appl.* 4, 49-67.
- Shi, M.F., Brindza, J.A., Michel P.F., Bucklin, P., Belanger, P.J. and Preneipe, J.M., 1997. *Static and dynamic dent resistance performance of automobile steel body panels*. SAE Technical Paper Series No. 970158.
- Smith, P.L. and Waldvogel, A., 1989. On the determination of maximal hailstone sizes from hailpad observations. *J. Appl. Meteorol.* 28, 71-76.
- Waldvogel, A., 1980. *Bericht über Testversuch: Einwirkung von Hagelkörnern auf Karosserieteile DATSUN*. Internal Report, Atmospheric Science ETH, Zurich, Switzerland, 6 p.
- Waldvogel, A. and Schmid, W., 1983. Single wavelength radar measurements of hailfall kinetic energy. *Preprints, 21st Conf. Radar Meteorology*, Edmonton, Amer. Meteor. Soc., 425-28.
- Waldvogel, A., Schmid, W. and Federer, B., 1978a. The kinetic energy of hailfalls, Part I. Hailstone spectra, *J. Appl. Meteorol.* 17, 515-20.
- Waldvogel, A., Federer, B., Schmid, W. and Mezeix, J.F., 1978b. The kinetic energy of hailfalls: Part II. Radar and hailpads. *J. Appl. Meteorol.* 17, 1680-93.

- Waldvogel, A., Federer, B. and Grimm, P., 1979. Criteria for the detection of hail cells. *J. Appl. Meteorol.* 18, 1521-25.
- Waldvogel, A., Federer, B. and Högl, D., 1980. On the correlation between hailpad and radar data. *Preprints, 19th Conf. Radar Meteorology*, Miami, Amer. Meteor. Soc., 493-98.
- Winterthur Insurance, 1997. *Hagelrisiko in der Schweiz*. Group Risk Management and Exposure Control, Internal Report, Winterthur Insurance, Winterthur, Switzerland, 47 p.
- Winterthur Insurance, 2000. <http://www.winterthur.com/prod/wincat/index-d.html>.
- Witt, A. and Nelson, S.P., 1991. The use of single-Doppler radar for estimating maximum hailstone size. *J. Appl. Meteorol.* 30, 425-31.
- Witt, A., Eilts, M.D., Stumpf, G.J., Johnson, J.T., Michell, E.D. and Thomas, K.W., 1998. An enhanced hail detection algorithm for the WSR-88D. *Wea. Forecasting* 13, 286-303.
- Wojtiw, L. and Ewing, C., 1986. The relationship of time-integrated radar reflectivity with hail crop damage. *Preprints, 23rd Conf. Radar Meteorology*, Snowmass, Amer. Meteor. Soc., 23-26.
- Yeo, S., Leigh, R. and Kuhnel, I., 1999. The April 1999 Sydney hailstorm. *Natural Hazard Quarterly* 5, issue 2, 4 p.

## Chapter 3

- Andrews, K.E and Blong, R.J., 1997. March 1990 hailstorm damage in Sydney, Australia. *Natural Hazards* 16, 1-13.
- Bailey, T.C. and Gatrell, A.C., 1996. *Interactive Spatial Data Analysis*. Longman, London, 413 p.
- Browning, K.A., 1977. The structure and mechanisms of hailstorms. In G.B. Foote and C.A. Knight (eds.) *Hail: A Review of Hail Science and Hail Suppression*. Meteor. Monogr. 16, Amer. Meteor. Soc., Boston, 1-43.
- Buckley, B.W., Leslie, L.M. and Wang, Y., 2001. The Sydney hailstorm of April 14, 1999: Synoptic description and numerical simulation. *Meteorol. Atmos. Phys.* 76, 167-82.
- Changnon, S.A., 1971. Note on hailstone size distribution. *J. Appl. Meteorol.* 10, 168-70.
- Changnon, S.A., 1977. Scales of hail. *J. Appl. Meteorol.* 16, 626-48.
- Changnon, S.A., 1999. Data and approaches for determining hail risk in the contiguous United States. *J. Appl. Meteorol.* 38, 1730-39.
- Changnon, S.A. and Changnon, D., 2000. Long-term fluctuations of hail incidents in the United States. *J. Climate* 13, 658-64.
- Changnon, S.A., Changnon D., Fosse E.R., Hoganson, D.C., Roth, R.J. and Totsch, J.M., 1997. Effects of recent weather extremes on the insurance industry: Major implications for the atmospheric sciences. *Bull. Amer. Meteor. Soc.* 78, 425-35.
- Charlton, R.B., Kachmann, B.M. and Wojtiw, L., 1995. Urban hailstorms: a view from Alberta. *Natural Hazards* 12, 29-75.

- Charlton, R.B., 1998. The Edmonton Tornado and Hailstorm: A Decade of Research. *Bulletin Canadian Meteorological and Oceanographic Society (CMOS)*, Ottawa, Canada, vol. 26, 56 p.
- Dessens, J., 1995. Severe convective weather in the context of night time global warming. *Geophys. Res. Lett.* 22, 1241-44.
- Etkin, D.A., Myers, M.F., 2000. Thunderstorms in a social context. In R. Jr. Pielke and R. Sr. Pielke (eds.) *Storms*. Volume II, Routledge Hazards and Disasters Series, Routledge, London, 43-59.
- Federer, B., Waldvogel, A., Schmid, W., Schiesser, H.H., Hampel, F., Schweingruber, M., Stahel, W., Bader, J., Mezeix, J.F., Doras, N., d'Aubigny, G., DerMegreditchian and G., Vento, D., 1986. Main results of Grossversuch IV. *J. Appl. Meteorol.* 25, 917-57.
- Foote, G.B. and Knight C.A., 1979. Results of a randomized hail suppression experiment in northeast Colorado. Parts 1-9. *J. Appl. Meteorol.* 18, 1526-39.
- Geotis, S.G., 1963. Some radar measurements of hailstorms. *J. Appl. Meteorol.* 2, 270-75.
- Giaiotti, D., Ganesini, E. and Stel, F., 2001. Heuristic considerations pertaining to hailstone size distributions in the plain of Friuli-Venezia Giulia. *Atmos. Res.* 57, 269-88.
- GVB, 1999. *Geschäftsbericht*, Gebäudeversicherung des Kantons Bern, Berne, Switzerland, 27 p.
- GVL, 1998. *Geschäftsbericht*, Gebäudeversicherung des Kanton Luzern, Lucerne, Switzerland, 40 p.
- Haase-Straub, S., Heimann, D., Hauf, T. and Smith, R.K., 1994. *The squall line of 21 July 1992 in Switzerland and southern Germany – a documentation*. DLR-Forschungsbericht 94-18, 226 p.
- Hill, C., 1996. May day. *Weatherwise* 49, 25-28.
- Hohl, R. and Schiesser, H.H., 2001. Cloud-to-ground lightning activity in relation to the radar-derived hail kinetic energy in Switzerland. *Atmos. Res.* 56, 375-96.
- Hohl, R., Schiesser, H.H. and Knepper, I., 2001. The use of weather radars to estimate hail damage to automobiles: An exploratory study in Switzerland. *Atmos. Res.*, accepted.
- Huntrieser, H., Schiesser, H.H., Schmid, W. and Waldvogel, A., 1997. Comparison of traditional and newly developed thunderstorm indices for Switzerland. *Wea. Forecasting* 12, 108-25.
- Joss, J. and Waldvogel, A., 1967. Ein Spektograph für Niederschlagstropfen mit automatischer Auswertung. *Pure Appl. Geophys.* 68, 240-46.
- Li, L., Schmid, W. and Joss, J., 1995. Nowcasting of motion and growth of precipitation over complex orography. *J. Appl. Meteorol.* 34, 1286-1300.
- Katz, R.W. and Garcia, R.R., 1981. Statistical relationships between hailfall and damage to wheat. *Agricult. Meteorol.* 24, 29-43.
- Leigh, R., 1998. *Hail damage to motor vehicles: an examination of economic costs*. Natural Hazards Research Centre, Macquarie University, Sydney, Australia, 9 p.

- Mahinfalah, M. and Skordahl, R.A., 1998. The effects of hail damage on the fatigue strength of a graphite/epoxy composite laminate. *Composite Structures*, 42, 101-106.
- Matson, R.J., Huggins A.W., 1980. The direct measurement of the size, shapes and kinematics of falling hailstones. *J. Atmos. Sci.* 37, 1107-25.
- Mezeix, J.F., Admirat, P., 1978. The measurement of hail at ground level. *Atmosph. Ocean* 16, 61-68.
- Munich Re, 1984. *Hagel*, Münchner Rückversicherungsgesellschaft, Munich, Germany, 56 p.
- Paterson, D.A. and Sankaran, R., 1994. Hail impact on Building envelopes. *J. Wind Engineer. Industr. Aerodyn.* 53, 229-46.
- PartnerRe, 1999. *Sydney Hailstorm, April 14, 1999*. PartnerResearch, PartnerRe Reinsurance Company Ltd., Zurich, Switzerland, 4 p.
- Paul, A., 1991. Studies of long-lived hailstorms in Saskatchewan, Canada from crop insurance data. *Natural Hazards* 4, 345-52.
- Prodi, F., 1974. Climatologia della grandine nella Valle Padana (1968-1972). *Rivista Italiana di Geophysica*, 23, 283-90.
- Render, P.M. and Pan, H., 1995. Experimental Studies into hail impact characteristics. *J. Propulsion Power* 11, 1224-30.
- Reuter, G.W. and Aktary, N., 1995. Convective and symmetrical instabilities and their effects on precipitation - Seasonal variations in central Alberta during 1990. *Mon. Wea. Rev.* 123, 153-62.
- Schiesser, H.H., 1990. Hailfall: the relationship between radar measurements and crop damage. *Atmos. Res.* 25, 559-82.
- Schiesser, H.H., 1998. *Wolkenparameter und Hagelkorngrößen von Hagelzellen mit Autoschadenpotential – Versuch einer Klimatologie anhand von Radardaten*. Projektskizze. Internal Report, Atmospheric Science ETH, Zurich, Switzerland, 10 p.
- Schiesser, H.H., Houze, R.A. Jr. and Huntrieser, H., 1995. The mesoscale structure of severe precipitation systems in Switzerland. *Mon. Wea. Rev.* 123, 2070-97.
- Schiesser, H.H., Waldvogel, A., Schmid, W. and Willemse, S. 1997. *Klimatologie der Stürme und Sturmsysteme anhand von Radar- und Schadendaten*. Schlussbericht NFP31. vdf Hochschulverlag, ETH Zurich, Switzerland, 132 p.
- Schiesser, H.H., Hohl, R. and Schmid, W., 1999. *Über die Beziehung Hagelfall-Gebäudeschäden: Fallstudie Luzern-Hagelsturm vom 21 Juli 1998*. Technical Report, Atmospheric Science ETH, Zurich, Switzerland, 37 p.
- Schmid, W. and Waldvogel, A., 1986. Radar hail profiles in Switzerland. *J. Climate and Appl. Meteorol.* 25, 1002-11.
- Schmid, W., Schiesser, H.H. and Waldvogel, A., 1992. The kinetic energy of hailfalls. Part IV: Patterns of hailpad and radar data. *J. Appl. Meteorol.* 31, 1165-78.
- Smith, S.B., Reuter, G.W. and Yau, M.K., 1998. The episodic occurrence of hail in central Alberta and the highveld of South Africa. *Atmosph. Ocean* 36, 169-178.



- Visser, P.J. and van Heerden J., 2000. Comparisons of hail kinetic energy derived from radar reflectivity with crop damage reports over the eastern Free State. *Water SA* 26, 91-96.
- VKF, 1999. *Schadenstatistik 1990-1998*. Vereinigung Kantonaler Feuerversicherungen. Berne, Switzerland, 12 p.
- Waldvogel, A. and Schmid, W., 1983. Single wavelength radar measurements of hailfall kinetic energy. *Preprints, 21st Conf. Radar Meteorology*, Edmonton, Amer. Meteor. Soc., 425-28.
- Waldvogel, A., Schmid, W. and Federer, B., 1978a. The kinetic energy of hailfalls, Part I. Hailstone spectra, *J. Appl. Meteorol.* 17, 515-20.
- Waldvogel, A., Federer, B., Schmid, W. and Mezeix, J.F., 1978b. The kinetic energy of hailfalls: Part II. Radar and hailpads. *J. Appl. Meteorol.* 17, 1680-93.
- Waldvogel, A., Federer, B. and Grimm, P., 1979. Criteria for the detection of hail cells. *J. Appl. Meteorol.* 18, 1521-25.
- Waldvogel, A., Federer, B. and Högl, D., 1980. On the correlation between hailpad and radar data. *Preprints, 19th Conf. Radar Meteorology*, Miami, Amer. Meteor. Soc., pp. 493-98.
- Witt, A., Eilts, M.D., Stumpf, G.J., Johnson, J.T., Michell, E.D. and Thomas, K.W., 1998. An enhanced hail detection algorithm for the WSR-88D. *Wea. Forecasting*. 13, 286-303.
- Wojtiw, L. and Ewing, C., 1986. The relationship of time-integrated radar reflectivity with hail crop damage. *Preprints, 23rd Conf. Radar Meteorology*, Snowmass, Amer. Meteor. Soc., 23-26.
- Yeo, S., Leigh, R. and Kuhnel, I., 1999. The April 1999 Sydney hailstorm. *Natural Hazard Quarterly* 5, issue 2, 4 p.

## Chapter 4

- Baker, M.B. and Dash, J.G., 1994. Mechanism of charge transfer between colliding ice particles in thunderstorms. *J. Geophys. Res.* 99, 10621-26.
- Branwick, M.L. and Doswell, C.A. III. 1992. An observation of the relationship between supercell structure and lightning ground strike polarity. *Wea. Forecasting* 7, 143-49.
- Carey, L.D. and Rutledge, S.A., 1995. Positive cloud-to-ground lightning in severe hailstorms: A multiparameter radar study. *Preprints, 27th Conf. Radar Meteorology*, Amer. Meteor. Soc., 629-32.
- Carey, L.D. and Rutledge, S.A., 1996. A multiparameter radar case study of the microphysical and kinematic evolution of a lightning producing storm. *Meteorol. Atmos. Phys.* 59, 33-64.
- Carey, L.D. and Rutledge, S.A., 1998. Electrical and multiparameter radar observations of a severe hailstorm. *J. Geophys. Res.* 103, 13979-14000.
- Changnon, S.A., 1992. Temporal and spatial relations between hail and lightning. *J. Appl. Meteor.* 31, 587-604.

- Curran, E.B. and Rust, W.D., 1992. Positive ground flashes produced by low-precipitation thunderstorms in Oklahoma on 26 April 1984. *Mon. Wea. Rev.* 120, 544-53.
- Dye, J.E., Winn, W.P., Jones, J.J. and Breed, D.W., 1989. The electrification of New Mexico thunderstorms 1. Relationship between precipitation development and the onset of electrification. *J. Geophys. Res.* 94, 8643-56.
- Engholm, C.D., Williams, E.R., Dole and R.M., 1990. Meteorological and electrical conditions associated with positive cloud-to-ground lightning. *Mon. Wea. Rev.* 118, 470-87.
- Federer, B., Waldvogel, A., Schmid, W., Schiesser, H.H., Hampel, F., Schweingruber, M., Stahel, W., Bader, J., Mezeix, J.F., Doras, N., d'Aubigny, G., DerMegreditchian G. and Vento, D., 1986. Main results of Grossversuch IV. *J. Appl. Meteorol.* 25, 917-57.
- Fister, V., von Rheinbaben H. and Zundl T., 1994. Analysis of the 1992 and 1993 lightning data in south Germany. *Preprints, 22nd Int. Conf. on Lightning Protection*, Budapest, 211-16.
- Geotis, S.G., 1963. Some radar measurements of hailstorms. *J. Appl. Meteorol.* 2, 270-75.
- Holle, R.L., Watson, A.I., Lopez, R.E., MacGorman, D.R. and Ortiz, R., 1994. The life cycle of lightning and severe weather in a 3-4 June 1985 PRE-STORM mesoscale convective system. *Mon. Wea. Rev.* 122, 1798-1808.
- Husson, D. and Pointin, Y., 1989. Quantitative estimation of the hailfall intensity with a dual polarization radar and a hailpad network. *Preprints, 24th Conf. Radar Meteorology*, Tallahassee, Amer. Meteor. Soc., 318-21.
- Jayarathne, E.R., Saunders, C.P.R. and Hallett, J., 1983. Laboratory studies of the charging of soft-hail during ice crystal interactions. *Quart. J. Roy. Meteor. Soc.* 109, 609-30.
- Joss, J. and Lee, R., 1995. The application of radar-gauge comparison to operational precipitation profile corrections. *J. Appl. Meteorol.* 34, 2612-30.
- Keighton, S.J., Bluestein, H.B. and MacGorman, D.R., 1991. The evolution of a severe mesoscale convective system: Cloud-to-ground lightning location and storm structure. *Mon. Wea. Rev.* 119, 1533-56.
- Keith, W.D. and Saunders, C.P.R., 1990. Further laboratory studies of the charging of graupel during ice crystal interactions. *Atmos. Res.* 25, 445-64.
- Knapp, D.I., 1994. Using cloud-to-ground lightning data to identify tornadic thunderstorm signatures and nowcast severe weather. *Nat. Wea. Assoc. Digest* 19, 35-42.
- Li, L., Schmid, W. and Joss, J., 1995. Nowcasting of motion and growth of precipitation over complex orography. *J. Appl. Meteorol.* 34, 1286-1300.
- MacGorman, D.R. and Nielson, K.E., 1991. Cloud-to-ground lightning in a tornadic storm on 8 May 1986. *Mon. Wea. Rev.* 119, 1557-74.
- MacGorman, D.R. and Burgess, D.W., 1994. Positive cloud-to-ground lightning in tornadic storms and hailstorms. *Mon. Wea. Rev.* 122, 1671-97.

- MacGorman, D.R. and Rust, W.D., 1998. *The Electrical Nature of Storms*. Oxford University Press. 422 p.
- Montandon, E., 1991. Blitzortung und Blitzparameterbestimmung – ein Forschungsprojekt der PTT. *Bull. SEV/VSE* 82, 27-32.
- Montandon, E., 1992. Lightning positioning and lightning parameter determination experiences and the results of the Swiss PTT research project. *Preprints, Int. Blitzschutzkonferenz*, Berlin, 6 p.
- Petersen, W.A., Rutledge, S.A. and Orville, R.E., 1996. Cloud-to-ground lightning observations from TOGA COARE: Selected results and lightning location algorithms. *Mon. Wea. Rev.* 124, 602-20.
- Radar Meteorology Group, 1993. *Monitoring of severe hailstorms in Switzerland 1992*, Atmospheric Science ETH Zürich, LAPETH-30, 163 p.
- Radar Meteorology Group, 1994. *Monitoring of severe hailstorms in Switzerland 1993*, Atmospheric Science ETH Zürich, LAPETH-31, 200 p.
- Radar Meteorology Group, 1995. *Monitoring of severe hailstorms in Switzerland 1994*, Atmospheric Science ETH Zürich, LAPETH-33, 243 p.
- Radar Meteorology Group, 1997. *Monitoring of severe hailstorms in Switzerland 1995 and 1996*, Atmospheric Science ETH Zürich, LAPETH-34, 300 p.
- Randell, S.C., Rutledge, S.A., Farley, R.D. and Helsdon, J.H. Jr., 1994. A modeling study on the early electrical development of tropical convection: Continental and oceanic (monsoon) storms. *Mon. Wea. Rev.* 122, 1852-77.
- Reap, R.M. and MacGorman, D.R., 1989, Cloud-to-ground lightning: climatological characteristics and relationships to model fields, radar observations, and severe local storms. *Mon. Wea. Rev.* 117, 518-35.
- Rubinstein, M., Montandon, E. and Ianoz, M., 1994. Analyzes of multi-station cloud lightning electric field pulses recorded with the Swiss LPATS network. *Preprints, 22nd Int. Conf. on Lightning Protection*, Budapest, 5 p.
- Rubinstein, M. and Montandon, E., 1996. The need for guidelines for the use of lightning data from lightning detection systems. *Preprints, 23rd Int. Conf. on Lightning Protection*, Florence, 6 p.
- Rust, W.D., Taylor, W.L., MacGorman, D.R. and Arnold, R.T., 1981a. Research on electrical properties of severe thunderstorms on the Great Plains. *Bull. Amer. Meteor. Soc.* 62, 1286-93.
- Rust, W.D., MacGorman, D.R. and Arnold, R.T., 1981b. Positive cloud-to-ground lightning flashes in severe storms. *Geophys. Res. Let.* 8, 791-94.
- Rust, W.D., MacGorman, D.R. and Goodman, S.J., 1985. Unusual positive cloud-to-ground lightning in Oklahoma storms on 13 May 1983. *Preprints, 14th Conf. on Severe Local Storms*, Indianapolis, Amer. Meteor. Soc., 372-75.

- Rutledge, S.A., Lu, C. and MacGorman, D.R., 1990. Positive cloud-to-ground lightning in mesoscale convective systems. *J. Atmos. Sci.* 47, 2085-2100.
- Rutledge, S.A. and Petersen, W.A., 1994. Vertical radar reflectivity structure and cloud-to-ground lightning in the stratiform region of MCS's: Further evidence for in-situ charging in the stratiform region. *Mon. Wea. Rev.* 122, 1760-76.
- Schiesser, H.H., 1990. Hailfall: the relationship between radar measurements and crop damage. *Atmos. Res.* 25, 559-82.
- Schiesser, H.H., Houze, R.A. Jr. and Huntrieser, H., 1995. The mesoscale structure of severe precipitation systems in Switzerland. *Mon. Wea. Rev.* 123, 2070-97.
- Schiesser, H.H., Waldvogel, A., Schmid, W. and Willemse, S., 1997. *Klimatologie der Stürme und Sturmsysteme anhand von Radar- und Schadendaten*. Schlussbericht NFP31. ETH Zurich, 132 p.
- Schmid, W. and Waldvogel A., 1986. Radar hail profiles in Switzerland. *J. Climate and Appl. Meteorol.* 25, 1002-11.
- Schmid, W., Schiesser, H.H. and Waldvogel, A., 1992. The kinetic energy of hailfalls. Part IV: Patterns of hailpad and radar data. *J. Appl. Meteorol.* 31, 1165-78.
- Seimon, A., 1993. Anomalous cloud-to-ground lightning in an F5-tornado-producing supercell thunderstorm on 28 August 1990. *Bull. Amer. Meteor. Soc.* 74, 189-203.
- Shafer, M.A., 1990. *Cloud-to-ground lightning in relation to digitized radar data in severe storms*. Master's thesis, Univ. Oklahoma, 93 p.
- Solomon, R. and Baker, M., 1994. Electrification of New Mexico thunderstorms. *Mon. Wea. Rev.* 122, 18787-88.
- Stolzenburg, M., 1990. Characteristics of the bipolar pattern of lightning locations observed in 1988 thunderstorms. *Bull. Amer. Meteor. Soc.* 71, 1331-38.
- Stolzenburg, M., 1994. Observation of high ground flash densities of positive lightning in summertime thunderstorms. *Mon. Wea. Rev.* 122, 1740-50.
- Stolzenburg, M., Rust, D.W. and Marshall, T.C., 1998. Electrical structure in thunderstorm convective regions. 3. Synthesis. *J. Geophys. Res.* 103, 14097-108.
- Waldvogel, A., Schmid, W. and Federer, B., 1978a. The kinetic energy of hailfalls, Part I. Hailstone spectra. *J. Appl. Meteorol.* 17, 515-20.
- Waldvogel, A., Federer, B., Schmid, W. and Mezeix, J.F., 1978b. The kinetic energy of hailfalls, Part II. Radar and hailpads. *J. Appl. Meteorol.* 17, 1680-93.
- Waldvogel, A., Federer, B. and Högl, D., 1980. On the correlation between hailpad and radar data. *Preprints, 19th Conf. Radar Meteorology*, Miami. Amer. Meteor. Soc., 493-98.
- Waldvogel, A. and Schmid, W., 1983. Single wavelength radar measurements of hailfall kinetic energy. *Preprints, 21st Conf. Radar Meteorology*, Edmonton, Amer. Meteor. Soc., 425-28.

- Watson, A.I., Holle, R.I. and López, R.E., 1995. Lightning from two national detection networks related to vertically integrated liquid water and echo-top information from WSR-88D radar. *Wea. Forecasting* 10, 592-605.
- Williams, E.R., 1989. The tripole structure of thunderstorms. *J. Geophys. Res.* 94, 13151-67.
- Williams, E.R., Boldi, B., Matlin A., Weber, M., Hodanish, S., Sharp, D., Goodman, S., Raghavan, R. and Buechler, D., 1999. The behavior of total lightning activity in severe Florida thunderstorms. *Atmos. Res.* 51, 245-65.
- Wojitiw, L. and Ewing, C., 1986. The relationship of time-integrated radar reflectivity with hail crop damage. *Preprints, 23rd Conf. Radar Meteorology*, Snowmass. Amer. Meteor. Soc., 23-26.

## Chapter 5

- Baker, M.B., Christian, H.J. and Latham, J., 1995. A computational study of the relationship linking lightning frequency and other thundercloud parameters. *Quart. J. Roy. Meteor. Soc.* 121, 1525-48.
- Changnon, S.A., 1992. Temporal and spatial relations between hail and lightning. *J. Appl. Meteor.* 31, 587-604.
- Cheze, J.L. and Sauvageot, H., 1997. Area-average rainfall and lightning activity. *J. Geophys. Res.* 102, 1707-15.
- Finke, U. and Hauf, T., 1996. The characteristics of lightning occurrence in southern Germany. *Contrib. Atmos. Phys.* 69, 361-74.
- Finke, U., 1999. Space-time correlations of lightning distributions. *Mon. Wea. Rev.* 127, 1850-61.
- Goodman, S.J., 1991. Sensor fusion techniques for predicting thunderstorm evolution using lightning and radar networks. *Preprints, 25th Int. Conf. Radar Meteorology*, Paris, Amer. Meteor. Soc., 97-102.
- Jameson, A.R., Murphy, M.J. and Krider, E.P., 1996. Multiple-parameter radar observations of isolated Florida thunderstorms during the onset of electrification. *J. Appl. Meteorol.* 35, 343-54.
- MacGorman, D.R. and Rust, W.D., 1998. *The Electrical Nature of Storms*. Oxford University Press. 422 p.
- Mohr, K.I., Toracinta, E.R., Zisper, E.J. and Orville, R.E., 1996. A comparison of WSR-88D reflectivities, SSM/I brightness temperatures and lightning for mesoscale convective systems in Texas. Part II: SSM/I brightness temperatures and lightning. *J. Appl. Meteorol.* 35, 919-39.
- Reap, R.M., 1994. Analysis and prediction of lightning strike distributions associated with synoptic map types over Florida. *Mon. Wea. Rev.* 122, 1698-1715.

- Schmid W., 1988. Hagelvorhersage mit Radar: Wolkenphysikalische Untersuchungen und ein statistisches Vorhersagemodell. Ph.D. thesis 8684, ETH Zurich, Switzerland, 113 p.
- Schmid, W., Schiesser, H.H. and Waldvogel, A., 1992. The kinetic energy of hailfalls. Part IV: Patterns of hailpad and radar data. *J. Appl. Meteorol.* 31, 1165-78.
- Solomon, R. and Baker, M., 1994. Electrification of New Mexico thunderstorms. *Mon. Wea. Rev.* 122, 18787-88.
- Steinacker, R., Dorninger, F., Wölfelmaier, F. and Krennert, T., 2000. Automatic tracking of convective cells and cell complexes from lightning and radar data. *Meteorol. Atmos. Phys.* 72, 101-10.
- Toracinta, E.R., Mohr, K.I., Zisper, E.J. and Orville, R.E., 1996. A comparison of WSR-88D reflectivities, SSM/I brightness temperatures and lightning for mesoscale convective systems in Texas. Part I: Radar reflectivity and lightning. *J. Appl. Meteorol.* 35, 902-08.
- Waldvogel, A., Schmid, W. and Federer, B., 1978a. The kinetic energy of hailfalls, Part I. Hailstone spectra. *J. Appl. Meteorol.* 17, 515-20.
- Waldvogel, A., Federer, B., Schmid, W. and Mezeix, J.F., 1978b. The kinetic energy of hailfalls, Part II. Radar and hailpads. *J. Appl. Meteorol.* 17, 1680-93.
- Watson, A.I., Lopez, R.E. and Holle, R.L., 1994. Diurnal cloud-to-ground lightning patterns in Arizona during the southwest monsoon. *Mon. Wea. Rev.* 122, 1716-25.

# Curriculum Vitae

Roman Marco Hohl

Born in St. Gallen, Switzerland on 14 June 1971

## Education

- 1978-1987 Primary and secondary school in Heerbrugg (SG), Switzerland
- 1987-1992 Kantonsschule Heerbrugg (SG), Switzerland  
*Matura: Typus C, Jan. 1992*
- 1992-1993 Genie rurale, Ecole Polytechnique Fédérale de Lausanne, Lausanne, Switzerland
- 1993-1998 Institute of Geography, University of Lausanne, Lausanne, Switzerland  
*Diploma thesis: July 1998*  
*Examiner: Prof. J. Winistörfer*  
*Advisors: Prof. F.H. Schweingruber, Dr. H.H. Schiesser*  
*Winner 2nd price for Ph.D. and diploma thesis in the field of wood research,*  
*Swiss Association of Wood Research (SAH), Zurich, Switzerland*
- 1996 Swiss Federal Institute for Forest, Snow and Landscape Research (WSL),  
Birmensdorf, Switzerland  
*Practical training (two months), advisor: Dr. J. Innes*
- 1998-2001 Institute of Geography, University of Fribourg, Fribourg, Switzerland  
Institute for Atmospheric Science, ETH, Zurich, Switzerland  
*Ph.D. student*  
*Examiner: Prof. M. Beniston*  
*Co-examiners: Prof. H. Richner, Dr. H.H. Schiesser*

## Presentations

- March 2000 Swiss Army, Weather Division of the Air Force  
*Oral presentation: Severe Thunderstorms and Tornadoes*
- Sept. 2000 International Agricultural Insurance Seminar, Locarno, Switzerland  
*Oral presentation: How to Make Climate-related Data and Satellite Technology Available for the Insurance Industry*
- March 2001 Swiss Army, Weather Division of the Air Force  
*Oral presentation: Extreme Precipitation Events in the Alps*
- Sept. 2001 International Agricultural Insurance Seminar, Diessenhofen, Switzerland  
*Oral presentation: Pricing Methodology for Crop Products*

## International Conferences

- Sept. 1999 2nd Ph.D. Students Meeting in the Field of Natural Hazards, Davos, Switzerland  
*Oral presentation: Lightning Location Measurements and their Contribution to Detect Severe Hailstorms and Storm Systems*
- Feb. 2000 1st Conference on European Tornadoes and Severe Storms, Toulouse, France  
*Oral presentation: Lightning Patterns and their Relation to the Radar-Derived Hail Kinetic Energy*
- Oct. 2000 3rd European Conference on Applied Climatology, Pisa, Italy
- Sept. 2001 5th International Workshop on Physics of Lightning, Nagoya, Japan  
*Oral presentation: Nowcasting of Severe Thunderstorms: The Relationship between Cloud-to-Ground Lightning Activity and Hailfall Intensity*



## List of Publications

- Schiesser, H.H., Hohl, R. and Schmid, W., 1999. *Über die Beziehung Hagelfall-Gebäudeschäden: Fallstudie Luzern-Hagelsturm vom 21 Juli 1998*. Technical Report, Atmospheric Science ETH, Zurich, Switzerland, 37 p.
- Aller, D., Schiesser, H.H. and Hohl, R., 2001. *Hagelschaden Potential Studie*. Gebäudeversicherung Bern, Technical Report, 15 p.
- Hohl, R., Schiesser, H.H., 2001. Cloud-to-ground lightning activity in relation to the radar-derived hail kinetic energy in Switzerland. *Atmospheric Research* 56, 375-96.
- Hohl, R., Schiesser, H.H. and Knepper, I., 2001. The use of weather radars to estimate hail damage to automobiles: An exploratory study in Switzerland. *Atmospheric Research*. Accepted September 2001.
- Hohl, R., Schiesser, H.H. and Aller, D., 2001. Hailfall: The relationship between hail kinetic energy and hail damage to buildings. *Atmospheric Research*. Submitted October 2001.
- Hohl, R., Schweingruber, F.H. and Schiesser, H.H., 2001. Reconstruction of severe hailstorm occurrence with tree rings: A case study in central Switzerland. *Tree-Ring Research*. Submitted June 2001.

Zurich, 22 November 2001



## Acknowledgement

My interest for hailstorms and radar meteorology started when I was looking for a topic and an advisor for my diploma thesis in early 1997. After a telephone call and brief meeting with Dr. Hans-Heinrich Schiesser of the Institute for Atmospheric Science ETH (LAPETH), I found an advisor with whom I could share the fascination for hailstorms. After having finished my diploma thesis in summer 1998, Hans-Heinrich asked me if I would like to continue working in the field of hailstorm research and radar meteorology as a Ph.D. student with him as an adviser. As at that time no professor was directly responsible for radar meteorology at ETH, Prof. Beniston (University of Fribourg) kindly agreed to be my referent, while I was working and reporting from the LAPETH in Zurich-Hönggerberg.

Writing the last lines of this thesis, I can look back to a very exciting and instructive time with Hans-Heinrich, both on a scientific as well as on a personal level.

I would like to express my gratitude to the examiner of this thesis, Prof. Martin Beniston, director of the Institute of Geography from the University of Fribourg. Although Prof. Beniston was busy leading his institute, he always had the time to discuss my research results and supported my ideas and conference wishes. I am also grateful to my co-examiner, Prof. Hans Richner (LAPETH), with whom I had many fruitful discussions on different topics of this thesis.

My particular thanks goes to the people that collaborated on the three articles contained in this thesis and provided the necessary data: Peter Reinhard and Ingeborg Knepper (Winterthur Insurance) for the hail damage claim data on automobiles, Dörte Aller and Peter Kamber (Intercantonal Union of Reinsurance) for the damage claim data on buildings, Eric Montandon (Swisscom) for lightning location data of the Swiss LPTS and Dr. Uli Finke (University of Hannover) for the corresponding Bayernwerk LPATS data. A special thanks goes to Prof. Zev Levin (Tel Aviv University) who spent a sabbatical semester at the LAPETH and Dr. Donald MacGorman (NSSL, Oklahoma) whom I met at IWPL 2001, for inspiring discussions on lightning activity and severe thunderstorms.

My thanks goes to all LAPETH-colleagues for the enjoyable work atmosphere, inspiring discussions and their support, particularly Marc Wüest my office and Ph.D. colleague, Dr. Willi Schmid, Dr. Eszter Barthasy, Dr. Susanne Mecklenburg and Donat Högel. I would also like to thank Prof. Huw Davies who supported and encouraged me working as an *external* Ph.D. student at the LAPETH.

I am particularly grateful to Dr. Erich Kasten and his team from PartnerRe Reinsurance Ltd who gave me the opportunity to start working as an underwriting assistant beside writing my Ph.D. thesis.

My heartfelt gratitude for my parents Ernst and Fridy as well as for my brother Andreas who always encouraged me. My biggest thanks goes to my wife Makiko who stood by me throughout my studies.